博士論文

Optical detection of symmetry breakings in ferroic materials

（光学現象を利用した強的秩序物質
における対称性の破れの検出）

林田　健志

Contents

Chapter 1
Introduction

1.1 Preface

Symmetry breaking is a fundamental concept in physics, referring to the phenomenon or property where a system transitions from a symmetrical state to an asymmetrical one. This concept has been extensively studied across various fields of physics. In condensed matter physics, an intriguing manifestation of symmetry breaking occurs in the form of ferroic orders. Representative examples of such ferroic orders include ferromagnetism and ferroelectricity, which emerge from the breaking of time-reversal and space-inversion symmetries, respectively. Notably, research on (ferro)magnetism has a rich history spanning millennia, and magnetic materials or products are found ubiquitously in modern society, such as commercial permanent magnets, motor rotors, and hard disk drives. It goes without saying that ferroelectricity, as well as another well-characterized ferroic order ferroelasticity, are also applied to various devices or products and contribute to the development of today's IT society.

The collective study of the above mentioned ferroic properties is called ferroics, and materials which show ferroic properties are referred to as ferroic materials. One of frontier research of ferroics is about multiferroic materials, in which two or more ferroic properties simultaneously appear [1]. Specifically, in materials that exhibit ferroelectricity and (ferro)magnetism in the same phase, polarization (magnetization) can be controlled by a magnetic (electric) field [2,3]. Such a crossover control is expected to be applied to power-saving memory devices [4]. Furthermore, multiferroic materials are great playgrounds at which various physical properties, such as crystal structures, spins, and electronic orbitals, are coupled and interacted to each other, giving rise to intriguing phenomena.

Studies on multiferroic materials have stimulated exploration of new types of ferroic properties. The representative example is ferrotoroidicity [5,6]. It is characterized by an ordered arrangement of magnetic vortices which is, for example, controlled by a simultaneous application of electric and magnetic fields [7,8]. Now, ferrotoroidicity is largely accepted as one of the ferroic orders and sometimes mentioned as the fourth ferroic order [9].

In addition to the above mentioned four types of ferroic order, the recent studies based on the symmetry of order parameters have predicted other distinct ferroic orders [5,10–14]. One example is ferroaxial order, which is characterized by a spontaneous ordering of a rotational distortion corresponding to a vortex arrangement of electric dipoles [12,15]. Some of those proposed ferroic orders are still hidden in materials, and exploring their properties could lead to discovery of new physical phenomena and functionalities. The first crucial step toward establishing such new ferroic candidates and widely recognizing them is their observation. For this purpose, using optical effects associated with

each ferroic order proves effective. The symmetry breaking in materials is closely linked to optical phenomena that are permitted in each ferroic order. For example, the Faraday effect, that is, rotation of the polarization plane of transmitted light, is coupled with the ferromagnetic order, and providing a means to detect spontaneous magnetization and distinguish its direction in materials. One advantage of utilizing optical phenomena is the ease of obtaining two-dimensional distributions, which allows one to visualize spatial distributions of ferroic orders, i.e., domain structures. Such visualization of domains not only provides important information including the domain size or shape but also serves to emphasize the existence of the ferroic order.

In this thesis, we demonstrate optical detection of symmetry breakings in three novel types of ferroic orders: ferrochiral, ferroaxial, and ferromonopolar orders. In this chapter, we provide an overall introduction by reviewing the definition of ferroic orders and discussing their classification based on vectorlike properties.

1.2 Definition of ferroic

The concept of ferroic was introduced by Aizu in 1970 [16]. At the bigging of that paper, it is mentioned as:

A crystal is provisionally referred to as being "ferroic" when it has two or more orientation states in the absence of magnetic field, electric field, and mechanical stress and can shift from one to another of these states by means of a magnetic field, an electric field, a mechanical stress, or a combination of these. [16].

This is the widely accepted definition of ferroic orders, and initially it was a general term of ferromagnetic, ferroelectric, and ferroelastic orders. Such a characteristic of ferroic orders is well depicted by a hysteresis relationship between an order parameter and an external field as shown in Fig. 1.1.

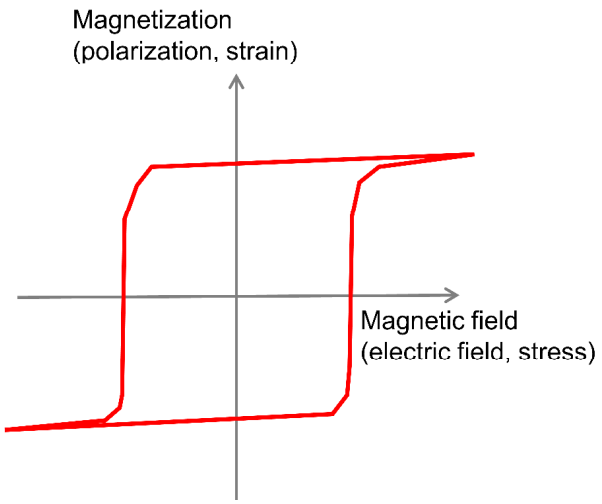

Fig. 1.1 Schematic illustration of a hysteresis loop. Ferroic materials show a spontaneous order (polarization, magnetization or stress) even in the absence of an external field (electric field, magnetic field or stress), and the sign of it can be switched by applying an external field.

As mentioned above, the fundamental characteristic of ferroic orders is the controllability of their order parameters or the orientation states (domain states) through the application of an external field (or combination of two or more different external fields). To achieve such a control using a finite magnitude of field, a ferroic crystal should have a certain non-ferroic structure (called prototype) in its high symmetry phase. Aizu classified the relationships between prototype point groups and ferroic point groups by introducing the concept of species. In total, there are 773 species, 212 of which are nonmagnetic [16,17].

Some of the 773 species have orientation states which are difficult to be shifted to one another by the application of external fields. In the 'narrow' definition of ferroic introduced above, materials which exhibit a phase transition corresponding to one of such species are not appropriate to be called ferroic materials. However, in ref. [16], Aizu mentioned to the 'broad' definition based on the existence of phase transition, irrespective of whether the state shift by applying external fields can be or has already been achieved. In this thesis, we adopt this broad definition for a comprehensive discussion. We note that some of the ordered states (the low symmetry states) are characterized by staggered (antiferroic) arrangements of order parameters, rather than uniform ordering. In Aizu's broad definition, such staggered orderings are also classified as ferroics. However, within the scope of this thesis, the term 'ferroic orders' will refer to uniform orders unless specifically stated otherwise. In the next section, we introduce the classification of such ferroic orders focusing on the symmetry of order parameters.

1.3 Classification of ferroic orders

Since the pioneering work by Aizu mentioned above, various approaches have been proposed for the classification of ferroic orders. For example, Newnham and Cross introduced the classification based on the orders of external fields that drive domain switching, termed as Primary, Secondary, and Tertiary ferroics [18–20]. Primary ferroics include ferroelectric and ferromagnetic order, where the external fields for reorienting domain states are the first order; electric field (**E**) and magnetic field (**H**), respectively. Secondary ferroics include ferro-magnetoelectric order, where the driving force of the reorientation of domain states is the second order; E_iH_j, where i and j refer to cartesian coordinates. Subsequently, Schmid extended this classification by introducing a toroidal moment (the concept of toroidal order was introduced by Dubovik and coworkers [21,22]) and ferrotoroidic order [5,7].

Recently, novel approaches have been proposed to further extend these classifications, expanding our understanding of ferroic orders. One such approach is the classification based on (cluster-)multipoles [23–28]. In these studies, not only the conventional electric dipole, magnetic dipole, or magnetic toroidal dipole are considered, but also higher orders of multipoles and a new class of electric toroidal multipoles are defined. This classification based on multipoles is effective especially for classification of complicated magnetic ordering. We will discuss further details of cluster multipoles in Chapter 5.

In the followings, we discuss another approach focusing on vectorlike (one-dimensional) properties introduced by Hlinka [11] and Cheong and coworkers [13,14,29]. This classification is useful

for broadly classifying ferroic orders and gaining an intuitive understanding of their related phenomena.

1.3.1 Eight types of vectorlike properties

Mathematically, vectors are classified into two categories: polar and axial vectors. A polar vector characterizes a property which has magnitude and direction, and changes its sign under space inversion ($\overline{1}$). In solid state physics, a representative polar vector symmetry property is an electric polarization. An axial vector is associated with a curl of polar vector or a cross-product of two polar vectors. It represents a rotation and does not change its sign under parity inversion. A representative axial vector symmetry property is magnetization, which has a time-odd symmetry.

In addition to the above-mentioned two common vectors, one can consider other two types of vectorlike (one-dimensional) properties by incorporating directional structures, which are characterized by a magnitude, an axis and a geometrical sign [11]. When taking into account the time-reversal symmetry, there are a total of eight types of vectorlike properties. Figure 1.2 depicts the eight types of vectorlike properties. The symmetry of these properties is characterized by the alteration in their signs when the following five operations are implemented.

(1) Identity operation (*E*), which is equivalent to a two-fold rotation around the axis parallel to the primary axis ($2_{\parallel}$)

(2) Time-reversal operation ($1'$)

(3) Inversion operation ($\overline{1}$), which is equivalent to a mirror operation whose mirror plane perpendicular to the primary axis ($m_{\perp}$)

(4) Two-fold rotation around the axis perpendicular to the primary axis ($2_{\perp}$)

(5) Mirror operation whose mirror plane containing the primary axis ($m_{\parallel}$)

While all rotational operations around the axis parallel to the primary axis are symmetry operations, rotational symmetries around the axis perpendicular to the primary axis, except for $2_{\perp}$, are broken. It should be noted that when these properties emerge in crystals, only two-, three-, four- and six-fold rotational symmetries are permitted around the primary (principal) axis.

The table in Fig. 1.2 summarizes the action of the five operations on each vectorlike property. While the conventional vectors change their signs under the $2_{\perp}$ operation, the additional two properties ($\mathcal{N}$ and $\mathcal{C}$) remain invariant, which are termed as bidirector [11]. In Fig. 1.3, the representative examples of objects, related ferroic orders and optical property are summarized. In the following, we briefly describe characteristics of each property. Here, we have adopted the symbol notations by Cheong and coworkers [14] with a few changes.

$\mathcal{N}$: Neutral bidirector. Fully symmetric property with no broken symmetry. It is related to the so-called director defined in nematic phases of liquid crystals [30]. In addition, species which allow for $\mathcal{N}$ is equivalent to those which allow for ferroelasticity [31]. Thus, $\mathcal{N}$ is closely related to ferroelasticity, but we note that a good order parameter of ferroelasticity is a strain tensor.

$\mathcal{N}'$: Time-odd neutral bidirector. A neutral bidirector with time-reversal symmetry broken. $\mathcal{N}'$ can be

an order parameter of directional antiferromagnetic order.

$\mathcal{C}$: Chiral bidirector. A bidirector with broken inversion and mirror symmetries. $\mathcal{C}$ is represented by a helix structure. The sign of $\mathcal{C}$ can reflect enantiomorphism of objects.

$\mathcal{C}'$: Time-odd chiral bidirector (False-chiral bidirector). A bidirector with broken inversion, mirror and time-reversal symmetries. $\mathcal{C}'$characterizes the monopole type (all-in or all-out) arrangement of magnetic dipoles, which is found in, for example, Cr_2O_3 [32,33]. The term of 'false' chirality was introduced as a contrast to the 'true' chirality in which time-reversal symmetry is preserved [34].

$\mathcal{P}$: Polar vector. Inversion symmetry is broken. The representative example is polarization.

$\mathcal{P}'$: Time-odd polar vector. A polar vector with broken time-reversal symmetry. Propagating wave vector (**k**) and magnetic toroidal moment (**T**) have the symmetry of $\mathcal{P}'$.

$\mathcal{A}$: Axial vector. Mirror symmetry is broken. Rotational distortion and ferroaxial moment (**A**) [or called electric toroidal moment (**G**)] are characterized by $\mathcal{A}$.

$\mathcal{A}'$: Time-odd axial vector. Mirror and time-reversal symmetries are broken. The representative example is magnetization (**M**).

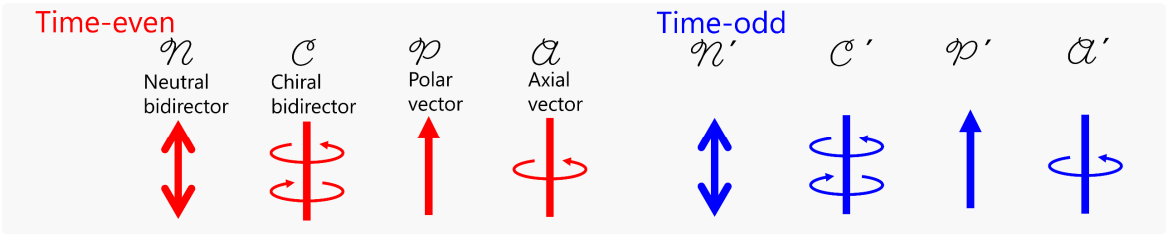

	$\mathcal{N}$	$\mathcal{C}$	$\mathcal{P}$	$\mathcal{A}$	$\mathcal{N}'$	$\mathcal{C}'$	$\mathcal{P}'$	$\mathcal{A}'$
$1'$	+1	+1	+1	+1	−1	−1	−1	−1
$E\,(2_{//})$	+1	+1	+1	+1	+1	+1	+1	+1
$2_{\perp}$	+1	+1	−1	−1	+1	+1	−1	−1
$\bar{1}\,(m_{\perp})$	+1	−1	−1	+1	+1	−1	−1	+1
$m_{//}$	+1	−1	+1	− 1	+1	−1	+1	− 1

Fig. 1.2 Eight types of vectorlike properties. In the schematical illustration of each property, time-even (time-odd) properties are depicted in red (blue) color. In the table, +1 (–1) stands for the invariance (sign reversal) under the operation of X (X = $1'$, E, $2_{\perp}$, $\bar{1}$, and $m_{\parallel}$). This table was made based on refs. [11,14].

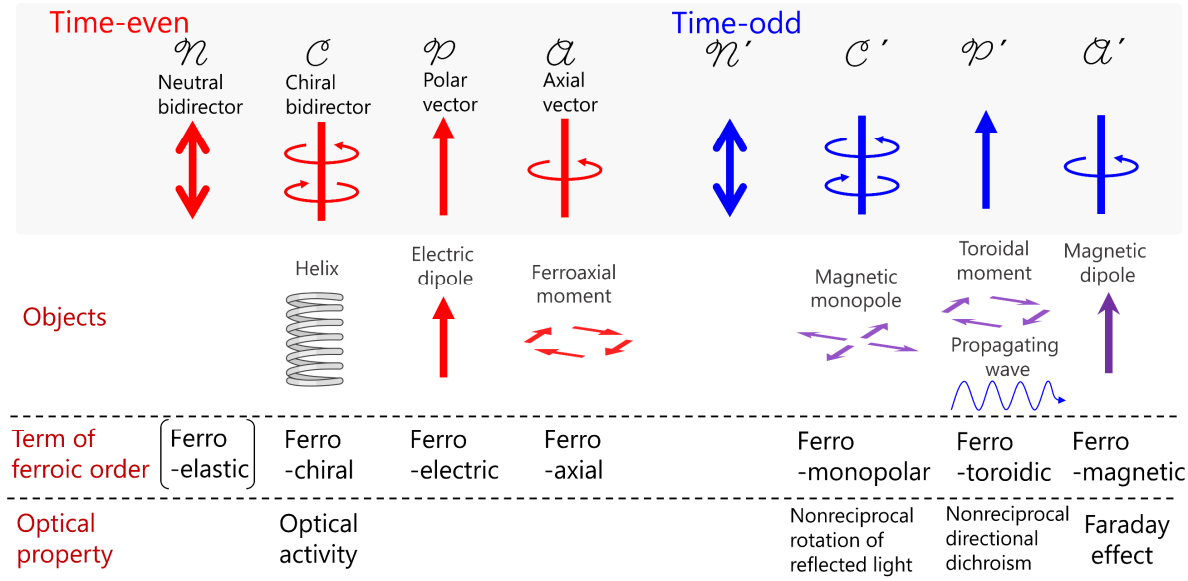

Fig. 1.3 Examples of objects, related ferroic orders and optical property of vectorlike properties.

1.3.2 Ferrochiral, ferroaxial, and ferromonopolar orders

If a phase transition is characterized by an order parameter with the symmetry of $\mathcal{X}$ ($\mathcal{X} = \mathcal{N}, \mathcal{N}', \mathcal{C}, \ldots$), such an order can be referred to as ferro-$\mathcal{X}$ like order. Then, in addition to the well-established ferroelectric ($\mathcal{P}$), ferromagnetic ($\mathcal{A}'$), and ferrotoroidic ($\mathcal{P}'$) orders (and ferroelastic ($\mathcal{N}$) order), one can consider ferrochiral ($\mathcal{C}$), ferroaxial ($\mathcal{A}$), and ferromonopolar ($\mathcal{C}'$) orders (see also Fig. 1.3). In principle, ferrochiral and ferroaxial orders are introduced in materials by structural phase transitions, while ferromonopolar order derive from magnetic ordering. Further details about each order will be given in Chapters 2, 3, and 5. In this thesis, we discuss these three distinct types of ferroic orders, particularly focusing on the observation of these orders and their related optical effects.

1.3.3 Symmetry of materials and phenomena

The abovementioned vectorlike properties are useful not only for classifying ferroic orders, but also for gaining intuitive insights into phenomena associated with each order, which is discussed as symmetry-operational similarity (SOS) in refs. [13,14]. Every physical phenomenon manifested by a crystal must possesses an equivalent or higher symmetry as the crystal itself, which is known as Neumann's principal. Consequently, if a given phenomenon is characterized by the same vectorlike property as an order in a crystal, it will be an excellent probe for the detection of the order. A good example is nonreciprocal directional dichroism (NDD), that is, asymmetry in absorption between two counterpropagating light beams. Both the toroidal moment **T** and the propagating light wave **k** have the symmetry of $\mathcal{P}'$, and thus NDD is expected to be allowed in ferrotoroidic systems. So far, NDD has been observed in several ferrotoroidic materials [35,36], and applied to visualization of ferrotoroidic domains [37,38]. Figure 1.4 shows the ferrotoroidic domains observed in Bi_2CuO_4 by spatial distribution measurements of NDD [38].

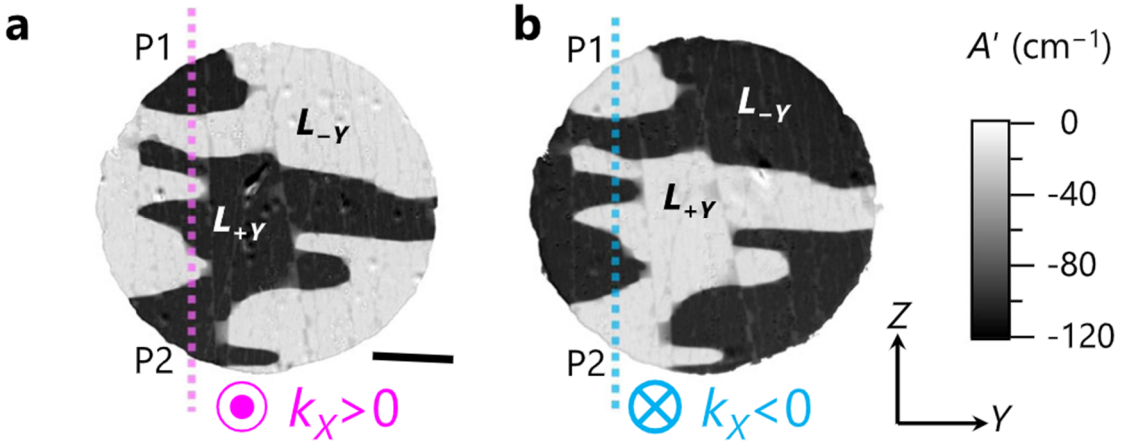

Fig. 1.4 Ferrotoroidic domains observed in Bi_2CuO_4 by NDD [38]. The contrasts of dark and bright correspond to the ferrotoroidic domains with opposite sign of **T**. The images in panels **a** and **b** correspond to two dimensional maps of absorption coefficient obtained with light propagating in opposite directions to each other. The contrast reversal between the two images suggests the nonreciprocity of the observed phenomenon. Scale bar: 0.2 mm.

1.3.4 Combination of different vectorlike properties

Assuming a situation where an external field is applied to a certain ordered state or where two or more distinct orders emerge simultaneously, it is beneficial to consider the resulting symmetry of combining two different vectorlike properties. Here, two situations are considered: the properties being parallel (dot product) and perpendicular (cross product) to each other. It should be noted that while the dot product of vectors mathematically yields a (pseudo-)scalar property, the focus of this discussion lies in the symmetrical similarity between the combination of two vectorlike properties and a single vectorlike property. The symmetry of dot products and cross products is summarized in Table 1.1 and 1.2, respectively, based on refs. [11,14]. For example, the dot product of $\mathcal{C}$ and $\mathcal{A}'$ exhibits the symmetry of $\mathcal{P}'$ ($\mathcal{C} \cdot \mathcal{A}' \approx \mathcal{P}'$, see Fig.1.5**a**), which well explains the optical effect of magnetochiral dichroism, that is, nonreciprocal absorption of two counter propagating light beams in magnetized chiral compounds [39–42] (see also Chapter 4). The cross product of $\mathcal{P}$ and $\mathcal{A}'$ also possesses the symmetry of $\mathcal{P}'$ ($\mathcal{P} \times \mathcal{A}' \approx \mathcal{P}'$, see Fig. 1.5**b**), which is consistent with that toroidal moment can be switched by the application of electric and magnetic fields orthogonal to each other [8,38].

Table 1.1 Dot product of vectorlike properties.

·	$\mathcal{n}$	$\mathcal{n}'$	$\mathcal{c}$	$\mathcal{c}'$	$\mathcal{p}$	$\mathcal{p}'$	$\mathcal{a}$	$\mathcal{a}'$
$\mathcal{n}$	$\mathcal{n}$	$\mathcal{n}'$	$\mathcal{c}$	$\mathcal{c}'$	$\mathcal{p}$	$\mathcal{p}'$	$\mathcal{a}$	$\mathcal{a}'$
$\mathcal{n}'$	$\mathcal{n}'$	$\mathcal{n}$	$\mathcal{c}'$	$\mathcal{c}$	$\mathcal{p}'$	$\mathcal{p}$	$\mathcal{a}'$	$\mathcal{a}$
$\mathcal{c}$	$\mathcal{c}$	$\mathcal{c}'$	$\mathcal{n}$	$\mathcal{n}'$	$\mathcal{a}$	$\mathcal{a}'$	$\mathcal{p}$	$\mathcal{p}'$
$\mathcal{c}'$	$\mathcal{c}'$	$\mathcal{c}$	$\mathcal{n}'$	$\mathcal{n}$	$\mathcal{a}'$	$\mathcal{a}$	$\mathcal{p}'$	$\mathcal{p}$
$\mathcal{p}$	$\mathcal{p}$	$\mathcal{p}'$	$\mathcal{a}$	$\mathcal{a}'$	$\mathcal{n}$	$\mathcal{n}'$	$\mathcal{c}$	$\mathcal{c}'$
$\mathcal{p}'$	$\mathcal{p}'$	$\mathcal{p}$	$\mathcal{a}'$	$\mathcal{a}$	$\mathcal{n}$	$\mathcal{n}$	$\mathcal{c}'$	$\mathcal{c}$
$\mathcal{a}$	$\mathcal{a}$	$\mathcal{a}'$	$\mathcal{p}$	$\mathcal{p}'$	$\mathcal{c}$	$\mathcal{c}'$	$\mathcal{n}$	$\mathcal{n}'$
$\mathcal{a}'$	$\mathcal{a}'$	$\mathcal{a}$	$\mathcal{p}'$	$\mathcal{p}$	$\mathcal{c}'$	$\mathcal{c}$	$\mathcal{n}'$	$\mathcal{n}$

Table 1.2 Cross product of vectorlike properties.

×	$\mathcal{n}$	$\mathcal{n}'$	$\mathcal{c}$	$\mathcal{c}'$	$\mathcal{p}$	$\mathcal{p}'$	$\mathcal{a}$	$\mathcal{a}'$
$\mathcal{n}$	$\mathcal{a}$	$\mathcal{a}'$	$\mathcal{p}$	$\mathcal{p}'$	$\mathcal{c}$	$\mathcal{c}'$	$\mathcal{n}$	$\mathcal{n}'$
$\mathcal{n}'$	$\mathcal{a}'$	$\mathcal{a}$	$\mathcal{p}'$	$\mathcal{p}$	$\mathcal{c}'$	$\mathcal{c}$	$\mathcal{n}'$	$\mathcal{n}$
$\mathcal{c}$	$\mathcal{p}$	$\mathcal{p}'$	$\mathcal{a}$	$\mathcal{a}'$	$\mathcal{n}$	$\mathcal{n}'$	$\mathcal{c}$	$\mathcal{c}'$
$\mathcal{c}'$	$\mathcal{p}'$	$\mathcal{p}$	$\mathcal{a}'$	$\mathcal{a}$	$\mathcal{n}'$	$\mathcal{n}$	$\mathcal{c}'$	$\mathcal{c}$
$\mathcal{p}$	$\mathcal{c}$	$\mathcal{c}'$	$\mathcal{n}$	$\mathcal{n}'$	$\mathcal{a}$	$\mathcal{a}'$	$\mathcal{p}$	$\mathcal{p}'$
$\mathcal{p}'$	$\mathcal{c}'$	$\mathcal{c}$	$\mathcal{n}'$	$\mathcal{n}$	$\mathcal{a}'$	$\mathcal{a}$	$\mathcal{p}'$	$\mathcal{p}$
$\mathcal{a}$	$\mathcal{n}$	$\mathcal{n}'$	$\mathcal{c}$	$\mathcal{c}'$	$\mathcal{p}$	$\mathcal{p}'$	$\mathcal{a}$	$\mathcal{a}'$
$\mathcal{a}'$	$\mathcal{n}'$	$\mathcal{n}$	$\mathcal{c}'$	$\mathcal{c}$	$\mathcal{p}'$	$\mathcal{p}$	$\mathcal{a}'$	$\mathcal{a}$

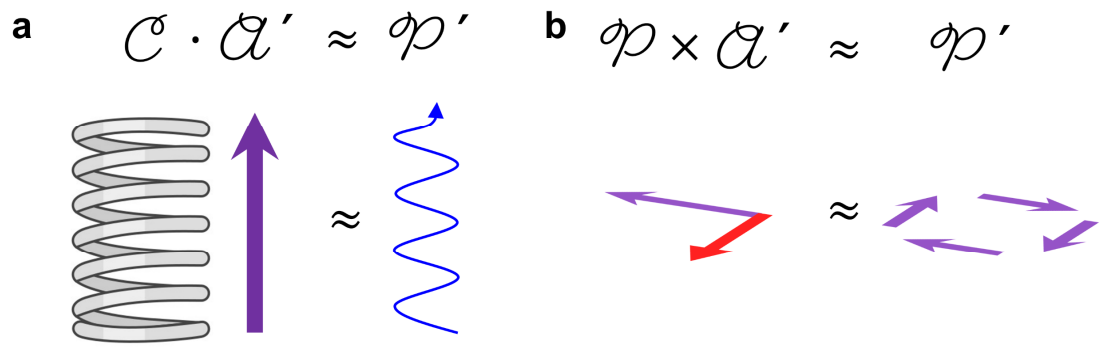

Fig. 1.5 Schematical illustration of symmetrical similarity between the combination of two vectorlike properties and a single vector property. **a**, Dot product of $\mathcal{c}$ (helix) and $\mathcal{a}'$ (magnetization) has the similar symmetry with $\mathcal{p}'$ (propagating light). **b**, Cross product of $\mathcal{p}$ (electric field) and $\mathcal{a}'$ (magnetic field) has the similar symmetry with $\mathcal{p}'$ (toroidal moment).

1.4 Purpose of this thesis

The main purpose of this thesis is the investigation of three types of ferroic orders: ferrochiral, ferroaxial, and ferromonopolar orders. Specifically, our focus is on optical phenomena that arise from the spontaneous and/or field-induced symmetry breakings in each order.

In Chapter 2, we examine ferrochiral order in $Ba(TiO)Cu_4(PO_4)_4$. By performing spatial distribution measurements of optical rotation over a wide temperature range, we visualize the emergence of ferrochiral order in $Ba(TiO)Cu_4(PO_4)_4$. Furthermore, we demonstrate switching of ferrochiral domains by laser irradiation.

Chapter 3 investigates ferroaxial order in two ferroaxial materials $NiTiO_3$ and $RbFe(MoO_4)_2$. By obtaining two dimensional maps of the linear electrogyration effect, that is, electric-field-induced optical rotation, we achieve the first direct observation of ferroaxial domains. In addition, detailed crystal structure analysis is performed by using x-ray or neutron diffraction methods, and we identify the relationship between the crystal structure and the optical effect of electrogyration.

Chapter 4 delves into a novel optical phenomenon of electric-field-induced magnetochiral dichroism in ferroaxial $NiTiO_3$. We expect that ferroaxial systems exhibit nonreciprocity under the simultaneous application of electric and magnetic fields, and demonstrate it by performing spectral measurements in the near-infrared regions. Through a discussion based on the electronic structure, we gain deep insights into the observed phenomenon.

In Chapter 5, we explore nonreciprocal optical effect related to ferromonopolar order in the archetypical magnetoelectric antiferromagnet Cr_2O_3. Our focus lies on the three different effects: the electric field-induced Faraday effect, the electric field-induced magnetic circular dichroism, and the spontaneous nonreciprocal rotation of reflected light. By measuring spectra of the former two effects, we observe relatively large enhancements of the effects in the visible light region. Furthermore, we demonstrate visualizing ferromonopolar domains in Cr_2O_3 by obtaining spatial distributions of all three nonreciprocal effects.

Finally, in Chapter 6, we summarize the results of this thesis and discuss prospects.

References

[1] H. Schmid, *Multi-Ferroic Magnetoelectrics*, Ferroelectrics **162**, 317 (1994).

[2] T. Kimura, T. Goto, H. Shintani, K. Ishizaka, T. Arima, and Y. Tokura, *Magnetic Control of Ferroelectric Polarization*, Nature **426**, 55 (2003).

[3] A. N. Spaldin and M. Fiebig, *The Renaissance of Magnetoelectric Multiferroics*, Science **309**, 391 (2005).

[4] J. F. Scott, *Multiferroic Memories*, Nat. Mater. **6**, 256 (2007).

[5] H. Schmid, *On Ferrotoroidics and Electrotoroidic, Magnetotoroidic and Piezotoroidic Effects*, Ferroelectrics **252**, 41 (2001).

[6] B. B. Van Aken, J. P. Rivera, H. Schmid, and M. Fiebig, *Observation of Ferrotoroidic Domains*, Nature **449**, 702 (2007).

[7] H. Schmid, *Some Symmetry Aspects of Ferroics and Single Phase Multiferroics*, J. Phys. Condens. Matter **20**, 434201 (2008).

[8] A. S. Zimmermann, D. Meier, and M. Fiebig, *Ferroic Nature of Magnetic Toroidal Order*, Nat. Commun. **5**, 4796 (2014).

[9] S. Gnewuch and E. E. Rodriguez, *The Fourth Ferroic Order: Current Status on Ferrotoroidic Materials*, J. Solid State Chem. **271**, 175 (2019).

[10] V. Gopalan and D. B. Litvin, *Rotation-Reversal Symmetries in Crystals and Handed Structures*, Nat. Mater. **10**, 376 (2011).

[11] J. Hlinka, *Eight Types of Symmetrically Distinct Vectorlike Physical Quantities*, Phys. Rev. Lett. **113**, 165502 (2014).

[12] J. Hlinka, J. Privratska, P. Ondrejkovic, and V. Janovec, *Symmetry Guide to Ferroaxial Transitions*, Phys. Rev. Lett. **116**, 177602 (2016).

[13] S.-W. Cheong, *SOS: Symmetry-Operational Similarity*, npj Quantum Mater. **4**, 53 (2019).

[14] S.-W. Cheong, S. Lim, K. Du, and F.-T. Huang, *Permutable SOS (Symmetry Operational Similarity)*, npj Quantum Mater. **6**, 58 (2021).

[15] R. D. Johnson, S. Nair, L. C. Chapon, A. Bombardi, C. Vecchini, D. Prabhakaran, A. T. Boothroyd, and P. G. Radaelli, *$Cu_3Nb_2O_8$: A Multiferroic with Chiral Coupling to the Crystal Structure*, Phys. Rev. Lett. **107**, 137205 (2011).

[16] K. Aizu, *Possible Species of Ferromagnetic, Ferroelectric, and Ferroelastic Crystals*, Phys. Rev. B **2**, 754 (1970).

[17] K. Aizu, *Possible Species of "Ferroelastic" Crystals and of Simultaneously Ferroelectric and Ferroelastic Crystals*, J. Phys. Soc. Jpn. **27**, 387 (1969).

[18] R. E. Newnham, *Domains in Minerals*, Am. Mineral. **59**, 906 (1974).

[19] R. E. Newnham and L. E. Cross, *Symmetry of Secondary Ferroics. I*, Mater. Res. Bull. **9**, 927 (1974).

[20] R. E. Newnham and L. E. Cross, *Symmetry of Secondary Ferroics. II*, Mater. Res. Bull. **9**, 1021 (1974).

[21] V. M. Dubovik, L. A. Tosunyan, and V. V. Tugushev, *Axial Toroidal Moments in Electrodynamics and Solid-State Physics*, Zh. Eksp. Teor. Fiz **90**, 590 (1986).

[22] V. M. Dubovik and V. V. Tugushev, *Toroid Moments in Electrodynamics and Solid-State Physics*, Phys. Rep. **187**, 145 (1990).

[23] N. A. Spaldin, M. Fiebig, and M. Mostovoy, *The Toroidal Moment in Condensed-Matter Physics and Its Relation to the Magnetoelectric Effect*, J. Phys. Condens. Matter **20**, 434203 (2008).

[24] M. T. Suzuki, T. Koretsune, M. Ochi, and R. Arita, *Cluster Multipole Theory for Anomalous Hall*

Effect in Antiferromagnets, Phys. Rev. B **95**, 094406 (2017).

[25] H. Watanabe and Y. Yanase, *Group-Theoretical Classification of Multipole Order: Emergent Responses and Candidate Materials*, Phys. Rev. B **98**, 245129 (2018).

[26] S. Hayami, M. Yatsushiro, Y. Yanagi, and H. Kusunose, *Classification of Atomic-Scale Multipoles under Crystallographic Point Groups and Application to Linear Response Tensors*, Phys. Rev. B **98**, 165110 (2018).

[27] M. Yatsushiro, H. Kusunose, and S. Hayami, *Multipole Classification in 122 Magnetic Point Groups for Unified Understanding of Multiferroic Responses and Transport Phenomena*, Phys. Rev. B **104**, 054412 (2021).

[28] H. Kusunose and S. Hayami, *Generalization of Microscopic Multipoles and Cross-Correlated Phenomena by Their Orderings*, J. Phys. Condens. Matter **34**, 464002 (2022).

[29] S.-W. Cheong, D. Talbayev, V. Kiryukhin, and A. Saxena, *Broken Symmetries, Non-Reciprocity, and Multiferroicity*, npj Quantum Mater. **3**, 19 (2018).

[30] S. T. Lagerwall, *Ferroelectric and Antiferroelectric Liquid Crystals*, Ferroelectrics **301**, 15 (2004).

[31] K. C. Erb and J. Hlinka, *Vector, Bidirector, and Bloch Skyrmion Phases Induced by Structural Crystallographic Symmetry Breaking*, Phys. Rev. B **102**, 024110 (2020).

[32] T. R. McGuire, E. J. Scott, and F. H. Grannis, *Antiferromagnetism in a Cr_2O_3 Crystal*, Phys. Rev. **102**, 1000 (1956).

[33] L. M. Corliss, J. M. Hastings, R. Nathans, and G. Shirane, *Magnetic Structure of Cr_2O_3*, J. Appl. Phys. **36**, 1099 (1965).

[34] L. D. Barron, *Molecular Light Scattering and Optical Activity (2nd Ed.)* (Cambridge University Press, Cambridge, 2004).

[35] V. Kocsis et al., *Identification of Antiferromagnetic Domains Via the Optical Magnetoelectric Effect*, Phys. Rev. Lett. **121**, 057601 (2018).

[36] T. Sato, N. Abe, S. Kimura, Y. Tokunaga, and T.-H. Arima, *Magnetochiral Dichroism in a Collinear Antiferromagnet with No Magnetization*, Phys. Rev. Lett. **124**, 217402 (2020).

[37] T. Sato, N. Abe, Y. Tokunaga, and T. H. Arima, *Antiferromagnetic Domain Wall Dynamics in Magnetoelectric $MnTiO_3$ Studied by Optical Imaging*, Phys. Rev. B **105**, 094417 (2022).

[38] K. Kimura, Y. Otake, and T. Kimura, *Visualizing Rotation and Reversal of the Néel Vector through Antiferromagnetic Trichroism*, Nat. Commun. **13**, 697 (2022).

[39] G. Wagnière and A. Meier, *The Influence of a Static Magnetic Field on the Absorption Coefficient of a Chiral Molecule*, Chem. Phys. Lett. **93**, 78 (1982).

[40] L. D. Barron and J. Vrbancich, *Magneto-Chiral Birefringence and Dichroism*, Mol. Phys. **51**, 715 (1984).

[41] G. L. J. A. Rikken and E. Raupach, *Observation of Magneto-Chiral Dichroism*, Nature **390**, 493 (1997).

[42] M. Atzori, G. L. J. A. Rikken, and C. Train, *Magneto-Chiral Dichroism: A Playground for Molecular Chemists*, Chem. Eur. J. **26**, 9784 (2020).

Chapter 2
Ferrochiral Domain Observation and Control

2.1 Introduction

Chirality, a concept that designates the handedness of a system, has long been a subject of considerable interest across various scientific disciplines, such as chemistry, biology, and solid-state physics [1,2]. In solid-state physics, chirality is closely related to wide array of physical phenomena and properties such as optical rotation [3], magneto-chiral dichroism [4], and formations of magnetic skyrmion lattice [5]. Despite the widely recognized importance of chirality in solid-state physics, it has not been acknowledged as a ferroic property. In this section, we first summarize classification of ferrochiral crystals based on crystallographic point group. We then introduce how the ferrochiral order is related to the optical phenomenon of optical rotation, which is used to observe the ferrochiral order. Finally, we present an overview of our target ferrochiral crystal $Ba(TiO)Cu_4(PO_4)_4$.

2.1.1 Symmetry aspect of ferrochiral order

In this thesis, we define ferrochiral order as a ferroic order characterized by the time-even chiral bidirector $\mathcal{C}$, which is introduced in Chapter 1. It is worth noting that phase transitions which allow for such ferrochiral order are referred to as chiroaxial transitions in ref. [6]. Nevertheless, to emphasize the ferroic nature of this order, we have opted to refer to it as 'ferrochiral order' instead of 'chiroaxial order'. We also acknowledge another classification related to chirality, so-called gyrotropic transition [7], which is the classification based on the gyration tensor. As detailed in 2.1.3, the gyration tensor describes optical rotation. It should be noted that achiral crystals belonging to point groups $\bar{4}$, $\bar{4}2m$, $mm2$, and m have non-zero gyration tensor components. Thus, ferrochiral transitions and gyrotropic transitions are not in a one-to-one relationship.

The ferrochiral order is characterized by a spontaneous torsional distortion, resulting from a combination of rotational and translational deformations. Of the 32 crystallographic point groups, there are nine pyrochiral point groups which allow for such a torsional distortion ($1,\ 2,\ 222,\ 3,\ 32,\ 4, 422, 6, 622$) [6,8]. (The term "pyrochiral" parallels "pyroelectric".) Among the 212 nonmagnetic species [9,10], there are in total 105 ferrochiral species (see Fig. 2.1) [6]. Notably, six of these 105 ferrochiral species are pure ones ($mmm \rightarrow 222, 4/mmm \rightarrow 422, \bar{3}m \rightarrow 32, \bar{6}2m \rightarrow 32,\ 6/mmm \rightarrow 622,$ and $6/mmm \rightarrow 32$), which accompany neither ferroelectric, ferroelastic, nor ferroaxial transitions [6,11,12] (see also 3.1.1 about ferroaxial transition). In this classification based on the chiral bidirector, cubic enantiomorphic point groups 23 and 432 are excluded. Nonetheless, in a broader definition of ferrochiral transition, species of $m\bar{3}m \rightarrow 432$, $\bar{4}3m \rightarrow 23$, and $m3 \rightarrow 23$ would be

included in the pure ferrochiral species.

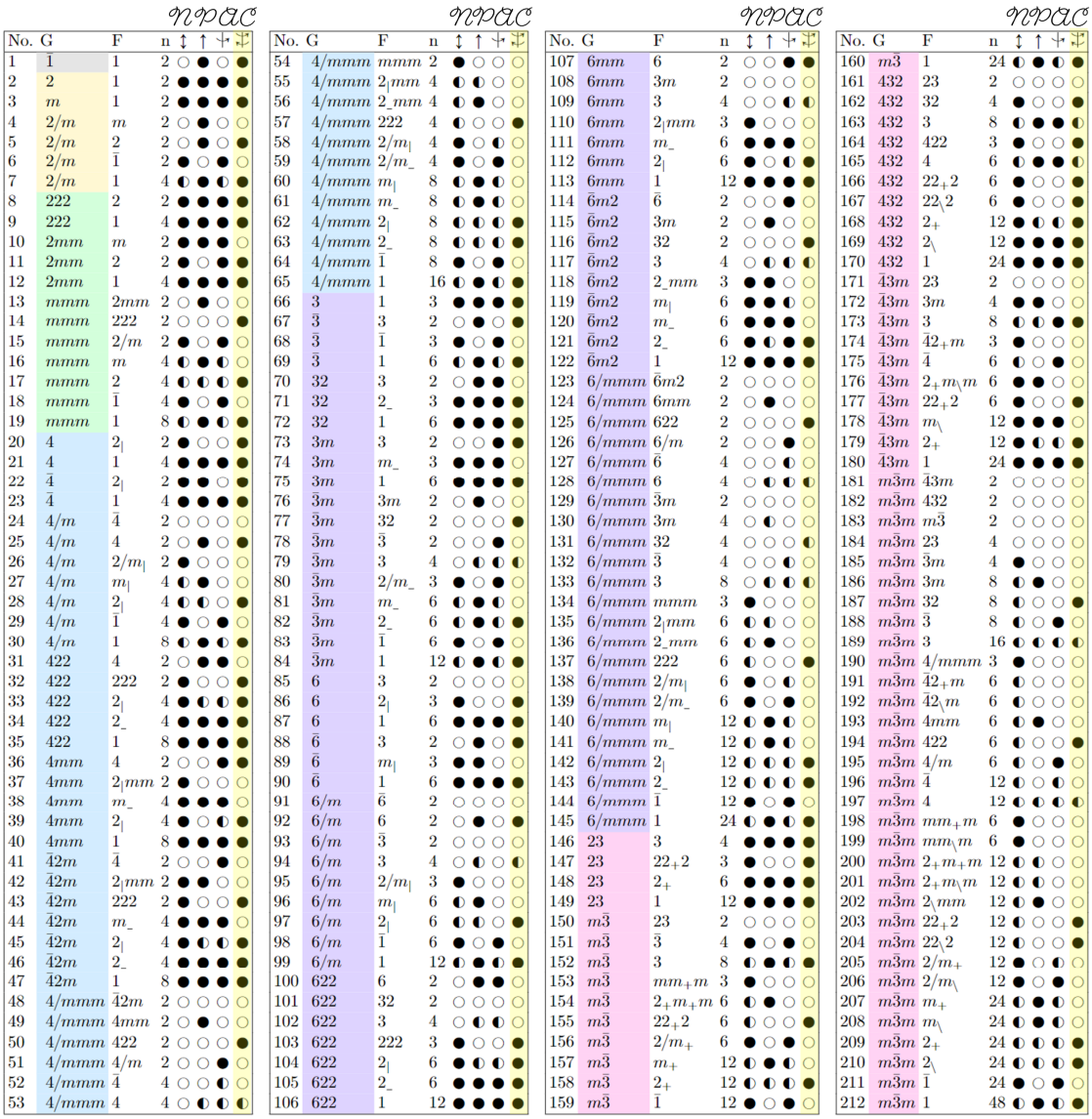

Fig. 2.1 List of 212 nonmagnetic species classifying ferroelastic, ferroelectric, ferroaxial and ferrochiral transitions. Reprinted with permission from ref. [12]. Copyright 2020 by the American Physical Society. *G* and *F* stand for the point groups of the high- and low-symmetry phases, respectively. A total number of the domain states is shown in column *n*. Full, semi-open, and open circles in column $\mathcal{N}$ stand for full ferroelastic, partial ferroelastic, and non-ferroelastic transitions, respectively. Here, partial ferroelastic means that some pairs of the domain states have the same ferroelastic property, i.e., the orientation of principal axis. Symbols in column $\mathcal{P}$, $\mathcal{A}$ and $\mathcal{C}$ refer to ferroelectricity, ferroaxiality, and ferrochirality, respectively. The columns corresponding to ferrochiral transitions ($\mathcal{C}$) are highlighted in yellow.

In Fig. 2.2, we schematically illustrate one of the pure ferroaxial transitions, 4/*mmm*→422. In the ferrochiral 422 phase, all the mirror symmetries of the parent 4/*mmm* phase are broken by the staggered rotation (torsional distortion) of the structural units (see the red plates in Fig 2.2**a**-**c**). The

parameter characterizing such distortions is a pseudoscalar ψ. In the model structure in Figs. 2.2**b**,**c**, ψ is defined as the scalar triple product $\psi \propto \mathbf{D} \cdot (\mathbf{B} \times \mathbf{C})$. Here, polar vectors **D**, **B,** and **C** are the vector from the center of the bottom plate to the top, the displacement of the top plate from the bottom, and the vector from the center of the rotations to **B**, respectively [13]. The sign and magnitude of ψ will correspond to those of the chiral bidirector $\mathcal{C}$.

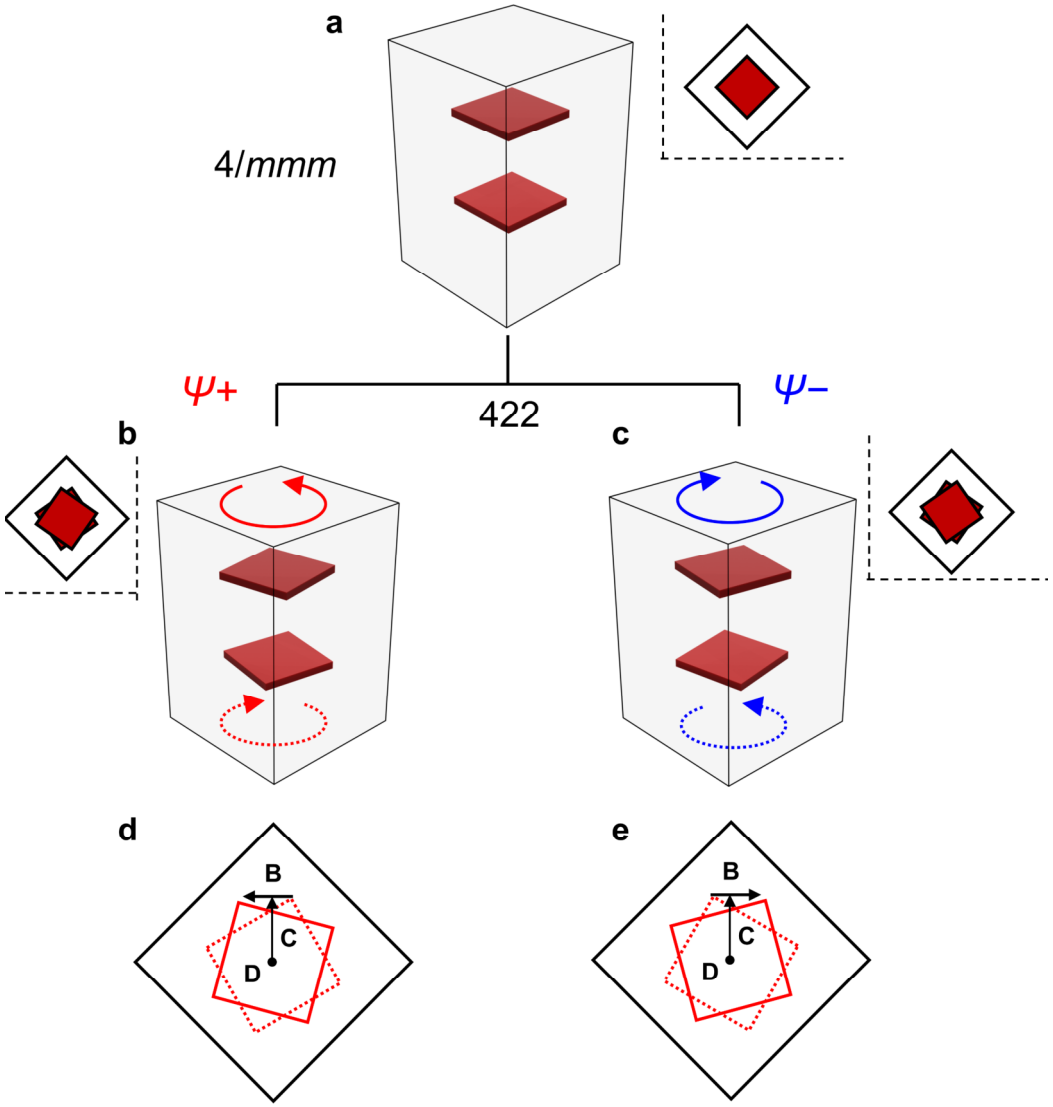

Fig. 2.2 Schematic illustration of ferrochiral transition. **a**, Non-ferrochiral (achiral) phase. **b, c**, Ferrochiral phase. The black rectangle and red plates represent a unit cell and structural units composed of ions in a crystal, respectively. The two red plates in panels **b** and **c** show staggered rotation, i.e., torsional distortion. The two domain states with opposite chirality to one another are depicted. The insets of each figure show rotations seen parallel to the rotational axis. Note that the two red plates are not in specific high-symmetry positions. **d, e,** Examples of coordinates to calculate $\psi \propto \mathbf{D} \cdot (\mathbf{B} \times \mathbf{C})$, where **B** denotes the displacement of the top plate from the bottom, and **C** is a vector from the center of the rotations to **B**. Therefore, $\mathbf{B} \times \mathbf{C}$ corresponds to the rotation of the upper plate from the bottom, that is opposite for **(b)** and **(c)** each other. **D** is a vector from the center of the bottom plate to the top.

When a crystal undergoes a ferrochiral transition, ferrochiral domains with different arrangements of Ψ form. The number of such domain states for each specie is summarized in Fig. 2.1. In the case of a pure ferrochiral transition, a pair of domains displaying opposite signs of Ψ emerge (see also Figs. 2.2**b**,**c**). These domain states of $\Psi+$ and $\Psi-$ have opposite chirality (handedness) to one another and are related to each other by mirror operations, which are symmetry operations in the parent non-ferrochiral phase.

Crystals that exhibit the above-mentioned pure ferrochiral transitions (pure ferrochiral crystals) provide excellent systems to examine characteristics of ferrochirality, unaffected by other ferroic properties. Examples of such pure ferrochiral crystals are listed in Table 2.1.

Table 2.1 Examples of pure ferrochiral crystals. The material discussed in this thesis $Ba(TiO)Cu_4(PO_4)_4$ is highlighted in gray.

Substance	Transition	T_c	Ref.
$Ba(TiO)Cu_4(PO_4)_4$	$P4/nmm \rightarrow P42_12$	~1033K	[14]
$CsCuCl_3$	$P6_3mmc \rightarrow P6_122$	423K	[15,16]
K_3NiO_2	$P4_2/mnm \rightarrow P4_12_12$	423K	[17]
$Na_2Ca_2Si_3O_9$	$R\bar{3}m \rightarrow P3_121$	~723K	[18]
$Ag_4P_2O_7$	$R\bar{3}c \rightarrow P3_112$	623K	[19]
$C_{12}H_{26}N_2$ $MnBrCl_3$	$Pnma \rightarrow P2_12_12_1$	245K	[20]
$(C_5H_{11}NH_3)_2ZnCl_4$	$Pnma \rightarrow P2_12_12_1$	249K	[21]

2.1.2 Previous studies related to ferrochirality

As detailed in the following subsections, the way to distinguish chirality, i.e., right-handed and left-handed structures, is well established. It employs optical phenomena such as (natural) optical rotation and circular dichroism. These techniques determining chirality have been mainly applied to enantiomers of organic molecules. On the other hand, the ferroic nature of chirality has been studied in a limited manner. One of the few examples is the chirality switching in a peculiar class of chiral materials, where ferrochiral order appears concomitantly with the onset of ferroelectric and/or ferroelastic orders. In this class of chiral materials, the ferrochiral order and the ferroelectric (ferroelastic) order are tightly coupled to each other, which allows for an electric-field [22–25] (stress [26]) switching of chirality through a reversal of spontaneous electric polarization(strain). However, there have been few reports on chirality switching without the aid of other order parameters. This is partly because there is no simple conjugate field to chirality, making chiral domain switching a highly challenging subject. For the demonstration of such a pure chirality control, the above mentioned pure ferrochiral crystals will be most appropriate, because the absence of other ferroic orders makes it easier to identify a unique field conjugated to chirality. Nonetheless, as listed in Table 2.1, only a limited number of examples of pure ferrochiral crystals are known. Furthermore, the formation process of ferrochiral domains has never been observed. Observation of ferrochiral domains, especially at temperature close to T_c, is important for control of

chirality, as the energy barrier between paired domain states of opposite chirality diminishes near T_c.

2.1.3 Optical rotation

Optical rotation (OR) was first discovered in a quartz crystal by Arago in 1811 [3]. Since then, it has been observed in various chiral materials and employed to distinguish their chirality [27]. OR is ascribed to an anisotropy of refractive index for left and right circularly polarized light. Circularly polarized light exhibits the symmetry of the chiral bidirector $\mathcal{C}$ (see Chapter 1), which shares the same symmetry with the ferrochirality. This symmetry matching gives an intuitive understanding that the ferrochiral domain states with opposite chirality can be distinguished by using optical rotation.

Optical rotatory power (ORP) ρ [deg mm^{-1}] is given as [27,28]

$$\rho = \frac{\pi}{\lambda n} g_{ij} k_i k_j \tag{2.1}$$

where λ denotes the wavelength of incident light, n is the refractive index of vacuum, k_i and k_j are direction cosines of the wave normal and the Einstein notation is adopted. g_{ij} is the gyration tensor which is a second-rank axial tensor and satisfies the relation $g_{ij} = g_{ji}$.

By examining the gyration tensor, one can know whether a crystal shows OR and its directions. Among the 32 point groups, 15 point groups (summarized in Fig 2.3 based on refs. [29,30]) have non-zero components of $[g]$.

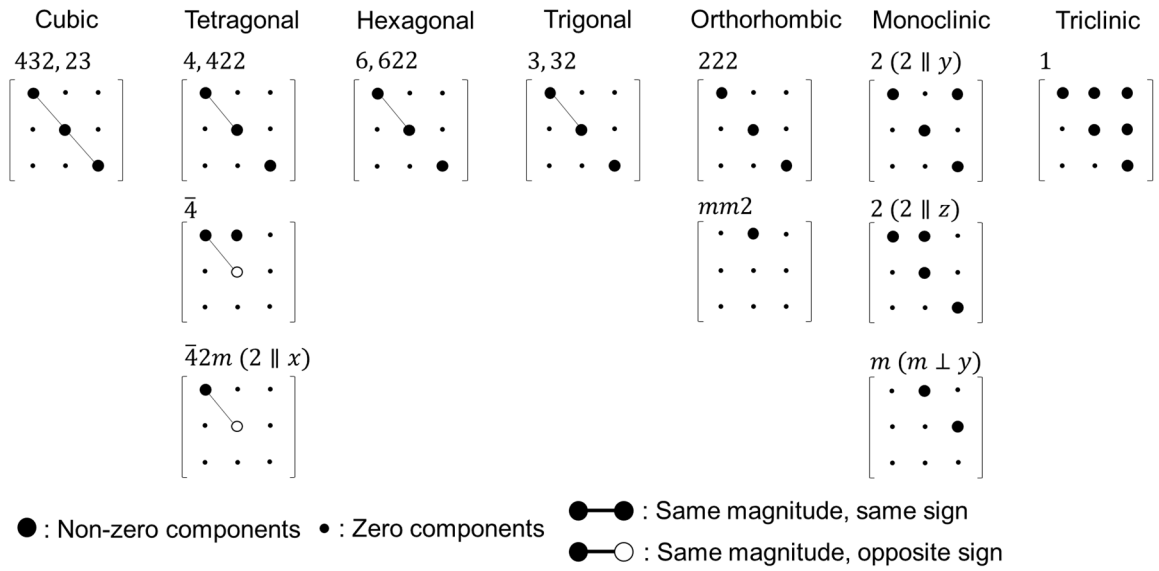

Fig. 2.3 Gyration tensor of 15 point groups. The gyration tensor of point group 2 is described in the two different ways depending on the direction of its principal axis.

Let us confirm that crystals with opposite chirality exhibit opposite directions of OR by conducting tensor calculations. Here we take point group 422 for an example. The gyration tensor of point group 422 is

$$[g] = \begin{bmatrix} g_{11} & 0 & 0 \\ 0 & g_{11} & 0 \\ 0 & 0 & g_{33} \end{bmatrix}. \tag{2.2}$$

Now we focus on the g_{33} component, which describes OR when light propagates along the *c* axis (the third axis). For a mirror operation [mirror plane ∥ (100)]

$$\sigma_v = \begin{bmatrix} a_{11} & a_{12} & a_{13} \\ a_{21} & a_{22} & a_{23} \\ a_{31} & a_{32} & a_{33} \end{bmatrix} = \begin{bmatrix} -1 & 0 & 0 \\ 0 & 1 & 0 \\ 0 & 0 & 1 \end{bmatrix} \tag{2.3}$$

which connects the states with opposite chirality (Ψ+ and Ψ–), the second rank axial tensor g_{33} is rewritten as

$$g'_{33} = -a_{3i}a_{3j}g_{ij} = -g_{33}. \tag{2.4}$$

This means that the sign of g_{33}, i.e., the direction of optical rotation in the configuration of $\boldsymbol{\kappa} \parallel c$, depends on that of Ψ, i.e., depends on chirality.

2.1.4 Target material: $Ba(TiO)Cu_4(PO_4)_4$

The crystal structure of $Ba(TiO)Cu_4(PO_4)_4$, hereafter called BTCPO, is reported in ref. [31], and a temperature dependence of the crystal structure has been investigated by single crystal x-ray diffraction (XRD) measurements, which were performed by Dr. Urushihara and Dr. Asaka at Division of Advanced Ceramics, Nagoya Institute of Technology [14]. As depicted in Figs. 2.4**b**-**e**, the crystal structure of BTCPO at room temperature (space group $P42_12$) is characterized by staggered rotations of Cu_4O_{12} units with up (Fig. 2.4**f**) and down (Fig. 2.4**g**) configurations. This material undergoes a structural phase transition at around 710 ℃, at which the staggered rotations are lost, and results in an achiral structure (space group *P*4/*nmm*, see Fig. 2.4**a**).

Figure 2.5 shows temperature dependences of lattice constants (**a** and **b**) and a rotation angle θ of Cu and O(3) ions (**c** and **d**) defined in the insets [14]. As seen in Figs. 2.5**a**, the lattice constant of the *a* axis shows a clear kink in its slopes without discontinuity around T_c = 710 ℃, indicative of a second order phase transition. Notably, such a second order nature of the phase transition is more evident in the temperature dependences of θ of Cu and O(3) ions (Fig. 2.5**c**,**d**). They are well fitted by the function of $\theta = \alpha(T_c - T)^{\beta}$ where α and β are fitting parameters, indicating that the *ab*-plane rotations of the ions about the *c* axis behave as a good order parameter of the phase transition. This is consistent with the result that the *c* axis lattice constant does not exhibit a detectable anomaly around T_c (Fig. 2.5**b**).

As described above, BTCPO shows one of the pure ferrochiral transitions (4/*mmm* → 422). Consequently, BTCPO has multi ferrochiral domains of Ψ+ (Fig. 2.4**b**,**d**) and Ψ– (Fig. 2,5**c**,**e**) at room temperature, which has been confirmed by a polarized microscope measurement [31]. Here, we define the structure in which the up Cu_4O_{12} units (see Fig. 2.4**f**) rotate counterclockwise as Ψ+ and the other one as Ψ– structure. From the comparison with the single crystal XRD measurements, it has been revealed that Ψ+ (Ψ–) domains show dextro- (levo-) optical rotatory at λ = 450 nm.

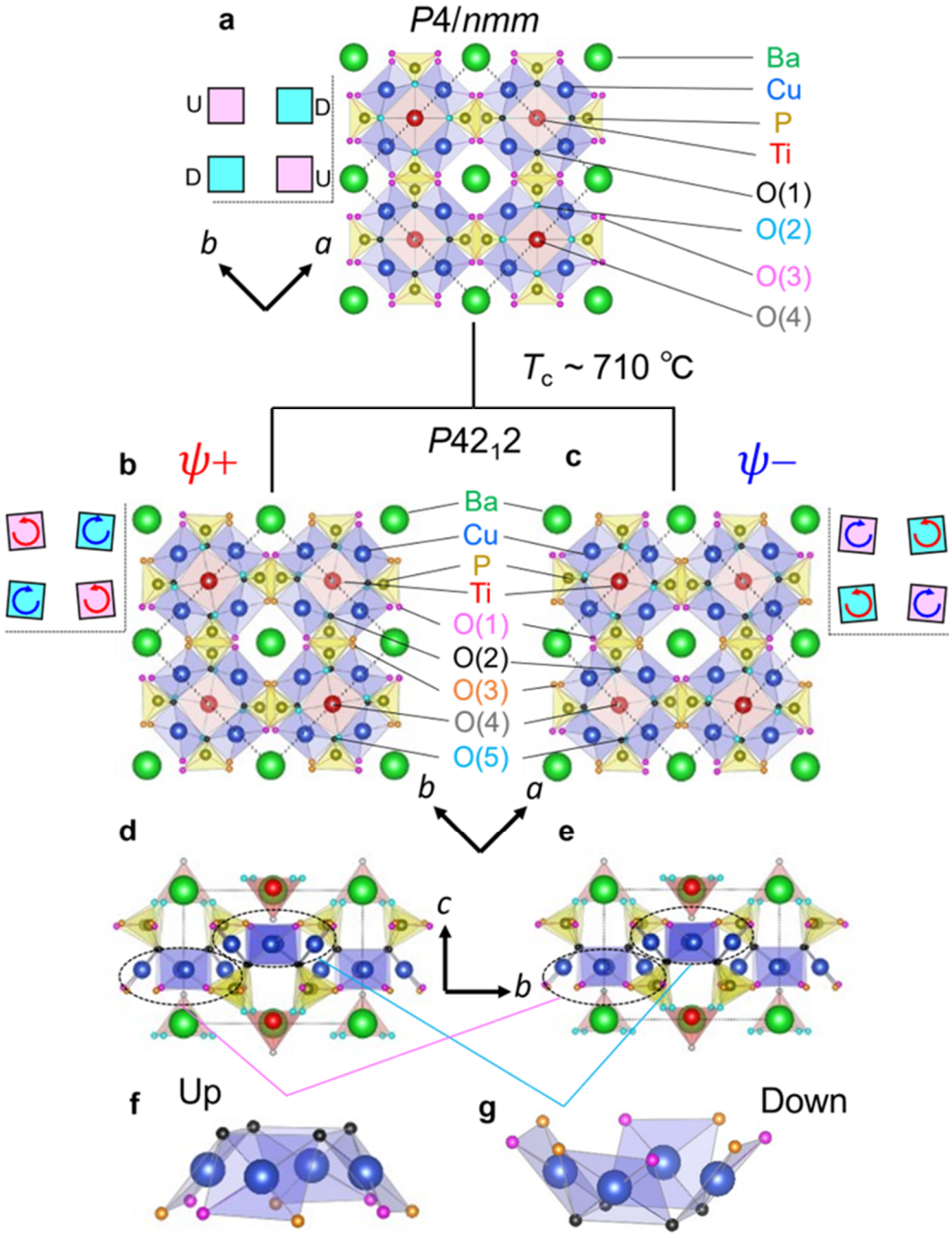

Fig. 2.4 Crystal structure of $Ba(TiO)Cu_4(PO_4)_4$. Reprinted with permission from ref. [14]. Copyright 2021 American Chemical Society. **a,** Crystal structure above T_c (at 900 ℃) viewed along the *c* axis. **b-e,** Crystal structures of Ψ+ (**b**,**d**) and Ψ− (**c**,**e**) domains below T_c (at 25 ℃) viewed along the *c* axis (**b**,**c**) and the *a* axis (**d**,**e**). The black dashed lines in (**a-e**) represent a unit cell. **f**,**g,** Up (U) and down (D) Cu_4O_{12} units. The squares in the insets of (**a-c**) schematically represent the rotations of Cu_4O_{12} units of up (magenta) and down (cyan). Here, we define the structure in which the up Cu_4O_{12} units rotate counterclockwise as Ψ+ (**b**,**d**) and the other one as Ψ− (**c**,**e**) structure.

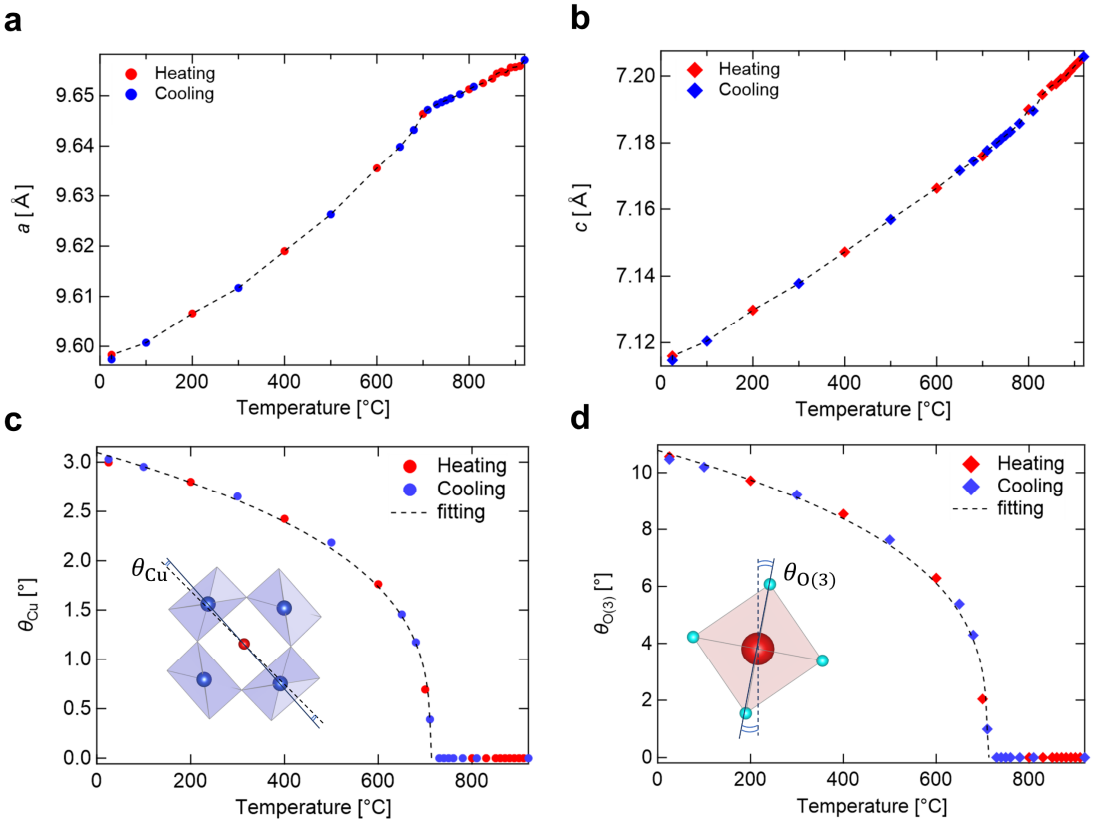

Fig. 2.5 Temperature dependence of lattice constants and atomic coordinates. Reprinted with permission from ref. [14]. Copyright 2021 American Chemical Society. **a**,**b,** Lattice constants of the *a* and *c* axis. That of the *a* axis shows slight changes of the slopes around T_c = 710 °C. **c,d,** Rotations of Cu and O(3) ions from their achiral positions above T_c. The dashed lines denote least squares fitting curves with the fitting function of $\theta = \alpha(T_c - T)^{\beta}$. The fitted parameters are α = 0.40(2), β = 0.311(1) and T_c = 710.7(5) for θ_{Cu} and α = 1.45(14), β = 0.305(2) and T_c = 710.2(3) for $\theta_{(O3)}$.

The above-mentioned ferrochiral transition in BTCPO is understood in the perspective of a combination of antipolar and antiferroaxial orders, which we newly propose as a guide to achieve a pure ferrochiral transition.

Recently, it has been recognized that symmetry-dependent macroscopic responses induced by two distinct ferroic orders can also be obtained by their antiferroic counterparts. For examples, a magnetoelectric effect is induced by the coexistence of ferromagnetic and ferroelectric orders or that of antiferromagnetic and antiferroelectric (antipolar) orders [32,33]. A magnetochiral effect is induced by the combination of ferromagnetic and ferrochiral orders or that of antiferromagnetic and antiferrochiral orders [34]. In addition, when ferroelectric and ferroaxial orders emerge simultaneously, ferrochiral order is also induced (𝒫 (polar) · 𝒜 (axial) ≈ 𝒞 (chiral), see Chapter 1 for details). Therefore, one naturally comes up with the idea that ferrochiral order is mediated by the combination of antipolar and antiferroaxial orders.

Figure 2.6 depicts a conceptual image of this idea. Here, we define the antipolar order as antipolar structural units in a unit cell, i.e., one structural unit with positive polarization (P+) and the other with negative polarization (P−). Likewise, the antiferroaxial order is defined as antiferroaxial

structural units in a unit cell, i.e., one structural unit with clockwise rotation (A+) and the other with counterclockwise rotation (A–). Since we are interested in the onset of chirality induced by a combination of these orders, we keep their own symmetries as high as possible. In this case, neither antipolar (P–, P+) nor antiferroaxial (A–, A+) orders give chirality due to the presence of mirror or glide (mirror operation with a fractional lattice translation) symmetries, as depicted in Fig. 2.6. On the other hand, when these two orders coexist, i.e., (P– A–, P+ A+) or (P– A+, P+ A–), the absence of common mirror or glide planes results in the breaking of all mirror and glide symmetries. The system thus becomes chiral without electric polarization nor strain (i.e., a distortion of the unit cell). Accordingly, the pure ferrochiral transition will be achieved by an antiferroaxial ordering of antipolar structural units, or by an antipolar ordering of antiferroaxial structural units. The former transition in the case of the (P–, P+) antipolar order is shown in Fig. 2.6. The transition produces a pair of ferrochiral states (P– A–, P+ A+) and (P– A+, P+ A–) with opposite signs of chirality, which are related to each other by the glide ($g_{\perp}$) and mirror ($m_{//1}$) symmetries that are broken by the transition. In the case of reversed antipolar order, i.e., (P+, P–), the ferrochiral transition yields another pair of ferrochiral states (P+ A–, P– A+) and (P+ A+, P– A–). The relationship among the four ferrochiral states in view of chirality signs is described in Fig. 2.7.

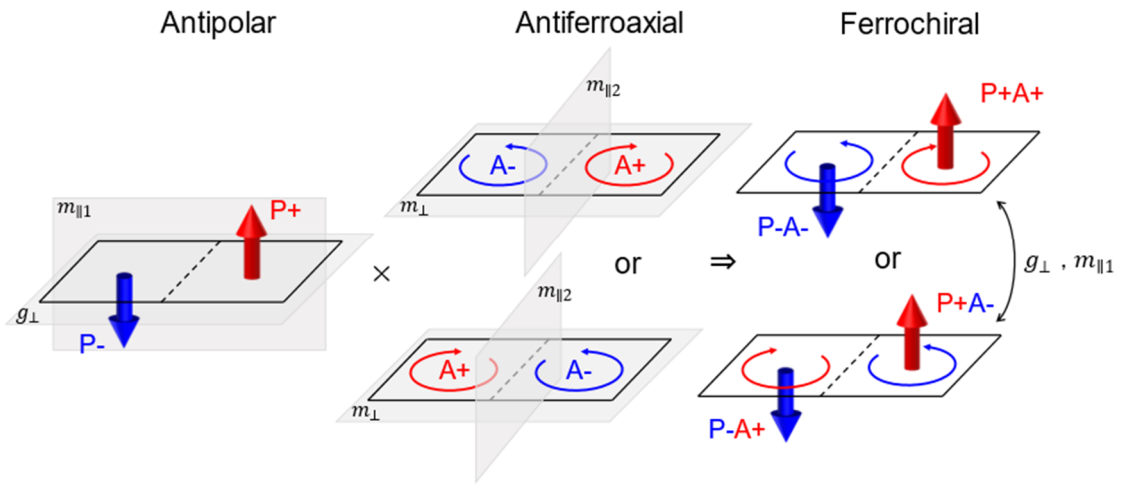

Fig. 2.6 Conceptual illustration of ferrochiral order achieved by a combination between antipolar and antiferroaxial orders. Reprinted with permission from ref. [14]. Copyright 2021 American Chemical Society. P+ and P– denote positive and negative polarizations, while A+ and A– denote clockwise and counterclockwise rotations. The black solid lines represent unit cells. The gray planes denoted as $m_{//1}$, $m_{//2}$, $m_{\perp}$, and $g_{\perp}$ represent parallel mirror (1 and 2), perpendicular mirror and perpendicular glide planes, respectively. In the ferrochiral state, there are no mirror symmetries.

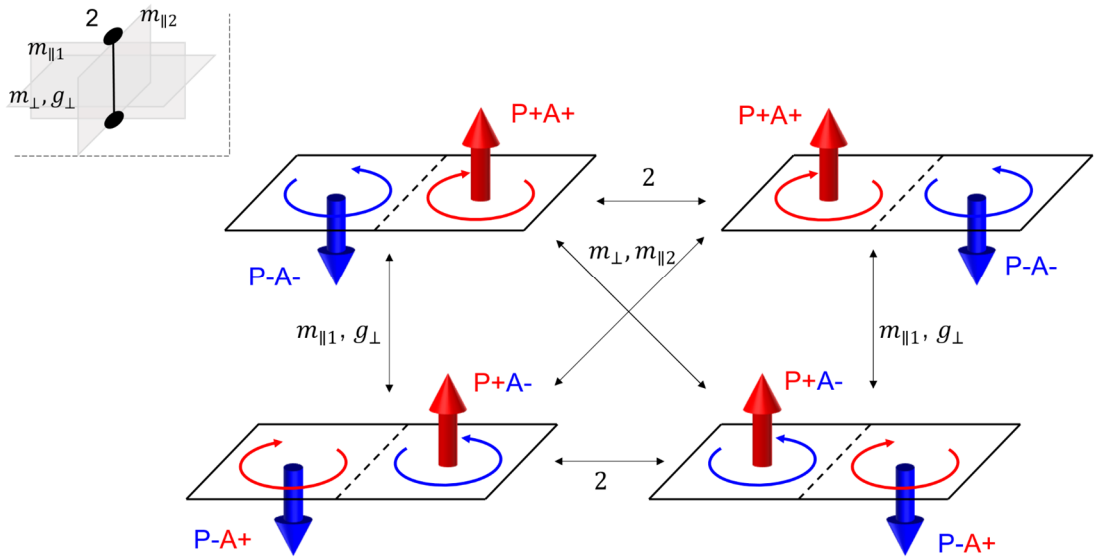

Fig. 2.7 Schematic image of the four types of antipolar-antiferroaxial coupling. Reprinted with permission from ref. [14]. Copyright 2021 American Chemical Society. The double head arrows connecting each motif show symmetrical operations which transform these types, where the mirror and glide planes of $m_{//1}$, $m_{//2}$, $m_{\perp}$ and $g_{\perp}$, and the two-fold rotation axis of 2 are depicted in the inset. The sign of chirality (i.e., handedness) is the same between (P– A–, P+ A+) and (P+ A+, P– A–), and between (P– A+, P+ A–) and (P+A–, P–A+), but is opposite between the first two and the latter two.

As illustrated in Fig. 2.8, the up and down configurations of Cu_4O_{12} units of BTCPO correspond to an antipolar order, and their staggered rotations correspond to an antiferroaxial order (other units like TiO_{4+1} or PO_4 polyhedrons also contribute to the antiferroaxial or antipolar orders but here we focus on Cu_4O_{12} units for simplification). In addition, the structural transition of BTCPO is well described by the rotation of the units (see Fig. 2.5**c**,**d**), and therefore our proposal for the emergence of ferrochiral order ("antipolar × antiferroaxial = ferrochiral") is achieved in BTCPO. Currently, there are only a few pure ferrochiral materials (see Table 2.1), and this new idea of antiferroaxial-antipolar combination will broaden opportunities for finding new pure ferrochiral materials.

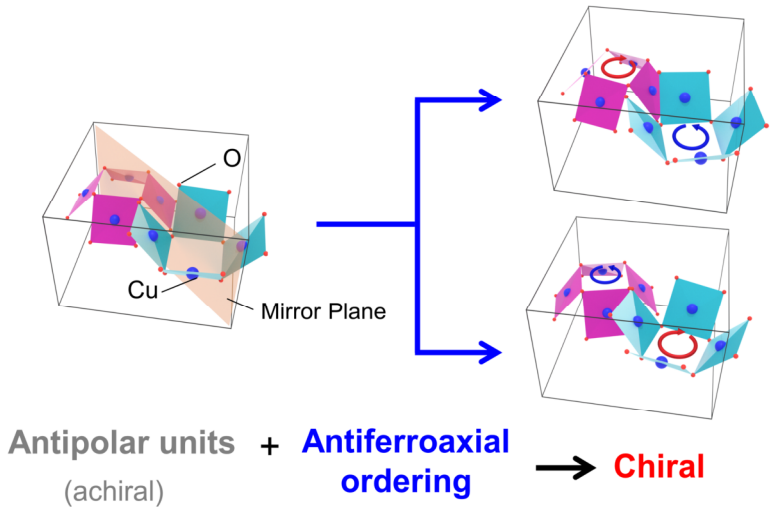

Fig. 2.8 Antiferroaxial-antipolar combination in $Ba(TiO)Cu_4(PO_4)_4$. Only Cu and O atoms are shown.

2.1.5 Motivation

BTCPO is one of the few pure ferrochiral crystals, making it an ideal subject for exploring pure control of chirality. In this research, we first examine the domain formation process upon a ferrochiral transition by measuring the spatial distributions of OR over a wide temperature range. Following this, we demonstrate chirality switching in BTCPO by irradiation of a laser beam. We adopt laser irradiation as an external stimulus inspired by recent studies that suggest thermal gradients induced by laser irradiation can drive the motion of magnetic domain walls in magnetic materials [35–37]. This approach offers a way to manipulate domains without using a conjugate field.

2.2 Experimental methods

2.2.1 Sample preparation

Single crystals of BTCPO grown from $Na_2Mo_2O_7$ flux [31] were provided by Dr. Kenta Kimura, University of Tokyo. The crystals were plate-shaped and transparent-blue in color, and their widest plane was the (001) plane. The obtained crystals were confirmed to be the single phase with the BTCPO structure by XRD measurements. The widest faces were polished by waterproof sandpapers down to 50 μm for absorption spectra measurement, 86 μm for optical rotation (OR) measurement, and 40 μm for domain control experiments. The surfaces were mirror polished by the polishing machine (IMT Co., Ltd.) with diamond slurry. Figure 2.9 shows a microscope image of the sample.

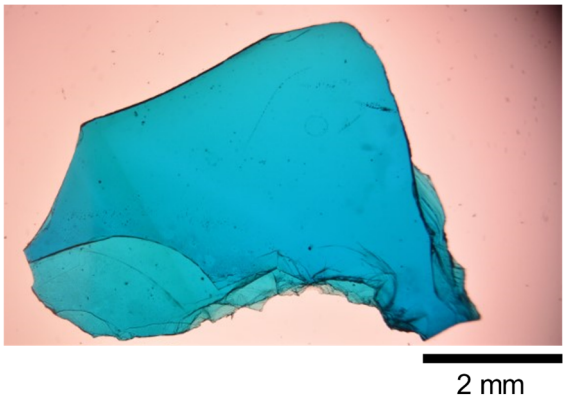

Fig. 2.9 Microscope image of the polished BTCPO single crystalline sample.

2.2.2 Absorption spectrum measurement

BTCPO is not fully transparent but exhibits finite absorptions in the visible light range. Such absorptions should influence OR, especially on optical rotatory dispersion. Therefore, we measured a temperature dependence of an absorption spectrum.

The measurements were performed with the optical setting depicted in Fig. 2.10. White light from a halogen lamp was irradiated into the specimen along the *c* axis and the transmitted light was

detected using a spectrometer (Flame-S, Ocean Optics). The sample temperature was controlled from 20 ℃ up to 850 ℃ by using a hot stage (HS1400G, INSTEC). Using obtained transmission spectra, absorption spectra were calculated as follows,

$$\alpha\ [\mathrm{cm}^{-1}] = -\left(\ln\frac{I - I_{bg}}{I_0 - I_{bg}}\right)/d \tag{2.5}$$

where α is the absorption coefficient, I is the intensity of the transmitted light, I_0 is the intensity of the incident light, I_{bg} is the intensity of backgrounds, and d [cm] is the sample thickness.

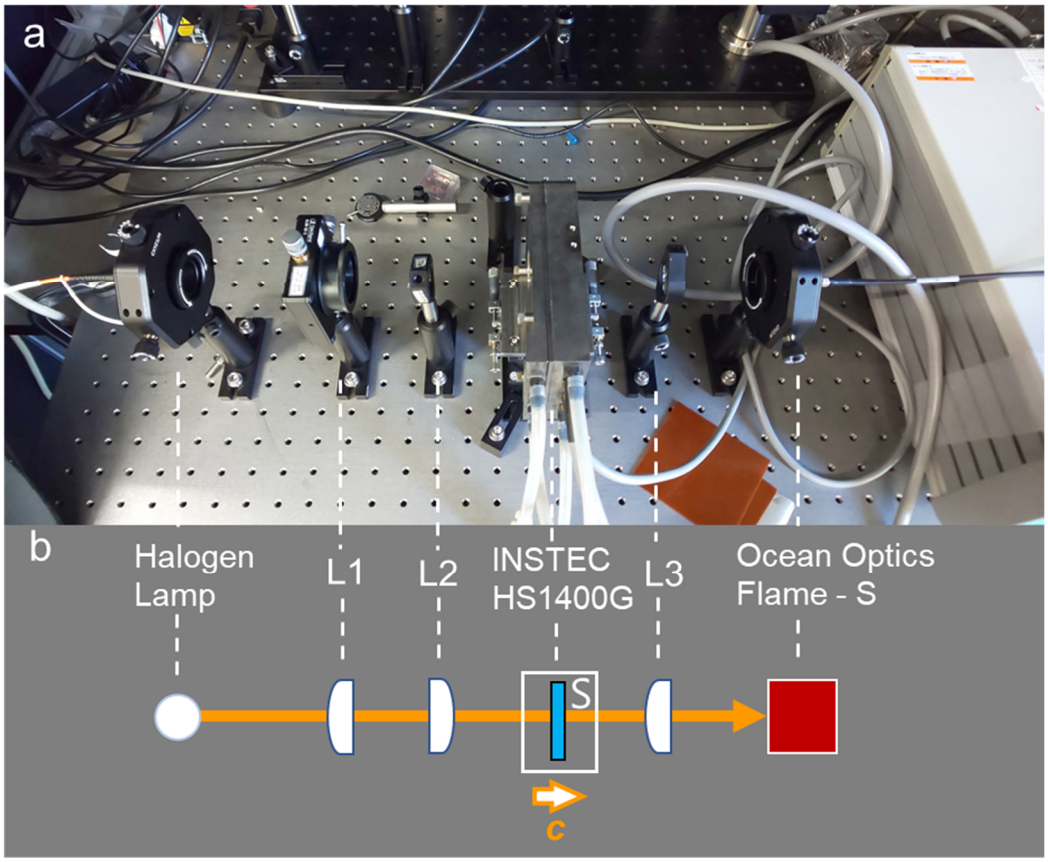

Fig. 2.10 Optical setting for absorption spectra measurement. **a,** Photograph, and **b,** Schematic image of the setting. Here, L and S denote lens and sample, respectively. Light propagates along the *c* axis of the sample. Adapted from ref. [14] with permission. Copyright 2021 American Chemical Society.

2.2.3 Chiral domain observation

・Measurement principle

Now we measure spatial distributions of OR of BTCPO when light propagates along the *c* axis (OR corresponding to the g_{33} component defined in 2.1.3). In this situation when light propagates in a uniaxial crystal along its optic axis, effects of birefringence are in principle avoidable, so that OR is easy to be observed. Thus, at room temperature, spatial distributions of OR can be obtained by using a conventional polarized-light microscope without any special experimental procedures [31]. However, at

high temperatures above 650 ℃, strong thermal radiation light will overlap the incident polarized light, which makes it difficult to observe domains. To overcome this problem, we take a difference between the images obtained at the angles between the orientation of a polarizer and an analyzer (Θ) of +45° and −45°. Here, the sign is defined as positive when the polarization direction of the analyzer rotates clockwise with respect to that of the polarizer from the observer's point of view. The intensity of transmitted light in such settings can be written as

$$I = \frac{I_0}{2}[\cos\{2(\pm 45° - \phi)\} + 1] + I_{bg}$$
$$= \frac{I_0}{2}\{\pm\sin(2\phi) + 1\} + I_{bg}, \quad (2.6)$$

where I_0 is the intensity of the transmitted light at the parallel Nicols setting, ϕ [deg] is the rotation angle of the polarization plane and I_{bg} is the background intensity. When OR is small enough, it can be assumed that $\sin(2\phi) \approx 2\phi'$, where $\phi'[\mathrm{rad}] = \frac{\pi}{180}\phi$ [deg], so that equation (2.6) is rewritten as

$$I \approx I_0\left(\pm\phi' + \frac{1}{2}\right) + I_{bg}$$
$$= I_0\left(\pm\frac{\pi}{180}\rho d + \frac{1}{2}\right) + I_{bg}, \quad (2.7)$$

where ρ [deg mm^{-1}] is optical rotatory power (ORP) and d [mm] is the sample thickness. Taking the difference between I obtained at Θ = +45° and −45° and dividing it by their average, we obtain the relative difference of the transmittance T for these angles as

$$\frac{\Delta T}{T} = \frac{I_0\left(\frac{\pi}{180}\rho d + \frac{1}{2}\right) - I_0\left(-\frac{\pi}{180}\rho d + \frac{1}{2}\right)}{\left\{I_0\left(\frac{\pi}{180}\rho d + \frac{1}{2}\right) + I_0\left(-\frac{\pi}{180}\rho d + \frac{1}{2}\right)\right\}/2 + I_{bg}}$$
$$= \frac{2I_0\frac{\pi}{180}\rho d}{\frac{I_0}{2} + I_{bg}}. \quad (2.8)$$

As the sign of ρ depends on that of chirality (ψ) (see 2.1.3), a spatial map of $\Delta T/T$ represents a chiral domain structure. In this configuration, taking the difference of the two images can significantly suppress the effect of the background light such as the thermal radiation light. Also, the background intensity can be estimated using an image captured under a crossed-Nicols setting. From this, ORP ρ [deg mm^{-1}] can be calculated.

Since BTCPO exhibits finite absorptions in the visible light range, OR will show anomalous dispersion. Consequently, the temperature dependence of OR will exhibit different behaviors for different wavelengths. Therefore, imaging measurements using OR were performed with several wavelengths as follows.

・Measurement sequence

Based on the above-mentioned measurement principle, imaging measurements were performed as the sequences below.

1) Evaluation of birefringence and optical rotatory dispersion measurement

In our setting, light propagates along the optic axis and thus, ideally, effects of birefringence do not appear. However, residual birefringence remains caused by unavoidable misalignments of both crystal orientation and optical setup. Thus, before heating measurements, to evaluate the effect of birefringence, images of $\Delta T/T$ were taken with changing the angle of the polarizer (Pol.) from 0° to 180° per 30° at different wavelengths, 415 nm, 455 nm, 565 nm, 600 nm, 624 nm, 650 nm, 700 nm, 730 nm, 780 nm, and 880 nm. (The origin (0°) of Pol. has no special meanings since it is based on that of the motorized rotator.) In this measurement, an optical rotatory dispersion was also obtained.

2) Temperature dependence of spatial distributions of OR

We performed the microscopy measurements with different wavelengths: 415, 455, 565, 624, and 880 nm. The temperature of the sample was controlled from 20 ℃ up to 800 ℃ by the hot stage. Heating the sample above T_c and subsequent cooling to room temperature were repeated three times, where different LEDs were used for each temperature cycle: During the first, second, and third cycles, the 455 nm LED, the 415 nm, 565 nm and 624 nm LEDs, and the 880 nm LED were employed, respectively.

・Optical setting

We captured polarized light images with a custom-built optical microscope, assembled by Dr. Kenta Kimura. The optical setting is shown in Fig. 2.11. As the light sources of 415 nm, 455 nm, 565 nm, 624 nm, 730nm, 780nm, and 880 nm, monochromatic LED light sources were used. To obtain 600 nm, 650 nm, and 700 nm wavelengths, a white LED light source was used with bandpass filters. The angles of the polarizer and analyzer were controlled by motorized rotators. The transmitted light was captured by a scientific CMOS camera (CS2100M, Thorlabs).

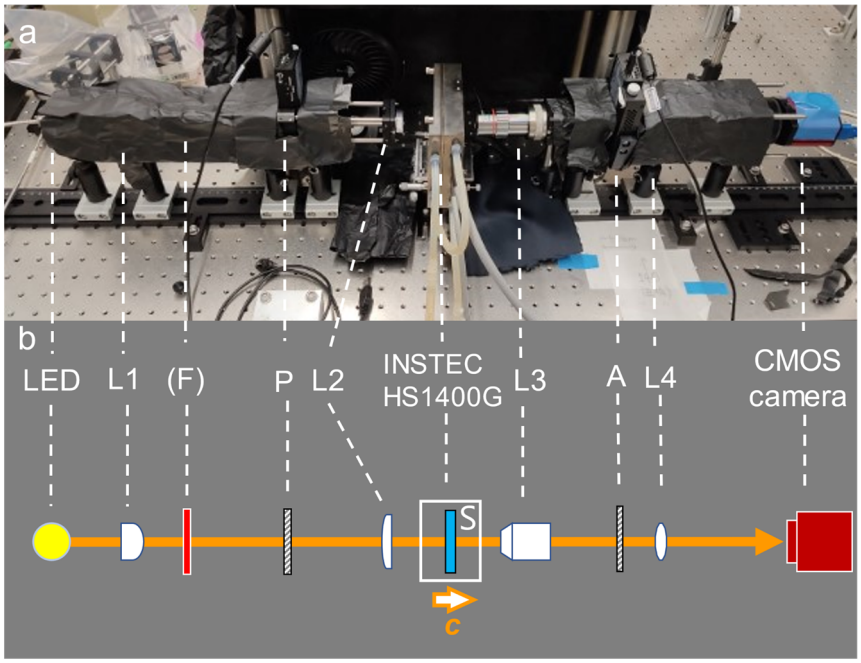

Fig. 2.11 Optical imaging system. **a,** Photograph, and **b,** Schematic image of the setting. Here, L, F, P, S, and A denote lens, bandpass filter, polarizer, sample, and analyzer, respectively. Light propagates along the *c* axis of the sample. Bandpass filters were only used for the measurements with 600 nm, 650 nm, and 700 nm wavelengths.

2.2.4 Laser irradiation

To control chiral domains in BTCPO, the sample was irradiated with a linearly-polarized Gaussian laser beam whose center wavelength was either 730 or 633 nm. At these wavelengths, BTCPO exhibits strong absorption (see Fig. 2.13). For *in situ* chiral domain observation, a beam splitter was used for laser irradiation (see Fig. 2.12). In addition, we used a polarization camera (CS505MUP1, Thorlabs) for spatial distribution measurements of OR. In the polarization camera, four polarizers with different polarization angles (0°, 45°, 90°, and 135°) are placed on each pixel. Thus, the spatial distribution of polarization angles of transmitted light can be obtained in a single camera shot without the above-mentioned successive image subtraction process. This method can achieve real-time observation of chiral domain motion under laser irradiation. The focus of the laser beam was reduced to a diameter of 20–120 μm at the sample position, and the beam's power density was 1000–3800 W cm^{-2}. The laser scanning for the domain control was achieved by moving the sample position with a motorized stage.

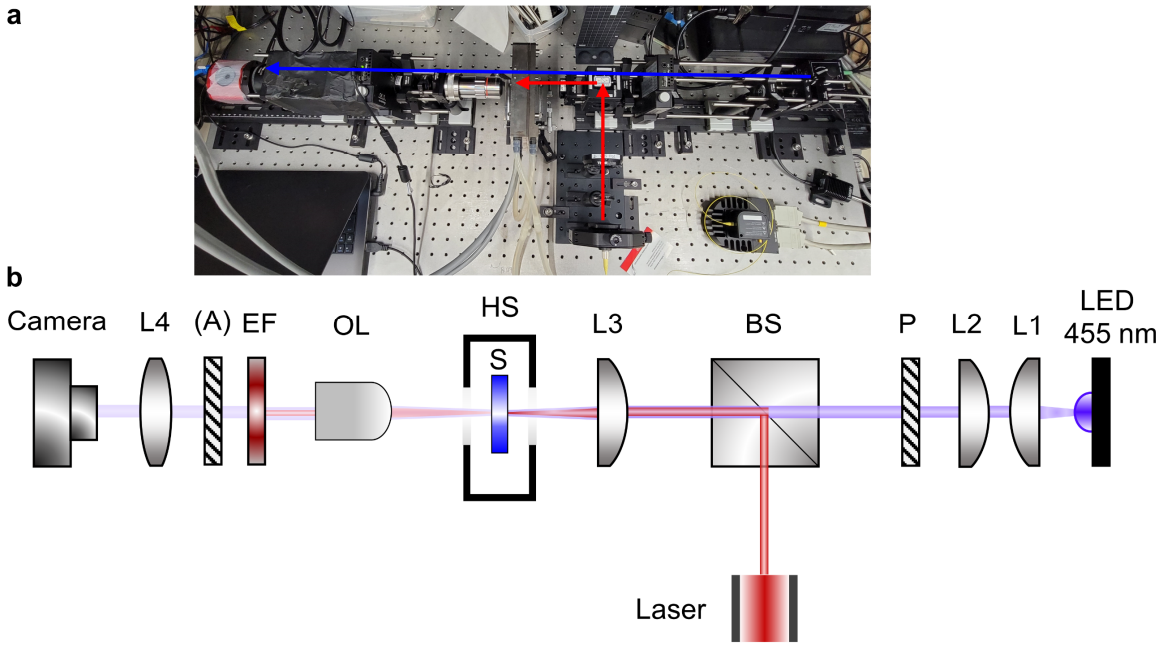

Fig. 2.12 Optical setup for laser irradiation and *in situ* chiral domain observation. **a**, Photograph. The blue and red arrows represent optical path of light from LED light and laser, respectively. **b**, Schematic illustration. L1– L4: Lens; OL: Objective lens; P: Polarizer; BS: Beam splitter; HS: Hot stage; S: Sample; EF: Edge pass filter; A: Analyzer. In the measurements using a polarization camera, no analyzer is used. Adapted from ref. [38] with permission. Copyright 2022 American Chemical Society (**b**).

2.3 Results and Discussion: Domain observation

2.3.1 Temperature dependence of an absorption spectrum

Figure 2.13 shows an obtained temperature dependence of an absorption spectrum. The two peaks around 650 nm and 850 nm at 25 ℃ are most likely attributable to *d-d* transitions of the Cu^{2+} ion [39].

Notably, in the ranges from 400 nm to 500 nm and from 650nm to 850 nm, significant spectral changes with respect to temperature variations are observed.

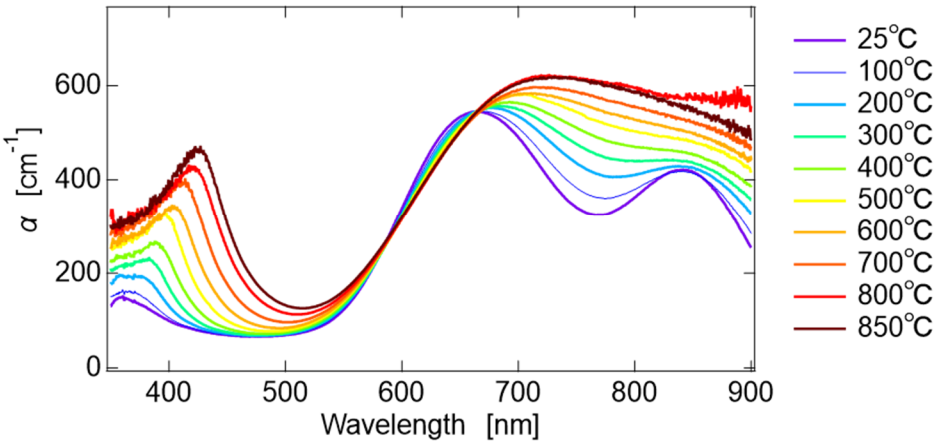

Fig. 2.13 Temperature dependence of an absorption spectrum. Reprinted with permission from ref. [14]. Copyright 2021 American Chemical Society.

2.3.2 Evaluation of effects of birefringence

At room temperature (20 ℃), we acquired difference images of $\Delta T/T$ changing the angle of the polarizer across various wavelengths. Figure 2.14 shows an example of the image in the setting when Pol. is set at 0 ° and the wavelength λ is 455 nm. The optical image shown in Fig. 2.14**a** corresponds to the average image obtained from the images captured at the angles between the orientation of a polarizer and an analyzer (Θ) of +45° and −45°, i.e., the image of *T*. In the difference image of $\Delta T/T$ (Fig. 2.14**b**), clear contrasts of red and blue colors are observed. The red regions with a positive sign of $\Delta T/T$ and blue regions with a negative sign correspond to dextro- and levo- optical rotatory, respectively. Therefore, the contrasts show the ferrochiral domains of the specimen. The domains which show dextro- (levo-) optical rotatory here correspond to $\psi+$ ($\psi-$) domains (see also Fig. 2.4). To evaluate the magnitudes of ORP, average values of $\Delta T/T$ were calculated at each single domain area denoted by white polyhedrons in Fig. 2.14**b**. The same measurements were repeated with changing the angle of Pol. and wavelengths. Figure 2.16 summarizes the angle of Pol. dependence of $\Delta T/T$ at different wavelengths. The averages of $\Delta T/T$ for each domain ($\Delta T/T_+$ for $\psi+$ domains and $\Delta T/T_-$ for $\psi-$ domains) vary for different angles of Pol. and they also behave differently for different wavelengths, due to the influence of birefringence. On the other hand, the differences between $\psi+$ and $\psi-$ domains' $\Delta T/T$ ($\Delta T/T_+ - \Delta T/T_-$) are almost constant even when changing the angle of Pol.. The difference of $\Delta T/T_+ - \Delta T/T_-$ reflects that of the optical rotatory power ($\rho_+ - \rho_-$) and thus by calculating $\rho'_+ = (\rho_+ - \rho_-)/2$, we can evaluate ORP with suppressing effects of birefringence.

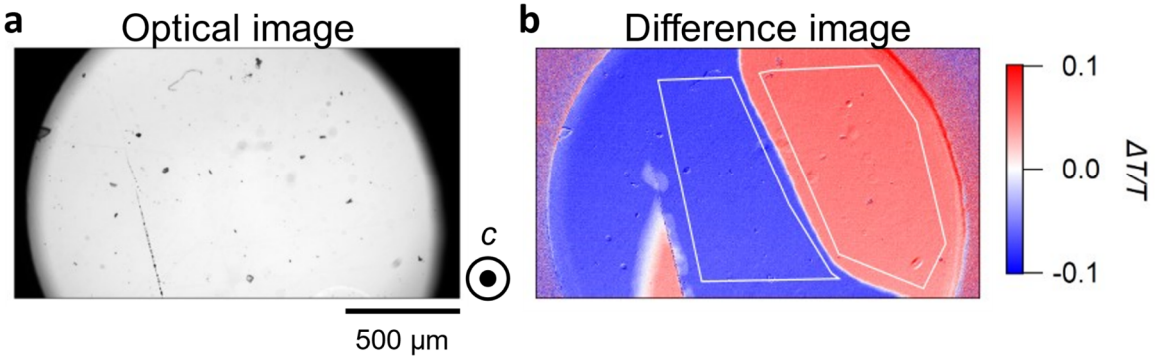

Fig. 2.14 Polarized light microscopy images obtained in the setting Pol. is set at 0 ° and at wavelength λ = 455 nm. **a,** Optical image corresponding to the image of T, **b**, Difference image of $\Delta T/T$. The red and blue contrasts in (**b**) correspond to $\psi+$ and $\psi-$ domains, respectively.

Fig. 2.15 Angle of Pol. dependence of $\Delta T/T$ at different wavelengths. Reprinted with permission from ref. [14]. Copyright 2021 American Chemical Society. The notations of Avg and SD at the top of each graph correspond to the average and standard deviation of $\Delta T/T_+ - \Delta T/T_-$, respectively. Here $\Delta T/T_+$ and $\Delta T/T_-$ are $\Delta T/T$ of $\psi+$ and $\psi-$ domains, respectively.

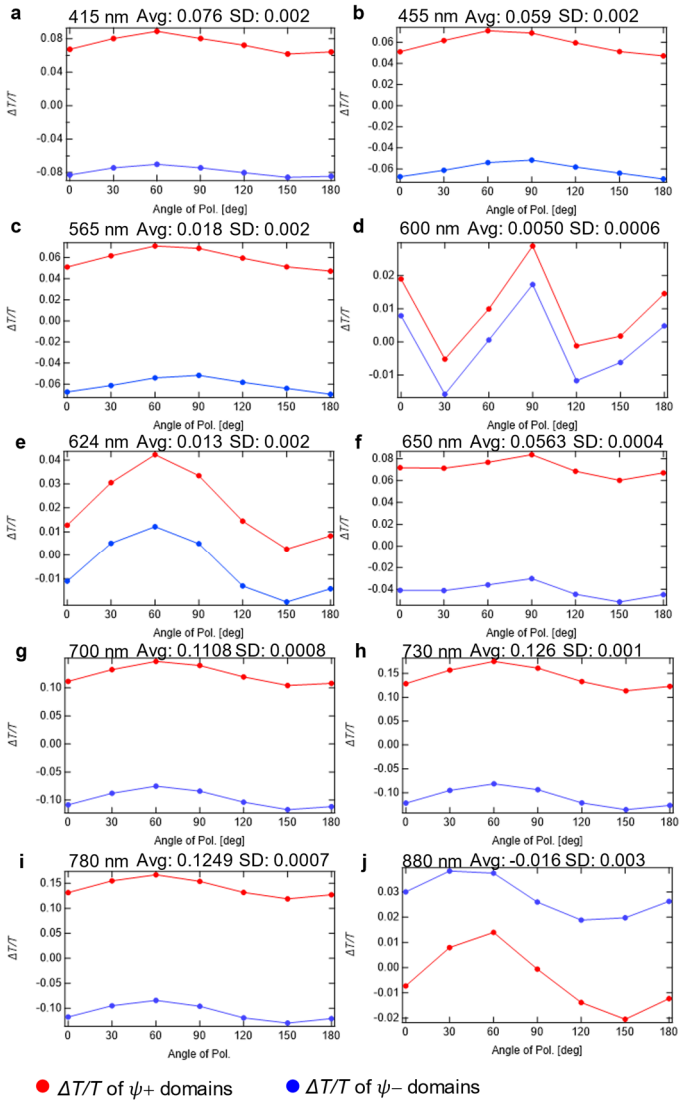

2.3.3 Temperature dependence of chiral domain structures

Figure 2.16 shows a temperature dependence of spatial distributions of $\Delta T/T$ obtained using a 455 nm LED light source. Note that these images were taken during a first heating of this sample above T_c after its crystal growth. At room temperature, an image of $\Delta T/T$ shows clear contrasts of red and blue, which correspond to $\psi+$ and $\psi-$ domains, respectively (Fig. 2.16**b**). As the sample is heated, the color contrasts gradually decrease, and at 750 ℃, they start to disappear. Then at 760 ℃, they completely vanish (Figs. 2.16**b**-**i**). This suggests that the sample exhibited a chiral-achiral phase transition at around 760 ℃. The discrepancy between the transition temperatures determined from the optical and the XRD experiments (around T_c= 710°C, see Fig. 2.5) is likely because the two experiments employ different sample heating methods, resulting in a different accuracy of the measured sample temperature. Even after the contrasts vanish, finite but uniform signals of $\Delta T/T$ are observed (Fig. 2.16**i**), most likely coming from residual birefringence. When the sample is cooled down, the color contrasts reemerge at 750 ℃ (Fig. 2.16**k**) and get increased with cooling (Figs. 2.16**i**-**p**). The domain structure obtained by heating the sample above T_c is almost the same with that of before heating (compare Fig. 2.16**b** and Fig. 2.16**p**), but some parts (the areas surrounded by black circles in Fig. 2.16**p)** show weaker magnitudes of $\Delta T/T$. This suggests a formation of opposite domains along the thickness direction.

Figure 2.17 shows spatial distributions of $\Delta T/T$ from 20 ℃ to 650 ℃ obtained using an 880 nm LED light source. Above 650 ℃, optical absorption was too strong to obtain enough intensities of transmitted light for domain observations. All the images in Fig. 2.17 were taken during heating. At room temperature, the directions of OR are opposite from those of 455 nm (compare Fig. 2.17**b** with Fig. 2.16**b**) and, surprisingly, they get reversed with heating the sample bordering ~100℃. This reversal of OR with heating most likely comes from the change of a circular dichroism spectrum as discussed later.

Let us mention the changes of the chiral domain structures after heating of the sample above T_c. Though the domain structures slightly changed after the first heating (compare Fig. 2.16**b** and 2.16**p**), they did not change after the second or third heating. Such a memory effect of domains was reported in ferroelastic systems and explained by the decoration of the domain boundary with defects [40–42]. Whether such an explanation based on defects is also applicable to our chiral domain case is an interesting future subject.

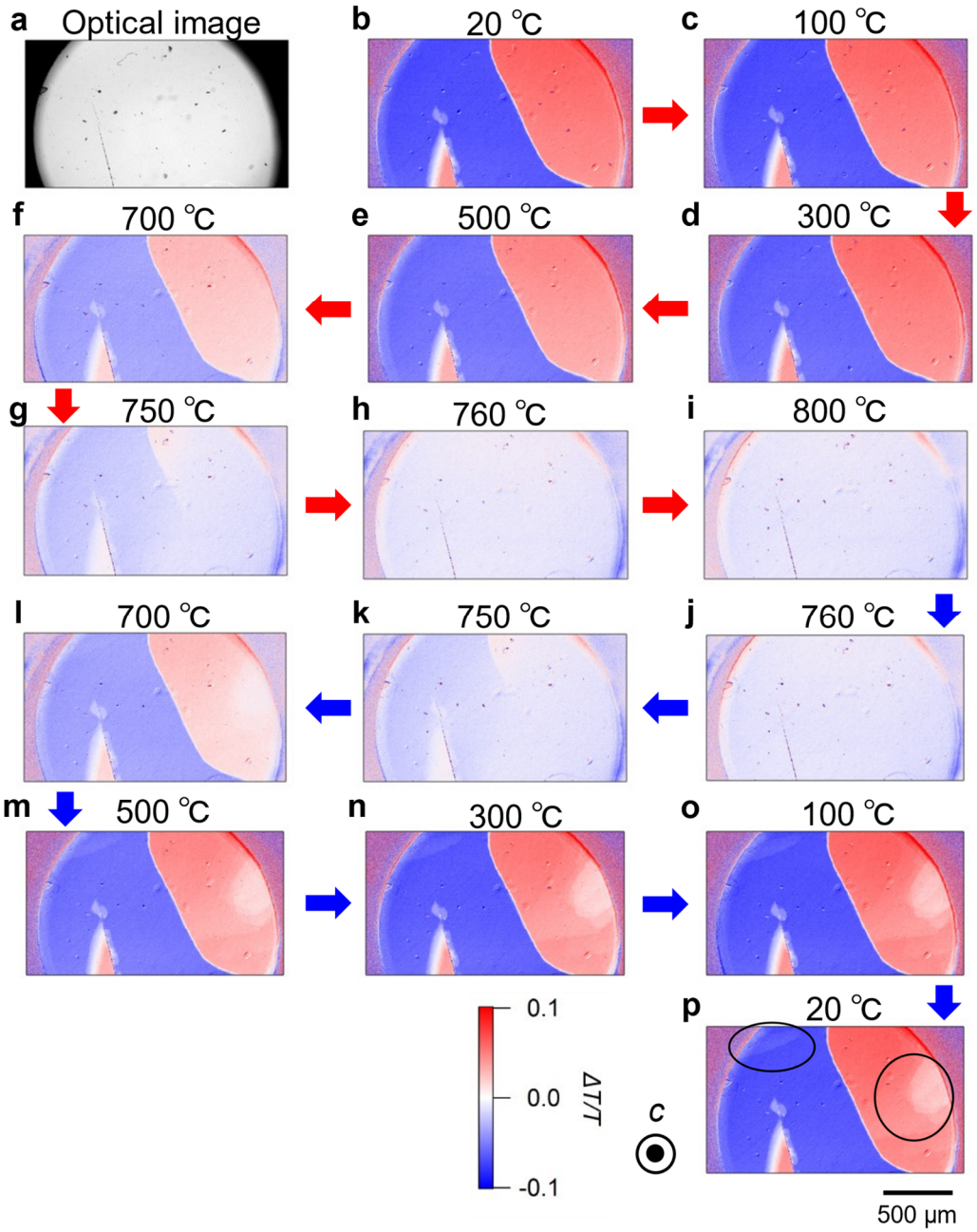

Fig. 2.16 Temperature dependence of OR spatial distribution with 455 nm LED light. Reprinted with permission from ref. [14]. Copyright 2021 American Chemical Society. **a,** Optical image corresponding to the image of *T* taken at 20 ℃ before heating. **b-p,** The two-dimensional maps of $\Delta T/T$ at the same area as panel **a,** Red and blue colors correspond to dextro and levo OR, respectively. The images of (**b-i**) were taken during heating and (**j-p**) were cooling. The circles in panel (**p**) indicate where domain structures were changed comparing with those before heating (panel (**b**)).

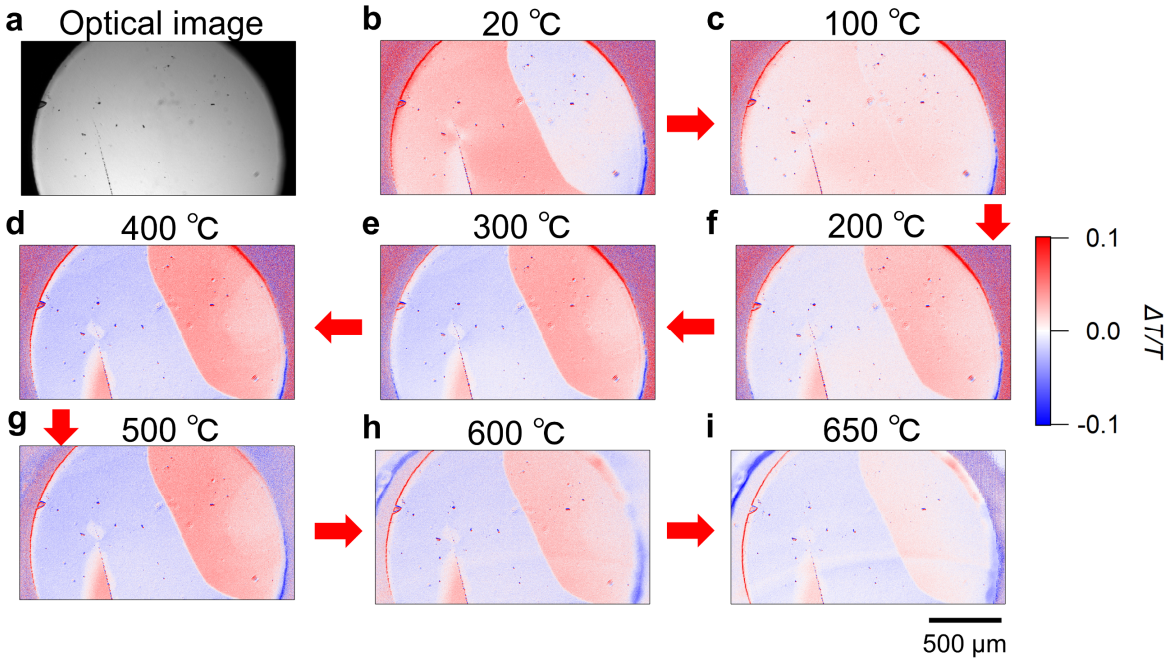

Fig. 2.17 Temperature dependence of OR spatial distribution measured with 880 nm LED light. Reprinted with permission from ref. [14]. Copyright 2021 American Chemical Society. **a**, Transmission optical microscopy image with the incidence of light along the *c* axis. This image was taken at 20 ℃ before heating. **b-g**, The two-dimensional maps of $\Delta T/T$ at the same area as panel (**a**). Red and blue colors correspond to dextro and levo OR, respectively. All the images of (**b**-**i**) were taken during heating. The scale bar of 500 μm below panel (**i**) is applied to all the panels (**a**-**g**). The $\Delta T/T$ color scale on the right side of panel (**d**) is applied to panels (**b**-**i**). The red and blue contrast gets reversed at around 100℃ (compare (**b**) and (**d**)), which means a reversal of OR.

2.3.4 Temperature dependence of optical rotatory power

The spatial distribution measurements of OR were repeated using different wavelengths of 415, 565, and 624 nm. Figure 2.18**a-d** shows the two-dimensional maps of $\Delta T/T$ for each wavelength at 20℃ before heating. We calculated ORP of $\psi+$ domains ρ'_+ [deg mm^{-1}] (see 2.3.2). The temperature profiles of obtained ρ'_+ for different wavelengths are shown in Fig. 2.18**f**. It shows different behaviors for different wavelengths. For 415 and 455 nm, ρ'_+ almost monotonically increases with decreasing temperature. On the other hand, ρ'_+ begins to decrease below 400 ℃ for 565, 624, and 880 nm and, moreover, even shows a sign reversal at 100 ℃ for 880 nm.

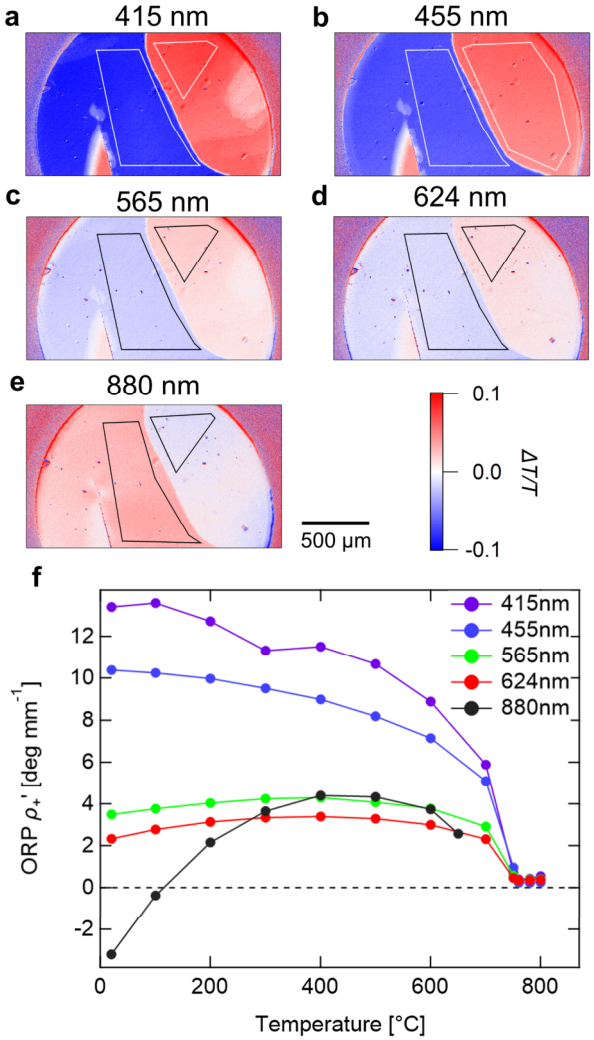

Fig. 2.18 Temperature dependence of ORP measured at various wavelengths. Reprinted with permission from ref. [14]. Copyright 2021 American Chemical Society. **a**-**e,** The two-dimensional maps of $\Delta T/T$ at almost the same area as Figure 5.14**a**. These maps were taken at 20 ℃ with using different wavelengths, (**a**) 415 nm, (**b**) 455 nm, (**c**) 565 nm, (**d**) 624 nm, and (**e**) 880 nm. **f,** Temperature dependence of optical rotatory power (ORP) for five different wavelengths 415 nm, 455 nm, 565 nm, 624 nm, and 880 nm. The averages of $\Delta T/T$ in the selected single domain areas (both $\psi+$ and $\psi-$ domains) which are denoted by white or black polygons in panels (**a**-**e**) were calculated for each temperature and $\rho'_+ = (\rho_+ - \rho_-)/2$ were evaluated. Note that with 880 nm at 20 ℃, ψ+ ($\psi-$) domains show levo (dextro) OR.

Such a wavelength dependence of ORP is attributable to that of circular dichroism (CD) spectra. Since OR and CD are related to each other by the Kramas-Kronig relation [43], a change of CD spectrum has a large effect on the wavelength dependence of OR. Fig. 2.19**a** shows a room temperature CD spectrum expressed as ellipticity Δ [deg], which was obtained using a Ψ+ monodomain BTCPO sample whose thickness was approximately 10 μm. The CD spectra measurements were performed by Mr. Ryohei Yamamoto at Osaka University. Fig. 2.19**b** shows optical rotatory dispersion at 20 ℃. The CD spectrum was transformed into the optical rotatory dispersion (the orange line in Fig. 2.19**b**) by the following Kramas-Kronig (KK) expression [43],

$$\phi(\omega)[\mathrm{deg}] = \frac{2}{\pi} PV \int_{\omega_{min}}^{\omega_{max}} \frac{(\omega^2 \Delta(\omega')}{\omega'(\omega'^2 - \omega^2)} \, d\omega' \qquad (2.9)$$

where ω is a frequency of light, ϕ is a magnitude of OR, and $PV \int d\omega'$ means principal value integral. In the KK relation, the interval of integration is [0, ∞], but here it is limited to [c/(1000 nm), c/(400 nm)] where c is the speed of light. Consequently, the calculated optical rotatory dispersion is not perfectly matched with that measured. However, at least their shapes are roughly matched (compare the red and orange lines in Fig. 2.19**b**).

Although we have not measured CD spectra at various temperature, we observe a significant change in the shape of absorption spectra as the temperature is varied (see Fig. 2.13). We suggest that this temperature variation of absorption spectra should give a strong impact on CD spectra especially in their shapes, which is responsible for the observed wavelength-dependent temperature variation of ORP.

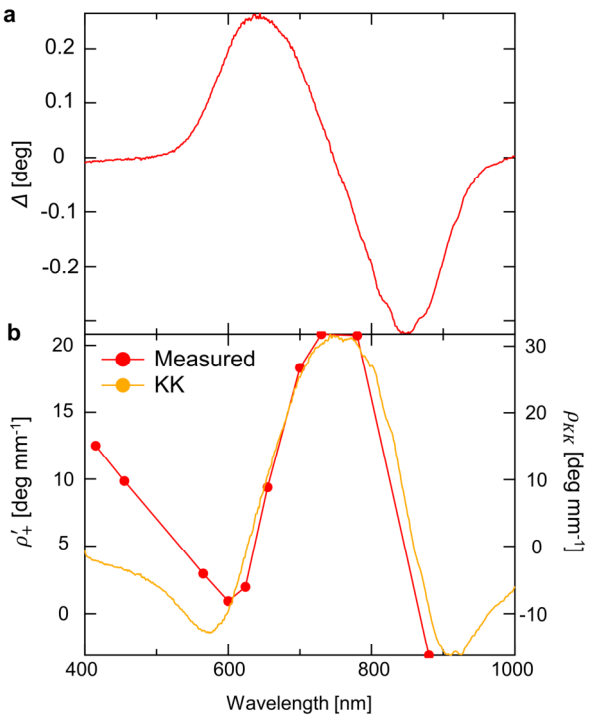

Fig. 2.19 Circular dichroism (**a**) and optical rotatory dispersion (**b**). The left and right axes in panel (**b**) correspond to the measured ORP (ρ'_+) and the calculated ORP(ρ_{KK}), respectively.

The relationship between the magnitude of OR and the degree of chirality in a crystal structure was previously discussed in a transparent quartz, using a so-called continuous chirality measures from which the degree of chirality of a given object is quantitatively calculated as a difference between the object and its nearest hypothetical achiral structure. According to that, the temperature dependence of the calculated degrees of chirality shows a remarkable fit to that of OR [44,45]. In the case of BTCPO, the finite angles of the rotations of Cu or O ions are nothing more or less than differences from the achiral structure and thus correspond to degrees of chirality. As seen from a comparison of Figs. 2.5**c**,**d** and Fig. 2.18**f**, the temperature dependence of the rotations shows a similar behavior with that of ORP at a temperature very close to T_c, which indicates the effect of the structural chirality to ORP. However, as the temperature is lowered away from T_c, the temperature dependence of the rotations deviates from that of ORP. This is because ORP in the studied wavelength is also affected by the temperature variation of absorption spectra, as discussed above.

2.4 Results and Discussion: Domain switching

In the previous section, we successfully visualized the pure ferrochiral transition process in BTCPO by measuring the spatial distributions of optical rotation (OR). This achievement enables us to take the next

step toward the domain control. In this section, we will demonstrate switching of the ferrochiral domains by means of laser irradiation.

2.4.1 Laser irradiation annealing

First, we investigated the effect of laser irradiation on chiral domain formation (Fig. 2.20). We used a diode laser whose wavelength is 730 nm at which BTCPO exhibits strong absorption (see Fig. 2.13). Figure 2.20**a** shows an initial as-grown domain pattern of the sample observed using OR. The sample size is 4 mm × 4 mm × 0.04 mm, but the domain observation area is limited to 1.5 mm in diameter to get enough thermal contact of the sample to a sample stage. Then the sample was heated up to 800 °C (> T_c) and cooled down to 600 °C or 500 °C at a cooling rate of 25–30 °C min^{-1} with laser irradiation. Linearly polarized light was irradiated during the cooling procedure. Then the laser was switched off, and domain images were captured using a polarization camera. The beam diameter and the power density in the measurements of Figs. 2.20**b**,**c** were 120 μm and 970 W cm^{-2}, respectively, whereas those of Fig. 2.20**d** were 20 μm and 1000 W cm^{-2}, respectively. All images in Figs. 2.20**b**-**d** are characterized by a bow-tie-shaped domain structure whose knot is located at the center of the laser irradiation position (red open circles). It is completely different from the as-grown domain structure (compare Figs. 2.20**b**-**d** with Fig. 2.20**a**). We also conducted the same measurements using circularly polarized laser beams. However, no substantial polarization dependence was observed on the bow-tie-shaped domain structure.

Let us consider how the laser irradiation results in such a unique domain structure. Because BTCPO strongly absorbs light with a wavelength of 730 nm, laser irradiation causes local heating and concentric heat distribution around the laser irradiation position. Thus, when the sample temperature is reduced from 800 °C (> T_c), the phase transition into the low-T chiral phase occurs from the outer edge of the laser irradiation position, forming the bow-tie-shaped domains. This domain formation procedure is directly visualized by *in situ* domain imaging during laser irradiation (see also Supplementary Movie S1 in ref. [38]). We note that the obtained domain structure is almost uniform in the thickness direction around the laser spot, and effects of thermal distributions along the thickness direction are expected to be negligible. Further details of the domain formation mechanism will be discussed later.

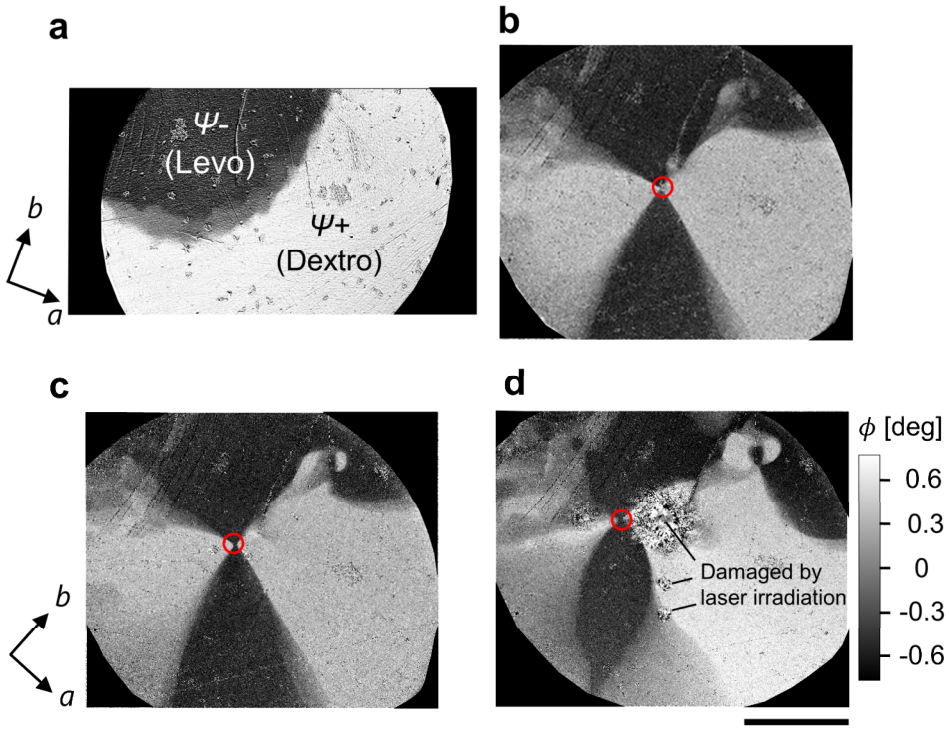

Fig. 2.20 Effect of laser irradiation on the formation of chiral domains. Reprinted with permission from ref. [38]. Copyright 2022 American Chemical Society. **a**, Chiral domains of an as-grown crystal. **b**–**d**, Chiral domains affected by laser irradiation. Prior to the respective observations, the sample was cooled down from 800 °C (> T_c) to a temperature below T_c (500 °C or 600 °C) with laser irradiation. All images were taken after switching off the laser source. The red circles denote laser irradiation positions. The diameter and the power density of the laser beam for the measurements of (**b**,**c**) were 70 μm and 970 W cm^{-2}, respectively, whereas those of (**d**) were 20 μm and 1000 W cm^{-2}, respectively. All images are characterized by a bow-tie-shaped domain structure whose knot is located at the laser irradiation position (red open circles). Some sample areas were damaged by extremely strong laser irradiation before the measurement of (**c**). The crystallographic axis labels next to panels (**a**) and (**c**) are applied to panels (**a**) and (**b**-**d**), respectively. Scale bar: 500 μm

2.4.2 Manipulation of a domain boundary by laser irradiation

Next, we performed the manipulation of a domain boundary by laser irradiation. Figure 2.21 shows domain patterns captured during (Figs. 2.21**c**,**e**,**g**) and after (Figs. 2,21**d**,**f**,**h**) laser irradiation with three different power densities (3200 W cm^{-2} for Figs. 2.21**c**,**d**, 3500 W cm^{-2} for Figs. 2.21**e**,**f**, and 3800 W cm^{-2} for Figs. 2.21**g**,**h**). Red open circles in Fig. 2.21 denote the laser irradiation position. During these measurements, the sample stage temperature was maintained at 600 °C (< T_c). Fig. 2.21**b** shows the domain image before laser irradiation, which corresponds to a part of Fig. 2.20**d**. Figure 2.21**a** shows a schematic illustration of the domain pattern in Fig. 2.21**b**. The experiments were conducted in the order shown in Figs. 2.21**c**–**h**. After laser irradiation with the lower power density of 3200 W cm^{-2}, the domain pattern does not change from the initial state (compare Fig. 2.21**d** with Fig. 2.21**b**). On the other hand, after laser irradiation with the power density of 3500 W cm^{-2}, the domain boundary near the laser irradiation position is slightly shifted toward the irradiation position, thereby expanding the Ψ+ domain

area (compare Fig. 2.21**f** with Fig. 2.21**b**). Such domain boundary movement is more clearly observed in the image after laser irradiation with the power density of 3800 W cm^{-2} (Fig. 2.21**h**). This result shows that laser irradiation with power density above a certain threshold can manipulate chiral domain boundaries.

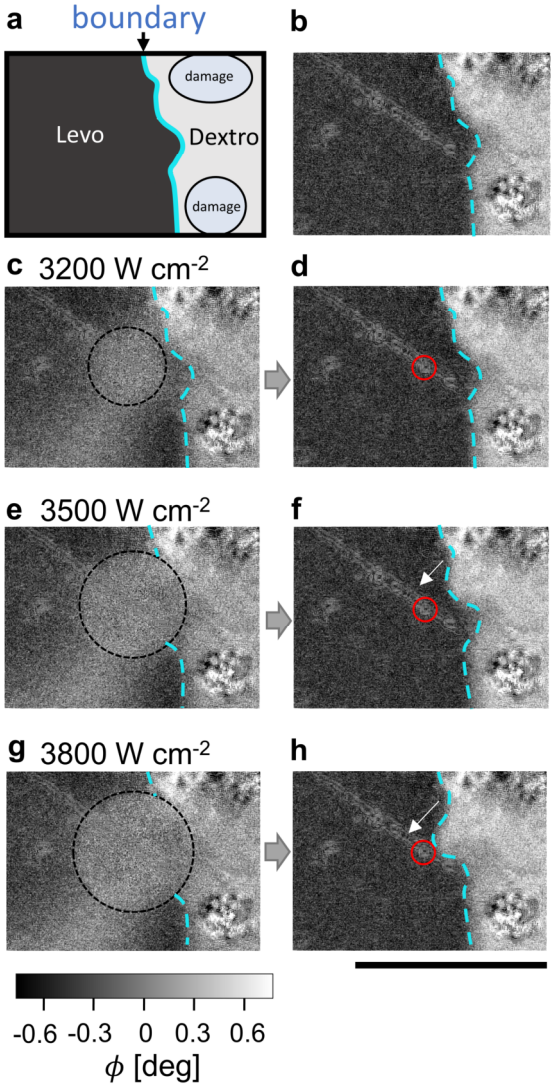

Fig. 2.21 Manipulation of domain boundary by tuning laser power. Reprinted with permission from ref. [38]. Copyright 2022 American Chemical Society. **a**, Schematic illustration of the domain pattern displayed in panel (**b**). **b**, Chiral domain pattern before the laser irradiation. The cyan dotted line denotes the domain boundary. **c,e,g,** *In situ* domain patterns captured during laser irradiation. The power density of the laser beam is (**c**) 3200, (**e**) 3500, and (**g**) 3800 W cm^{-2}. The area surrounded by the black dotted circle in each panel is heated to temperatures above T_c by laser irradiation. **d,f,h**, Domain patterns after switching off the laser. Panels (**d**), (**f**), and (**h**) correspond to the images after switching off laser source from panels (**c**), (**e**), and (**g**), respectively. The red circles denote laser irradiation positions. The white arrows in (**f**) and (**h**) depict the direction of boundary movement. These images were taken at 600 °C. Scale bar: 250 μm.

Let us consider the process of domain boundary movement by laser irradiation. At gray regions inside dotted circles in Figs. 2.21**c**, **e** and **g**, the magnitude of OR ϕ is approximately 0°, implying that

they are heated to temperatures above T_c during laser irradiation. At the lower power density of 3200 W cm^{-2}, the initial boundary is still observed, as denoted by the cyan dotted curve in Fig. 2.21**c**. By contrast, at the higher power density (3500 and 3800 W cm^{-2}), a portion of the boundary is no longer observed (Figs. 2.21**e**,**g**), implying that the areas, including the domain boundary, are heated to temperatures above T_c, namely, they transition into the high-T achiral phase. This indicates that at the higher power density, the domain boundary is reconstructed by undergoing the ferrochiral transition, and this reconstruction is a key factor of domain boundary movement.

2.4.3 Writing of a chiral domain pattern by laser scanning

We demonstrate the writing of a chiral domain pattern by scanning the laser beam on the sample surface based on the observed domain reconstruction by laser irradiation (Fig. 2.22). In this writing experiment, we scan the laser beam along the dotted arrow in Fig. 2.22**a**, starting at the domain boundary, with a scanning speed of 1 μm s^{-1}. During these measurements, the sample stage temperature was maintained at 600 °C (< T_c). The dimeter and power density of the laser beam are 120 μm and 970 W cm^{-1}, respectively. A Ψ+ domain (light gray) penetrates a Ψ– domain (dark gray), as it follows the laser irradiation position during the scanning, and finally divides the Ψ– domain into two regions (compare Figure 2.22**a** with 2.22**b**). In the written domain structure, the width of the line-shaped dextro domain on the entrance side (left side in Fig. 2.22**b**) is larger than that on the exit side (right side in Fig. 2.22**b**). This taper-shaped domain formation is well explained by a model that we will discuss as follows. In addition, the Ψ– domain at the exit side of the scanning is slightly displaced to the end point of the scanning. *In situ* imaging of this laser scanning experoment is depicted in Supplementary Movie S2 in ref. [38]. This result shows that we have written a Ψ+ domain into a Ψ– domain, namely, achieved chirality switching.

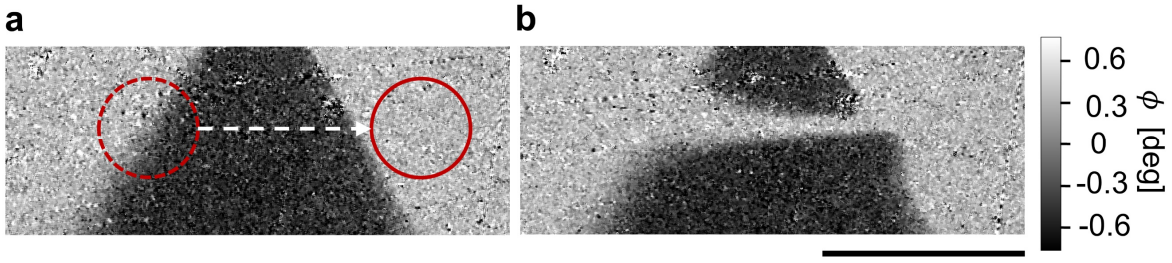

Fig. 2.22 Laser writing of a chiral domain pattern. Reprinted with permission from ref. [38]. Copyright 2022 American Chemical Society. **a**, Initial domain pattern before scanning laser beam. Bright- and dark-gray regions correspond to Ψ+ and Ψ– domains, respectively. **b**, Domain pattern after laser scanning. The red dotted and solid circles in (**a**) represent the start and the end points of laser scanning, respectively. The white arrow represents the scanning direction. The laser beam's diameter and the power density were 120 μm and 970 W cm^{-2}, respectively. The scanning speed was 1 μm s^{-1}. These images were taken at 600 °C. Scale bar: 250 μm.

2.4.4 Mechanism of the chirality switching by laser irradiation.

Here, we discuss a possible mechanism of the observed chirality switching by laser irradiation. As previously mentioned, no light polarization dependence was observed during domain formation, and therefore, local heating induced by laser irradiation should be a dominant factor. Unlike in laser control of ferroelectric domains [46,47], an electric field, which can be induced by local heating, differs from a conjugate field of ferrochiral order, and thus, induced thermal distributions purely affect the reconstruction of domain structures. Furthermore, because the domain structure remained unchanged unless the domain boundary was heated to temperatures above T_c (Fig. 2.21), a mechanism based on the entropy of domains and thermal gradient discussed for ferromagnets [36,48] cannot be applied to the present case. In the following, we propose a model that explains the observed domain reconstruction by laser irradiation in terms of domain boundary minimization, as shown in Fig. 2.23.

Figures 2.23**a**-**h** schematically illustrate how the domain pattern evolves when the sample is cooled from T above T_c with laser irradiation (Fig. 2.20), or when the sample is irradiated by laser at a fixed ambient temperature below T_c (Fig. 2.21). Here, we assume that domain boundaries must be locally minimized in their formation to minimize an energy loss caused by structural mismatches at domain boundaries. First, we shall consider the initial domain structure with a domain boundary, as depicted in Fig. 2.23**a**. Then, due to laser irradiation, a part of the initial state, including the domain boundary is heated to temperatures above T_c, which corresponds to the red circle area in Fig. 2.23**b**. In the figure, the edge of the red circle corresponds to the boundary between the low-T chiral and the high-T achiral phases. Note that the center of the red circle, i.e., the laser irradiation position, is slightly away from the initial domain boundary. Subsequently, by reducing the sample temperature or laser power, the red circle area ($T > T_c$) becomes smaller, as shown in Fig. 2.23**c**. If the edge of the red circle area touches chiral domain boundaries in the low-T chiral phase, the boundaries will be elongated in a direction perpendicular to the tangent line of the red circle area to locally minimize the domain boundary. This type of domain formation continuously occurs with decreasing temperature or laser power, expanding the dextro domain toward the center of the laser irradiation position (Fig. 2.23**d**). This model agrees well with the results in Fig. 2.21, including the presence of a threshold of laser power to move the domain boundary.

The formation of a bow-tie-shaped domain pattern by laser irradiation (Fig. 2.20) can be also explained using this model when the area at $T > T_c$ covers two domain boundaries as shown in Fig. 2.23**e**. At positions away from the laser irradiation position, domains are formed without the impact of laser irradiation. In these areas, the domain pattern is the same as the initial one, most likely due to a pinning effect on domain boundary (Fig. 2.23**f,** see also 2.3.3). After the ambient temperature is further decreased, the domain formation influenced by laser irradiation becomes dominant (Fig. 2.23**g**). The newly constructed domain boundaries (the solid blue line) should be perpendicular to the tangent line of the red circle area. Consequently, domain boundaries are accumulated at the irradiation position (Fig. 2.23**h**). In this process, boundaries are forced to extend to the laser spot, which makes straight-line sahped boundaries, rather than as-grown round shaped boundries (compare Figs. 2.20**b**-**d** with Fig. 2.20**a**). The

observed initial domain structure (Fig. 2.20**a**) is different from the model structure in Fig. 2.23**e**. However, this model is still reasonable, considering the effect of domain structures out of the observation area. In this model, the resulting domain pattern will differ from sample to sample, as it should be affected by initial domain structures and pinning effects on domain boundaries. We observed such sample-dependent domain patterns, as depicted in Fig. 2.24.

The illustrations in Figs. 2.23**i-l** correspond to the writing of the chiral domain pattern by laser scanning. In the case of laser scanning, the red circle area ($T > T_c$) is shifted by moving the laser position. At the edge of the red circle area, the domain boundary is reconstructed so that it is perpendicular to the tangent line of the red circle area, as discussed above. In this case, however, as the center of the red circle area is continuously moved (Fig. 2.23**k**), its tangent line is continuously changed. This leads to a tapered domain, as shown in Fig. 2.23**l**. This matches well with the domain structure obtained by laser scanning (Fig. 2.22**b**).

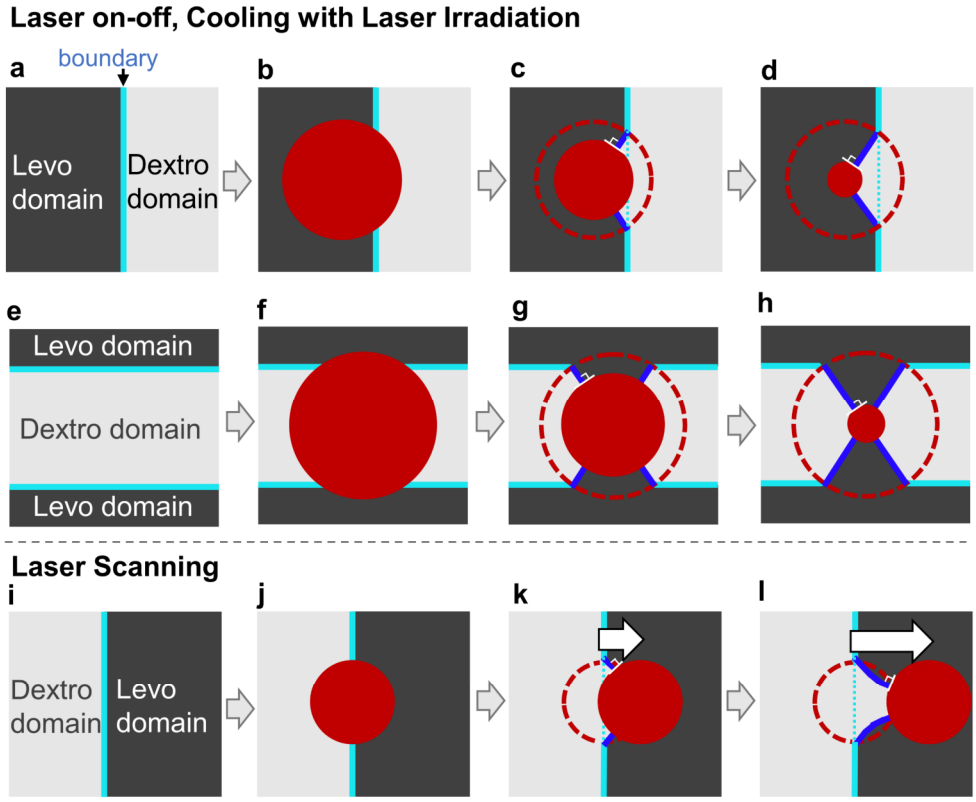

Fig. 2.23 Possible mechanism of chirality switching by laser irradiation. Reprinted with permission from ref. [38]. Copyright 2022 American Chemical Society. **a-h**, Effect of laser irradiation on the formation of chiral domains with cooling across T_c or changing laser power below T_c. The cyan solid line denotes the initial domain boundary. The red circles represent the areas heated to temperatures above T_c by laser irradiation. The situations in which the area covers one (**a-d**) and two (**e-h**) domain boundaries. The dotted cyan line and the blue solid line depict the positions of the initial and newly constructed domain boundaries, respectively. **i-l**, Effect of laser scanning on the writing of domain patterns. The situation in which the laser position is moved from left to right is considered. The white arrows represent the laser scanning direction.

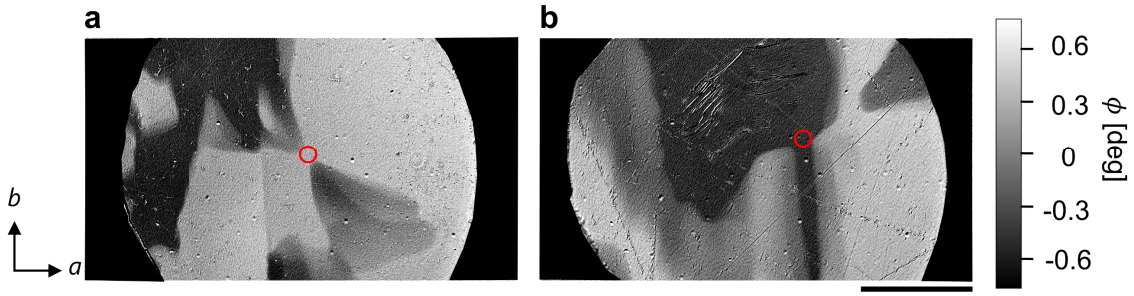

Fig. 2.24 Effect of laser irradiation on the domain formation in different samples. Reprinted with permission from ref. [38]. Copyright 2022 American Chemical Society. **a**,**b,** Spatial distributions of chiral domains in two different samples distinct from the sample shown in the main text. The sample thickness is 50 μm for (**a**) and 45 μm for (**b**). Prior to the respective observations, the samples were cooled from 800 °C (> T_c) to a temperature below T_c (500 °C) with laser irradiation. The cooling rate was 5 °C min^{-1} from 800 °C to 700 °C and 25 °C min^{-1} from 700 °C to 500 °C. All images were taken after switching off the laser source. The red open circles denote the laser irradiation positions. Here, we used a laser beam with a wavelength of 633 nm. The beam's diameter and power density were 140 μm and 300 W cm^{-1}, respectively. In both samples, domain boundaries accumulated at the irradiation position. Scale bar: 500 μm.

2.5 Summary

In this chapter, we have studied ferrochiral domains in a pure ferrochiral material $Ba(TiO)Cu_4(PO_4)_4$ (BTCPO). First, we have successfully obtained spatial distributions of optical rotation (OR) over a wide temperature range, enabling us to visualize the ferrochiral domain formation process. Moreover, by evaluating the optical rotatory power (ORP) using the OR images taken at various wavelengths, we have found that the temperature dependence of OR in BTCPO is strongly wavelength-dependent, which even causes the unusual temperature-induced reversal of OR at 880 nm. Subsequently, we have succeeded in manipulating ferrochiralchiral domains, namely, switching chirality in BTCPO by laser irradiation. We have proposed a possible mechanism of the laser irradiation effect on chirality in terms of local heating that leads to the reconstruction of domain boundaries, enabling control of chiral domains. Based on this effect, we wrote chiral domain patterns by scanning a laser beam on the sample surface. Our success in switching ferrochiral domains in a pure ferrochiral material offers a unique approach for manipulating crystallographic chirality.

References

[1] L. D. Barron, *Symmetry and Molecular Chirality*, Chem. Soc. Rev. **15**, 189 (1986).

[2] L. D. Barron, *Chirality and Life*, Space Sci. Rev. **135**, 187 (2008).

[3] D. F. J. Arago, *Mémoire Sur Une Modification Remarquable Qu'éprouvent Les Rayons Lumineux Dans Leur Passage à Travers Certains Corps Diaphanes et Sur Quelques Autres Nouveaux Phénomènes d'optique*, Mémoires de La Classe Des Sciences Mathématiques et Physiques de l'Institut Impérial de France **12**, 93 (1811).

[4] G. L. J. A. Rikken and E. Raupach, *Observation of Magneto-Chiral Dichroism*, Nature **390**, 493 (1997).

[5] S. Mühlbauer, B. Binz, F. Jonietz, C. Pfleidere, A. Rosch, A. Neubauer, R. Georgii, and P. Böni, *Skyrmion Lattice in a Chiral Magnet*, Science **323**, 915 (2011).

[6] K. C. Erb and J. Hlinka, *Symmetry Guide to Chiroaxial Transitions*, Phase Transitions **91**, 953 (2018).

[7] C. Konak, V. Kopsky, and F. Smutny, *Gyrotropic Phase Transitions*, J. Phys. C: Solid State Phys. **11**, 2493 (1978).

[8] J. Hlinka, *Eight Types of Symmetrically Distinct Vectorlike Physical Quantities*, Phys. Rev. Lett. **113**, 165502 (2014).

[9] K. Aizu, *Possible Species of Ferroelectrics*, Phys. Rev. **146**, 423 (1966).

[10] K. Aizu, *Possible Species of "Ferroelastic" Crystals and of Simultaneously Ferroelectric and Ferroelastic Crystals*, J. Phys. Soc. Jpn. **27**, 387 (1969).

[11] J. Hlinka, J. Privratska, P. Ondrejkovic, and V. Janovec, *Symmetry Guide to Ferroaxial Transitions*, Phys. Rev. Lett. **116**, 177602 (2016).

[12] K. C. Erb and J. Hlinka, *Vector, Bidirector, and Bloch Skyrmion Phases Induced by Structural Crystallographic Symmetry Breaking*, Phys. Rev. B **102**, 024110 (2020).

[13] V. Janovec, *Axial Crystals–Macroscopic Symmetry and Tensor Properties*, Phase Transitions **90**, 1 (2017).

[14] T. Hayashida, K. Kimura, D. Urushihara, T. Asaka, and T. Kimura, *Observation of Ferrochiral Transition Induced by an Antiferroaxial Ordering of Antipolar Structural Units in $Ba(TiO)Cu_4(PO_4)_4$*, J. Am. Chem. Soc. **143**, 3638 (2021).

[15] A. W. Schlueter, R. A. Jacobson, and R. E. Rundle, *A Redetermination of the Crystal Structure of $CsCuCl_3$*, Inorg. Chem. **5**, 277 (1966).

[16] S. Vasudevan, A. M. Shaikh, and C. N. R. Rao, *Jahn-Teller Effect Induced Phase Transitions In $CsCuCl_3$*, Phys. Lett. A **70**, 44 (1979).

[17] K. Duriš, U. Müller, and M. Jansen, *K_3NiO_2 Revisited, Phase Transition and Crystal Structure Refinement*, Z. Anorg. Allg. Chem. **638**, 737 (2012).

[18] R. X. Fischer and E. Tillmanns, *Revised Data for Combeite, $Na_2Ca_2Si_3O_9$*, Acta Crystallogr. **C43**, 1852 (1987).

[19] T. Yamada and H. Koizumi, *Czochralski Growth of $Ag_4P_2O_7$ Crystals*, J. Cryst. Growth **64**, 558 (1983).

[20] L.-Z. Chen, D. D. Huang, Q. J. Pan, and J. Z. Ge, *Novel Pure Pnma-$P2_12_12_1$ Ferroelastic Phase Transition of 1,4-Diisopropyl-1,4-Diazonia-Bicyclo-[2.2.2]Octane Tetra-Chlorobromo-M(Ii) (M = Mn and Co)*, RSC Adv. **5**, 13488 (2015).

[21] A. G. Cuevas, J. M. P. Mato, M. J. Tello, G. Madariaga, J. Fernandez, and L. Echarri, *Gyrotropic Phase Transition in the Layer Crystal $(C_5H_{11}NH_3)_2ZnCl_4$ at 249 K*, Phys. Rev. B **29**, 2655 (1984).

[22] H. Iwasaki, K. Sugii, T. Yamada, and N. Niizeki, *$5PbO{\cdot}3GeO_2$ Crystal; A New Ferroelectric*, Appl.

References

Phys. Lett. **18**, 444 (1971).

[23] H. Iwasaki, K. Sugii, N. Niizeki, and H. Toyoda, *Switching of Optical Rotatory Power in Ferroelectric $5PbO{\cdot}3GeO_2$ Single Crystal*, Ferroelectrics **3**, 157 (1972).

[24] J. Kobayashi, K. Uchino, H. Matsuyama, and K. Saito, *Optical Study on Domain Switching of Ferroelectric Triglycine Sulfuric Acid and Rochelle Salt*, J. Appl. Phys. **69**, 409 (1991).

[25] D. D. Khalyavin, R. D. Johnson, F. Orlandi, P. G. Radaelli, P. Manuel, and A. A. Belik, *Emergent Helical Texture of Electric Dipoles*, Science **369**, 680 (2020).

[26] A. Sawada, Y. Ishibashi, and Y. Takagi, *Ferroelasticity and the Origin of Optical Activity of $Ca_2Sr(C_2H_5CO_2)_6$ (DSP)*, J. Phys. Soc. Jpn. **43**, 195 (1977).

[27] L. D. Barron, *Molecular Light Scattering and Optical Activity (2nd Ed.)* (Cambridge University Press, Cambridge, 2004).

[28] W. Kaminsky, *Experimental and Phenomenological Aspects of Circular Birefringence and Related Properties in Transparent Crystals*, Rep. Prog. Phys. **63**, 1575 (2000).

[29] J. F. Nye, *Physical Properties of Crystals: Their Representation by Tensors and Matrices* (Clarendon Press, 1985).

[30] J. Sakai, *Metamaterial No Tame No Kogaku Nyumon (Introduction to Optics in Metamaterial , in Japanese)* (Morikita-shuppan, Tokyo, 2017).

[31] K. Kimura, M. Sera, and T. Kimura, *A^{2+} Cation Control of Chiral Domain Formation in $A(TiO)Cu_4(PO_4)_4$ (A = Ba, Sr)*, Inorg. Chem. **55**, 1002 (2016).

[32] Y. Yanase, *Magneto-Electric Effect in Three-Dimensional Coupled Zigzag Chains*, J. Phys. Soc. Jpn. **83**, 014703 (2014).

[33] H. Watanabe and Y. Yanase, *Group-Theoretical Classification of Multipole Order: Emergent Responses and Candidate Materials*, Phys. Rev. B **98**, 245129 (2018).

[34] T. Sato, N. Abe, S. Kimura, Y. Tokunaga, and T.-H. Arima, *Magnetochiral Dichroism in a Collinear Antiferromagnet with No Magnetization*, Phys. Rev. Lett. **124**, 217402 (2020).

[35] J. P. Tetienne et al., *Nanoscale Imaging and Control of Domain-Wall Hopping with a Nitrogen-Vacancy Center Microscope*, Science **344**, 1366 (2014).

[36] S. Moretti, V. Raposo, E. Martinez, and L. Lopez-Diaz, *Domain Wall Motion by Localized Temperature Gradients*, Phys. Rev. B **95**, 064419 (2017).

[37] N. Hedrich, K. Wagner, O. V. Pylypovskyi, B. J. Shields, T. Kosub, D. D. Sheka, D. Makarov, and P. Maletinsky, *Nanoscale Mechanics of Antiferromagnetic Domain Walls*, Nat. Phys. **17**, 574 (2021).

[38] T. Hayashida, K. Kimura, and T. Kimura, *Switching Crystallographic Chirality in $Ba(TiO)Cu_4(PO_4)_4$ by Laser Irradiation*, J. Phys. Chem. Lett. **13**, 3857 (2022).

[39] K. Kimura, T. Katsuyoshi, Y. Sawada, S. Kimura, and T. Kimura, *Imaging Switchable Magnetoelectric Quadrupole Domains via Nonreciprocal Linear Dichroism*, Commun. Mater. **1**, 39 (2020).

[40] V. I. Voronkova and T. Wolf, *Thermomechanical Detwinning of $YBa_2Cu_3O_{7-x}$ Single Crystals under Reduced Oxygen Partial Pressure*, Phys. C **218**, 175 (1993).

[41] H. Xu and P. J. Heaney, *Memory Effects of Domain Structures during Displacive Phase Transitions: A High-Temperature TEM Study of Quartz and Anorthite*, Am. Mineral. **82**, 99 (1997).

[42] E. K. H. Salje, S. A. Hayward, and W. T. Lee, *Ferroelastic Phase Transitions: Structure and Microstructure*, Acta Crystallogr. A **61**, 3 (2005).

[43] J. A. Schellman, *Circular Dichroism and Optical Rotation*, Chem. Rev. **75**, 323 (1975).

[44] D. Yogev-Einot and D. Avnir, *Quantitative Symmetry and Chirality of the Molecular Building Blocks of Quartz*, Chem. Mater. **15**, 464 (2003).

[45] D. Yogev-Einot and D. Avnir, *The Temperature-Dependent Optical Activity of Quartz: From Le*

Châtelier to Chirality Measures, Tetrahedron Asymmetry **17**, 2723 (2006).

[46] C. Y. J. Ying, A. C. Muir, C. E. Valdivia, H. Steigerwald, C. L. Sones Collin L., R. W. Eason, E. Soergel, and S. Mailis, *Light-Mediated Ferroelectric Domain Engineering and Micro-Structuring of Lithium Niobate Crystals*, Laser and Photonics Rev. **6**, 526 (2012).

[47] X. Chen, P. Karpinski, V. Shvedov, K. Koynov, B. Wang, J. Trull, C. Cojocaru, W. Krolikowski, and Y. Sheng, *Ferroelectric Domain Engineering by Focused Infrared Femtosecond Pulses*, Appl. Phys. Lett. **107**, 3 (2015).

[48] F. Schlickeiser, U. Ritzmann, D. Hinzke, and U. Nowak, *Role of Entropy in Domain Wall Motion in Thermal Gradients*, Phys. Rev. Lett. **113**, 097201 (2014).

Chapter 3
Ferroaxial Domain Observation

3.1 Introduction

Ferroaxial order represents an intriguing and appealing field of research, still in its early stages of exploration. This nascent topic promises a potential ground for discovering novel physical phenomena and functionalities. In this section, we first summarize the symmetry aspect of the ferroaxial order, along with the current stage of research on this subject. Following this, we introduce how the ferroaxial order is related to the optical phenomenon of electrogyration. Finally, the two ferroaxial materials discussed in this section, $NiTiO_3$ and $RbFe(MoO_4)_2$, are introduced.

3.1.1 Symmetry aspect of ferroaxial order

As introduced in Chapter 1, the order parameter of the ferroaxial order is a time-even axial vector. In crystals, ferroaxial order arises from a spontaneous rotational distortion that breaks the mirror symmetry, whose mirror plane includes the axis of rotation. Among the 32 crystallographic point groups, there are 13 pyroaxial point groups which allow for such a rotational distortion $(1, \bar{1}, 2, m, 2/m, 3, \bar{3}, 4, \bar{4}, 4/m, 6, 6/m, \bar{6})$ [1,2]. (The term "pyroaxial" is an analogue to the term "pyroelectric".) Then, among the 212 nonmagnetic species [3,4], a total of 124 ferroaxial species exist, as shown in Fig. 3.1 [2,5]. We note that 8 of the 124 ferroaxial species are pure ones ($\bar{4}2m \rightarrow \bar{4}, 4/mmm \rightarrow 4/m, 4/mmm \rightarrow \bar{4}, \bar{3}m \rightarrow \bar{3}, \bar{6}2m \rightarrow \bar{6}, 6/mmm \rightarrow 6/m, 6/mmm \rightarrow \bar{6},$ and $6/mmm \rightarrow \bar{3}$), which accompany neither ferroelectric, ferroelastic, nor ferrochiral transitions [2,5,6].

In Fig. 3.2, we schematically illustrate one of the pure ferroaxial transitions 4/*mmm*→4/*m*. This transition involves the rotation of structural units (depicted as red plates in Fig. 3.2**a**-**c**), which breaks the mirror symmetries present in the parent 4/*mmm* phase. In crystals, the rotation is carried out by charged ions, resulting in a vortex arrangement of electric dipoles which corresponds to the ion displacement. Consequently, a ferroaxial moment (sometimes called electric-toroidal-dipole moment) **A** defined as $\mathbf{A} \propto \sum_i \mathbf{r}_i \times \mathbf{p}_i$ is a good order parameter characterizing the ferroaxial order (see Figs. 3.2**d**,**e**) [7,8]. Here $\mathbf{r}_i$ denotes a position vector of electric dipole $\mathbf{p}_i$ from the symmetrical center of a structural unit.

When a crystal undergoes a ferroaxial transition, ferroaxial domains with different arrangements of **A** are formed. The number of such domain states for each transition is summarized in Fig. 3.1. In the case of the pure ferroaxial transition, a pair of domains with the opposite signs of **A** is formed (see also Figs. 3.2**b**,**c**). These domains, A+ and A−, are related to each other by a mirror operation, which is a symmetry operation in the parent non-ferroaxial phase.

Crystals that exhibit the above-mentioned pure ferroaxial transitions (pure ferroaxial crystals) will provide an ideal platform for examining the characteristics of the ferroaxial order, unaffected by other ferroic properties. Examples of such pure ferroaxial crystals are listed in Table 3.1.

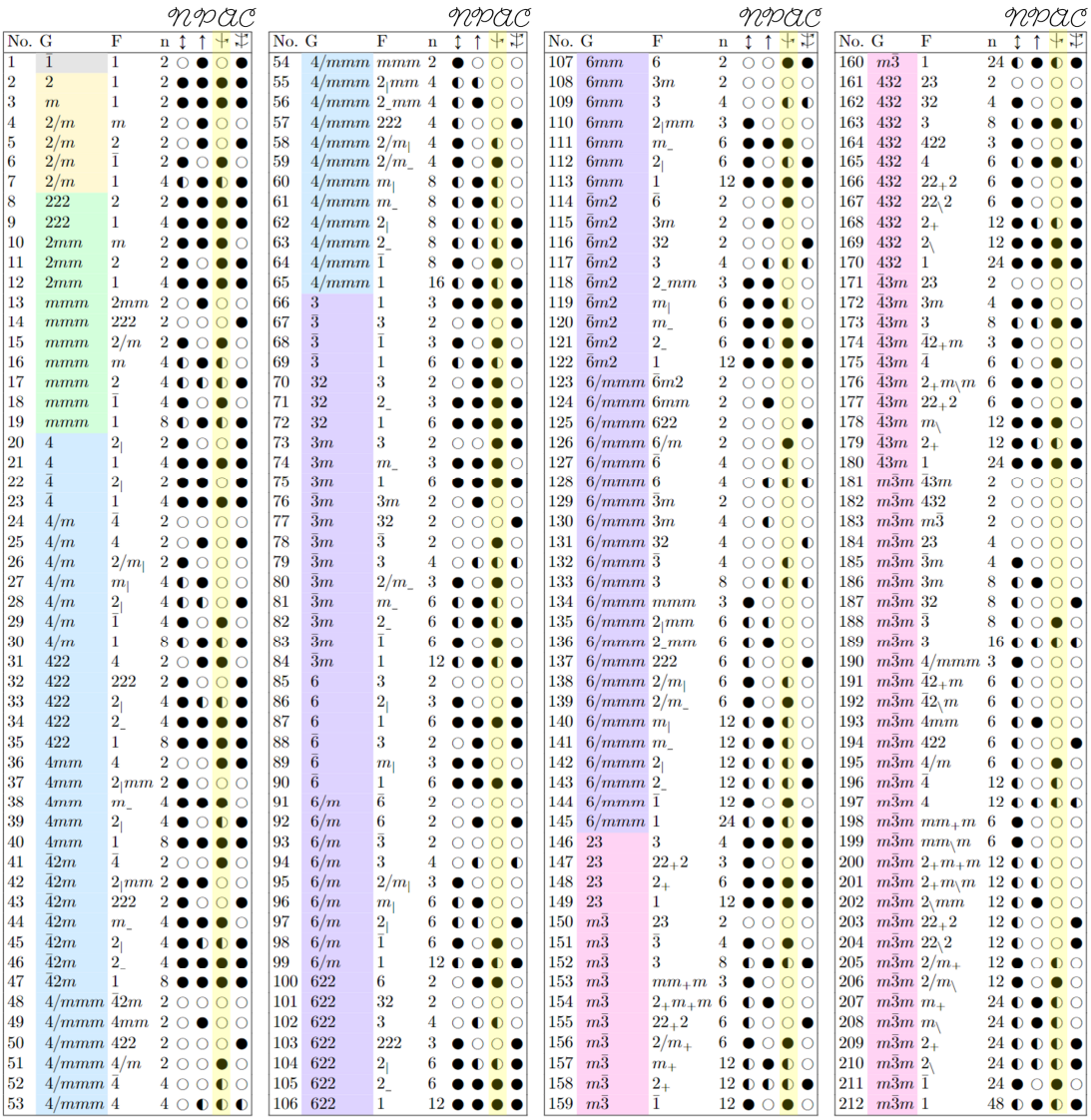

No.	G	F	n	𝒫	𝒫𝒜
1	$\bar{1}$	1	2	○	●
2	2	1	2	●	●
3	m	1	2	●	●
4	$2/m$	m	2	○	○
5	$2/m$	2	2	○	●
6	$2/m$	$\bar{1}$	2	●	○
7	$2/m$	1	4	◐	●
8	222	2	2	●	●
9	222	1	4	●	●
10	$2mm$	m	2	●	○
11	$2mm$	2	2	○	●
12	$2mm$	1	4	●	●
13	mmm	$2mm$	2	○	○
14	mmm	222	2	○	●
15	mmm	$2/m$	2	●	○
16	mmm	m	4	◐	○
17	mmm	2	4	◐	●
18	mmm	$\bar{1}$	4	○	○
19	mmm	1	8	◐	●
20	4	$2_{\vert}$	2	●	●
21	4	1	4	●	●
22	$\bar{4}$	$2_{\vert}$	2	●	○
23	$\bar{4}$	1	4	●	●
24	$4/m$	$\bar{4}$	2	○	○
25	$4/m$	4	2	○	●
26	$4/m$	$2/m_{\vert}$	2	●	○
27	$4/m$	$m_{\vert}$	4	◐	○
28	$4/m$	$2_{\vert}$	4	◐	●
29	$4/m$	$\bar{1}$	4	●	○
30	$4/m$	1	8	◐	●
31	422	4	2	○	●
32	422	222	2	●	○
33	422	$2_{\vert}$	4	●	◐
34	422	$2_{\backslash}$	4	●	●
35	422	1	8	●	●
36	$4mm$	4	2	○	●
37	$4mm$	$2_{\vert}mm$	2	●	○
38	$4mm$	$m_{\backslash}$	4	●	●
39	$4mm$	$2_{\vert}$	4	○	◐
40	$4mm$	1	8	●	●
41	$\bar{4}2m$	$\bar{4}$	2	○	●
42	$\bar{4}2m$	$2_{\vert}mm$	2	●	○
43	$\bar{4}2m$	222	2	●	○
44	$\bar{4}2m$	$m_{\backslash}$	4	●	●
45	$\bar{4}2m$	$2_{\vert}$	4	◐	◐
46	$\bar{4}2m$	$2_{\backslash}$	4	●	●
47	$\bar{4}2m$	1	8	●	●
48	$4/mmm$	$\bar{4}2m$	2	○	○
49	$4/mmm$	$4mm$	2	○	○
50	$4/mmm$	422	2	○	●
51	$4/mmm$	$4/m$	2	○	○
52	$4/mmm$	$\bar{4}$	4	○	◐
53	$4/mmm$	4	4	○	◐
54	$4/mmm$	mmm	2	●	○
55	$4/mmm$	$2_{\vert}mm$	4	◐	◐
56	$4/mmm$	$2_{\backslash}mm$	4	◐	●
57	$4/mmm$	222	4	◐	○
58	$4/mmm$	$2/m_{\vert}$	4	●	○
59	$4/mmm$	$2/m_{\backslash}$	4	●	○
60	$4/mmm$	$m_{\vert}$	8	◐	●
61	$4/mmm$	$m_{\backslash}$	8	◐	●
62	$4/mmm$	$2_{\vert}$	8	◐	◐
63	$4/mmm$	$2_{\backslash}$	8	◐	◐
64	$4/mmm$	$\bar{1}$	8	●	○
65	$4/mmm$	1	16	◐	●
66	$\bar{3}$	1	3	●	●
67	$\bar{3}$	3	2	○	●
68	$\bar{3}$	$\bar{1}$	3	●	○
69	$\bar{3}$	1	6	◐	●
70	32	3	2	○	●
71	32	$2_{\backslash}$	3	●	●
72	32	1	6	●	●
73	$3m$	3	2	○	●
74	$3m$	$m_{\backslash}$	3	●	●
75	$3m$	1	6	●	●
76	$\bar{3}m$	$3m$	2	○	●
77	$\bar{3}m$	32	2	○	○
78	$\bar{3}m$	$\bar{3}$	2	○	●
79	$\bar{3}m$	3	4	○	◐
80	$\bar{3}m$	$2/m_{\backslash}$	3	●	○
81	$\bar{3}m$	$m_{\backslash}$	6	◐	●
82	$\bar{3}m$	$2_{\backslash}$	6	◐	●
83	$\bar{3}m$	$\bar{1}$	6	●	○
84	$\bar{3}m$	1	12	◐	●
85	6	3	2	○	○
86	6	$2_{\vert}$	3	●	○
87	6	1	6	●	●
88	$\bar{6}$	3	2	○	●
89	$\bar{6}$	$m_{\vert}$	3	●	○
90	$\bar{6}$	1	6	●	●
91	$6/m$	$\bar{6}$	2	○	○
92	$6/m$	6	2	○	●
93	$6/m$	$\bar{3}$	2	○	○
94	$6/m$	3	4	○	◐
95	$6/m$	$2/m_{\vert}$	3	●	○
96	$6/m$	$m_{\vert}$	6	◐	●
97	$6/m$	$2_{\vert}$	6	◐	◐
98	$6/m$	$\bar{1}$	6	●	○
99	$6/m$	1	12	◐	●
100	622	6	2	○	●
101	622	32	2	○	○
102	622	3	4	○	◐
103	622	222	3	●	○
104	622	$2_{\vert}$	6	●	◐
105	622	$2_{\backslash}$	6	●	●
106	622	1	12	●	●
107	$6mm$	6	2	○	●
108	$6mm$	$3m$	2	○	○
109	$6mm$	3	4	○	◐
110	$6mm$	$2_{\vert}mm$	3	●	○
111	$6mm$	$m_{\backslash}$	6	●	●
112	$6mm$	$2_{\vert}$	6	●	◐
113	$6mm$	1	12	●	●
114	$\bar{6}m2$	$\bar{6}$	2	○	○
115	$\bar{6}m2$	$3m$	2	○	●
116	$\bar{6}m2$	32	2	○	○
117	$\bar{6}m2$	3	4	○	◐
118	$\bar{6}m2$	$2_{\backslash}mm$	3	●	○
119	$\bar{6}m2$	$m_{\vert}$	6	●	●
120	$\bar{6}m2$	$m_{\backslash}$	6	●	●
121	$\bar{6}m2$	$2_{\backslash}$	6	●	◐
122	$\bar{6}m2$	1	12	●	●
123	$6/mmm$	$\bar{6}m2$	2	○	○
124	$6/mmm$	$6mm$	2	○	●
125	$6/mmm$	622	2	○	○
126	$6/mmm$	$6/m$	2	○	●
127	$6/mmm$	$\bar{6}$	4	○	○
128	$6/mmm$	6	4	○	◐
129	$6/mmm$	$\bar{3}m$	2	○	○
130	$6/mmm$	$3m$	4	○	○
131	$6/mmm$	32	4	○	◐
132	$6/mmm$	$\bar{3}$	4	○	○
133	$6/mmm$	3	8	○	◐
134	$6/mmm$	mmm	3	●	○
135	$6/mmm$	$2_{\vert}mm$	6	◐	○
136	$6/mmm$	$2_{\backslash}mm$	6	◐	●
137	$6/mmm$	222	6	◐	○
138	$6/mmm$	$2/m_{\vert}$	6	●	○
139	$6/mmm$	$2/m_{\backslash}$	6	●	○
140	$6/mmm$	$m_{\vert}$	12	◐	●
141	$6/mmm$	$m_{\backslash}$	12	◐	○
142	$6/mmm$	$2_{\vert}$	12	◐	◐
143	$6/mmm$	$2_{\backslash}$	12	◐	●
144	$6/mmm$	$\bar{1}$	12	●	○
145	$6/mmm$	1	24	◐	●
146	23	3	4	●	●
147	23	$22_{+}2$	3	●	○
148	23	2_{+}	6	●	●
149	23	1	12	●	●
150	$m\bar{3}$	23	2	○	○
151	$m\bar{3}$	$\bar{3}$	4	●	○
152	$m\bar{3}$	3	8	◐	●
153	$m\bar{3}$	$mm_{+}m$	3	●	○
154	$m\bar{3}$	$2_{+}m_{+}m$	6	◐	○
155	$m\bar{3}$	$22_{+}2$	6	◐	○
156	$m\bar{3}$	$2/m_{+}$	6	●	○
157	$m\bar{3}$	m_{+}	12	◐	○
158	$m\bar{3}$	2_{+}	12	◐	◐
159	$m\bar{3}$	$\bar{1}$	12	●	○
160	$m\bar{3}$	1	24	◐	●
161	432	23	2	○	○
162	432	32	4	●	○
163	432	3	8	◐	●
164	432	422	3	●	○
165	432	4	6	◐	●
166	432	$22_{+}2$	6	●	○
167	432	$22_{\backslash}2$	6	●	○
168	432	2_{+}	12	●	◐
169	432	$2_{\backslash}$	12	●	●
170	432	1	24	●	●
171	$\bar{4}3m$	23	2	○	○
172	$\bar{4}3m$	$3m$	4	●	●
173	$\bar{4}3m$	3	8	◐	●
174	$\bar{4}3m$	$\bar{4}2_{+}m$	3	●	○
175	$\bar{4}3m$	$\bar{4}$	6	◐	○
176	$\bar{4}3m$	$2_{+}m_{\backslash}m$	6	●	●
177	$\bar{4}3m$	$22_{+}2$	6	●	○
178	$\bar{4}3m$	$m_{\backslash}$	12	●	●
179	$\bar{4}3m$	2_{+}	12	●	◐
180	$\bar{4}3m$	1	24	●	●
181	$m\bar{3}m$	$43m$	2	○	○
182	$m\bar{3}m$	432	2	○	○
183	$m\bar{3}m$	$m\bar{3}$	2	○	○
184	$m\bar{3}m$	23	4	○	○
185	$m\bar{3}m$	$3m$	4	●	○
186	$m\bar{3}m$	$3m$	8	◐	○
187	$m\bar{3}m$	32	8	◐	○
188	$m\bar{3}m$	$\bar{3}$	8	◐	○
189	$m\bar{3}m$	3	16	◐	◐
190	$m\bar{3}m$	$4/mmm$	3	●	○
191	$m\bar{3}m$	$\bar{4}2_{+}m$	6	◐	○
192	$m\bar{3}m$	$\bar{4}2_{\backslash}m$	6	◐	○
193	$m\bar{3}m$	$4mm$	6	◐	●
194	$m\bar{3}m$	422	6	◐	○
195	$m\bar{3}m$	$4/m$	6	◐	○
196	$m\bar{3}m$	$\bar{4}$	12	◐	○
197	$m\bar{3}m$	4	12	◐	◐
198	$m\bar{3}m$	$mm_{+}m$	6	●	○
199	$m\bar{3}m$	$mm_{\backslash}m$	6	●	○
200	$m\bar{3}m$	$2_{+}m_{+}m$	12	◐	◐
201	$m\bar{3}m$	$2_{+}m_{\backslash}m$	12	◐	○
202	$m\bar{3}m$	$2_{\backslash}mm$	12	◐	●
203	$m\bar{3}m$	$22_{+}2$	12	◐	○
204	$m\bar{3}m$	$22_{\backslash}2$	12	◐	○
205	$m\bar{3}m$	$2/m_{+}$	12	●	○
206	$m\bar{3}m$	$2/m_{\backslash}$	12	●	○
207	$m\bar{3}m$	m_{+}	24	◐	◐
208	$m\bar{3}m$	$m_{\backslash}$	24	◐	●
209	$m\bar{3}m$	2_{+}	24	◐	◐
210	$m\bar{3}m$	$2_{\backslash}$	24	◐	●
211	$m\bar{3}m$	$\bar{1}$	24	●	○
212	$m\bar{3}m$	1	48	◐	●

Fig. 3.1 List of 212 nonmagnetic species classifying ferroelastic, ferroelectric, and ferroaxial transitions [5]. Reproduced from Fig. 2.1. The columns corresponding to ferroaxial transitions ($\mathcal{A}$) are highlighted in yellow.

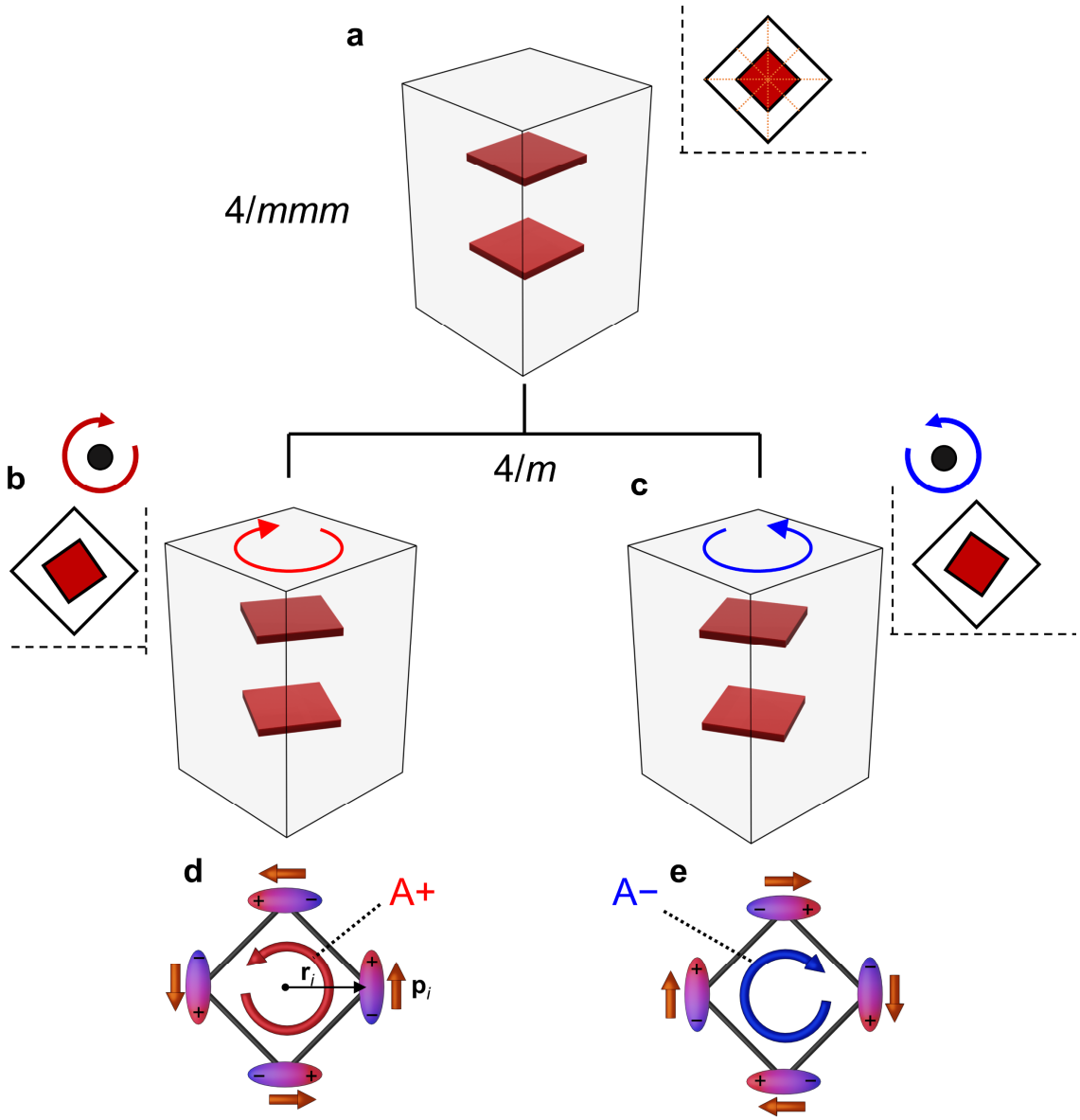

Fig. 3.2 Schematic illustration of ferroaxial transition. **a**, Non-ferroaxial (non-distorted) phase. **b, c**, Ferroaxial phase. The black rectangle and red plates represent a unit cell and structural units composed of ions in a crystal, respectively. In the ferroaxial phase, clockwise (**b**) and counterclockwise (**c**) rotational distortions are depicted. The insets of the respective panels show rotations seen parallel to the rotational axis. The orange dashed lines in the inset of panel **a** represent mirror planes, which are lost in the ferroaxial phase (**b**,**c**). **d, e,** Ferroaxial moment defined as $\mathbf{A} \propto \sum_i \mathbf{r}_i \times \mathbf{p}_i$, where $\mathbf{r}_i$ denotes a position vector of electric dipole $\mathbf{p}_i$ from the symmetrical center of a structural unit. The sign of $\mathbf{A}$ is characterized by the rotation direction of the electric dipoles. Here rotations of anions are assumed and rotations of red squares in (**b,c**) are opposite from those of electric dipoles in (**d,e**).

Table 3.1 Examples of pure ferroaxial crystals. The materials discussed in this thesis, $NiTiO_3$ and $RbFe(MoO_4)_2$, are highlighted in gray.

Substance	Transition	T_c	Reference
$NiTiO_3$	$R\bar{3}c \rightarrow R\bar{3}$	1560K	[9]
$RbFe(MoO_4)_2$	$P\bar{3}m1 \rightarrow P\bar{3}$	190K	[10]
$CsFe(MoO_4)_2$	$P\bar{3}m1 \rightarrow P\bar{3}$	220K	[11]
$K_2Zr(PO_4)_2$	$P\bar{3}m1 \rightarrow P\bar{3}$	~ 700K	[12]
Sr_2CuWO_6	$I4/mmm \rightarrow I4/m$	873K	[13]
$N(CH_3)_4CdBr_3$	$P6_3/mmc \rightarrow P6_3/m$	390K	[14]
$Cu_4(OH)_6FBr$	$P6_3/mmc \rightarrow P6_3/m$	262K	[15]

3.1.2 Current stage of research on the ferroaxial order

The concept of ferroaxiality was initially introduced by Johnson and coworkers in 2011 as an underlying factor of the spin-driven ferroelectric properties, i.e., multiferroicity, in $Cu_3Nb_2O_8$ [16]. So far, multiferroicity induced by similar mechanisms has been reported in $CaMn_7O_{12}$ [17], In_2NiMnO_6 [18], and $RbFe(MoO_4)_2$ [19]. In 2016, Hlinka and coworkers provided comprehensive analysis of ferroaxial transitions from symmetry analysis based on crystallographic point groups, as introduced in 3.1.1. This work triggered studies about the ferroaxial order as a distinct ferroic order. Then, in 2020, Jin and coworkers achieved a significant milestone by experimentally observing the ferroaxial order in $RbFe(MoO_4)_2$ using rotational anisotropy second harmonic generation (SHG) [20]. In that work, the temperature variation of the areal ratio of the ferroaxial domains was shown (see 3.1.5 for details). However, spatial distributions of ferroaxial domains have never been observed through the nature inherent in the ferroaxial order. Visualizing ferroic domain provides valuable information such as a domain size, shape, thickness of domain boundaries, and domain behavior in response to external fields. Thus, the visualization of ferroaxial domains plays a crucial role in advancing research in the emerging field of ferroaxial order. In this chapter, we present a significant breakthrough in the visualization of ferroaxial domains using electrogyration.

3.1.3 Electrogyration

Electrogyration (EG), that is, optical rotation induced by an external electric field, was first described by Aizu [21] and Zheludev [22] independently in 1964 and then demonstrated in quartz by Vlokh in 1970 [23]. The linear and quadratic EG effects are known, and the former one is closely related to the ferroaxial order. So far, there have not been a lot of studies on the EG effect, but recently it has attracted interests due to its effectiveness for observing the ferroaxial order. In this subsection, first we briefly summarize the symmetric relationship between the ferroaxial order and the EG effect, and then introduce the mathematical descriptions of the effect.

Introduction

As discussed in Chapter 1, the dot product of axial ($\mathcal{A}$) and polar ($\mathcal{P}$) has the same symmetry with chiral ($\mathcal{C}$). Thus, when an electric field (**E**) is applied parallel to the ferroaxial moment (**A**), chirality and consequently optical rotation is induced in a ferroaxial crystal. This can be understood as the remaining mirror symmetry (or space inversion symmetry) in a ferroaxial system is broken by the applied electric field. Importantly, the two domain states A+ and A− exhibit opposite chirality under the same direction of an electric field, and thus the sign of EG, i.e., the direction of optical rotation, will also get opposite between the two. Therefore, ferroaxial domains are expected to be observed by obtaining a two-dimensional map of EG.

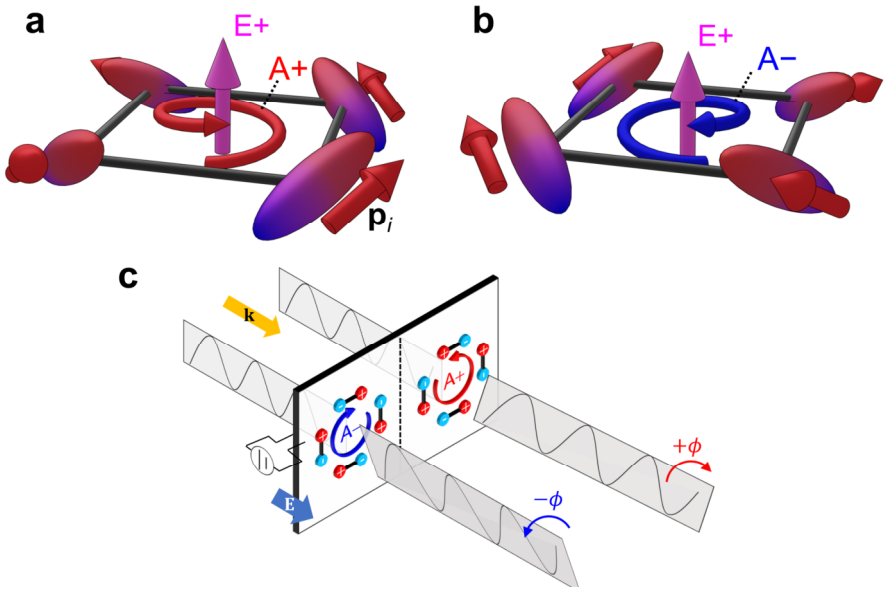

Fig. 3.3 Electric-field-induced chirality and electrogyration (EG) in a ferroaxial system. **a**,**b** Ferroaxial moment under an electric field. Here, each electric dipole moment is tilted toward the applied electric field, inducing chirality in the system. Under an electric field in the same direction, the A+ and A- states exhibit opposite chirality. **c** Conceptual diagram of EG in a ferroaxial crystal [24]. When linearly polarized light propagates thorough a ferroaxial crystal, the sign of optical rotation angle ϕ induced via EG depends on that of **A**.

In the following, we present the mathematical descriptions of the EG effect. The EG effect is described by the change in the gyration tensor g_{ij} as a function of an applied electric field *E*. Equation (2.1) is then expressed as a power series [25],

$$\rho = \frac{\pi}{\lambda n} g_{ij} k_i k_j = \frac{\pi}{\lambda n} \left(g_{ij}^{(0)} + \gamma_{ijk} E_k + \beta_{ijkl} E_k E_l + \cdots \right) k_i k_j. \tag{3.1}$$

Here, $g_{ij}^{(0)}$ represents natural optical rotation, and $\gamma_{ijk}(\beta_{ijkl})$ represents the linear (quadratic) EG effect. The linear EG effect characterized by the third-rank axial tensor γ_{ijk} is allowed in all point groups except for $m3m$, $\bar{4}3m$, and 432, while the quadratic one by the fourth-rank axial tensor β_{ijkl} is finite only in non-centrosymmetric point groups.

Now let us focus on the liner EG effect and consider the situation when light propagates in a

ferroaxial crystal along its optic axis (the third axis), and an electric field is applied in the same direction. In this case, optical rotatory power is given as,

$$\rho = \frac{\pi}{\lambda_0 n_0}\gamma_{333}E_3\kappa_3\kappa_3 = \frac{\pi}{\lambda_0 n_0}\gamma_{333}E_3. \tag{3.2}$$

where $\kappa_3 = 1$. Furthermore, the effect of the sample thickness is cancelled out and the magnitude of rotation of polarization plane ($\phi\ [\mathrm{deg}] = \rho[\mathrm{deg\,mm^{-1}}] \cdot d[\mathrm{mm}]$) is described as

$$\phi = \frac{\pi d}{\lambda n}\gamma_{333}E_3 = \frac{\pi}{\lambda n}\gamma_{333}V_3 \tag{3.3}$$

where $V = E/d$. Therefore, ϕ is proportional to V at fixed λ and is expressed as

$$\phi[\mathrm{deg}] = \alpha[\mathrm{deg\,V^{-1}}] \times V[\mathrm{V}] \tag{3.4}$$

in which the coefficient $\alpha(\propto \gamma_{333})$ represents the magnitude of the linear EG.

Next, we demonstrate that the sign of γ_{333}, i.e., the sign of linear EG, depends on the sign of the ferroaxial moment **A**. Here, we take point group $\bar{3}$ for an example. Table 3.2 shows the linear EG tensor of point group $\bar{3}$. For a mirror operation [mirror plane ∥ (110)]

$$\sigma_{\mathrm{v}} = \begin{bmatrix} a_{11} & a_{12} & a_{13} \\ a_{21} & a_{22} & a_{23} \\ a_{31} & a_{32} & a_{33} \end{bmatrix} = \begin{bmatrix} \frac{1}{2} & -\frac{\sqrt{3}}{2} & 0 \\ -\frac{\sqrt{3}}{2} & -\frac{1}{2} & 0 \\ 0 & 0 & 1 \end{bmatrix} \tag{3.5}$$

which connects two opposite ferroaxial domain states (A+ and A–), the component of γ_{333} is rewritten as

$$\gamma'_{333} = -a_{3i}a_{3j}a_{3k}\gamma_{ijk} = -(1)(1)(1)\gamma_{333} = -\gamma_{333}. \tag{3.6}$$

This means that the sign of γ_{333}, i.e., the direction of electric-field-induced optical rotation in the configuration of $\mathbf{E} \parallel \boldsymbol{\kappa} \parallel \mathbf{A}$, depends on that of **A**. Therefore, it is confirmed that the ferroaxial domains can be distinguished by using the linear EG effect from the viewpoint of tensor calculations.

Table 3.2 Linear electrogyration matrix of point group $\bar{3}$ (orthogonal basis). This table was made based on Bilbao Crystallographic Server [26–28]. The component γ_{333} is highlighted in gray. The orthogonal basis ($\mathbf{a}_o, \mathbf{b}_o$, and $\mathbf{c}_o$) is obtained from the hexagonal basis ($\mathbf{a}_h, \mathbf{b}_h$, and $\mathbf{c}_h$) according to the relations, $\mathbf{a}_o \parallel \mathbf{a}_h, \mathbf{b}_o \parallel \mathbf{a}_h \times \mathbf{c}_h$ and $\mathbf{c}_o \parallel \mathbf{c}_h$.

γ_{ijk}		k		
		1	2	3
ij	11	γ_{111}	$-\gamma_{222}$	γ_{113}
	12	$-\gamma_{222}$	$-\gamma_{111}$	0
	13	γ_{131}	γ_{132}	0
	21	$-\gamma_{222}$	$-\gamma_{111}$	0
	22	$-\gamma_{111}$	γ_{222}	γ_{113}
	23	$-\gamma_{132}$	γ_{131}	0
	31	γ_{131}	γ_{132}	0
	32	$-\gamma_{132}$	γ_{131}	0
	33	0	0	γ_{333}

Finally, we show some examples of the previous EG measurements. Materials in which the EG effect has been measured are relatively limited most likely because of its smallness (typically, $\alpha \leq 10^{-4}\,\mathrm{deg\,V^{-1}}$ for the linear EG effect). Figure 3.4 summarizes such a few examples. The highest magnitude of the linear EG effect is reported in Cr doped $Pb_5Ge_3O_{11}$ at temperature around its ferroelectric transition ($\alpha = 3.94 \times 10^{-3}\ \mathrm{deg\,V^{-1}}, \lambda = 632.8\ \mathrm{nm}$) [29].

[Electrogyration figures of merit for different crystals]					
Dielectric crystals	$LiIO_3$	α-HIO_3	$LiNbO_3$	SiO_2	TeO_2
	γ_{33}=(1.5 ±0.3)×10^{-13} m/V	γ_{52}=(4.3 ±0.7)×10^{-13} m/V	γ_{41}=(3.4 ±1.3)×10^{-12} m/V	$\beta_{31}=\beta_{32}$=(4.5 ±0.3)×10^{-20} m^2/V^2 (quadratic electrogyration)	β_{33}=(6.6 ±1.7)×10^{-20} m^2/V^2 (quadratic electrogyration)
Wide-band semiconductors	$CdGa_2S_4$	$AgGaS_2$	$Bi_{12}SiO_{20}$	$Bi_{12}GeO_{20}$, and $Bi_{12}TiO_{20}$ (N. C. Deliolanis et al. 2006)	$Sn_2P_2S_6$ (R. Vlokh et al. 2008)
	γ_{41}=1.52×10^{-12} m/V Δρ/*E*.0.2 deg/kV λ=489 nm	γ_{41}=2.03×10^{-12} m/V Δρ/*E*.0.3 deg/kV λ=498 nm	γ_{41}=9.5×10^{-13} m/V Δρ/*E*.0.1 deg/kV λ=632.8 nm	γ_{41}=(0.5–3.75)×10^{-13} m/V (visible spectral range) Δρ/*E*.0.01–0.04 deg/kV	the estimated values γ_{eff}<0.4×10^{-10} m/V Δρ/*E*<3 deg/kV λ=632.8 nm
Optically uniaxial crystals	$Pb_5SeO_4(VO_4)_2$	$NaBi(MoO_4)_2$	$Pb_5Ge_3O_{11}$:Cr (D. Adamenko et al. 2008)	$Pb_5Ge_{2.4}Si_{0.6}O_{11}$ (Shopa Y. et al. 2007)	$PbMoO_4$
	Δρ/*E*.0.1 deg/kV λ=632.8 nm	Δρ/*E*.0.1 deg/kV λ=632.8 nm	γ_{33}=(3.1 ±0.3)×10^{-11} m/V Δρ/*E*=3.94 deg/kV at T_c	γ_{33}.9×10^{-11} m/V Δρ/*E*.12 deg/kV at T_c	λ=517 nm γ_{33}=(1.2 ±0.1)×10^{-12} m/V λ=400 nm Δρ/*E*=0.5 deg/kV

Fig. 3.4 Examples of EG measured materials [30]. γ and β correspond to the linear and quadratic electrogyration tensor defined in equation (2.22), respectively. $\Delta\rho$ represents induced optical rotatory power and $\Delta\rho/E$ corresponds to the coefficient α in equation (3.4).

3.1.4 Target material 1: $NiTiO_3$

The temperature dependence of the crystal structure of $NiTiO_3$ is reported in refs. [9,31]. At temperatures

above $T_c \approx 1560$ K, the crystal structure is described by the corundum structure (space group $R\bar{3}c$) which is envisage as a hexagonal close packing of the oxygen ions with Ni^{2+} and Ti^{4+} cations randomly occupying 2/3 of the octahedral interstices (Fig. 3.5**a**). With lowering temperature, cation ordering takes place at T_c and results in a structural phase transition into the ilmenite structure (space group $R\bar{3}$). The low-temperature structure is characterized by an alternating sequence of Ni^{2+} and Ti^{4+} along the stacking direction of the closed-packed layers (Fig. 3.5**b**). Depending on the stacking sequence (Ni-Ti-Ni-Ti- or Ti-Ni-Ti-Ni-), two possible domain states develop at temperatures below T_c (Fig. 3.5**b**, **c**). This transition from the point group $\bar{3}m$ into $\bar{3}$ is one of the pure ferroaxial transitions described in 3.1.1. Indeed, as seen in Figs. 3.5**d**, **e** which depict two specific Ti ions and six oxygen ions bonded to the Ti ions, the direction of rotational distortions of oxygen ions (red arrows), i.e., the sign of **A** (||**c**), is opposite in these two domain states (A+ and A− domains). Therefore, $NiTiO_3$ can be regarded as an order-disorder type ferroaxial crystal.

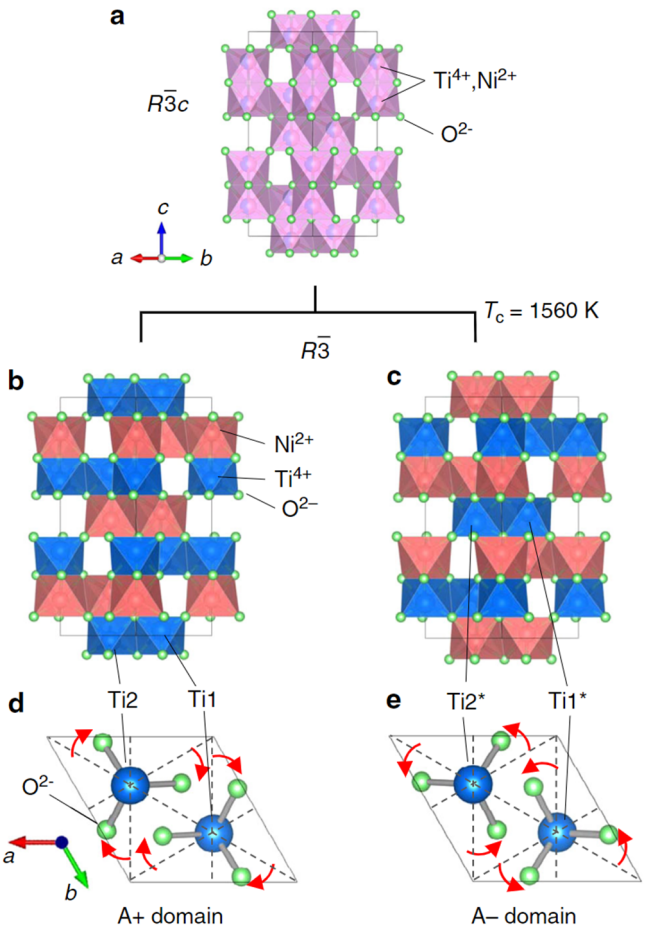

Fig. 3.5 Order-disorder phase transition and formation of ferroaxial domains in $NiTiO_3$ [24]. The crystal structures of $NiTiO_3$ above (**a**) and below (**b,c**) the ferroaxial transition temperature ($T_c \approx$ 1,560 K). Below T_c, thus, a pair of ferroaxial domain states with the opposite rotation direction, i.e., the opposite sign of axial vector **A**, are present (A+ and A– domains). **d,e,** The *c*-axis views of the ferroaxial domains. Only two Ti ions [$Ti1^{(*)}$ and $Ti2^{(*)}$] and six oxygen ions are depicted. These ions form two TiO_3 triangular pyramids which are related by the space inversion with the inversion center at the midpoint between Ti1 and Ti2 ions. Red arrows denote the direction of rotational displacements of oxygen ions from the (110)-type planes (dotted lines) that correspond to the average oxygen positions between A+ and A–.

3.1.5 Target material 2: $RbFe(MoO_4)_2$

The crystal structure of $RbFe(MoO_4)_2$ belongs to space group $P\bar{3}m1$ at room temperature [10]. The structure is built of FeO_6 octahedra sharing vertices with MoO_4 tetrahedra, and they form oxygen layers

perpendicular to the c axis. Rb atoms are in the interlayer (Figs. 3.6**a,b**). $RbFe(MoO_4)_2$ undergoes a structural transition at $T_c \approx 195$ K [10,20], which is characterized by rotations of MoO_4 tetrahedra (FeO_6 octahedra) and results in the structure which belongs to space group $P\bar{3}$ (Figs 3.6**c**,**d**). This transition from the point group $\bar{3}m$ into $\bar{3}$ is one of the pure ferroaxial transitions, which is the same one with the ferroaxial transition in $NiTiO_3$. While the transition in $NiTiO_3$ is an order-disorder type, that in $RbFe(MoO_4)_2$ is a displacive type. Depending on the directions of the rotations, two possible domain states develop below T_c, namely A+ and A− domains. Here, the domain with clockwise rotations of MoO_4 tetrahedra is defined as A+ domain while that with counterclockwise rotations is defined as A− domain.

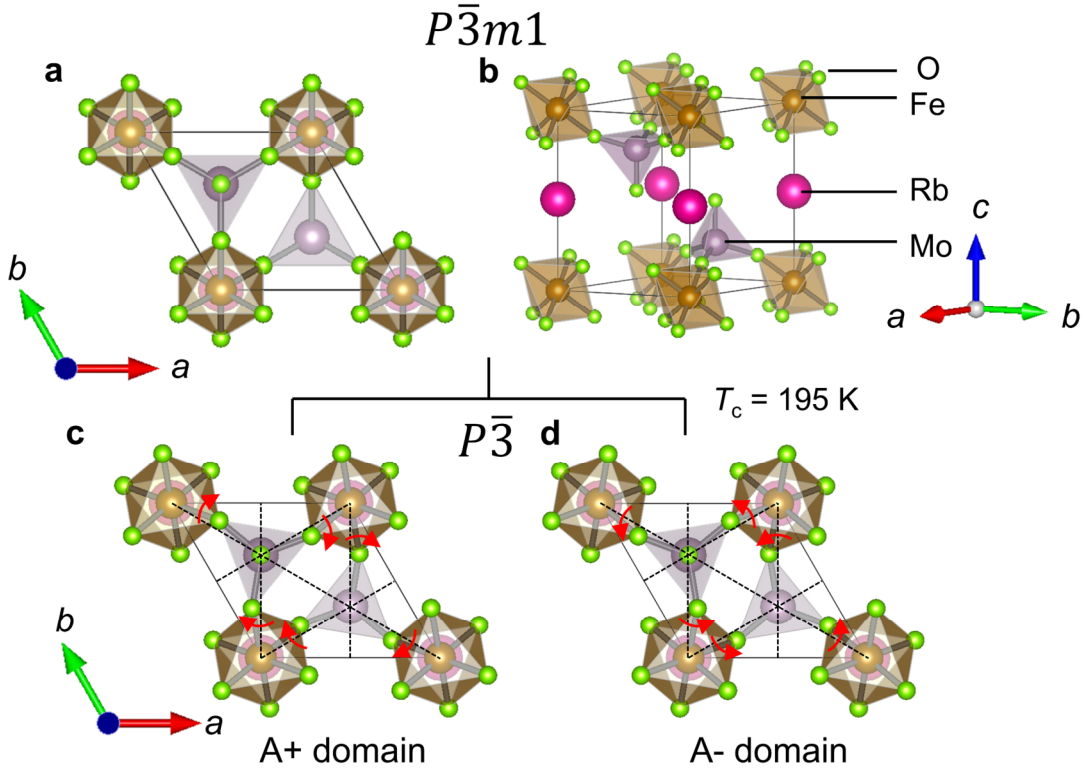

Fig. 3.6 Displacive type phase transition and formation of ferroaxial domains in RFMO. The crystal structures of RFMO above (**a,b**) and below (**c,d**) the ferroaxial transition temperature (T_c =195 K). The crystal structure above T_c belongs to a non-ferroaxial space group ($P\bar{3}m1$). At T_c, oxygen ions slightly rotate about the c axis, which results in a structural transition into a ferroaxial phase with a space group $P\bar{3}$. Below T_c, thus, a pair of ferroaxial domain states with the opposite rotation direction, i.e., the opposite sign of a ferroaxial moment **A**, are present (A+ and A− domains). Red arrows denote the direction of rotational displacements of oxygen ions from the (110)-type planes (dotted lines) that correspond to the mirror planes which are present in the phase above T_c.

Very recently, the ferroaxial order of RFMO has been observed using high-sensitivity rotational anisotropy second-harmonic generation (RA-SHG) [20]. Usually, SHG is used to detect phases with broken spatial inversion symmetry where the electric dipole contribution is dominant. However, in ref. [20], the authors consider SHG from electric quadrupole (EQ) contributions and apply

it to detect the ferroaxial order in the centrosymmetric system (Fig. 3.7**b**). Furthermore, EQ SHG in $RbFe(MoO_4)_2$ depends on azimuth angles of a specimen, and at the ferroaxial phase such a rotational anisotropy reflects the sign of the ferroaxial moment, i.e., clockwise or counterclockwise rotations of MoO_4 tetrahedra (FeO_6 octahedra) (Fig. 3.7**a**). By using this characteristic, the authors clarified the temperature dependences of areal ratio of ferroaxial domains (Fig. 3.7**c**). According to that, at the observation area with a diameter of 50 μm, the two opposite ferroaxial domains appear with uneven populations at T_c and asymptotic to even populations with lowering temperature. These are the first experimental results of direct observation of ferroaxial order. However, spatial distributions of ferroaxial domains have not been observed.

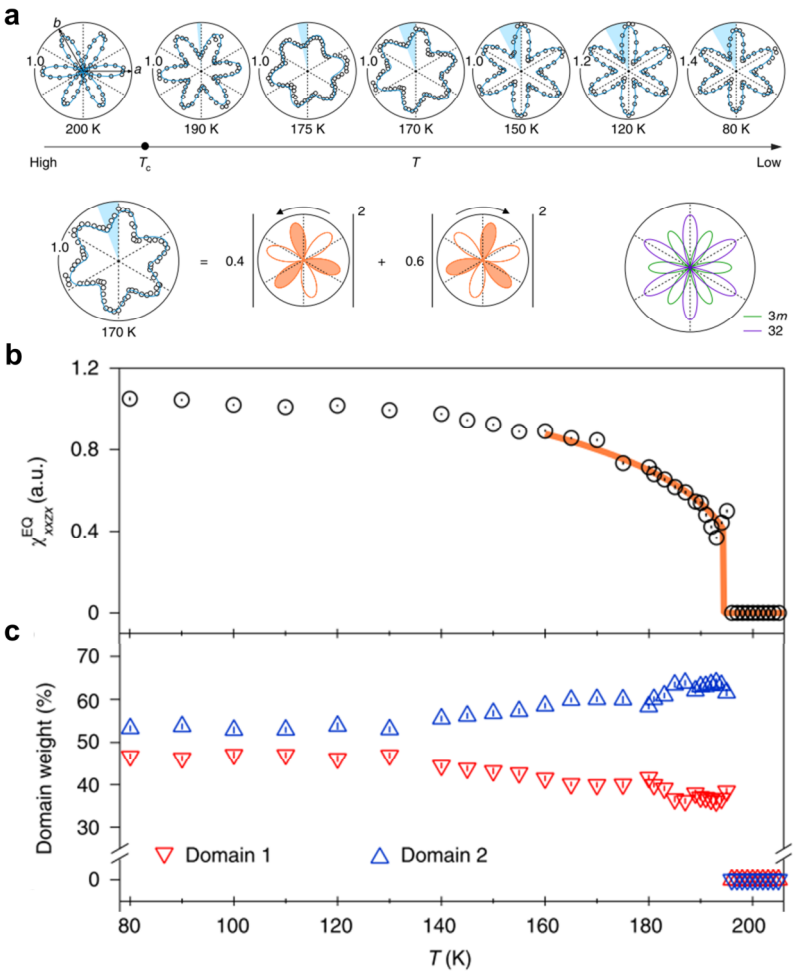

Fig. 3.7 Ferroaxial order in $RbFe(MoO_4)_2$ observed by using RA-SHG [20]. Reproduced with permission from Springer Nature. **a**, Patterns reflecting the rotational anisotropy of EQ-SHG. The patterns below T_c are interpreted as average contributions of the opposite domains. **b**, Temperature dependence of EQ-SHG susceptibility χ^{EQ}_{xxzx}, which is proportional to the ferroaxial order. **c**, Temperature dependence of areal ratios of ferroaxial domains. Domains 1 and 2 correspond to A+ and A− domains defined in Fig. 3.5, respectively.

$RbFe(MoO_4)_2$ shows an interesting coupling between the ferroaxial and magnetic orders. Below $T_N \approx 4$ K, the Fe spins order in the *ab* plane in a 120° structure with incommensurate helicity

along the *c* axis, which is characterized by the wave vector $\mathbf{q} = (1/3, 1/3, 0.458)$ [32]. Here, the triangular chirality is defined as $\sigma_t = 1$ if the spins rotate counterclockwise as one circumscribes counterclockwise upward MoO_4 tetrahedra and otherwise $\sigma_t = -1$, while the magnetic helicity is defined as $\sigma_h = +1$ and -1 for a right- and left- handed magnetic screw, respectively [19] (see Fig. 3.8). Notably, σ_t, σ_h, and the ferroaxial moment $\mathbf{A} = (0, 0, A)$ need to satisfy the relation $\sigma_t \sigma_h A/|A| = -1$ to minimize the exchange energy. Thus, the trilinear coupling between the spins 120° structure in the *ab* plane, the magnetic helicity along the *c* axis, and the ferroaxial order emerges. Furthermore, not only a spontaneous polarization is induced by the 120° structure, but also the coupling of $\sigma_h A/|A|$ is related to the polarization, as is reported in $CaMn_7O_{12}$ [17]. Therefore, the observation of ferroaxial domains in $RbFe(MoO_4)_2$ will lead to insights into the magnetic domain structures, and the manipulation of the ferroaxial domains consequently will allow the control the magnetic orders and even the polarization. Such couplings between a ferroaxial order and other ferroic orders are one of the most interesting subjects in studies on the ferroaxial order.

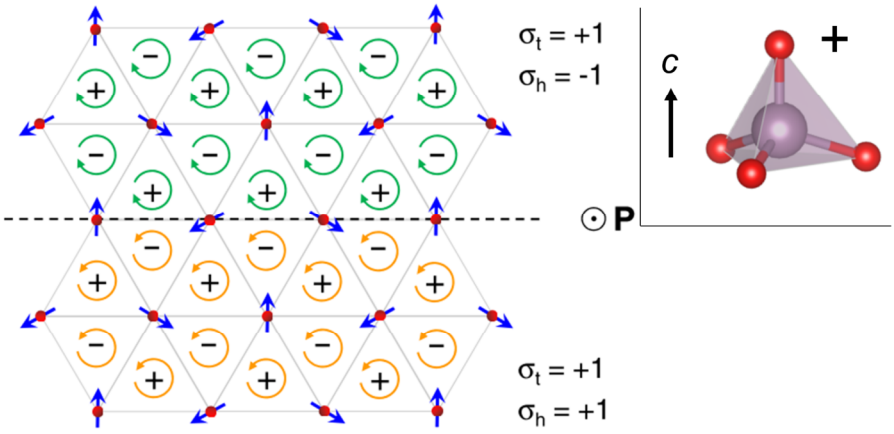

Fig. 3.8 Coupling between the ferroaxial and magnetic orders in $RbFe(MoO_4)_2$ [19]. Reprinted with permission from ref. [19]. Copyright 2012 by the American Physical Society. The blue arrows denote the Fe spins. The green and yellow circled arrows denote the rotations of MoO_4 tetrahedra, which correspond to A+ and A− domains, respectively. The $\pm$ signs in the middle of the triangles correspond to upward and downward MoO_4 tetrahedra, respectively. In the inset, the upward MoO_4 tetrahedra is depicted. Here, the triangular chirality is fixed to be $\sigma_t = 1$, and consequently the spontaneous polarization is to be positive (along the *c* axis). In this case, the magnetic helicity σ_h and the ferroaxial moment *A* need to satisfy the relation $\sigma_h A/|A| = -1$. In this figure, the situation when $\sigma_h = -1, A/|A| = 1$ is depicted above the dashed line, and $\sigma_h = 1, A/|A| = -1$ is depicted below the dashed line.

3.1.6 Motivation

The main purpose of this chapter is to demonstrate ferroaxial domain observation by using the linear EG effect and to reveal detailed characteristics of ferroaxial domains, such as domain size, shape and the effects of ferroaxial transitions on the domain formation. In $NiTiO_3$, we perform ferroaxial domain observations in several types of single crystalline samples grown by two different methods (floating

zone and flux methods) and annealed under different conditions. We also show that scanning x-ray diffraction (XRD) can be another powerful method for visualizing ferroaxial domains. In $RbFe(MoO_4)_2$, we examine the evolution of domain formation upon a ferroaxial transition by measuring the temperature dependence of the spatial distributions of EG over a wide temperature range. Furthermore, we investigate the temperature dependence of the rotation of MoO_4 tetrahedra by the powder neutron diffraction method, and compare it with the temperature profile of the EG effect.

3.2 Experimental Methods

3.2.1 Sample preparation and characterization

$NiTiO_3$

Single crystal growth

Single crystals of $NiTiO_3$ were grown by the floating zone (FZ) method [33] and the flux method [34].

-FZ

First, polycrystalline feed rods were prepared by a solid-state reaction. Powders of NiO and TiO_2 with 99.9% purity were weighted to the prescribed ratios, mixed, well grounded, and heated at 1000 °C for 10 h in air. The resulting polycrystalline samples were ground into powders again and then pressed into rods with a dimension of about 6 mm in diameter and 100 mm in length. The rods were sintered again at 1100 °C for 15 h in air. The crystal growth was carried out on the sintered rods with the use of a halogen-lamp image furnace (Canon Machinery Inc.) at a feed rate of 1.0 mm/h in flowing air. Figure 3.9 shows a schematic illustration of the FZ furnace. As a result, yellowish-brown crystals were obtained as shown in Fig. 3.10.

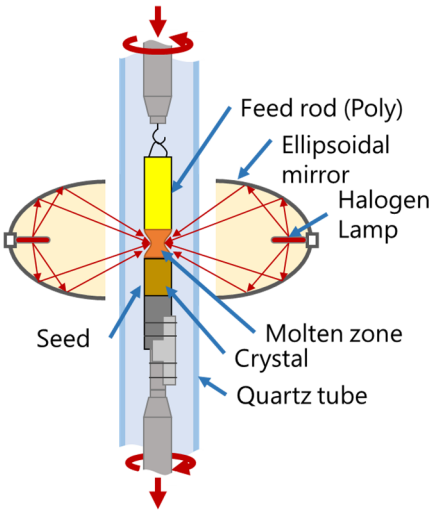

Fig. 3.9 A schematic illustration of the FZ furnace. Focused halogen light melts the polycrystalline rods and by sweeping them downward, single crystals are grown.

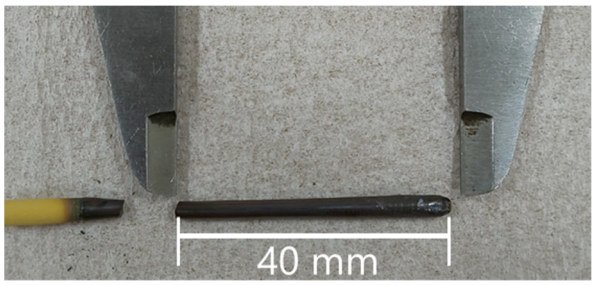

Fig. 3.10 $NiTiO_3$ single crystal obtained by the FZ method. A typical dimension was 6 mm in diameter and 40 mm in length.

-Flux

Single crystals of $NiTiO_3$ were grown by using PbO and V_2O_5 as flux. Powders of NiO, TiO_2, PbO, and V_2O_5 were weighted to the mass ratio 5.6:6:103:45, mixed, well-grounded and put into a platinum crucible with a tightly fitting lid. The crucible was heated as the procedure depicted in Figure 3.11. As a result, dark brown plate like single crystals with typical dimensions of $3\ \text{mm} \times 3\ \text{mm} \times 0.1\ \text{mm}$ were obtained (see Fig. 3.12).

In addition to the as-grown samples, we prepared two different types of annealed samples: rapidly cooled and slowly cooled samples which were obtained by annealing the as-grown crystals in air from a temperature above T_c to a temperature below T_c at a cooling rate of 275 and 1 K/h, respectively.

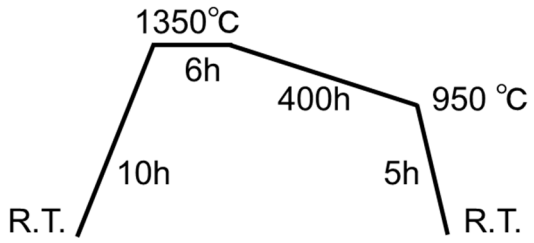

Fig. 3.11 Sequence of the flux growth. Here, R.T. means room temperature.

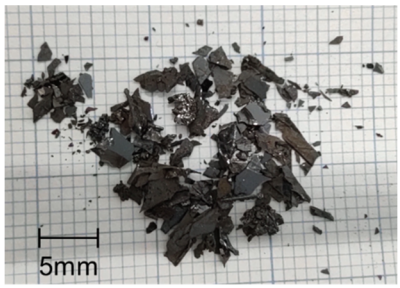

Fig. 3.12 $NiTiO_3$ single crystals obtained by the flux method.

Characterization

Powder x-ray diffraction (XRD) and scanning electron microscopy-energy dispersive x-ray spectroscopy (SEM-EDX) revealed that the obtained crystals mainly consist of the ilmenite-type $NiTiO_3$ phase but include a small amount of NiO and TiO_2 impurities. The SEM-EDX measurements were performed by Dr. Hamane at The Institute for Solid State Physics, the University of Tokyo. Figure 3.13 shows the SEM images of the samples and Table 3.3 summarizes the results of EDX analysis. From these measurements, it was revealed that island shape impurities in the FZ-grown sample are mainly composed of NiO, and thin lines in the annealed flux-grown samples are composed of TiO_2.

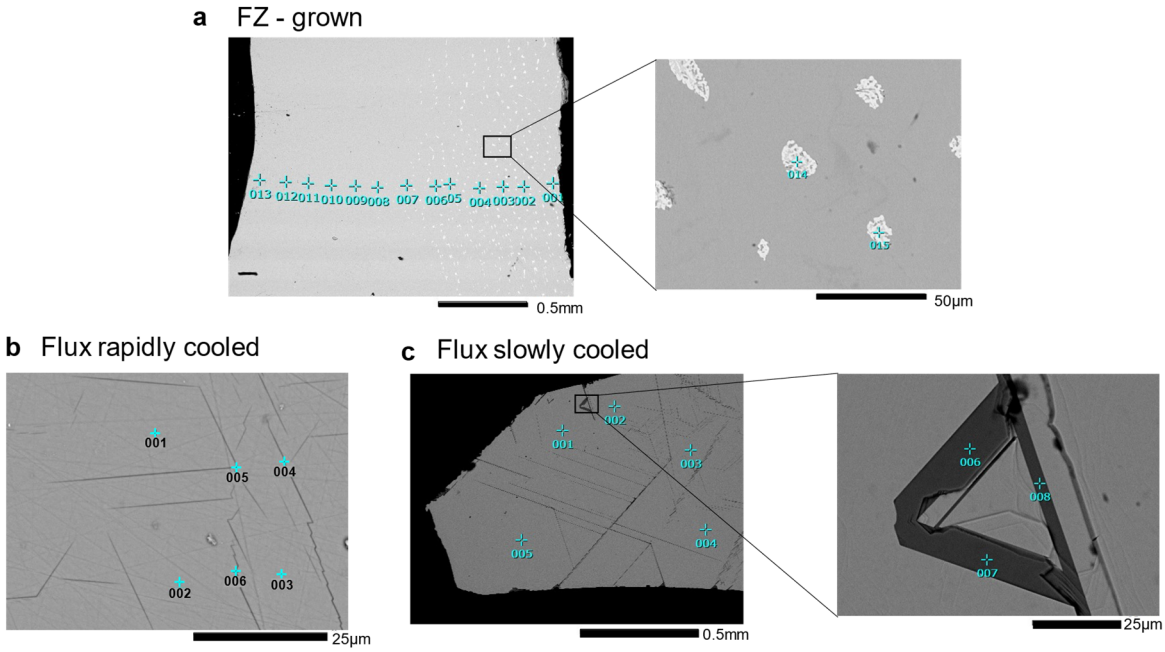

Fig. 3.13 SEM images of $NiTiO_3$ samples. **a,** FZ-grown. **b**, flux rapidly cooled. **c**, flux slowly cooled. The crosses in each image show the EDX measurement points and the attached numbers correspond to those in Table 3.3.

Table 3.3 Summary of EDX analysis. Molar ratios of each element at the positions corresponding to Figure 3.12 are shown. Impurities of Si in the FZ-grown sample possibly come from an agate mortar which was used for grinding powders. The analyzed points on impurities are highlighted in gray.

	a. FZ grown			**b**. Flux rapidly cooled		**c**. Flux slowly cooled	
	Ni	Ti	Si	Ni	Ti	Ni	Ti
1	0.98	1.01	–	0.95	1.02	0.98	1.01
2	0.97	1.01	–	0.96	1.02	0.99	1.00
3	0.95	1.03	–	1.00	1.00	0.98	1.01
4	0.98	1.01	–	0.57	1.21	0.98	1.01
5	0.97	1.02	–	0.80	1.10	0.96	1.02
6	0.98	1.01	–	0.71	1.15	0.02	0.99
7	0.99	1.01	–	–	–	0.01	0.99
8	0.96	1.02	–	–	–	0.02	0.99
9	0.98	1.01	–	–	–	–	–
10	0.98	1.01	–	–	–	–	–
11	0.97	1.02	–	–	–	–	–
12	0.97	1.02	–	–	–	–	–
13	0.94	1.03	–	–	–	–	–
14	0.81	0.09	0.01	–	–	–	–
15	0.64	0.17	0.01	–	–	–	–

Molding

The (001) plane of one of the FZ-grown sample was determined from the Laue XRD pattern. The oriented crystal was cut into a plate shape whose widest faces are parallel to (001). The widest faces of the flux as-grown crystals were parallel to (001), which was confirmed from the XRD measurement.

Experimental Methods

The oriented single crystals were polished down to around 50 μm with pieces of abrasive paper and the surfaces were mirror polished by the polishing machine (IMT Co., Ltd.) with diamond slurry. To form transparent electrodes that allow the application of a voltage parallel to the *c* axis, indium/tin-oxide (ITO) was spattered onto the widest faces.

$RbFe(MoO_4)_2$

Polycrystalline sample growth

Polycrystalline samples for measurements of neutron diffraction were synthesized by the solid-state reaction [35]. First, a mixture of Fe_2O_3 and MoO_3 in the molar ratio 1:3 and a mixture of Rb_2CO_3 and MoO_3 in the molar ratio 1:1 were heated at 923 K for 24 hours in air and obtained powders of $Fe_2(MoO_4)_3$ and Rb_2MoO_4, respectively. Subsequently, these powders were mixed in the molar ratio 1:1 and heated at 923 K for 24 hours in air, and polycrystalline $RbFe(MoO_4)_2$ was obtained.

Single crystal growth

Single crystals of $RbFe(MoO_4)_2$ were grown by the flux method [10]. Powders of Rb_2CO_3, Fe_2O_3, and MoO_3 were weighted to the molar ratio 2:1:6, mixed, well-grounded, and put into a platinum crucible with a lid. The crucible was heated as the procedure depicted in Fig. 3.14. As a result, plate-shaped transparent yellowish single crystals with typical dimensions of 2 mm × 2 mm × 0.2 mm were obtained (see Fig. 3.15).

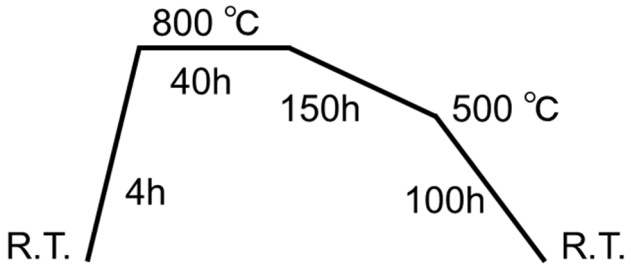

Fig. 3.14 Sequence of the flux growth. Here, R.T. means room temperature.

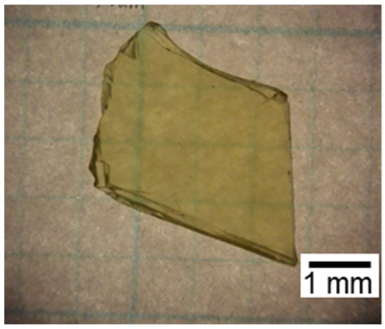

Fig. 3.15 $RbFe(MoO_4)_2$ single crystal obtained by the flux method.

Characterization and Molding

The obtained crystals were confirmed to be the single phase with the $RbFe(MoO_4)_2$ structure by XRD measurements. The widest faces of the as-grown single crystals were the (001) plane, which were polished down to around 50 μm in the same manner as in $NiTiO_3$. ITO was spattered onto the widest face.

3.2.2 Electrogyration measurement

To observe ferroaxial domains in $NiTiO_3$ and $RbFe(MoO_4)_2$, induced optical rotation when the directions of light propagation and an applied electric field were both parallel to the *c* axis, i.e., EG corresponding to the γ_{333} component, needs to be probed. However, as mentioned in 3.1.3, the magnitude of EG is usually small ($\alpha \leq 10^{-4}$ deg V^{-1}). To spatially resolve such small EG signals, we adopted a field-modulation-image-sensing technique, which was developed for ferroelectric domain imaging [36].

As shown in Fig. 3.16, the field-modulation-image-sensing is based on a polarized microscope. A crystal with ITO electrodes is placed between a polarizer and an analyzer and the angle between the orientations of the polarizer and the analyzer (Θ) is set at $\Theta = \pm 45°$. In this setting, the intensity of the transmitted light is described as

$$I = \frac{I_0}{2}[\cos\{2(\pm 45° - \phi)\} + 1]$$

$$= \frac{I_0}{2}\{\pm\sin(2\phi) + 1\} \tag{3.7}$$

where I_0 is the intensity of the transmitted light at the parallel-Nicols setting, and ϕ [deg] is the rotation angle of the polarization plane induced by an applied electric field E [V m^{-1}]. Because the EG effect is usually small, it can be assumed that $\sin(2\phi) \approx 2\phi'$, where $\phi'[\text{rad}] = \frac{\pi}{180}\phi\,[\text{deg}]$, and equation 3.7 is rewritten as

$$I \approx I_0\left(\pm\phi' + \frac{1}{2}\right)$$

$$= I_0\left(\pm\alpha' V + \frac{1}{2}\right), \tag{3.8}$$

where α' [rad V^{-1}] = $\frac{\pi}{180}\alpha$ [deg V^{-1}] is rotation angle of the polarization plane per applied voltage V [V] and represents the magnitude of the linear EG effect. The difference between *I* obtained in positive and negative applied voltages divided by their average is expressed as

$$\frac{\Delta T}{T} = \frac{I_0\left(\pm\alpha'(+V) + \frac{1}{2}\right) - I_0\left(\pm\alpha'(-V) + \frac{1}{2}\right)}{\left\{I_0\left(\pm\alpha'(+V) + \frac{1}{2}\right) + I_0\left(\pm\alpha'(-V) + \frac{1}{2}\right)\right\}/2}$$

$$= \pm 4\alpha' V \tag{3.9}$$

Thus, EG can be readily obtained by measuring the intensity of transmitted light in the polarization configurations of $\Theta = \pm 45°$ at applied voltages of $\pm V$. Because the sign of α depends on that of **A**, a spatial map of $\Delta T/T$ is nothing more or less than that of ferroaxial domains. We also note that $\Delta T/T$ will be opposite in sign in the polarization configurations between $\Theta = +45°$ and $-45°$. Therefore, domain contrasts will get reversed by changing the polarization configuration from $\Theta = +45°$ to $-45°$. Such a contrast reversal confirms that the obtained contrasts are induced by EG, but not by other effects such as electric-field-induced optical birefringence and absorption.

Since the magnitude of EG is small, that of $\Delta T/T$ is also small (~ 10^{-4}). To obtain a spatial map of such small signals with suppressing noises, a large number of $\Delta T/T$ images were acquired and

averaged as the following sequences.

A square-wave bias voltage (up to ±200 V) was applied between the electrodes at a frequency of 20 (or 30) Hz. Pulsed light at a frequency of 40 (or 60) Hz from the LED was irradiated onto the specimen, where the pulsed irradiation was synchronized with the applied square-wave voltage. Microscopy images of transmitted light were captured by the CMOS-area-image sensor (pco. edge 5.5, Excelitas Technologies) while positive and negative voltages applied and the difference between the positive- and negative-voltage images divided by the average of them ($\Delta T/T$) was calculated for each pixel detection. To suppress noise, 15,000 ~ 20,000 images are captured for the positive- and negative-voltage states and sequentially obtained spatial maps of $\Delta T/T$ are averaged. The inset of Fig, 3.16**b** shows a schematic diagram of the above-mentioned steps. Also, a 3 × 3 median filter was applied to the raw images. By this field-modulation imaging technique, a $\Delta T/T$ signal of the order of 10^{-5} can be detected.

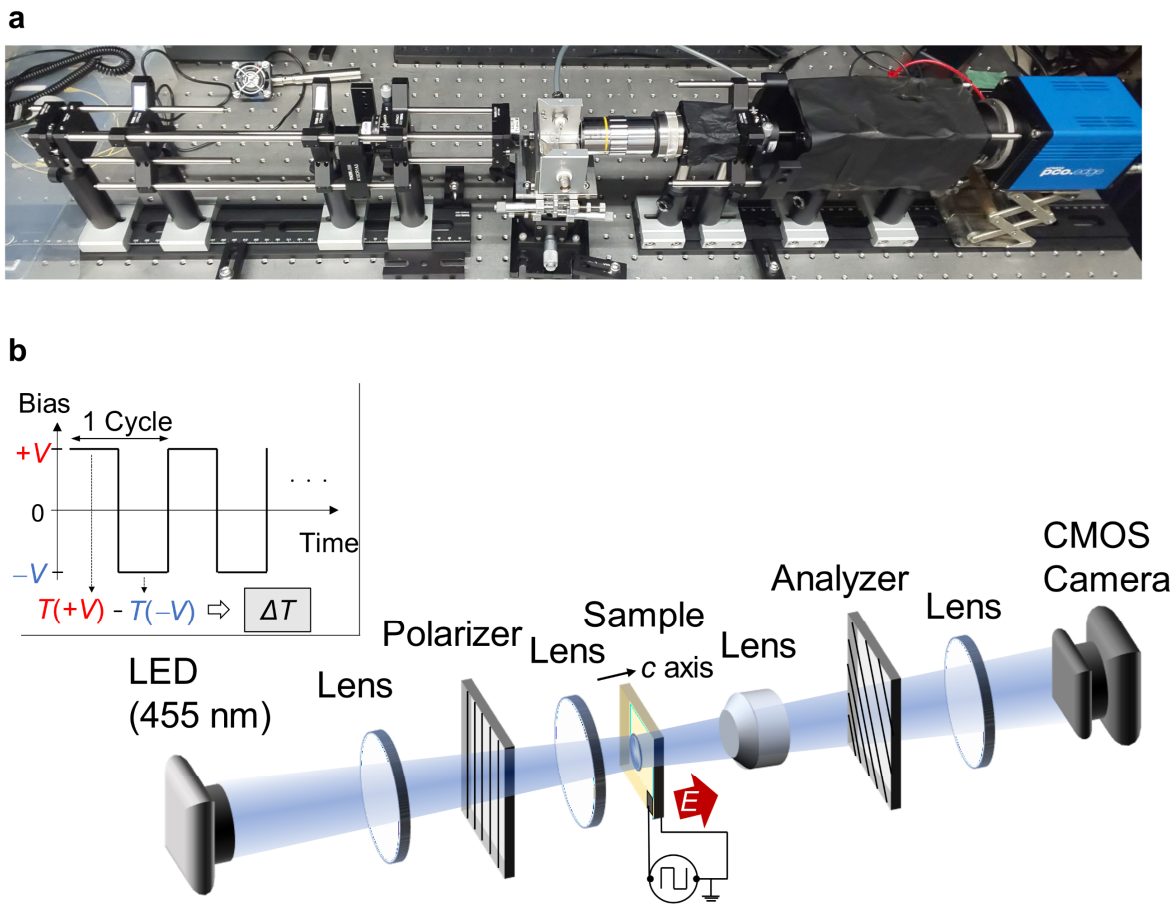

Fig. 3.16 Photograph (**a**) and schematic image (**b**) of a difference image-sensing technique. The inset shows temporal evolution of applied voltage *V* during the measurement. Images under positive and negative voltages were taken alternatively and the differences of it were calculated. Adapted from ref. [37] with permission. Copyright 2022 by the American Physical Society.

3.2.3 Scanning x-ray diffraction measurement

A+ and A− domains in $NiTiO_3$ are crystallographically inequivalent, allowing for their distinction through diffraction methods. In fact, twin domains, which correspond to ferroaxial domains, were observed in ilmenite-hematite solid solutions, $FeTiO_3$-Fe_2O_3, which undergo the same $R\bar{3}c \rightarrow R\bar{3}$ transition as $NiTiO_3$, using electron diffraction method [38]. Furthermore, ferroaxial domains in $NiTiO_3$ were also observed by scanning transmission electron microscopy combined with convergent-beam electron diffraction, which was performed by Dr. Morikawa and Prof. Tsuda at Tohoku University using our FZ-grown sample [24].

Scanning XRD is another way to obtain a spatial distribution of ferroaxial domains. We calculated the crystal structure factor F of $NiTiO_3$ using a software VESTA [39] based on the room-temperature structure given in ref. [9]. As a result, we found that the reflection intensity ($\propto |F|^2$) at $hkil = 11\bar{2}\underline{3n}$ strongly depends on the ferroaxial domain. For example, the crystal structure factor $|F_{11\bar{2}\underline{15}}|$ is 40.1 for A+ domain while 3.87 for A− domain. Therefore, by mapping reflection $11\bar{2}\underline{15}$, one can obtain spatial distributions of ferroaxial domains in $NiTiO_3$. Furthermore, the domain contrast will get reversed by mapping reflection $\bar{1}\bar{1}2\underline{15}$ which is related to reflection $11\bar{2}\underline{15}$ by the mirror or the two-fold rotation operation, as $|F_{\bar{1}\bar{1}2\underline{15}}| = 3.87$ for A+ domain and $|F_{11\bar{2}\underline{15}}| = 40.1$ for A− domain.

Scanning XRD measurements in a flux-grown slowly cooled $NiTiO_3$ sample were performed at room temperature by using a multi-purpose x-ray diffractometer (Bruker AXS GmbH, D8 DISCOVER), operated by Mr. Morioka at Bruker Japan. Cu Kα radiation was used for an incident x-ray beam which was collimated with 50 μm diameter pinhole. The sample was mounted on the diffractometer so that the *c* plane (parallel to the sample surface) was parallel to the XY stage of the diffractometer. For the ferroaxial domain mapping, sample-position profiles of reflection intensities at $11\bar{2}\underline{15}$ and $\bar{1}\bar{1}2\underline{15}$ were detected while translating the sample position with 25 μm step size. We chose the diffraction geometry close to the orthogonal incidence (the angle between the incident x-ray beam and the sample surface was about 83 deg). This means that the spatial resolution of our scanning XRD measurements is nearly the beam size.

3.2.4 Neutron diffraction measurement

In $RbFe(MoO_4)_2$, we investigated the temperature dependence of the rotation of MoO_4 tetrahedra by the powder neutron diffraction method. Neutron diffraction measurements were performed on a polycrystalline sample of $RbFe(MoO_4)_2$ using a high resolution powder diffractometer (BL08, SuperHRPD) at MLF of J-PARC [40]. The high resolution up to $\Delta d/d$ = 0.035 % allows to distinguish a lot of Bragg reflections, which is essential for accurate estimates of magnitudes of the rotational distortion. The measurements were done across T_c from 210 K to 100 K during cooling the sample, and the Rietveld refinements of the obtained data were carried out using Z-Rietveld software [41,42].

3.3 Results and Discussion: $NiTiO_3$

3.3.1 Observation of ferroaxial domains in the FZ-grown sample

Figures 3.17**b**,**c** show the obtained spatial distributions of $\Delta T/T$ under the applied voltage of ±100 V in the polarization configurations at $\Theta = \pm 45°$, which were taken at the same area as the optical image of Fig. 3.17**a**. The images were taken at room temperature, that is, in the $R\bar{3}$ ferroaxial phase (All the following measurements in $NiTiO_3$ were performed at room temperature). The wavelength of incident light was 660 nm. As mentioned in 3.2.1, the sample includes NiO impurities (dark island-shaped inclusions in Fig. 3.17**a**). These NiO impurities appear purple (mixture of red and blue) in Figs. 3.17**b**,**c** because the intensity of transmitted light is too small to get meaningful signals. Except for the impurity regions, the images of Figs 3.17**b**,**c** show clear contrasts of red and blue which correspond to positive and negative signals of $\Delta T/T$. In addition, these two images show a complete reversal of the contrasts by switching Θ from $+45°$ to $-45°$. This means that the observed $\Delta T/T$ is due to electric-field-induced change in optical rotation, i.e., electrogyration, but not to that in optical absorption. Therefore, red and blue regions in Figures 3.17**b**,**c** correspond to either A+ or A− ferroaxial domains, and the color contrasts of these figures reflect the ferroaxial domain pattern in $NiTiO_3$.

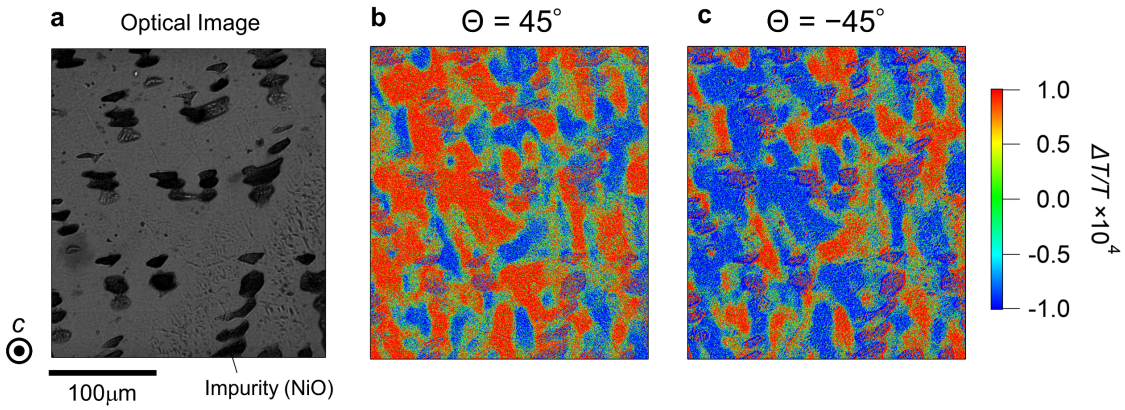

Fig. 3.17 Spatial distribution of ferroaxial domains in FZ-grown $NiTiO_3$ [24]. **a**, Transmission optical microscopy image with the incidence of light along the *c* axis. Dark areas in the image correspond to NiO impurity. **b,c**, The two-dimensional maps of $\Delta T/T$, which corresponds to EG, at the same area as panel (**a**). A 3×3 median filter was applied to the raw images. The polarization direction of the analyzer was set at (**b**) $\Theta = +45°$ and (**c**) $-45°$. Red and blue regions correspond to either A+ or A− ferroaxial domains. Purple-colored regions represent areas of NiO impurity.

To check whether EG observed in $NiTiO_3$ is ascribed to the linear effect and/or higher-order ones, we carried out measurements of the EG spatial distributions as a function of applied voltage *V*. Figures 3.18**b-e** show spatial distributions of $\Delta T/T$ obtained in selected applied voltages at $\Theta = +45°$ (**b**-**d**) and $-45°$ (**e**). The data were taken at a slightly different area from that of Figs. 3.17**a-c**. The color contrasts monotonically increase with increasing the magnitude of *V* (Figs. 3.18**b-d**), and the contrasts get reversed by switching Θ from $+45°$ to $-45°$ (compare Figs. 3.18**d** and 3.18**e**). We calculated the average of $\Delta T/T$ in the pixels at selected single ferroaxial domain areas (both red and

blue) denoted by boxes in Figures 3.18**b-d** and took its V dependence. As seen in Fig. 3.18**f**, the magnitude of $\Delta T/T$, i.e., the magnitude of EG, is proportional to V. These results confirm that the electric-field-induced change in $\Delta T/T$ observed in $NiTiO_3$ is ascribed to the linear EG effect. We also calculated the magnitude of EG using the average of $\Delta T/T$ of the areas denoted by black and white boxes in Figure 3.18**d** (± 100 V, $\Theta = +45°$), and obtained $\alpha = (2.0 \pm 1.0) \times 10^{-5}$ deg V^{-1} for the red area and $(-1.9 \pm 0.9) \times 10^{-5}$ deg V^{-1} for the blue area. The errors were calculated from the standard deviation of $\Delta T/T$.

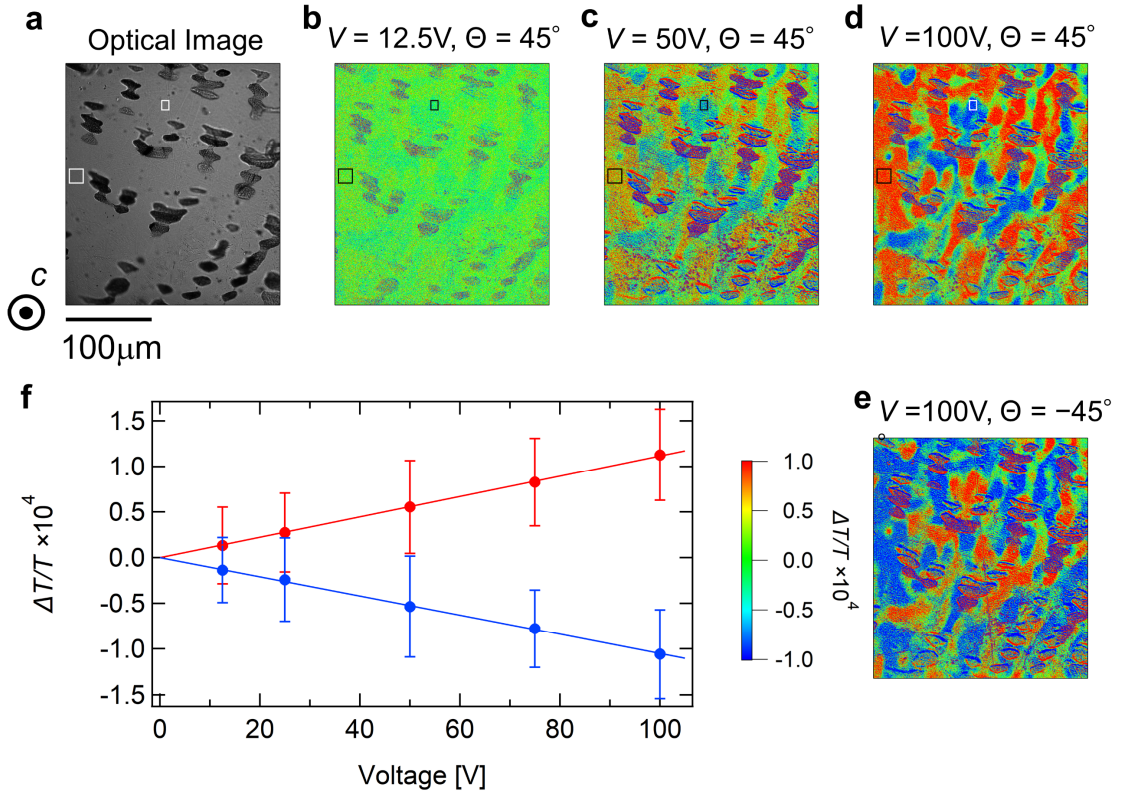

Fig. 3.18 Applied voltage dependence of the intensity map of EG in the FZ-grown $NiTiO_3$ [24]. **a**, Transmission optical microscopy image with the incidence of light along the c axis. Dark areas in the image correspond to NiO impurity. **b-e**, The two-dimensional maps of $\Delta T/T$ at the same area as panel **a**. A 3×3 median filter was applied to the raw images. The polarization configuration was set at (**b**-**d**) $\Theta = +45°$ and (**e**) $-45°$. The applied voltage V was (**b**) ± 12.5 V, (**c**) ± 50 V, and (**d**,**e**) ± 100 V. **f**, The V dependence of the average of $\Delta T/T$ taken at $\Theta = +45°$ in the selected single domain areas denoted by boxes in (**a**-**d**). The red and blue dots correspond to the data of the areas surrounded by large and small boxes, respectively, in each panel. The standard deviation is shown as an error bar. The lines denote least squares fitting lines.

3.3.2 Observation of ferroaxial domains in the flux-grown samples

Figure 3.19 summarizes the results of the ferroaxial domain observation in the three different types of flux-grown $NiTiO_3$: as-grown, rapidly cooled, and slowly cooled samples. The experimental setting was the same with that for the FZ-grown sample. All the $\Delta T/T$ maps show the contrast reversal between the polarization angles of $\Theta = +45°$ and $-45°$ (compare Figs. 3.19**e**-**h** with Figs. 3.19**i**-**l**), meaning that the contrast originates definitely from EG. As shown in Fig. 3.19**e**, the $\Delta T/T$ map of the as-grown sample

shows a monotonous contrast of red, suggesting that the directions of *E*-induced rotation of polarization plane, i.e., the signs of α, are the same in the whole observation area. Therefore, the as-grown sample consists of a single ferroaxial domain, at least in the observation area. On the other hand, the $\Delta T/T$ maps of the annealed samples exhibit both contrasts of red and blue, suggesting that they consist of multi-ferroaxial domains, namely, A+ and A− domains (see Figs. 3.19**f**–**h**). Note that in the optical images of the annealed samples (Figs. 3.19**b**–**d**), dark inclusions are seen, which were identified as TiO_2 impurities by the SEM-EDX measurements as mentioned in 3.2.1. Tiny TiO_2 impurities are dense almost all over the rapidly cooled sample (Figs. 3.19**b** and **c**), whereas large line-shaped impurities are sparsely located in the slowly cooled sample (Fig. 3.19**d**). Because these impurities are not observed in the as-grown sample (Fig. 3.19**a**) they were produced by the annealing process, most likely due to an interaction between the sample surfaces and oxygen at high temperature [43].

Next let us mention the domain sizes of the annealed samples. The rapidly cooled sample contains large domains in several areas (see middle-left side of Fig. 3.19**f**). However, it mainly consists of tiny domains, sized on the micrometer scale, or regions with weak $\Delta T/T$ signals (green regions of Fig. 3.19**g**). The green regions in the rapidly cooled sample likely correspond to the areas in which A+ and A− domains coexist in the length scale below the resolution limit of the measurement system. By contrast, the slowly cooled sample contains larger domains, several hundreds of micrometers in size (Fig. 2**h**). The magnitude of EG in the single domain areas was found to be almost the same in all the samples, which gives $\alpha \approx 2\times10^{-5}$ [deg V^{-1}]. This value is consistent with that of the sample grown by the floating zone method.

The as-grown sample consists of a single domain. This is probably because it crystallized at a temperature below T_c during the flux growth without undergoing the ferroaxial phase transition. By contrast, the annealed samples consist of multidomain, indicating that the multidomain state is formed upon the ferroaxial transition at T_c during the annealing procedure. Furthermore, the domain sizes of the slowly cooled sample are much larger than those of the rapidly cooled sample, which suggests that slower cooling speed, especially around T_c, increases domain size. This relationship between the cooling speed and domain size is reasonable, considering that slow cooling around T_c promotes the nucleus growth of each domain. The similar relationship between the cooling speed and domain size has been observed in the ilmenite/hematite solid solutions [38]. Also, in the annealed samples, not all but some of the TiO_2 impurities are clamped to the domain boundaries (compare Fig. 3.19**d** with 3.19**h**). The density of those impurities is much larger in the rapidly cooled than in the slowly cooled samples (compare Figs. 3.19**b** and 3.19**c** with 3.19**d**), potentially influencing domain formation and size. We note that the domain sizes in the FZ-grown sample are larger than those in the rapidly-cooled sample but smaller than those in the slowly-cooled sample. This may indicate that the FZ-grown crystal was cooled down across T_c during its growth at a rate intermediate between the rapidly- and slowly-cooled samples.

Finally, we mention the structures of ferroaxial domains in $NiTiO_3$. Except for the TiO_2 related boundaries in the flux-grown slowly-cooled sample, the domain structures are irregular in shape. These randomly shaped domains suggest that the ferroaxial domain boundaries in $NiTiO_3$ do not align with

specific planes, but can form in arbitrary directions. Therefore, strain energy induced by the boundaries is expected to be less anisotropic.

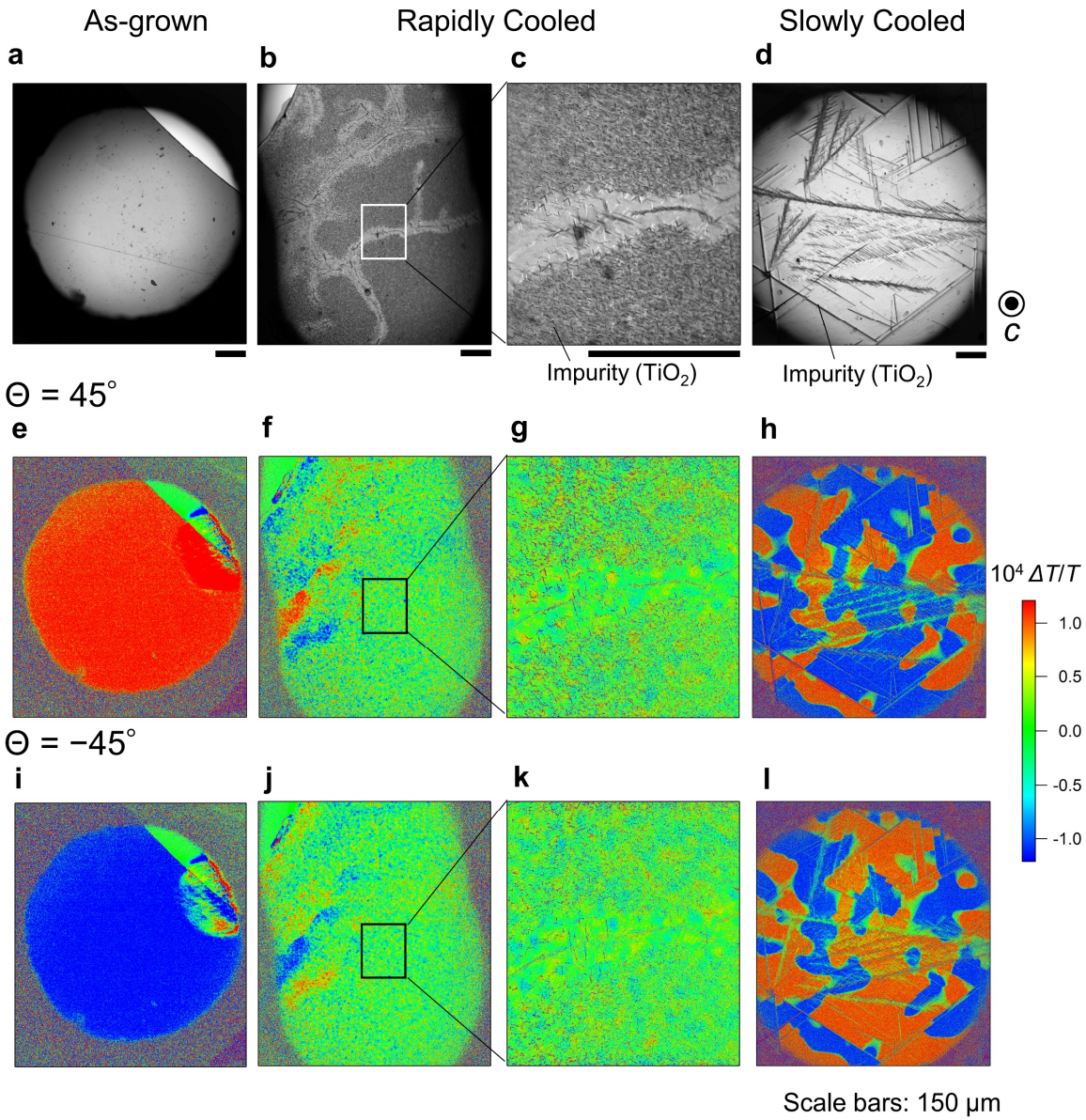

Fig. 3.19. Spatial distributions of ferroaxial domains in flux-grown $NiTiO_3$. Adapted from ref. [37] with permission. Copyright 2022 by the American Physical Society. **a**–**d** Transmission optical microscopy images of as-grown (**a**), rapidly cooled (**b**,**c**), and slowly cooled (**d**) samples with the incidence of light along the *c* axis (scale bars: 150μm). Bright areas [right upper part of panel (**a**) and left upper part of panel (**b**)] correspond to blank areas. The image of (**d**) shows an enlarged view of a part of panel (**d**). Dark areas in the annealed samples (**b**–**d**) correspond to impurities of TiO_2. **e**–**l** Two-dimensional maps of $\Delta T/T$, which corresponds to EG, in the polarization configuration of $\Theta = +45°$ (**e**-**h**) and $\Theta = -45°$(**i**-**l**). The $\Delta T/T$ maps in panels (**e**-**h**) [(**i**-**l**)] were taken at the same area as panels (**a**-**d**), respectively.

3.3.3 Comparison of electrogyration and x-ray diffraction images

Considering the structure-property relationship between the ferroaxial order and EG in terms of the symmetry (see 3.1.3), the $\Delta T/T$ maps shown in Figs. 3.17-3.19 will reflect ferroaxial domains. However, there has been no study which provides direct comparison between the sign of EG and that of rotational structural distortion characterizing the ferroaxial order. In this subsection, we compare a $\Delta T/T$ map obtained by EG and reflection-intensity maps by scanning XRD. For this comparison, we prepared a slowly cooled sample. This is because the domain size of slowly cooled samples is the order of 10^2 ~ 10^3 μm (see Fig. 3.19**h**), which is larger than the spatial resolution of the x-ray diffractometer used in this study (see 3.2.3).

Figures 3.20**a** and **b** show the two-dimensional intensity maps of reflections $11\bar{2}\underline{15}$ and $\bar{1}\bar{1}2\underline{15}$, respectively, obtained by scanning XRD measurements. To index these reflections (including their signs), we adopt the setting of crystal axes as shown in Fig. 3.20**c**. In these maps, there are both red (high intensity) and blue (low intensity) areas, and the contrasts are reversed between the two maps (compare Fig. 3.20**a** with 3.20**b**). Considering the difference in the crystal structure factors between A+ and A− domains (see 3.2.3), the observed contrasts correspond to ferroaxial domains.

To compare domains observed by XRD with that by EG, we performed the EG measurements on the same sample used for the abovementioned XRD measurements. For sufficient light intensity and an application of voltage, the surface opposed to that was used for the XRD measurements was polished down to the thickness of 33 μm, and ITO was sputtered to both surfaces (Fig. 3.20**c**). This EG measurement was performed in the same settings described in 3.3.1 and 3.3.2, except that the wavelength of incident light was 625 nm. Figure 3.20**d** shows the obtained spatial distribution of $\Delta T/T$, which corresponds to the map of EG. In most of the regions, the observed contrast is well matched with that observed by the XRD mapping measurements (compare Fig. 3.20**d** with the area surrounded by the dotted circle in Fig. 3.20**a**). This matching between the domains observed by the two different methods complementarily supports their effectiveness for the observation of ferroaxial domains. In addition, whereas the XRD maps reflect domain structures near the surface, the EG maps show the domains averaged in the thickness direction. This suggests that the ferroaxial domains in this sample are almost uniform (single domain) in its thickness direction ($\| c$).

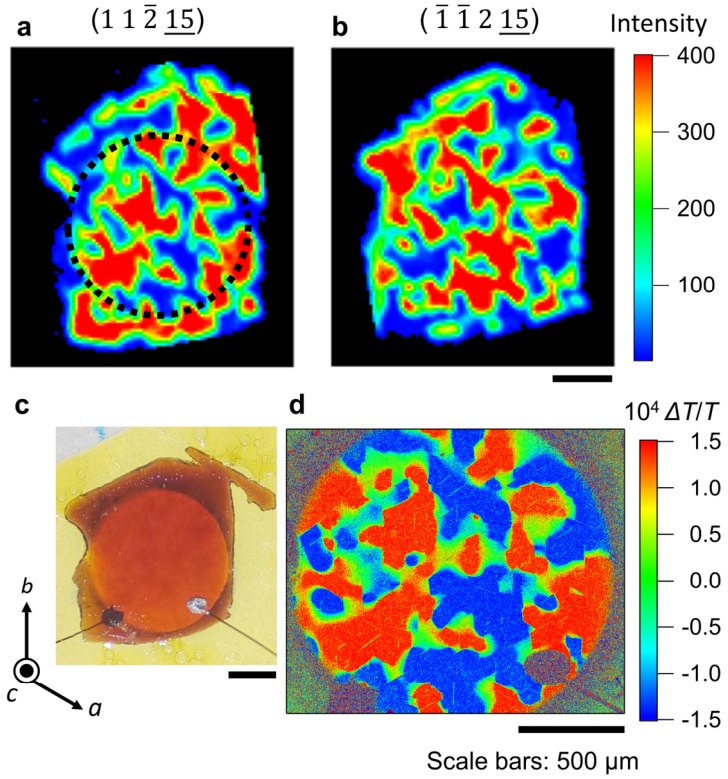

Fig. 3.20 Comparison of ferroaxial domains observed in a slow cooled sample of $NiTiO_3$ by x-ray diffraction (XRD) and electrogyration (EG) measurements. Adapted from ref. [37] with permission. Copyright 2022 by the American Physical Society. **a**,**b**, XRD results showing two-dimensional maps of diffraction intensities of reflections $11\bar{2}15$ (**a**) and $\bar{1}\bar{1}215$ (**b**). The color contrasts of **a** and **b** are reversed with each other. **c**, A photograph of the sample prepared for the EG measurement. **d**, EG result showing a two-dimensional map of $\Delta T/T$. The dotted circle in panel (**a**) corresponds to the EG observation area of panel (**d**) [a hole on the substrate in panel (**c**)]. Scale bars: 500 μm. Red and blue areas in panels (**a**,**d**) are well matched with each other and correspond to either A+ or A− domains.

3.4 Results and Discussion: $RbFe(MoO_4)_2$

3.4.1 Temperature evolution of ferroaxial domains

To investigate the evolution of domain formation upon a ferroaxial transition, we measured temperature dependence of $\Delta T/T$ maps, that is, spatial distributions of EG in $RbFe(MoO_4)_2$ over a broad temperature range. The experimental setup was the same with that for measurements on $NiTiO_3$ except for the wavelength of incident light (λ = 455 nm) and applied voltages (V = ±200 V). The sample temperature was controlled by a liquid nitrogen flow cold stage. Figures 3.21**d**-**k** show spatial distributions of the EG effect in $RbFe(MoO_4)_2$ obtained at various temperatures. We repeated the cooling sequence twice, and the results upon the first and the second cooling runs are displayed in Figs. 3.21**d**-**g** and Figs. 3.21**h**-**k**, respectively. Above the transition temperature in the non-ferroaxial phase ($P\bar{3}m1$), the $\Delta T/T$ maps show a monotonous and weak (green) contrast as shown in Figs. 3.21**d**,**h**. This is because the EG effect corresponding to the γ_{333} component is symmetrically forbidden in the non-ferroaxial phase. As the sample temperature decreases, contrasts of red and blue corresponding to opposite directions of EG start

to grow from the upper side in the images (Figs. 3.21**e**,**i**). These red and blue regions correspond to either A+ or A− domains, indicating that the sample undergoes the ferroaxial transition at 187 K. Then, at 183 K, the contrasts spread almost all over the sample (Figs. 3.21**f**,**j**) and increase with further decreasing temperature (Figs. 3.21**g**,**k**). It is noteworthy that the domain structures obtained during the first and the second cooling are different (e.g., compare Fig. 3.21**g** with **k**). This suggests that the ferroaxial domains were reconstructed by undergoing the transition. In both the results, various sizes of domains with the orders of 10^1 ~ 10^2 μm are seen. Broad green areas corresponding to weak EG signals imply opposite domains along the thickness directions and/or domains whose sizes are much smaller than the spatial resolution of the imaging system (a few micrometers). In ref. [20], it was reported that the ferroaxial domain size of $RbFe(MoO_4)_2$ is less than 50 μm in diameter, and our results do not contradict it. It was also reported in ref. [20] that the ratio of A+ and A− domains in the observation area (50 μm in diameter) gradually changed with decreasing temperature from just below T_c to 130 K. In our measurements, although we observed gradual growth of domains most likely due to thermal conduction, we did not observe a motion of domains with decreasing temperature.

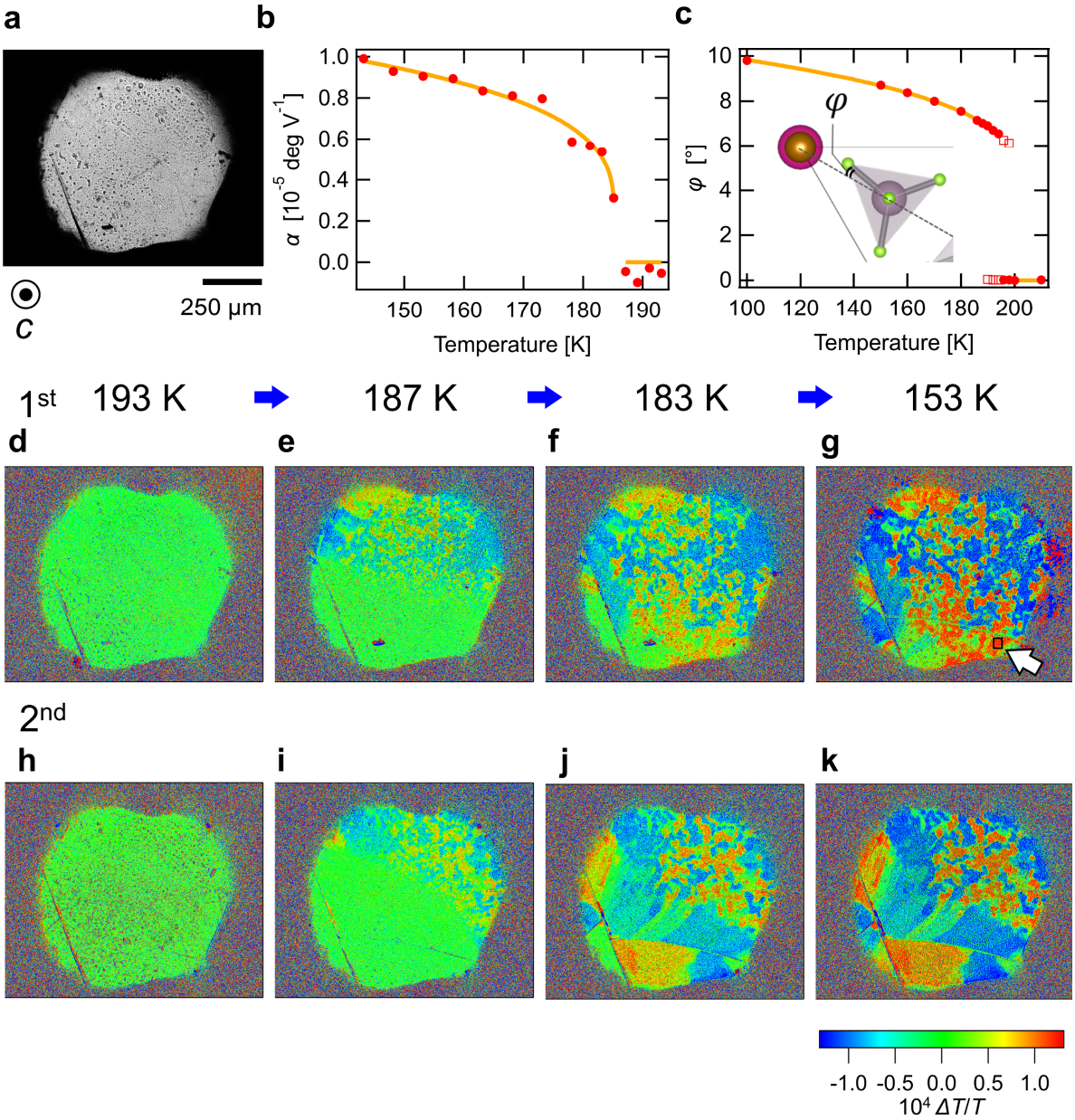

Fig. 3.21. Temperature evolution of ferroaxial order in $RbFe(MoO_4)_2$. Adapted from ref. [37] with permission. Copyright 2022 by the American Physical Society. **a**, Transmission optical microscopy image with the incidence of light along the *c* axis (scale bar: 250μm). **b**, Temperature dependence of the magnitude of EG at the single domain area denoted by a black box pointed by a white arrowhead in panel (**g**). The orange curve is the fitting by the function of the order parameter in the first-order phase transition given in equation (3.10). **c**, Temperature dependence of the rotation angle of the MoO_4 tetrahedra obtained by the Rietveld refinements of the neutron diffraction data. The rotation angles of the minority phase are denoted by open squares. The orange curve is the fitting by the function given in equation (3.10). The inset shows the definition of the angle φ. **d-k**, Two dimensional maps of $\Delta T/T$ obtained at various temperatures in the same area as panel (**a**). The first column (**d-g**) and the second column (**h-k**) show the results obtained upon the first and the second cooling of the sample, respectively.

3.4.2 Temperature dependence of electrogyration and structural rotation

In Fig. 3.21**b**, we show the temperature dependence of the magnitude of EG (α [deg V^{-1}]) obtained in the first cooling. The α at each temperature was calculated from the averages of $\Delta T/T$ in the pixels at a selected single ferroaxial domain area denoted by a black box in Fig. 3.21**g**.

To compare the temperature dependence of the magnitude of EG with that of the rotation of MoO_4 tetrahedra, we performed temperature dependent neutron diffraction measurements. Figures3.22**a** and 3.22**b** show the powder neutron diffraction patterns of $RbFe(MoO_4)_2$ at 210 K and 150 K, respectively. According to our Rietveld refinements, the patterns at 210 K and 150 K were well reproduced by the high temperature $P\bar{3}m1$ structure and the low temperature $P\bar{3}$ structure, respectively. Tables 3.4 and 3.5 list the crystal structure parameters obtained by the Rietveld refinements.

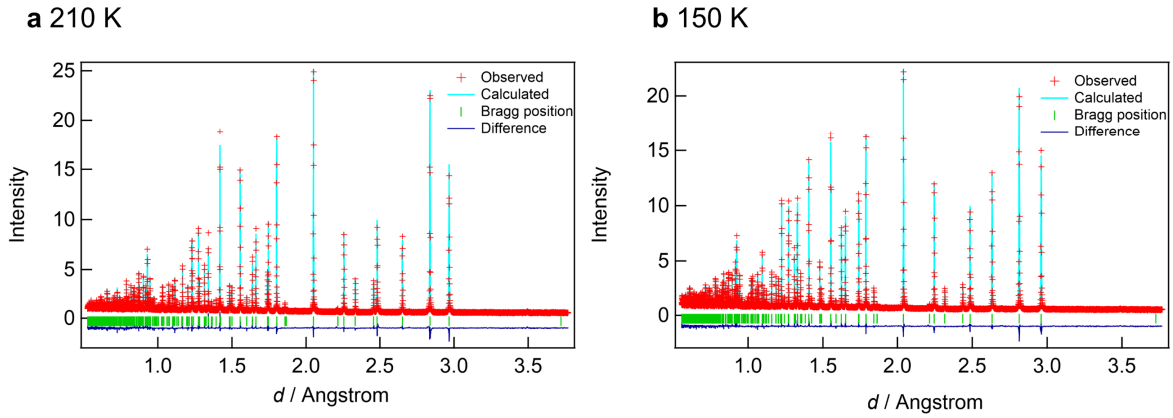

Fig. 3.22 Powder neutron diffraction patterns of $RbFe(MoO_4)_2$ measured at 210 K (**a**) and 150 K (**b**). Adapted from ref. [37] with permission. Copyright 2022 by the American Physical Society. The solid sky-blue lines are calculated intensities obtained by Rietveld refinements. The green vertical lines are calculated peak positions. The blue solid lines below the peak positions represent the differences between the observed and calculated intensities.

Table 3.4. Lattice parameters of $RbFe(MoO_4)_2$ at 210 K and 150 K obtained by Rietveld refinement. Adapted from ref. [37] with permission. Copyright 2022 by the American Physical Society. The space groups are $P\bar{3}m1$ at 210 K and $P\bar{3}$ at 150 K.

T (K)	a (Å)	c (Å)	R_p (%)	R_{wp} (%)	R_{exp} (%)	χ^2 (%)
210	5.674778(2)	7.443849(7)	3.94	5.16	2.59	3.97
150	5.626816(2)	7.45614(7)	3.33	4.12	2.49	2.72

Table 3.5. Atomic parameters of $RbFe(MoO_4)_2$ at 210 K (**a**) and 150 K (**b**) obtained by Rietveld refinement. Adapted from ref. [37] with permission. Copyright 2022 by the American Physical Society. In the refinement, isotropic atomic displacement parameters (B_{eq}) of Fe and Mo, and O(1) and (2) were fixed to be equal.

a 210 K

atom	x	y	z	B_{eq} (Å^2)
Rb	0	0	0.5	1.10(2)
Fe	0	0	0	0.064(6)
Mo	0.33333	0.66667	0.23141(7)	0.064(6)
O(1)	0.33333	0.66667	0.4629(1)	1.055(7)
O(2)	0.16139(5)	0.8385(1)	0.15706(8)	1.055(7)

b 150 K

atom	x	y	z	B_{eq} (Å^2)
Rb	0	0	0.5	0.725(2)
Fe	0	0	0	0.017(6)
Mo	0.33333	0.66667	0.23118(7)	0.017(6)
O(1)	0.33333	0.66667	0.46223(9)	0.509(6)
O(2)	0.11577(8)	0.79305(7)	0.15701(9)	0.509(6)

We also performed Rietveld refinements on power neutron diffraction data collected at other temperatures. In the refinement on the data at 100 K, isotropic atomic displacement parameters (B_{eq}) were not refined but fixed in the values at 150 K. From the refinements, we found that the high temperature $P\bar{3}m1$ and the low temperature $P\bar{3}$ phases coexist in the temperature range from 198 K to 190 K. The refined weight ratios of the $P\bar{3}m1$ were 92.97(4) %, 68.76(8) %, 44.07(7) %, 20.38(6) %, and 2.77(3) % at 198 K, 196 K, 194 K, 192 K, and 190 K, respectively. Figure 3.23 shows the lattice constants as a function of temperature. In the temperature range from 198 K to 190 K, the lattice constants of the minority phase are shown as open squares. The results are well matched with those of the previous work [10].

Fig. 3.23 The lattice constants as a function of temperature. Adapted from ref. [37] with permission. Copyright 2022 by the American Physical Society. From 198 K to 190 K, the lattice constants of the minority phase are denoted by open squares.

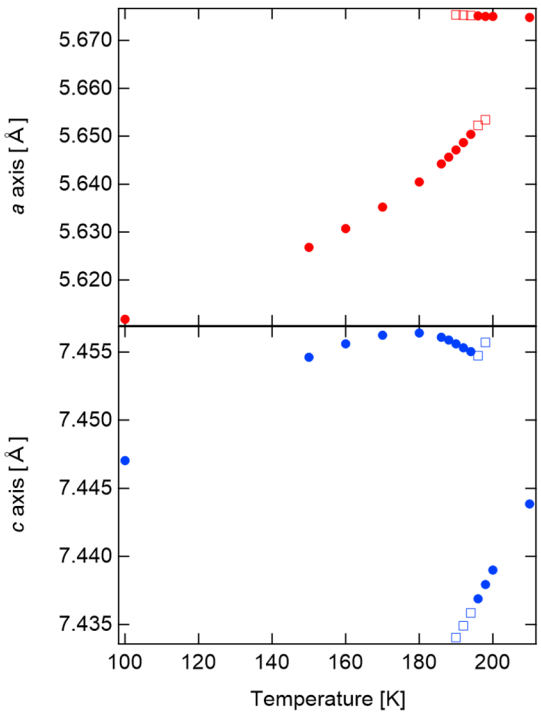

Summary

In Fig. 3.21**c**, we plot the temperature dependence of the rotation angle φ of the MoO_4 tetrahedra obtained by the Rietveld refinements of the neutron diffraction data. Here, φ is taken as the displacement angle from the $[\bar{1}100]$ axis (see the inset of Fig. 3.21**c**). In the temperature range from 198 K to 190 K where the high temperature $P\bar{3}m1$ phase and the low temperature $P\bar{3}$ phase coexist, the rotation angles for the minority phase are shown as open squares in Fig. 3.21**c**.

The temperature profiles of α and φ are similar to each other, though they show different behaviors around T_c. This is most likely because α just below T_c will reflect the averaged magnitude of EG of the coexisting high temperature and low temperature phases. The temperature profiles of α and φ are fitted by the function of [20,44,45]

$$\alpha(T), \varphi(T) = \begin{cases} 0, T > T_c \\ \sqrt{a + b\sqrt{T_d - T}}, T \leq T_c \end{cases} \quad (3.10)$$

which characterizes the first-order phase transition. Here, a, b, and T_d are the fitting parameters, where $T_d = T_c + \frac{a^2}{b^2}$. The fitting yields $T_c = 185.5 \pm 0.5$ K for $\alpha(T)$ and $T_c = 190 \pm 3$ K for $\varphi(T)$, which are consistent with the previously reported values of T_c (= 190 ~ 195 K) [10,20]. The slight difference in the value obtained from the EG measurement is probably due to a poor thermal contact between the sample and the cold stage. The success of the fitting clearly shows that the rotation angle of the MoO_4 tetrahedra behaves as the order parameter, and one can also deduce the order parameter of ferroaxial order from EG.

3.5 Summary

In summary, this study represents the first successful visualization of ferroaxial domains of $NiTiO_3$ and $RbFe(MoO_4)_2$, through spatial distribution measurements of the linear electrogyration (EG) effect. In $NiTiO_3$, a comparison of FZ-grown and flux-grown samples, both in as-grown and annealed ones, revealed the formation of multi-domains during the ferroaxial transition. Furthermore, it was observed that the domain size tends to increase with decreasing cooling rate around T_c. In addition, we confirmed that the observed spatial distributions of EG is nothing other than ferroaxial domains by comparing the results of EG and scanning XRD on the same sample. In other words, scanning XRD measurements is another way to visualize ferroaxial domains. In $RbFe(MoO_4)_2$, we performed EG measurements over a wide temperature range across T_c and confirmed that ferroaxial domains were formed below T_c. Furthermore, the temperature evolution of the rotation angle of the MoO_4 tetrahedra was determined from powder neutron diffraction measurements. The temperature profiles of EG and the rotation angle of the MoO_4 tetrahedra exhibit similar trends and are well fitted by the function of the order parameter in the first order transition. This confirms the effectiveness of EG measurements to observe the evolution of ferroaxial order.

References

[1] J. Hlinka, *Eight Types of Symmetrically Distinct Vectorlike Physical Quantities*, Phys. Rev. Lett. **113**, 165502 (2014).

[2] J. Hlinka, J. Privratska, P. Ondrejkovic, and V. Janovec, *Symmetry Guide to Ferroaxial Transitions*, Phys. Rev. Lett. **116**, 177602 (2016).

[3] K. Aizu, *Possible Species of Ferroelectrics*, Phys. Rev. **146**, 423 (1966).

[4] K. Aizu, *Possible Species of "Ferroelastic" Crystals and of Simultaneously Ferroelectric and Ferroelastic Crystals*, J. Phys. Soc. Jpn. **27**, 387 (1969).

[5] K. C. Erb and J. Hlinka, *Vector, Bidirector, and Bloch Skyrmion Phases Induced by Structural Crystallographic Symmetry Breaking*, Phys. Rev. B **102**, 024110 (2020).

[6] K. C. Erb and J. Hlinka, *Symmetry Guide to Chiroaxial Transitions*, Phase Transitions **91**, 953 (2018).

[7] S. Prosandeev, I. Ponomareva, I. Kornev, I. Naumov, and L. Bellaiche, *Controlling Toroidal Moment by Means of an Inhomogeneous Static Field: An Ab Initio Study*, Phys. Rev. Lett. **96**, 237601 (2006).

[8] S.-W. Cheong, D. Talbayev, V. Kiryukhin, and A. Saxena, *Broken Symmetries, Non-Reciprocity, and Multiferroicity*, npj Quantum Mater. **3**, 19 (2018).

[9] H. Boysen, F. Frey, M. Lerch, and T. Vogt, *A Neutron Powder Investigation of the High-Temperature Phase Transition in $NiTiO_3$*, Zeitschrift Für Kristallographie - Crystalline Materials **210**, 328 (1995).

[10] A. Waśkowska, L. Gerward, J. Staun Olsen, W. Morgenroth, M. MacZka, and K. Hermanowicz, *Temperature- and Pressure-Dependent Lattice Behaviour of $RbFe(MoO_4)_2$*, J. Phys. Condens. Matter **22**, 055406 (2010).

[11] A. Gągor, P. Zajdel, and D. Többens, *The Phase Transitions in $CsFe(MoO_4)_2$ Triangular Lattice Antiferromagnet, Neutron Diffraction and High Pressure Studies*, J. Alloys Compd. **607**, 104 (2014).

[12] S. Yamagishi, T. Hayashida, R. Misawa, K. Kimura, M. Hagihala, T. Murata, S. Hirose, and T. Kimura, *Ferroaxial Transitions in Glaserite-Type Compounds: Database Screening, Phonon Calculations, and Experimental Verification*, Chem. Mater. **35**, 747 (2023).

[13] M. Gateshki and J. M. Igartua, *Second-Order Structural Phase Transition in Sr_2CuWO_6 Double-Perovskite Oxide*, J. Phys. Condens. Matter **15**, 6749 (2003).

[14] K. Gesi, *Dielectric Properties and Structural Phase Transitions in TMMnC ($N(CH_3)_4MnCl_3$) Type Crystals*, Ferroelectrics **137**, 209 (1992).

[15] R. W. Smaha et al., *Materializing Rival Ground States in the Barlowite Family of Kagome Magnets: Quantum Spin Liquid, Spin Ordered, and Valence Bond Crystal States*, npj Quantum Mater. **5**, 23 (2020).

[16] R. D. Johnson, S. Nair, L. C. Chapon, A. Bombardi, C. Vecchini, D. Prabhakaran, A. T. Boothroyd, and P. G. Radaelli, *$Cu_3Nb_2O_8$: A Multiferroic with Chiral Coupling to the Crystal Structure*, Phys. Rev. Lett. **107**, 137205 (2011).

[17] R. D. Johnson, L. C. Chapon, D. D. Khalyavin, P. Manuel, P. G. Radaelli, and C. Martin, *Giant Improper Ferroelectricity in the Ferroaxial Magnet $CaMn_7O_{12}$*, Phys. Rev. Lett. **108**, 067201 (2012).

[18] N. Terada, D. D. Khalyavin, P. Manuel, W. Yi, H. S. Suzuki, N. Tsujii, Y. Imanaka, and A. A. Belik, *Ferroelectricity Induced by Ferriaxial Crystal Rotation and Spin Helicity in a B -Site-Ordered Double-Perovskite Multiferroic In_2NiMnO_6*, Phys. Rev. B **91**, 104413 (2015).

References

[19] A. J. Hearmon, F. Fabrizi, L. C. Chapon, R. D. Johnson, D. Prabhakaran, S. V. Streltsov, P. J. Brown, and P. G. Radaelli, *Electric Field Control of the Magnetic Chiralities in Ferroaxial Multiferroic $RbFe(MoO_4)_2$*, Phys. Rev. Lett. **108**, 237201 (2012).

[20] W. Jin, E. Drueke, S. Li, A. Admasu, R. Owen, M. Day, K. Sun, S.-W. Cheong, and L. Zhao, *Observation of a Ferro-Rotational Order Coupled with Second-Order Nonlinear Optical Fields*, Nat. Phys. **16**, 42 (2020).

[21] K. Aizu, *Reversal in Optical Rotatory Power - "Gyroelectric" Crystals Crystals and "Hypergyroelectric" Crystals*, Phys. Rev. **133**, A1584 (1964).

[22] I. S. Zheludev, *Axial Tensors of the Third Rank and the Ohysical Effects They Describe*, Kristallografiya **9**, 501 (1964).

[23] O. G. Vlokh, *Electrooptical Activity of Quartz Crystals*, Ukr. Fiz. Zhurn **15**, 758 (1970).

[24] T. Hayashida, Y. Uemura, K. Kimura, S. Matsuoka, D. Morikawa, S. Hirose, K. Tsuda, T. Hasegawa, and T. Kimura, *Visualization of Ferroaxial Domains in an Order-Disorder Type Ferroaxial Crystal*, Nat. Commun. **11**, 4582 (2020).

[25] W. Kaminsky, *Experimental and Phenomenological Aspects of Circular Birefringence and Related Properties in Transparent Crystals*, Rep. Prog. Phys. **63**, 1575 (2000).

[26] M. I. Aroyo, A. Kirov, C. Capillas, J. M. Perez-Mato, and H. Wondratschek, *Bilbao Crystallographic Server. II. Representations of Crystallographic Point Groups and Space Groups*, Acta Crystallogr. A **62**, 115 (2006).

[27] M. I. Aroyo, J. M. Perez-Mato, D. Orobengoa, E. Tasci, G. De La Flor, and A. Kirov, *Crystallography Online: Bilbao Crystallographic Server*, Bulg. Chem. Commun. **43**, 183 (2011).

[28] S. V. Gallego, J. Etxebarria, L. Elcoro, E. S. Tasci, and J. M. Perez-Mato, *Automatic Calculation of Symmetry-Adapted Tensors in Magnetic and Non-Magnetic Materials: A New Tool of the Bilbao Crystallographic Server*, Acta Crystallogr. A **75**, 438 (2019).

[29] D. Adamenko, I. Klymiv, V. M. Duda, R. Vlokh, and O. Vlokh, *Electrogyration and Faraday Rotation in Pure and Cr-Doped Lead Germanate Crystals*, J. Phys. Condens. Matter **20**, 075101 (2008).

[30] O. G. Vlokh and R. O. Vlokh, *The Electrogyration Effect*, Opt. Photonics News **20**, 34 (2009).

[31] M. Lerch, H. Boysen, R. Neder, F. Frey, and W. Laqua, *Neutron Scattering Investigation of the High Temperature Phase Transition in $NiTiO_3$*, J. Phys. Chem. Solids **53**, 1153 (1992).

[32] M. Kenzelmann et al., *Direct Transition from a Disordered to a Multiferroic Phase on a Triangular Lattice*, Phys. Rev. Lett. **98**, 267205 (2007).

[33] M. Ohgaki, K. Tanaka, F. Marumo, and H. Takei, *Electron-Density Distribution in Ilmenite-Type Crystals III. Nickel (II) Titanium (IV) Trioxide, $NiTiO_3$*, Mineral. J. **14**, 133 (1988).

[34] G. Garton, S. H. Smith, and B. M. Wanklyn, *Crystal Growth From The Flux Systems PbO-V_2O_5 AND Bi_2O_3-V_2O_5*, J. Cryst. Growth **13/14**, 588 (1972).

[35] T. Inami, *Neutron Powder Diffraction Experiments on the Layered Triangular-Lattice Antiferromagnets $RbFe(MoO_4)_2$and $CsFe(SO_4)_2$*, J. Solid State Chem. **180**, 2075 (2007).

[36] Y. Uemura, S. Arai, J. Tsutsumi, S. Matsuoka, H. Yamada, R. Kumai, S. Horiuchi, A. Sawa, and T. Hasegawa, *Field-Modulation Imaging of Ferroelectric Domains in Molecular Single-Crystal Films*, Phys. Rev. Appl. **11**, 014046 (2019).

[37] T. Hayashida, Y. Uemura, K. Kimura, S. Matsuoka, M. Hagihala, S. Hirose, H. Morioka, T. Hasegawa, and T. Kimura, *Phase Transition and Domain Formation in Ferroaxial Crystals*, Phys. Rev. Mater. **5**, 124409 (2021).

[38] G. L. Nord and C. A. Lawson, *Order-Disorder Transition-Induced Twin Domains and Magnetic Properties in Ilmenite-Hematite*, Am. Mineral. **74**, 160 (1989).

[39] K. Momma and F. Izumi, *Vesta3 for Threedimensional Visualization of Crysal, Volumetric and Morphology Data*, J. Appl. Crystallogr. **44**, 1272 (2011).

[40] S. Torii et al., *Super High Resolution Powder Diffractometer at J-PARC*, J. Phys. Soc. Jpn. **80**, SB020 (2011).

[41] R. Oishi, M. Yonemura, Y. Nishimaki, S. Torii, A. Hoshikawa, T. Ishigaki, T. Morishima, K. Mori, and T. Kamiyama, *Rietveld Analysis Software for J-PARC*, Nuclear Inst. and Methods in Physics Research, A **600**, 94 (2009).

[42] R. Oishi-Tomiyasu, M. Yonemura, and T. Morishima, *Application of Matrix Decomposition Algorithms for Singular Matrices to the Pawley Method in Z-Rietveld*, J. Appl. Crystallogr. **45**, 299 (2012).

[43] H. Takei, *Preferentially Orientated Precipitation in $MnTiO_3$ Single Crystals*, J. Mater. Sci. **16**, 1310 (1981).

[44] A. F. Devonshire, *Theory of Ferroelectrics*, Adv. Phys. **3**, 85 (1954).

[45] J. C. Tolédano and P. Tolédano, *The Landau Theory of Phase Transitions*, Vol. 3 (World Scientific, Singapore, 1987).

Chapter 4
Observation of electric-field-induced magneto chiral dichroism in a ferroaxial crystal

4.1 Introduction

In Chapter 3, we reported on the observation of ferroaxial domains by using the linear electrogyration effect. This effect is considered a result of electric-field-induced chirality in ferroaxial materials. As discussed in Chapter 2, controlling chirality and its associated phenomena in crystalline materials is challenging. In ferroaxial materials, however, chirality can be induced by applying an electric field and switched by changing the direction of the field. Thus, ferroaxial materials provide a platform for controlling chirality-related-phenomena. In this chapter, we demonstrate the observation of another representative chirality-related optical effect, magnetochiral dichroism, by applying an electric field to a ferroaxial crystal.

4.1.1 Magnetochiral dichroism

Magnetochiral dichroism (MChD) is an asymmetry in the absorption of two counter propagating unpolarized electromagnetic waves in magnetized chiral materials. MChD was predicted in the 1980s [1,2], and firstly observed as luminescence anisotropy in 1997 [3]. So far, it has been verified in various chiral systems including liquid molecular systems [3,4], ferromagnets [5,6], organic compounds [7], and magnetic nanohelices [8]. MChD provides a way to study the spectroscopy of chiral media and to develop new magneto-optical devices [9–11]. Furthermore, it has also been suggested as a potential source of the homochirality of life in the context of fundamental interactions between light and matter [9,10,12].

MChD is defined as a difference in an absorption coefficient α of a medium for unpolarized light between with and without a magnetic field ($\Delta\alpha_{\mathrm{MChD}}$) and described as [13]

$$\Delta\alpha_{\mathrm{MChD}}^{D/L} \propto X^{D/L}\mathbf{k}\cdot\mathbf{H}, \tag{4.1}$$

where **k** is a light propagation vector and **H** is a magnetic field. The superscripts denote the handedness of the medium (*D*: dextro, *L*: levo), and MChD shows sign reversal against handedness reversal, i.e., $X^D = -X^L$.

The vector-like properties introduced in Chapter 1 are useful to understand the symmetry aspect of MChD. Considering the situation when a magnetic field (time-odd axial vector $\mathcal{A}'$) is applied parallel to the chiral director ($\mathcal{C}$) in a medium, the dot product of $\mathcal{A}'$ and $\mathcal{C}$ has the symmetry of time-odd polar vector ($\mathcal{P}'$), which is the same symmetry with the propagating light wave (see Fig. 1.5 in

1.3.4). Thus, the nonreciprocal effect of MChD is expected in a magnetized chiral medium.

Microscopically, MChD is induced by electronic transition processes of electric dipole (ED) – magnetic dipole (MD) and/or ED – electric quadrupole (EQ) [2,13], details of which will be discussed later.

4.1.2 Electric-field-induced magnetochiral dichroism

As discussed in Chapter 3, a ferroaxial system itself is achiral, but it can be made chiral by the application of an electric field. Thus, MChD is expected to be induced in a ferroaxial material by applying an electric field, which will appear as a nonreciprocal absorption under simultaneous application of magnetic and electric fields. However, such a phenomenon of electric-field-induced MChD (*E*-MChD) has never been reported today.

In the similar manner with the usual MChD, *E*-MChD is described as a difference in α for unpolarized light between with and without magnetic and electric fields:

$$\Delta\alpha_{\mathrm{EMChD}} \propto (\mathbf{A}\cdot\mathbf{E})(\mathbf{k}\cdot\mathbf{H}) \tag{4.2}$$

where **A** is a ferroaxial moment and **E** is an electric field. Here, the cross product of $\mathbf{A}\cdot\mathbf{E}$ define the chirality of the system. Thus, the sign of $\Delta\alpha_{\mathrm{EMChD}}$ is opposite between the domain states of A+ and A− under the same direction of an electric field. In a single domain ferroaxial state, on the other hand, switching the direction of **E** corresponds to that of chirality and changes the sign of $\Delta\alpha_{\mathrm{EMChD}}$ (see Fig. 4.1 for schematical illustration). In the following, for simplification, we refer to $\Delta\alpha_{\mathrm{EMChD}}$ of the A+ domain state as just $\Delta\alpha$.

Nonreciprocal optical phenomena due to simultaneously applied electric and magnetic fields or spontaneous polarization (**P**) and magnetization (**M**) have been studied in the context of magnetoelectric nonreciprocity or optical magnetoelectric effect [14]. So far, such nonreciprocal phenomena have been observed mostly in the setting of $\mathbf{k}\perp\mathbf{E}(\mathbf{P})\perp\mathbf{H}(\mathbf{M})$ [15,16] or $\mathbf{k}\perp\mathbf{E}(\mathbf{P})\parallel\mathbf{H}(\mathbf{M})$ [17,18]. *E*-MChD studied here is regarded as a distinct type of magnetoelectric nonreciprocity with the setting of $\mathbf{k}\parallel\mathbf{E}\parallel\mathbf{H}$. As can be seen in equation (4.2), the ferroaxial moment **A** plays an important role in the *E*-MChD.

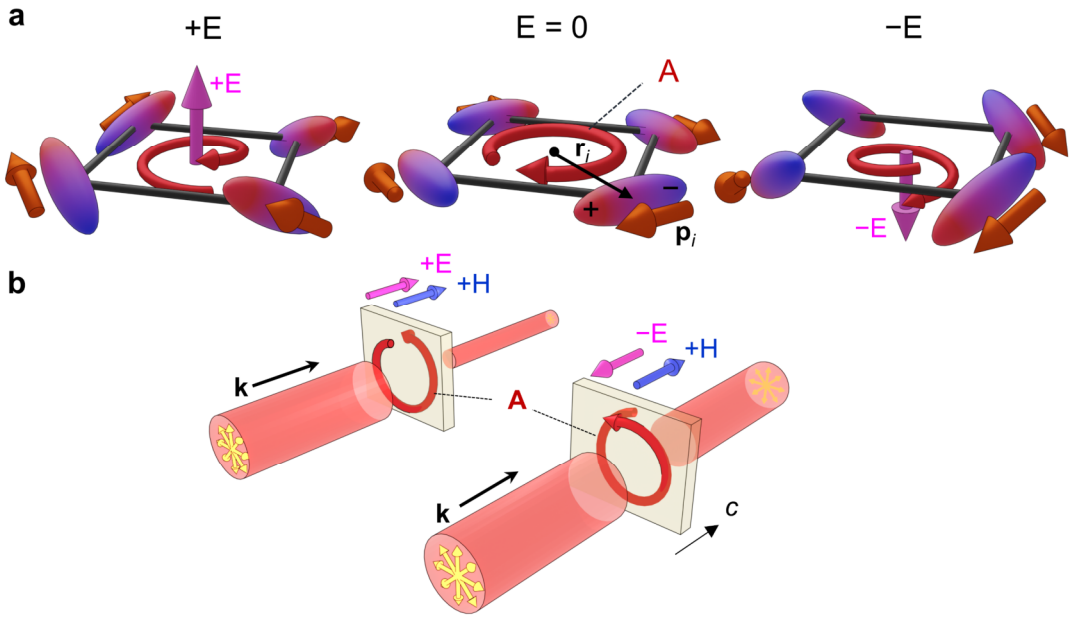

Fig. 4.1 Schematic illustration of Electric-field-induced magnetochiral dichroism (*E*-MChD) in a ferroaxial material [19]. **a**, Schematic illustrations of the ferroaxial moment **A** generated by head-to-tail arrangements of electric dipoles. The middle panel of (**a**) shows the arrangement in the absence of an electric field (**E**). The left and right panels show the modification of the arrangement by applying positive (+E) and negative (−E) electric fields, respectively. Here, each electric dipole moment is tilted toward the applied **E**, inducing chirality in the system. Note that the +E and −E states exhibit opposite chirality. **b,** Conceptual diagram of *E*-MChD in a ferroaxial material. The cylinders denote unpolarized light propagating along the *c* axis. The diameter of each cylinder represents the intensity of incident or transmitted light. The magenta and blue arrows denote electric (**E**) and magnetic (**H**) fields, respectively. MChD in a ferroaxial system is controlled via **E** and the intensity of transmitted light is different between when **E** and **H** are parallel (left) and antiparallel (right) to each other.

4.1.3 Motivation

In this chapter, we report on the discovery of *E*-MChD in the ferroaxial antiferromagnet $NiTiO_3$ (see also 3.1.4 about the crystal structure of $NiTiO_3$). We examine *E*-MChD spectra in various conditions of light propagation, magnetic fields, and electric fields. The observed spectra are discussed in the framework of the mechanism by combining the theory of MChD and the pseudo-Stark splitting.

4.2 Experimental methods

4.2.1 Sample preparation

For the spectrum measurements of *E*-MChD, the flux-as grown sample with a single ferroaxial domain, which is the same one with that used for the domain observation in Figs. 3.19**e**,**i**, was used (see 3.2.1 about the crystal growth and characterization). The sample thickness was 32 μm, and indium/tin oxide (ITO) was sputtered to the widest faces (*c* plane) to form transparent electrodes.

4.2.2 *E*-MChD spectrum measurement

The optical measurements of $NiTiO_3$ were performed using a fiber-based optical system, which was designed and built by Dr. Kenta Kimura. Figure 4.2 shows a photograph and schematic illustration of the optical setup. As an unpolarized light source, a tungsten-halogen lamp was used. The light transmitted through the sample along the *c* axis was detected by a spectrometer (MS3504i, SOL Instruments) equipped with an InGaAs camera detector (HLS 190IR-1, SOL Instruments) in the spectrum measurements. In the lock-in measurements described below, a Ge amplified detector (PDA50B2, Thorlabs) was used. The optical system was inserted into a commercial physical property measurement system (PPMS, Quantum Design), which enabled us to control sample temperature, a magnetic field, and an electric field.

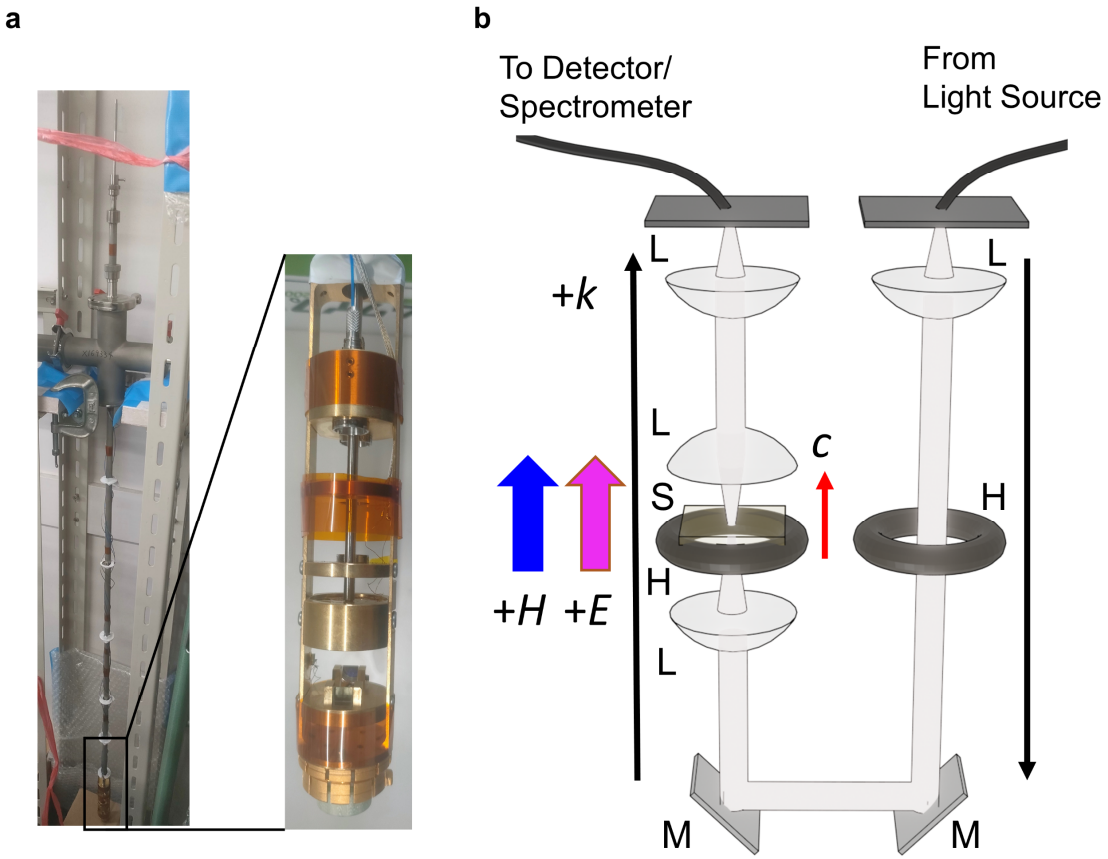

Fig. 4.2 Photograph (**a**) and schematic illustration (**b**) of optical setup [19]. L: lens, H: sample holder, M: mirror, S: sample.

The spectra of *E*-MChD (Δa) were calculated by using the transmission spectra obtained with the application of positive (I_{V+}) and negative (I_{V-}) voltages at a certain magnetic field as

$$\frac{1}{d}\frac{I_{V-}-I_{V+}}{I_{V-}+I_{V+}} = \frac{1}{d}\frac{I_0 e^{-(\alpha_0-\Delta\alpha)d} - I_0 e^{-(\alpha_0+\Delta\alpha)d}}{I_0 e^{-(\alpha_0-\Delta\alpha)d} + I_0 e^{-(\alpha_0+\Delta\alpha)d}} \approx \Delta\alpha, \tag{4.3}$$

where I_0 is the intensity of incident light, α_0 is an absorption coefficient without electric and magnetic

fields, and d is a sample thickness. Here, we assume that $\Delta\alpha d$ is small and $e^{\Delta\alpha d} \approx (1 + \Delta\alpha d)$.

In the lock-in measurements of *E*-MChD, a sinusoidal voltage $V_0\sin(\omega t)$ was applied to the sample at a certain magnetic field. Under such a sinusoidal voltage, the intensity of transmitted light is described as

$$I_0 e^{-(\alpha_0 + \widetilde{\Delta\alpha} V_0 \sin(\omega t)/d)d} \approx I_0 e^{-\alpha_0 d}\left(1 - \widetilde{\Delta\alpha} V_0 \sin(\omega t)\right) \quad (4.4)$$

where $\Delta\alpha = \widetilde{\Delta\alpha}\, V_0 \sin(\omega t)/d$. Then, the intensity of transmitted light oscillating at the angular frequency ω was detected by using a lock-in amplifier and $\widetilde{\Delta\alpha}$ was calculated. In the lock-in measurements, monochromatic light with a photon energy of 0.886 eV obtained by using a bandpass filter was used.

4.3 Results and discussion

4.3.1 *E*-MChD spectra

To obtain *E*-MChD spectra, measurements of absorption spectra were performed at various magnetic fields, electric fields, and temperatures in the photon energy range of 0.75 eV < E_{ph} < 1.29 eV. The directions of light propagation ($\pm k_c$), an electric field ($\pm E_c$), and a magnetic field ($\pm H_c$) are all along the hexagonal *c* axis, where the signs are defined as positive (negative) when the vectors are parallel (antiparallel) to the *c* direction (see a schematic illustration of the optical setup in Fig. 4.2). As a representative spectrum, the absorption coefficient in the absence of external fields α_0 at 23 K is shown in Fig. 4.3**a**. (Note that the magnetic susceptibility of $NiTiO_3$ is maximized at the Néel temperature T_N = 22.5 K [20,21].) In the photon energy range of 0.8 eV < E_{ph} < 1.1 eV, absorption peaks assigned to the spin allowed Ni^{2+} *d-d* transition from the $^3A_{2g}$ ground state to the $^3T_{2g}$ excited state are observed [22]. Here, $^3A_{2g}$ and $^3T_{2g}$ refer to the energy states split by the cubic O_h crystal field.

Figure 4.3**b** shows the *E*-MChD spectrum obtained at 23 K in the setting of $+k_c$, V_c = 100 V, and $\mu_0 H_c$ = 9 T. Here $\Delta\alpha = \alpha(V_c = 100\text{ V}, \mu_0 H_c = 9\text{ T}) - \alpha_0$. Under the application of 100 V voltage, the magnitude of an electric field is 3.1×10^4 V cm^{-1}. In the following, we denote the magnitude of voltage instead of electric field for simplification. In the *E*-MChD spectrum, sharp peaks are observed in the energy range of 0.80 eV < E_{ph} < 0.85 eV, at which sharp peaks are also observed in the absorption spectrum (compare Fig. 4.3**a** with 4.3**b**). These absorption peak structures will be assigned to the magnetic dipole transition to the excited states split by the trigonal crystal field and the spin-orbit interaction, as we will discuss in detail in 4.3.3. Other than the sharp peaks, one can find a small and relatively broad peak around 0.9 eV. At 0.95 eV < E_{ph} < 1.29 eV, finite $\Delta\alpha$ was not observed in the current resolution.

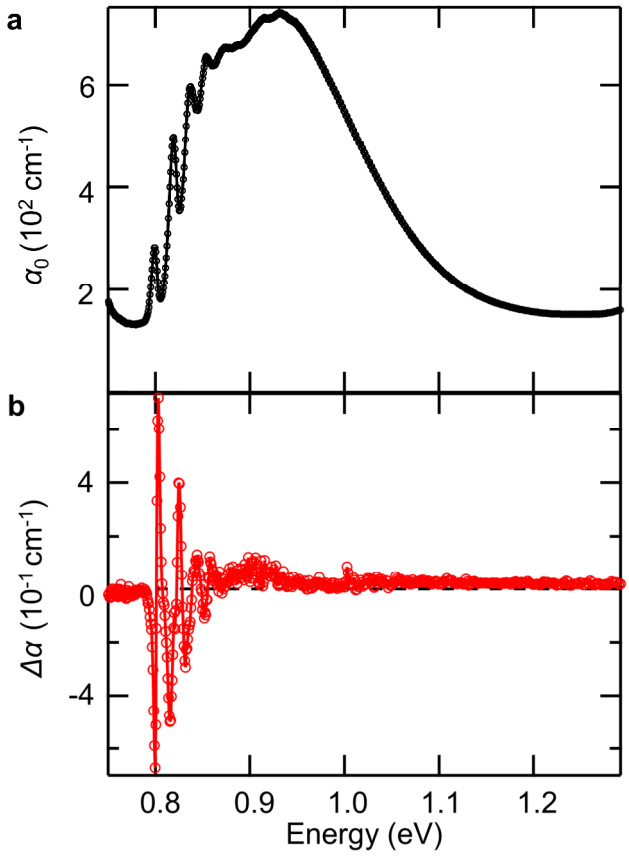

Fig. 4.3 Spectrum of *E*-MChD at 23 K. **a**, Absorption spectrum obtained at 23 K in the geometry of **k** ∥ *c* in the photon energy of 0.75 eV < E_{ph} < 1.29 eV [19]. The broad peak around 0.9 eV corresponds to the transition from the ground state $^3A_{2g}$ to the excited state $^3T_{2g}$. **b**, Spectrum of *E*-MChD obtained at 23 K in the geometry of **k** ∥ **E** ∥ **H** ∥ *c* in the photon energy of 0.75 eV < E_{ph} < 1.29 eV. Here, $\Delta\alpha$ corresponds to the magnitude of *E*-MChD under the 100 V voltage and 9 T magnetic field.

To identify whether the observed absorbance difference $\Delta\alpha$ originates from *E*-MChD, we performed measurements with changing light propagation direction, magnetic fields, and electric fields (Fig. 4.4). Figure 4.4**a** shows the $\Delta\alpha$ spectra obtained for $+k_c$ (red) and $-k_c$ (blue) in the setting of V_c = 100 V and $\mu_0 H_c$ = 9 T. The spectra show almost complete sign reversal against the light propagation direction switching, which indicates the nonreciprocity of the observed optical phenomena.

Figure 4.4**b** shows the magnetic-field dependence of $\Delta\alpha$. Here, the light propagation and a voltage are set as $+k_c$ and V_c = 100 V, respectively, and the measurements were performed at selected magnetic fields from −9 T to 9 T. When comparing the spectra obtained in the positive and negative magnetic fields [e.g., compare the spectra at 9 T (red) and −9T (purple)], an almost complete sign reversal is observed. Furthermore, $|\Delta\alpha|$ gets larger with increasing the magnitude of magnetic field. The inset of Fig. 4.4**b** shows $\Delta\alpha$ at 0.799 eV as a function of magnetic field, which is extracted from the spectra in Fig. 4.4**b**. As seen in this graph, $\Delta\alpha$ responds linearly to the applied magnetic field, supporting that $\Delta\alpha$ comes from MChD.

Finally, Fig. 4.4**c** shows the electric-field dependence of $\Delta\alpha$. Here the light propagation and a

magnetic field are set as $+k_c$ and $\mu_0 H_c$ = 9 T, respectively, and the spectra were obtained at selected voltages from 0 V to 100 V. $|\Delta\alpha|$ gets larger with increasing the magnitude of voltage. The inset of Fig. 4.4**c** shows $\Delta\alpha$ at 0.799 eV as a function of voltage, which is extracted from the spectra in Fig. 4.4**c**. $\Delta\alpha$ responds linearly to the applied voltage, fulfilling the requirements for *E*-MChD. The finite $\Delta\alpha$ even at zero magnetic (the inset of Fig. 4.4**b**) or electric fields (the inset of Fig. 4.4**c**) is most likely due to temporal changes in incident light intensity which causes temporal changes in calculated transmittance. From the spectra in Figs. 4.4**b** and 4.4**c**, we omit the spectra obtained in 0 T and 0 V, respectively. Based on the results of these **k**, **H**, and **V** dependent measurements, we conclude that the observed $\Delta\alpha$ is nothing more or less than *E*-MChD.

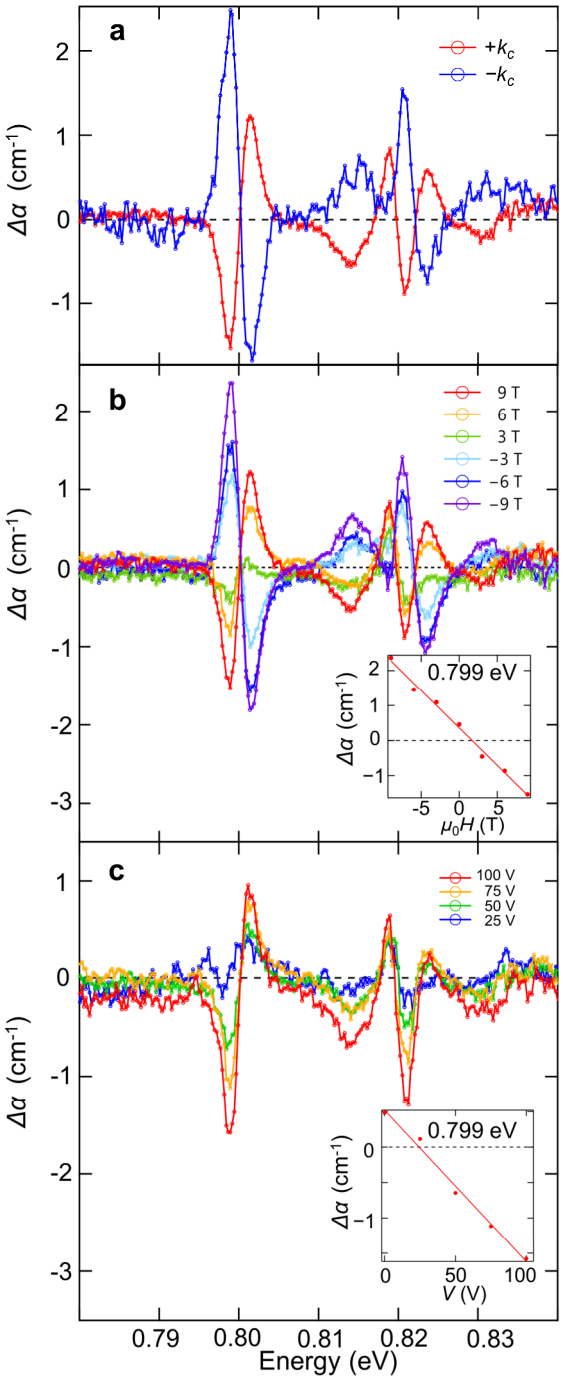

Fig. 4.4 Effect of light propagation direction, magnetic field, and electric field on *E*-MChD [19]. The spectra were obtained at 23 K in the photon energy of 0.763 eV < E_{ph} < 0.90 eV. **a**, Spectra of *E*-MChD obtained for $+k_c$ (red) and $-k_c$ (blue). Here, $\Delta\alpha$ corresponds to the magnitude of *E*-MChD under the 100 V voltage and 9 T magnetic field. **b**, Magnetic field dependence of *E*-MChD spectra. The spectra were obtained with changing the magnitude of the magnetic field from –9 T to 9 T by 3 T, under the fixed magnitude of voltage 100 V. The inset shows the magnetic field dependence of *E*-MChD at 0.799 eV. **c**, Voltage dependence of *E*-MChD spectra. The spectra were obtained with changing the magnitude of the electric field from 0 V to 100 V by 25 V under the fixed magnitude of magnetic field 9 T. The inset shows the voltage dependence of *E*-MChD at 0.799 eV.

4.3.2 Temperature dependence of *E*-MChD

Next, we measured the temperature (T) dependence of *E*-MChD to elucidate the relationship between *E*-MChD and electronic properties of $NiTiO_3$. Figure 4.5 shows absorption spectra (Fig. 4.5**a**) and *E*-MChD spectra (Fig. 4.5**b**) obtained at 100 K, 50 K, 23 K, and 5 K. The setting for the *E*-MChD spectra is $+k_c$, V_c = 100 V, and $\mu_0 H_c$ = 9 T. As seen in Fig. 4.5**a**, absorption peaks at 0.799 eV, 0.820 eV, and 0.836 eV develop with decreasing T. From 100 K to 23 K, the peak positions are unchanged while the peak intensities get increased. This may suggest that phonons are suppressed with lowering T, and the transitions to the split excited states get apparent. By contrast, the peak positions at 5 K are shifted from those above 23 K. This is possibly due to the exchange field activated below T_N. Corresponding to the development of the absorption peaks, the peak structures of the *E*-MChD spectrum also develop, which is clearly observed by comparing the spectrum at 100 K (red line in Fig. 4.5**b**) with those at 50 K or 23 K (green or blue lines in Fig. 4.5**b**). About the spectrum at 5 K, not only the peak positions at 0.799 eV and 0.82 eV are shifted, but also the peak structures around 0.82 eV are drastically changed (compare the purple line with the green or blue lines in Fig.4.5**b**). Although any peak splitting due to the exchange field is not seen in the absorption spectrum, it is still possible that *E*-MChD is more sensitive to the splitting of the excited energy states.

We also measured the T dependence of *E*-MChD from 5 K to 100 K at a fixed photon energy. Here, we chose the energy of 0.886 eV at which sharp peaks were not observed (see Fig. 4.3**b**) to discuss the T profile of *E*-MChD not affected by developments of peak structures and the exchange field. *E*-MChD at each temperature was measured by the lock-in technique. The measurements were performed at 9 T for $\pm k_c$. The amplitude of AC voltage applied along c was 100 V. The result is shown in Fig. 4.6. As seen in Fig. 4.6, the T dependence for $+k_c$ (red) is almost completely reversed from that for $-k_c$. We also confirmed that $\Delta\alpha$ is proportional to the applied magnetic field (Fig. 4.7). The T dependence of $\Delta\alpha$ at 0.886 eV is well matched with that of the magnetic susceptibility along the c axis, taking a cusp around T_N = 22.5 K [21]. The inverse *E*-MChD ($1/\Delta\alpha$) is nearly linear to T above T_N (see the inset of Fig. 4.6), which indicates that *E*-MChD reflects the magnetic susceptibility showing a linear $1/T$ dependence in the paramagnetic phase.

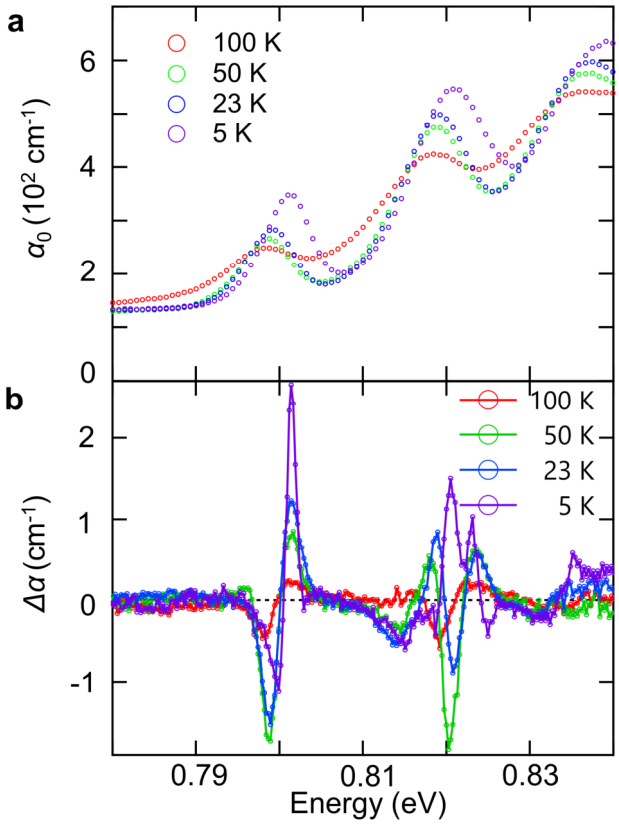

Fig. 4.5 Temperature dependence of absorption spectra (**a**) and *E*-MChD spectra (**b**) [19]. The data obtained at 100 K, 50 K, 23 K and 5 K are shown in red, green, blue and purple colors, respectively. $\Delta\alpha$ in panel (**b**) corresponds to the magnitude of *E*-MChD under the 100 V voltage and 9 T magnetic field in the geometry of the $+k_c$ setting.

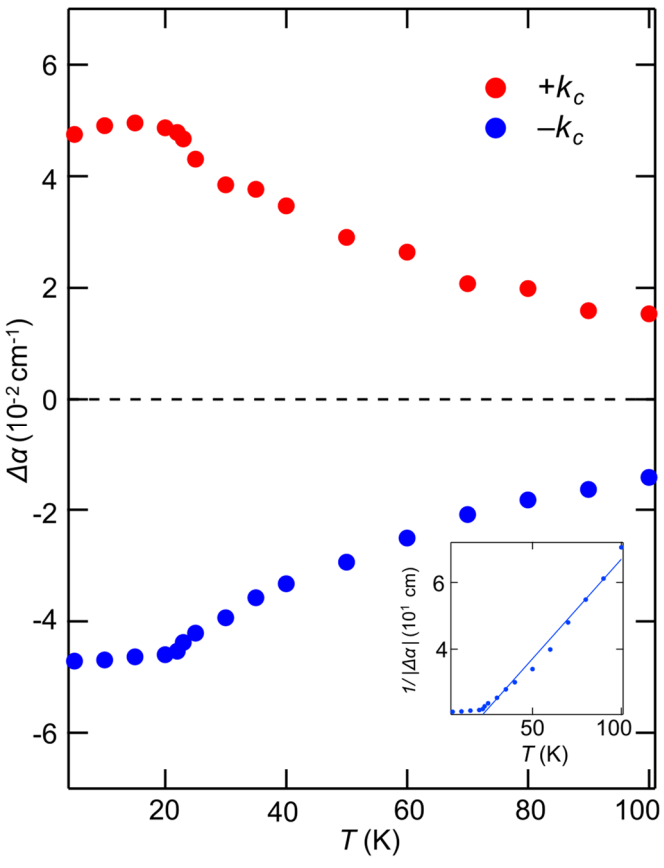

Fig. 4.6 Temperature (T) dependence of *E*-MChD at 0.886 eV obtained by the lock-in measurement [19]. The red and blue dots correspond to the results in the geometry of the $+k_c$ and $-k_c$ settings, respectively. Here, $\Delta\alpha$ corresponds to the magnitude of *E*-MChD under the 100 V voltage and 9 T magnetic field. The inset shows the T dependence of inverse $\Delta\alpha$ calculated using the absolute values of $\Delta\alpha$ obtained in the $-k_c$ setting.

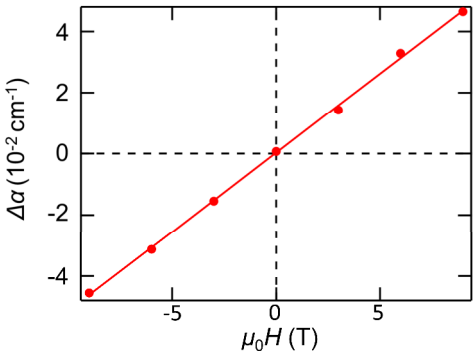

Fig. 4.7 Magnetic field dependence of *E*-MChD obtained by the lock-in measurement at 0.886 eV [19]. Here, $\Delta\alpha$ corresponds to the magnitude of *E*-MChD under the 100 V voltage and the selected magnitude of magnetic field in the geometry of the $+k_c$ setting.

4.3.3 Discussion: Microscopic origin of *E*-MChD

Here, we discuss the mechanism of *E*-MChD observed in ferroaxial $NiTiO_3$. For that, we first introduce the microscopic origin of MChD [2,13]. There are two types of transition processes which contribute to MChD, electric dipole (ED) – magnetic dipole (MD) and ED – electric quadrupole (EQ). For the concerned ${}^3A_{2g} \rightarrow {}^3T_{2g}$ transition in Ni^{2+}, MD transition gives a predominant contribution [23,24]. Thus, here, we only consider the ED-MD process. The ED-MD process is further divided into the three terms, named as A, B and C terms. Among them, only the C term, which originates from the splitting of the ground states due to the Zeeman effect, is the T dependent term described as

$$\Delta\alpha_{\mathrm{MChD}} \propto H_z \omega_{jn} g(\omega) \frac{C(G)}{kT}. \tag{4.5}$$

Here, we assume directions of a magnetic field and light propagation in the z axis. $\hbar\omega_{jn}$ is the energy difference between the ground state n and the excited state j. $g(\omega)$ represents the frequency dependence of $\Delta\alpha_{\mathrm{MChD}}$ and is described as

$$g(\omega) = \frac{\omega\Gamma_j}{\left(\omega_{jn}^2 - \omega^2\right)^2 + \omega^2\Gamma_j^2}, \tag{4.6}$$

where Γ_j is a damping factor. $g(\omega)$ shows an absorptive structure, i.e., takes a single peak at the resonance frequency ω_{jn}. $C(G)$ represents the contributions from the ED-MD process as

$$C(G) = \epsilon_{\alpha\beta\gamma} \frac{1}{d_n} \sum_n < n|m_\gamma|n > \mathrm{Re}\left(< n|\mu_\alpha|j >< j|m_\beta|n >\right), \tag{4.7}$$

where α, β, and γ denote the coordinate axes, $\epsilon_{\alpha\beta\gamma}$ is the Levi-Civita symbol, d_n is the degeneracy of the ground state n, μ_α is the electric dipole moment, and m_β and m_γ are the magnetic dipole moments. Since the observed *E*-MChD signal shows the linear $1/T$ dependence (inset of Fig. 4.6) as the C term does [equation (4.5)], we will consider this C term in the following discussion.

Now we are ready to discuss the mechanism of *E*-MChD in $NiTiO_3$. The key factors are the two Ni^{2+} sites (Site 1 and Site 2, see the crystal structure in right top of Fig. 4.8**a**) related by the space inversion operation and the pseudo-Stark splitting induced by an applied electric field. Figure 4.8**a**

shows the energy diagram of Ni^{2+} in $NiTiO_3$. The $^3A_{2g}$ and $^3T_{2g}$ states in the cubic (O_h) field are further split by the trigonal (C_3) distortion and the spin orbit interaction (S.O.) [25]. We assume that the absorption peak observed at 0.80 eV corresponds to the lowest energy excitation to this split level and focus on this excitation. Note that both ED and MD transitions are allowed between the ground and excited E states. Under an applied magnetic field, both the ground and excited states are further split due to the Zeeman effect. Under this consideration, since the local symmetry of Ni^{2+} is chiral C_3, MChD is locally induced at each Ni^{2+} site. However, the contributions to MChD from Site 1 ($\Delta\alpha^{(1)}_{\mathrm{MChD}}$) and Site 2 ($\Delta\alpha^{(2)}_{\mathrm{MChD}}$) are in the same magnitude but opposite in sign, i.e., $\Delta\alpha^{(1)}_{\mathrm{MChD}} = -\Delta\alpha^{(2)}_{\mathrm{MChD}}$. This is because the sign of the electric dipole moment $< n|\mu_\alpha|j >$ is opposite between the two. Thus, MChD is canceled out as a unit cell. Under an electric field, however, each level is shifted, and the excitation energy is slightly modified in proportion to an applied electric field. The sign of this energy shift ($\Delta_E \propto E$) is opposite for Site 1 and Site 2 of Ni^{2+} ions (pseudo-Stark effect [26,27]). Thus, the contributions from them are not canceled out and $\Delta\alpha_{\mathrm{EMChD}}$ is described as

$$\Delta\alpha_{\mathrm{EMChD}} \propto H_z\omega_{jn}\frac{C(G)}{kT}\{g_{(1)}(\omega) - g_{(2)}(\omega)\}, \tag{4.8}$$

where

$$g_{(1)}(\omega) - g_{(2)}(\omega) = \frac{\omega\Gamma_j}{\left(\left(\omega_{jn}+\Delta_E\right)^2 - \omega^2\right)^2 + \omega^2\Gamma_j^2} - \frac{\omega\Gamma_j}{\left(\left(\omega_{jn}-\Delta_E\right)^2 - \omega^2\right)^2 + \omega^2\Gamma_j^2}. \tag{4.9}$$

By assuming that Δ_E is small enough and $(\Delta_E)^2 \approx 0$, equation (4.9) is rewritten as

$$g_{(1)}(\omega) - g_{(2)}(\omega) \approx \frac{8\omega\omega_{jn}\Gamma_j\left(\omega_{jn}^2 - \omega^2\right)\Delta_E}{\left(\omega_{jn}^4 + \omega^4 - 2\omega^2\omega_{jn}^2 + \omega^2\Gamma_j^2\right)^2}, \tag{4.10}$$

and $g_{(1)}(\omega) - g_{(2)}(\omega)$ shows a dispersive structure, i.e., takes two peaks with opposite sign around the resonance frequency ω_{jn}. Also, $\Delta\alpha_{\mathrm{EMChD}}$ is proportional to an applied electric field. We fit the obtained E-MChD spectrum around 0.80 eV ($+k_c$, V_c = 100 V, and $\mu_0 H_c$ = 9 T, a part of red dots in Fig. 4.4**a**). The result is shown in Fig. 4.8**b**. The fitting yields $\omega_{jn} = 0.8011$ eV, $\Gamma_j = 0.0036$ eV, and $\Delta_E = 7.4 \times 10^{-6}$ eV. The obtained parameters of ω_{jn} and Γ_j are well matched with those observed in the absorption spectrum (see Fig. 4.3**a**). About the pseudo-Stark splitting Δ_E at 3.1×10^4 V cm^{-1}, it is also consistent with that of the R1 line of ruby, whose crystal structure is corundum-type and similar to ilmenite $NiTiO_3$, 1.2×10^{-4} eV at 1.7×10^5 V cm^{-1} [26]. This model based on the pseudo-Stark splitting well explains the peak structure at 0.80 eV. However, it is difficult to fully explain the complicated peak structures around 0.82 eV. Some of the fine peak structures around the $^3A_{2g} \rightarrow {}^3T_{2g}$ transition are sometimes explained as phonon sidebands [24,28,29], and they may be related to the peak structures.

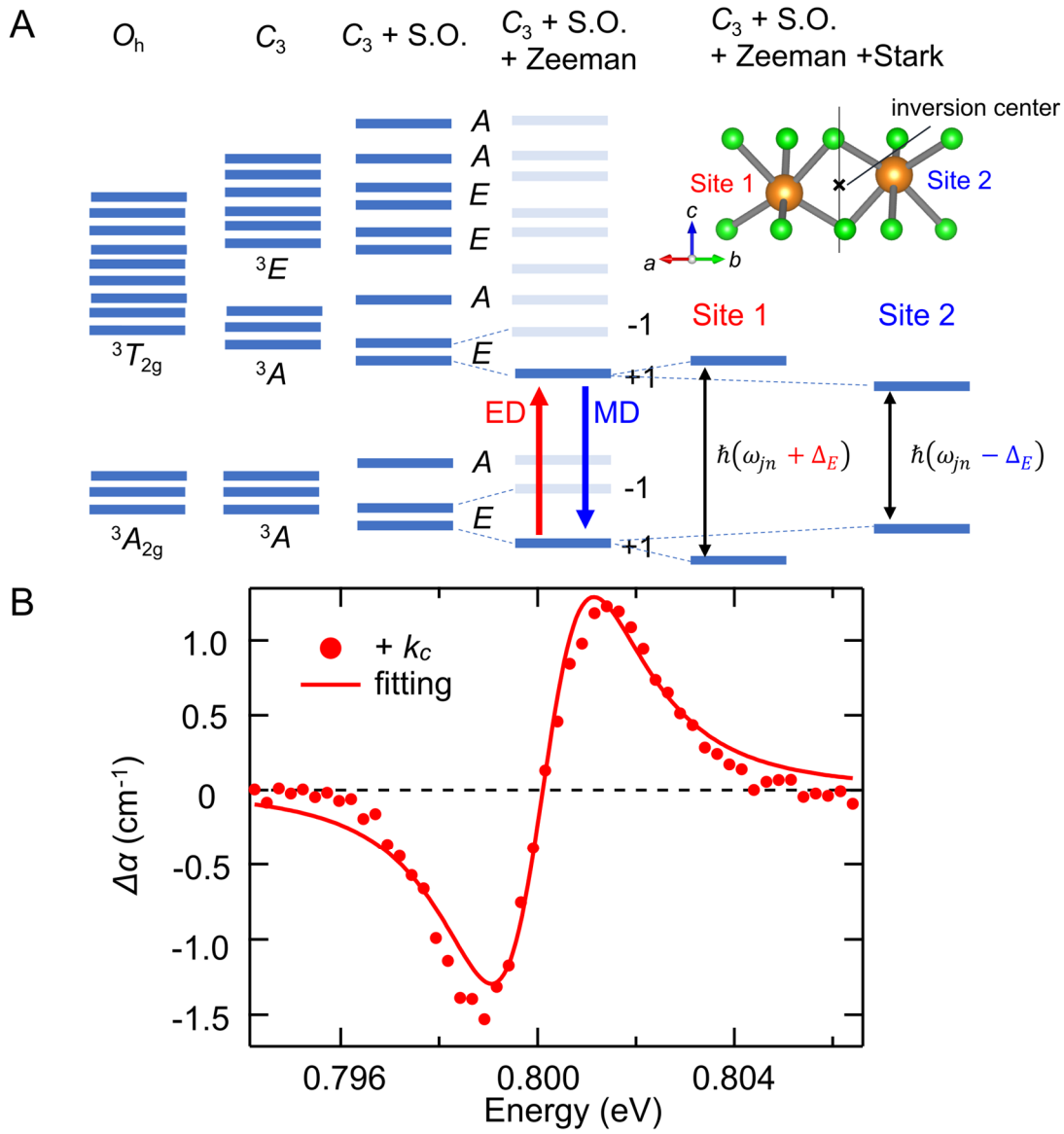

Fig. 4.8 The energy diagram of Ni^{2+} in $NiTiO_3$ (**a**) and the fitting of *E*-MChD spectrum (**b**) [19]. The energy diagram of panel (**a**) shows splitting of the ground $^3A_{2g}$ and excited $^3T_{2g}$ states (first column) due to the trigonal field (C_3, second column), spin-orbit interaction (S.O., third column), the Zeeman effect (fourth column), and the Stark effect (fifth column for Site 1 and sixth line for Site 2). "+1" and "–1" in the fourth column depict the total spin angular momentum of each state. The electric dipole (ED) – magnetic dipole (MD) transition process contributes to MChD. In the fourth column, the states other than those related to the considered transition are depicted in a pale color. The crystal structure in the right top of panel (**a**) shows Site 1 and Site 2 of Ni^{2+} related to each other via the inversion operation. The sign of the Stark effect (Δ_E) at Site 1 is opposite to that at Site 2, which contributes to the emergence of *E*-MChD. Panel (**b**) shows the fitting result of *E*-MChD spectrum with equation (4.8) in the main text in the photon energy range of 0.794 eV < E_{ph} < 0.807 eV. The fitted spectrum corresponds to a part of the red dots in Fig. 4.4**a**.

4.3.4 Discussion: Magnitude of *E*-MChD

Finally, let us mention the magnitude of *E*-MChD of $NiTiO_3$. When considering the normalized

magnitude of *E*-MChD, i.e., $\Delta\alpha_{EMChD}/\alpha_0$, the largest value of $\Delta\alpha_{EMChD}/\alpha_0 \approx 0.06$ % per 1 T was obtained under $E_c = 3.1\times10^4$ V cm^{-1} around 0.80 eV at 23 K. It is comparable to MChD in Ni_3TeO_6 ($\Delta\alpha_{EMChD}/\alpha_0$ ≈ 0.16 % per 1 T around 0.8 eV at 4 K) [29]. Ni_3TeO_6 is a chiral corundum-like antiferromagnet (space group *R*3) with Ni^{2+} located in a trigonally distorted oxygen octahedron as $NiTiO_3$. Thus, it can be said that *E*-MChD signals of ferroaxial $NiTiO_3$ under $E_c = 3.1\times10^4$ V cm^{-1} are comparable to MChD signals in a similar chiral material. It will be interesting for future work to compare the applied electric field with the internal crystal electric field in Ni_3TeO_6.

4.4 Summary

In conclusion, we successfully observed *E*-MChD in a ferroaxial antiferromagnet $NiTiO_3$. The obtained spectrum can be effectively explained by combining the established theory of MChD and the pseudo-Stark effect. In *E*-MChD of ferroaxial materials, the transmittance of light can be controlled by changing an electric field under a fixed magnetic field. This could potentially lead to the development of new energy-saving optical devices in ferromagnetic ferroaxial materials, where transmittance can be controlled through the application of an electric field alone. It is also worth noting that magneto-chiral effects are not limited to nonreciprocal light propagation but also extended to the nonreciprocal propagation of electrons, magnons, and phonons [11,14]. Thus, research developments toward such directions can also be expected for electric-field-induced magneto-chiral effects in ferroaxial materials. Currently, the research on ferroaxial order has primally focused on inorganic compounds. However, as chirality-related phenomena have been widely studied in both organic and inorganic compounds, our discovery on *E*-MChD in $NiTiO_3$ will also stimulate research on ferroaxial-related properties in organic crystals or molecules.

References

[1] G. Wagnière and A. Meier, *The Influence of a Static Magnetic Field on the Absorption Coefficient of a Chiral Molecule*, Chem. Phys. Lett. **93**, 78 (1982).

[2] L. D. Barron and J. Vrbancich, *Magneto-Chiral Birefringence and Dichroism*, Mol. Phys. **51**, 715 (1984).

[3] G. L. J. A. Rikken and E. Raupach, *Observation of Magneto-Chiral Dichroism*, Nature **390**, 493 (1997).

[4] G. L. J. A. Rikken and E. Raupach, *Enantioselective Magnetochiral Photochemistry*, Nature **405**, 932 (2000).

[5] M. Saito, K. Taniguchi, and T. H. Arima, *Gigantic Optical Magnetoelectric Effect in CuB_2O_4*, J. Phys. Soc. Jpn. **77**, 013705 (2008).

[6] C. Train, R. Gheorghe, V. Krstic, L. M. Chamoreau, N. S. Ovanesyan, G. L. J. A. Rikken, M. Gruselle, and M. Verdaguer, *Strong Magneto-Chiral Dichroism in Enantiopure Chiral Ferromagnets*, Nat. Mater. **7**, 729 (2008).

[7] Y. Kitagawa, H. Segawa, and K. Ishii, *Magneto-Chiral Dichroism of Organic Compounds*, Angew. Chem. Int. Ed Engl. **50**, 9133 (2011).

[8] S. Eslami, J. G. Gibbs, Y. Rechkemmer, J. van Slageren, M. Alarcón-Correa, T.-C. Lee, A. G. Mark, G. L. J. A. Rikken, and P. Fischer, *Chiral Nanomagnets*, ACS Photonics **1**, 1231 (2014).

[9] K. Ishii, S. Hattori, and Y. Kitagawa, *Recent Advances in Studies on the Magneto-Chiral Dichroism of Organic Compounds*, Photochem. and Photobiol. Sci. **19**, 8 (2020).

[10] M. Atzori, G. L. J. A. Rikken, and C. Train, *Magneto-Chiral Dichroism: A Playground for Molecular Chemists*, Chem. Eur. J. **26**, 9784 (2020).

[11] M. Atzori, C. Train, E. A. Hillard, N. Avarvari, and G. L. J. A. Rikken, *Magneto-Chiral Anisotropy: From Fundamentals to Perspectives*, Chirality **33**, 844 (2021).

[12] G. Wagni and A. Meier, *Difference in the Absorption Coefficient of Enantiomers for Arbitrarily Polarized Light in a Magnetic Field: A Possible Source of Chirality in Molecular Evolution*, Experientia **39**, 1090 (1983).

[13] M. Atzori et al., *Validation of Microscopic Magnetochiral Dichroism Theory*, Sci Adv **7**, eabg28 (2021).

[14] Y. Tokura and N. Nagaosa, *Nonreciprocal Responses from Non-Centrosymmetric Quantum Materials*, Nat. Commun. **9**, 3740 (2018).

[15] G. L. J. A. Rikken, C. Strohm, and P. Wyder, *Observation of Magnetoelectric Directional Anisotropy*, Phys. Rev. Lett. **89**, 133005 (2002).

[16] J. H. Jung, M. Matsubara, T. Arima, J. P. He, Y. Kaneko, and Y. Tokura, *Optical Magnetoelectric Effect in the Polar $GaFeO_3$ Ferrimagnet*, Phys. Rev. Lett. **93**, 037403 (2004).

[17] T. Kurumaji, Y. Takahashi, J. Fujioka, R. Masuda, H. Shishikura, S. Ishiwata, and Y. Tokura, *Optical Magnetoelectric Resonance in a Polar Magnet $(Fe,Zn)_2Mo_3O_8$ with Axion-Type Coupling*, Phys. Rev. Lett. **119**, 077206 (2017).

[18] M. Ogino, Y. Kaneko, Y. Tokura, and Y. Takahashi, *Gyrotropic Birefringence via Electromagnon Resonance in a Multiferroic of Spin Origin*, Phys. Rev. Research **2**, 023345 (2020).

[19] T. Hayashida, K. Kimura, and T. Kimura, *Electric Field-Induced Magnetochiral Dichroism in a Ferroaxial Crystal*, Proc. Natl. Acad. Sci. *in press*.

[20] G. S. Heller, J. J. Stickler, S. Kern, and A. Wold, *Antiferromagnetism in $NiTiO_3$*, J. Appl. Phys. **34**, 1033 (1963).

[21] K. Dey, S. Sauerland, J. Werner, Y. Skourski, M. Abdel-Hafiez, R. Bag, S. Singh, and R. Klingeler,

References

Magnetic Phase Diagram and Magnetoelastic Coupling of $NiTiO_3$, Phys. Rev. B **101**, 195122 (2020).

[22] G. R. Rossman, R. D. Shannon, and R. K. Waring, *Origin of the Yellow Color of Complex Nickel Oxides*, J. Solid State Chem. **39**, 277 (1981).

[23] J. Ferguson, H. J. Guggenheim, L. F. Johnson, and H. Kamimura, *Magnetic Dipole Character of the $^3A_{2g} \leftrightarrow {}^3T_{2g}$ Transition in Octahedral Nickel (II) Compounds*, J. Chem. Phys. **38**, 2579 (1963).

[24] M. Kozielski, I. Pollini, and G. Spinolo, *Electronic Absorption Spectra of Ni^{2+} in $NiCl_2$ and $NiBr_2$ (Phonon and Magnon Sidebands)*, J. Phys. C: Solid State Phys. **5**, 1253 (1972).

[25] Z.-Y. Yang, C. Rudowicz, and Y.-Y. Yeung, *Microscopic Spin-Hamiltonian Parameters and Crystal Field Energy Levels for the Low C3 Symmetry Ni^{2+} Centre in $LiNbO_3$ Crystals*, Physica B Condens. Matter **348**, 151 (2004).

[26] W. Kaiser, S. Sugano, and D. L. Wood, *Splitting of the Emission Lines of Ruby by an External Electric Field*, Phys. Rev. Lett. **6**, 605 (1961).

[27] B. B. Krichevtsov, V. V. Pavlov, and R. V. Pisarev, *Nonreciprocal Optical Effects in Antiferromagnetic Cr_2O_3 Subjected to Electric and Magnetic Fields*, Zh. Eksp. Teor. Fiz **94**, 284 (1988).

[28] J. Tylicki, W. M. Yen, J. P. van der Ziel, and H. J. Guggenheim, *Magnetic Effects on the Optical Absorption Spectrum of $RbNiF_3$*, Phys. Rev. **187**, 758 (1969).

[29] M. O. Yokosuk et al., *Nonreciprocal Directional Dichroism of a Chiral Magnet in the Visible Range*, npj Quantum Mater. **5**, 20 (2020).

Chapter 5

Observation of nonreciprocal optical effects in a ferromonopolar antiferromagnet Cr_2O_3

5.1 Introduction

Cr_2O_3 is the archetypal magnetoelectric (ME) antiferromagnet, wherein the linear ME effect was predicted and observed for the first time [1,2]. The magnetic ordering in Cr_2O_3 is commonly referred to as antiferromagnetic (AFM) ordering or AFM ordering which breaks space inversion and time reversal symmetries. However, based on the recently developed theory of cluster multipoles [3–10] and the classification of ferroic orders discussed in Chapter 1, the magnetic order of Cr_2O_3 can be more specifically classified as 'ferromonopolar order'. Such a detailed classification rather than a broad categorization as antiferromagnetic ordering enables a clear understanding of the characteristics associated with the order. In this section, we first give a brief introduction to cluster multipoles and discuss the ME effect and optical effects in Cr_2O_3.

5.1.1 Cluster multipoles

The microscopic electronic degrees of freedom are well described by the electronic multipoles. There are four types of multipoles and their operators in many-electron systems are described as [9,11,12]

$$\hat{Q}_{lm} = -e\sum_j \sqrt{\frac{4\pi}{2l+1}} r^l Y_{lm}^*(\hat{\mathbf{r}}_j), \tag{5.1}$$

$$\hat{M}_{lm} = -\mu_B \sum_j \mathbf{m}_l(\mathbf{r}_j)\cdot\nabla_j \sqrt{\frac{4\pi}{2l+1}} r^l Y_{lm}^*(\hat{\mathbf{r}}_j), \tag{5.2}$$

$$\hat{T}_{lm} = -\mu_B \sum_j \mathbf{t}_l(\mathbf{r}_j)\cdot\nabla_j \sqrt{\frac{4\pi}{2l+1}} r^l Y_{lm}^*(\hat{\mathbf{r}}_j), \tag{5.3}$$

$$\hat{G}_{lm} = -e\sum_j \sum_{\alpha\beta}^{x,y,z} g_l^{\alpha\beta}(\mathbf{r}_j)\nabla_\alpha\nabla_\beta \sqrt{\frac{4\pi}{2l+1}} r^l Y_{lm}^*(\hat{\mathbf{r}}_j), \tag{5.4}$$

where $\hat{Q}_{lm}$, $\hat{M}_{lm}$, $\hat{T}_{lm}$, and $\hat{G}_{lm}$ are electric (E), magnetic (M), magnetic toroidal (MT), and electric toroidal (ET) moments, respectively. Here, $\mathbf{r}_j$ is a position vector of the *j*th electron, *e* is electron charge, and μ_B is Bohr magneton. *l* and *m* are the azimuthal and magnetic quantum numbers, respectively.

$Y_{lm}(\hat{\mathbf{r}}_j)$ is the spherical harmonic as a function of $\hat{\mathbf{r}} = \mathbf{r}/|\mathbf{r}|$. The azimuthal quantum number l corresponds to the rank of multipoles, i.e., monopole (l = 0), dipole (l = 1), quadrupole (l = 2), and octupole (l = 3). $\mathbf{m}_l(\mathbf{r}_j)$, $\mathbf{t}_l(\mathbf{r}_j)$, and $g_l^{\alpha\beta}(\mathbf{r}_j)$ describe magnetic moment, magnetic toroidal moment, and electric toroidal tensor, respectively and expressed as

$$\mathbf{m}_l(\mathbf{r}_j) = \frac{2\boldsymbol{l}_j}{l+1} + \boldsymbol{\sigma}_j, \tag{5.5}$$

$$\mathbf{t}_l(\mathbf{r}_j) = \frac{2\boldsymbol{r}_j}{l+1}\left(\frac{2\boldsymbol{l}_j}{l+1} + \boldsymbol{\sigma}_j\right), \tag{5.6}$$

$$g_l^{\alpha\beta}(\mathbf{r}_j) = m_l^{\alpha}(\mathbf{r}_j)t_l^{\beta}(\mathbf{r}_j), \tag{5.7}$$

where $\boldsymbol{l}_j$ and $\boldsymbol{\sigma}_j/2$ are the orbital and spin angular momentum operators, respectively. Figure 5.1 summarizes the four types of multipoles with their parities respect to space-inversion and time-reversal operations.

type	symbol	spatial inversion	time reversal	monopole	dipole	quadrupole	octupole
E	Q_{lm}	$(-1)^l$ polar	+	$(+,+)$	E / ET		
M	M_{lm}	$(-1)^{l+1}$ axial	−	$(-,-)$	M / MT		
MT	T_{lm}	$(-1)^l$ polar	−	$(+,-)$	MT / M		
ET	G_{lm}	$(-1)^{l+1}$ axial	+	$(-,+)$	ET / E		

Fig. 5.1 Four types of multipoles. Used with permission of IOP Publishing, Ltd, from ref. [10]; permission conveyed through Copyright Clearance Center, Inc. Copyright 2022 by IOP Publishing, Ltd. E: electric, M: magnetic, MT: magnetic toroidal, ET: electric toroidal. In column 3 and 4, parities of the multipoles respect to spatial-inversion and time-reversal operations are listed. Here, + and – correspond to even and odd parity, respectively.

The multipole operators in equations (5.1)-(5.4) are defined on a single atom and well describe electronic degrees of freedom in strongly-correlated *f*-electron systems [10,13–15]. Meanwhile, these multipoles are applied to describe the symmetry defined with multiple atoms in a unit cell, which is so called (site-)cluster multipoles [3,6–10]. For example, assuming a *N*-site magnetic structures, M cluster multipoles are expressed by replacing the position vector of electron $\mathbf{r}_j$ with the position vector of the *j*th atom $\mathbf{R}_j$ as [9]

$$\widehat{M}^{(c)}{}_{lm} = \sum_{j=1}^{N} \boldsymbol{\sigma}_j \cdot \nabla_j \sqrt{\frac{4\pi}{2l+1}} r^l Y^*_{lm}(\mathbf{R}_j) \ , \tag{5.8}$$

where the superscript (c) denotes 'cluster' multipoles. In ref. [9], all 122 magnetic point groups are classified by the cluster multipoles, and in ref. [7], magnetic species are classified based on what types of multipoles are activated on the symmetry reduction. Following the definition of ferroic order discussed in Chapter 1, if a phase transition is characterized by a multipole X, such an order can be referred to as ferro-X order, as represented by the ferrotoroidic order. We note that the MT (ET) dipole moment has the symmetry of time-odd polar vector $\mathcal{P}'$ (time-even axial vector $\mathcal{A}$) introduced in Chapter 1. It is also noteworthy that the ET monopole is closely related to chirality and ferrochiral order discussed in Chapter 2 [16,17].

Among the different types of multipoles, M monopole, MT dipole, and M quadrupole, where P and T symmetries are simultaneously broken, are related to the ME effect and nonreciprocal optical effects on which are our focus lies in this chapter. Figure 5.2 schematically illustrates these three types of cluster multipoles. The magnetic monopole and quadrupole depicted in Fig. 5.2 have the symmetry of time-odd chiral bidirector (false-chiral) $\mathcal{C}'$ (see 1.3.1), where $\mathcal{C}'$ is perpendicular to the spin plane.

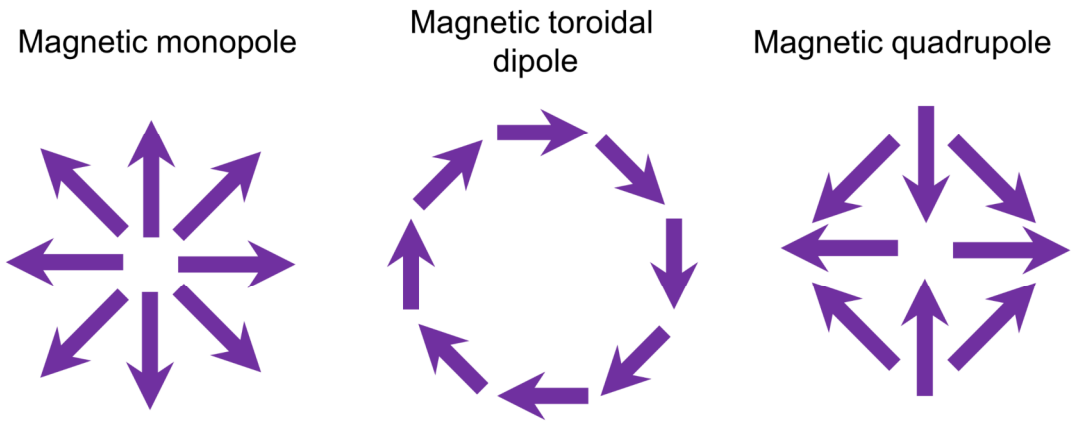

Fig. 5.2 Cluster multipoles which breaks *P* and *T* symmetries. The purple arrow represents a magnetic moment defined on a single atom site.

By adopting the linear response theory with the concept of multipoles, one can decompose the liner ME tensor α_{ij} into contributions from the M monopole, MT dipole, and M quadrupole [3,8,18]. The tensor α_{ij} describes the liner ME effect as $P_i = \alpha_{ij}H_j$ ($\mu_0 M_i = \alpha_{ij}E_j$), where P_i, H_j, M_i, E_j, and μ_0 are polarization, a magnetic field, magnetization, an electric field, and permeability of vacuum, respectively. The components of α_{ij} are expressed as [8]

$$\alpha_{ij} = \begin{pmatrix} \mathrm{M}_0 - \mathrm{M}_u + \mathrm{M}_v & \mathrm{M}_{xy} + \mathrm{T}_z & \mathrm{M}_{xz} - \mathrm{T}_y \\ \mathrm{M}_{xy} - \mathrm{T}_z & \mathrm{M}_0 - \mathrm{M}_u - \mathrm{M}_v & \mathrm{M}_{yz} - \mathrm{T}_x \\ \mathrm{M}_{xz} + \mathrm{T}_y & \mathrm{M}_{yz} - \mathrm{T}_x & \mathrm{M}_0 + 2\mathrm{M}_u \end{pmatrix}, \tag{5.9}$$

where $\mathrm{M}_0 = (\mathrm{M}_{xx} + \mathrm{M}_{yy} + \mathrm{M}_{zz})$, $\mathrm{M}_u = (2\mathrm{M}_{zz} - \mathrm{M}_{xx} - \mathrm{M}_{yy})/6$, and $\mathrm{M}_v = (\mathrm{M}_{xx} - \mathrm{M}_{yy})/2$. M_0 describes the

isotropic longitudinal response from the M monopole, while M_u, M_v, and M_{ij} ($i \neq j$) are the anisotropic symmetric response from the M quadrupole. T_i represents the anti-symmetric component from the MT dipole.

5.1.2 Magnetic structure and the liner ME effect of Cr_2O_3

The crystal structure of Cr_2O_3 is described by the corundum structure (space group $R\bar{3}c$). At temperatures below $T_N \approx 307$ K [19,20], it shows an AFM ordering, and the magnetic symmetry in the AFM phase is $\bar{3}'m'$. This magnetic transition $\bar{3}m1' \rightarrow \bar{3}'m'$ is characterized by the ordering of magnetic monopole and magnetic quadrupole moment [7,9]. Thus, the magnetic order of Cr_2O_3 can be termed as, for example, ferro-monopolar-quadrupolar or ferro-false-chiral order. In the following, for simplification, we term it ferromonopolar order. The ferromonopolar order of Cr_2O_3 allows the diagonal ME effects with nonzero ME tensor components of $\alpha_{11} = \alpha_{22}$ and α_{33} [21–23]. Figure 5.3 shows the temperature dependence of the ME tensors of $\alpha_\perp = \alpha_{11} = \alpha_{22}$ and $\alpha_\parallel = \alpha_{33}$ [21].

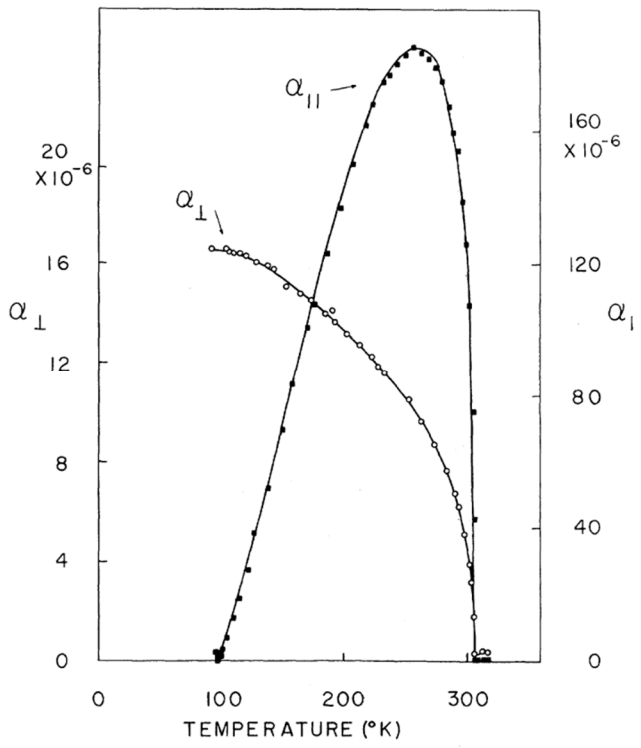

Fig. 5.3 Temperature dependence of the ME tensor of Cr_2O_3. Reprinted with permission from ref. [21]. Copyright 1961 by the American Physical Society. The $\alpha_\perp$ and $\alpha_\parallel$ are dimensionless in the Gaussian units.

In the ferromonopolar AFM phase, a pair of domain states (L+ and L–), which is related by either time reversal or space inversion, develops (see Fig. 5.4). So far, such domain structures have been visualized by using second-harmonic generation (SHG) [24], magnetoelectric force microscopy [25], x-ray magnetic circular dichroism [26,27], and nanoscale scanning diamond magnetometry [28–30]. As an example, Fig. 5.5 shows the domain images obtained by SHG.

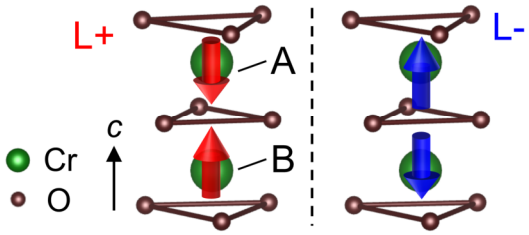

Fig. 5.4 Antiferromagnetic domain states of Cr_2O_3 [31]. The red and blue arrows represent Cr spins. Here, the two Cr sites denoted as A and B, which characterize the two domain states of L+ and L-, are depicted.

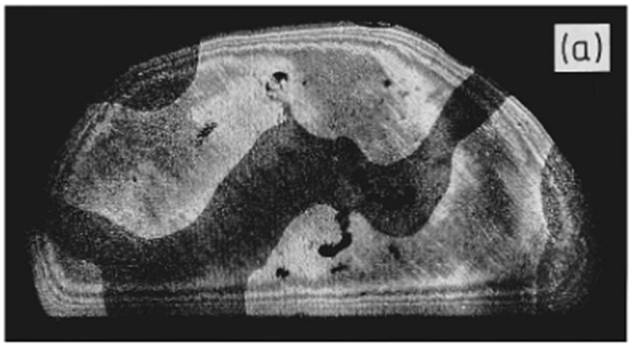

Fig. 5.5 Antiferromagnetic domain images of Cr_2O_3 obtained by SHG [24]. Reprinted from ref. [24], with the permission of AIP publishing. Sample size is 6×3 mm^2, and thickness is 70 μm. Right-circularly polarized light is used as incident light.

5.1.3 Nonreciprocal optical effects in Cr_2O_3

The ferromonopolar order of Cr_2O_3 allows for the diagonal ME effects, and such diagonal ME tensor components give rise to characteristic nonreciprocal optical effects. In the following, we introduce the three types of nonreciprocal optical effects: the electric-field-induced (*E*-induced) Faraday, the electric-field-induced magnetic circular dichroism (*E*-induced MCD), and the spontaneous nonreciprocal rotation of reflected light (NRR).

***E*-induced Faraday and *E*-induced MCD**

The *E*-induced Faraday refers to the polarization rotation of transmitted light induced by applying an electric field. Though there exist linear and quadratic *E*-induced Faraday effects [32], we refer to the former one as *E*-induced Faraday effect in this chapter. ME materials with the diagonal components of α_{ij} (diagonal ME materials) exhibit the *E*-induced Faraday effect when an electric field is applied (anti)parallel to light propagation direction. This effect is intuitively understood considering that a magnetization is induced in the same direction with an applied electric field due to the linear ME effect. However, an antiferromagnetic order parameter also contributes to this effect as discussed in the followings. In addition, akin to the magnetic circular dichroism, which is a counterpart of the Faraday effect related by the Kramers-Kronig relation, diagonal ME materials will also exhibit the electric field induced magnetic circular dichroism (*E*-induced MCD).

Experimentally, to avoid the contribution of birefringence, it is convenient to adopt an experimental setting where both **E** and **k** are oriented along the hexagonal *c* axis. Thus, the *E*-induced effects in this setting (**E** || **k** || *c*) are discussed below.

The *E*-induced Faraday effect is described by the polarization rotation ϕ [deg] induced in

proportion to an applied electric field as

$$\phi = \beta \times E_c \times d = \beta V_c, \tag{5.10}$$

where β [deg V^{-1}] is the coefficient representing the magnitude of the *E*-induced Faraday effect, E_c [V cm^{-1}] = V_c [V] / d [cm] is an applied electric field along the *c* axis, V_c [V] is an applied voltage, and d [cm] is a sample thickness. In a similar manner, the *E*-induced MCD is defined as a difference in an absorption coefficient for right (α_R) and left (α_L) circularly polarized light ($\alpha_{MCD} = \alpha_R - \alpha_L$ [cm^{-1}]) induced in proportion to an applied electric field and described as

$$\alpha_{MCD} = (\alpha_0 - \beta' E_c) - (\alpha_0 + \beta' E_c) = -2\beta' E_c, \tag{5.11}$$

where β' [V^{-1}] is the coefficient representing the magnitude of *E*-induced MCD and α_0 is an absorption coefficient for right and left circularly polarized light in zero electric field. So far, the *E*-induced Faraday effect has been measured at some wavelengths in the near-infrared region and at 632.8 nm (e.g., $\beta \approx 10^{-5} \sim 10^{-6}$ deg V^{-1}) [32–36], but a comprehensive spectrum has yet to be provided. To our best knowledge, *E*-induced MCD has never been observed in Cr_2O_3 or in any other materials.

The *E*-induced Faraday effect (and the associated *E*-induced MCD) in Cr_2O_3 consists of two principal contributions [34,35]. The first is the term proportional to the ME coefficient α_{33}, while the second is the term proportional to the AFM order parameter *l*. Here, *l* is defined as the difference of the magnetic moments at site A and site B with opposite spins (see Fig. 5.4 for a schematic illustration of the magnetic structure), i.e., $l = m_A - m_B$ [34,35]. Upon application of an electric field, not only net magnetization $\alpha_{33}E_c$ is induced but also the Cr^{3+} ions at site A and B show slight displacement along the *c* axis in opposing directions. This displacement makes the crystal-field around the Cr^{3+} ions at site A and site B distinct from each other, consequently leading to the *E*-induced Faraday effect and related *E*-induced MCD proportional to *l*. In short, the coefficients β and β' are described as

$$\beta = p\alpha_{33} + ql \tag{5.12}$$

$$\beta' = p'\alpha_{33} + q'l \tag{5.13}$$

where p (p') and q (q') are the contribution coefficients from α_{33} and *l* to the *E*-induced Faraday effect (*E*-induced MCD), respectively. The contribution ratio of p/q depends on the frequency of incident light, and such frequency dependence was discussed based on the *T* dependence of β in ref. [35]. We will discuss the microscopical origins of β and β' in 5.3.2. Importantly, because the signs of α_{33} and *l* get reversed when the domain states (L+ and L-) are flipped, the signs of β and β' depend on the domain states. Thus, the domain states of Cr_2O_3 can be distinguished by using these effects.

NRR

NRR refers to the rotation of the polarization plane of light upon reflection from a sample surface, which is similar to the well-known magneto-optical Kerr (MOKE) effect. By using the symmetry similarity of vectorlike properties discussed in Chapter 1, one can find a similarity between NRR and MOKE. As mentioned above, the magnetic structure of Cr_2O_3 is characterized by the time-odd chiral bidirector ($\mathcal{C}$), where $\mathcal{C}$ can be defined parallel or perpendicular to the *c* axis. Here, we assume that light propagates along the *c* axis (**k** ∥ *c*) and consider $\mathcal{C}$ to be parallel to the *c* axis. Then, the discontinuity on the sample

surface breaks the space inversion symmetry, allowing one to define a normal vector to the sample surface. This normal vector exhibits the time-even polar vector symmetry ($\mathcal{P}$). The coupling of the bulk symmetry $\mathcal{C}$ and the surface symmetry $\mathcal{P}$ results in the emergence of time-odd axial vector ($\mathcal{C} \cdot \mathcal{P} \approx \mathcal{A}'$), which is equivalent to magnetization, inducing a MOKE like effect (see Table 1.1 in 1.3.4). Importantly, the directions of $\mathcal{A}'$ on the top and bottom surfaces are opposing. Therefore, the Faraday like effect, i.e., spontaneous rotation of the polarization plane of transmitted light, is forbidden in ferromonopolar ($\mathcal{C}$) systems.

Although the above discussion based on the symmetry similarity gives an intuitive inspection of NRR, it may lead to a misunderstanding that NRR derives from net surface magnetization. In ref. [37], circular dichroism of reflected light, which is a counterpart of NRR effect related by the Kramers-Kronig relation, is ascribed to surface magnetization. However, NRR can be attributed to the diagonal components of the ME tensor α_{ij} expanded to optical frequencies and it does not necessarily rely on the presence of net surface magnetization for its origin. Based on this ME effect expanded to optical frequencies, that is, so called optical ME (OME) effect [38,39], rotation θ and ellipticity ε of reflected light in geometry **k** ∥ c are given by [40,41]

$$\theta + i\varepsilon = 2\alpha_{\perp}\frac{1+n_{\perp}}{1-n_{\perp}}, \tag{5.14}$$

where $\alpha_{\perp} = \alpha_{11}(\omega) = \alpha_{22}(\omega)$ is the ME coefficients expanded to the optical frequencies and $n_{\perp}^2 = \epsilon_{11}(\omega) = \epsilon_{22}(\omega)$ is the dielectric constant. Here, the sign of $\alpha_{\perp}$ depends on the domain states of L+ and L-, and thus NRR is also useful to distinguish AFM domains of Cr_2O_3. The NRR spectra in the visible light regions were observed in ref. [41], revealing that the magnitude of θ is of the order of 10^{-3} deg (see Fig. 5.6).

Microscopically, this NRR originating from OME arises from the interference effect between electric dipole and magnetic dipole transitions. Theoretical calculations based on the crystal-field theory successfully explain the observed spectrum shape [42], without assuming net magnetization on the surface. In contrast, the MOKE effect due to net magnetization solely arises from electric dipole transitions (or magnetic dipole transitions) [43]. If the MOKE effect caused by surface magnetization were dominant in NRR of Cr_2O_3, its spectrum would not be adequately explained by the OME contribution. Therefore, it is highly likely that NRR in Cr_2O_3 predominantly originates from the OME, although further discussion will be required.

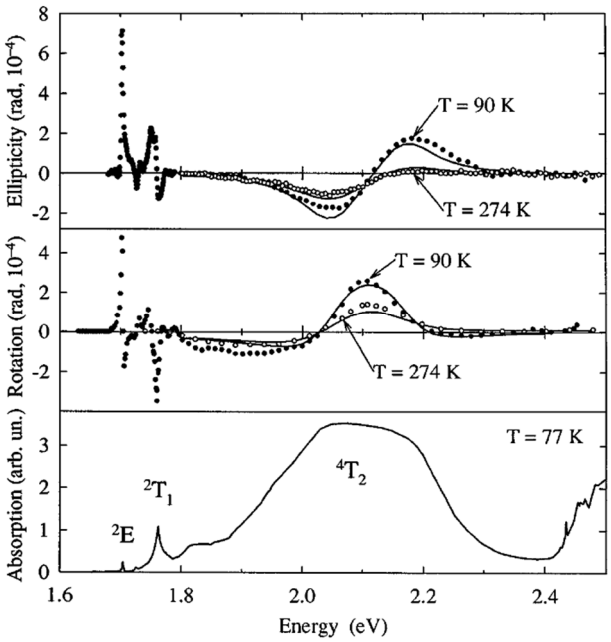

Fig. 5.6 NRR spectra in the visible light regions. Reprinted with permission from ref. [41]. Copyright 1996 by the American Physical Society. The top and bottom panels show the ellipticity ε and the rotation angle θ, respectively. The bottom panels show the absorption spectrum.

5.1.4 Motivation

The nonreciprocal optical effects of *E*-induced Faraday, *E*-induced and NRR are sensitive to the electric field-induced or spontaneous symmetry breakings in ferromonopolar systems. Moreover, all these effects are expected to be useful to distinguish the ferromonopolar AFM domain states (see Fig. 5.7 for schematic illustration), although no reports to date have documented domain visualization utilizing these effects.

In this study, we explore the abovementioned nonreciprocal optical effects in Cr_2O_3 to achieve the visualization of AFM domains via the diagonal ME effect. First, we measure spectra of the *E*-induced Faraday effect and *E*-induced MCD in the visible light region and demonstrate that Cr_2O_3 exhibits large enhancements of the effects at wavelengths around the spin allowed *d*-*d* transitions. Following that, we visualize AFM domains of Cr_2O_3 using the *E*-induced Faraday effect, *E*-induced MCD, and NRR. This success is achieved by adopting the electric-field modulation imaging and the polarization modulation imaging, both of which are effective to resolve spatial distributions of small signals.

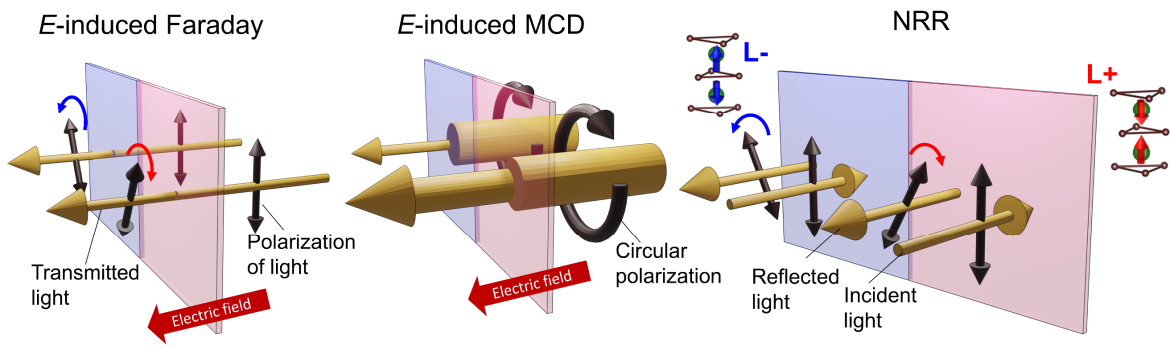

Fig 5.7 Conceptual illustration of the three nonreciprocal optical effects in Cr_2O_3 [31].

5.2 Experimental methods

5.2.1 Sample preparation

Single crystals of Cr_2O_3 grown by the laser floating-zone method [44] was provided by Mr. Takahiko Oshima, University of Tokyo. The obtained crystals were confirmed to be the single phase with the Cr_2O_3 corundum structure by XRD measurements. For measurements of optical properties, some of the crystals were oriented by using Laue XRD patterns, cut into thin plate shapes with the widest faces normal to the hexagonal *c* axis, and polished down to the thickness of about 20 μm. For measurements of the *E*-induced Faraday effect and the *E*-induced MCD, indium/tin oxide (ITO) was sputtered onto the widest faces of the samples to form a pair of transparent electrodes which allow the experimental setup with $\mathbf{k} \parallel \mathbf{E} \parallel c$.

5.2.2 Spectral measurements of optical absorption

The absorption spectrum of Cr_2O_3 was obtained by using a homebuilt fiber-based optical system in the photon energy range of 1.58 eV < E_{ph} < 2.48 eV. Unpolarized light from a tungsten-halogen lamp (AvaLight-HAL-S-MINI, Avantes) was incident on a sample along the *c* axis, and the transmitted light was detected by a spectrometer (Flame-S, Ocean Optics). The system was set in a commercial physical property measurement system (PPMS, Quantum Design) to control the sample temperature. Figure 5.8 shows the obtained absorption spectrum at 83 K. Although the sample was as thin as 20 μm, the spectra at 1.94 eV < E_{ph} < 2.25 eV could not be measured due to strong absorption.

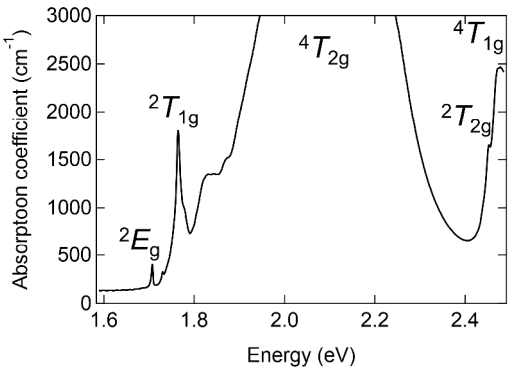

Fig. 5.8 Absorption spectrum obtained at 83 K in geometry of $\mathbf{k} \parallel c$ in the photon energy range of 1.58 eV < E_{ph} < 2.48 eV [31]. The labels ^2E_g, $^2T_{1g}$, $^4T_{2g}$, $^2T_{2g}$, and $^4T_{1g}$ are the irreducible representations of the excited states corresponding to the absorption peaks.

5.2.3 Spectral measurements of *E*-induced Faraday and *E*-induced MCD

Figure 5.9 shows a photograph and schematic illustrations of the optical setups for spectral measurements of the *E*-induced Faraday effect and the *E*-induced MCD. A supercontinuum laser (SC-Pro, YSL Photonics) was used as a light source. Monochromatic light with a selected wavelength was obtained by using an acousto-optic wavelength tunable filter (AOTF-PRO, YSL Photonics).

In the measurements of the *E*-induced Faraday effect, a sample is set between a polarizer and an analyzer, where the angle between the transmission axes of the polarizer and analyzer is set at Θ =

45°. In this setting, the intensity of light transmitted through a material exhibiting the *E*-induced Faraday effect is given by

$$I = \frac{I_0}{2}\{\sin(2\phi) + 1\} \tag{5.15}$$

where I_0 is the intensity of transmitted light at parallel-Nicols setting and ϕ [deg] is the rotation angle of the polarization plane induced by applying an electric field. Because the *E*-induced Faraday effect is usually small effect, it can be assumed that $\sin(2\phi) \approx \frac{2\pi}{180}\phi$ and equation (5.15) is rewritten as

$$I \approx I_0\left(\frac{\pi}{180}\beta V + \frac{1}{2}\right) \tag{5.16}$$

where β [deg V^{-1}] is the coefficient representing the magnitude of the *E*-induced Faraday effect and *V* [V] is an applied voltage. To detect small signals, a sinusoidal voltage $V_0\sin(\omega t)$ at a frequency of 999 Hz is applied, and the intensity of the transmitted light oscillating at the same frequency with the applied voltage $\frac{\pi}{180} I_0 \beta V_0$ was detected by using a lock-in amplifier [33]. The coefficient β is calculated by dividing the AC component by the DC component $I_0/2$.

In the measurements of the *E*-induced MCD, right circularly polarized (RCP) or left circularly polarized (LCP) light is irradiated onto the sample. Here, the intensity of transmitted light $I_{\mathrm{RCP,\,LCP}}$ is described as

$$I_{\mathrm{RCP,LCP}} = I_0 \exp\{-(\alpha_0 \mp \beta' E)d\} \tag{5.17}$$

where I_0 is the intensity of incident light, α_0 [cm^{-1}] is an absorption coefficient for RCP and LCP light in zero electric field, and β' [V^{-1}] is the coefficient representing the magnitude of *E*-induced MCD. Here, the sign of ± depends on the helicity of incident light (+ for RCP and – for LCP). Since *E*-induced MCD is usually small, equation 5.17 can be assumed as

$$I_{\mathrm{RCP,LCP}} \approx I_0 \mathrm{e}^{-\alpha_0 d}(1 \pm \beta' E d) = I_0 \mathrm{e}^{-\alpha_0 d}(1 \pm \beta' V). \tag{5.18}$$

In the same manner with *E*-induced Faraday, a sinusoidal voltage $V_0\sin(\omega t)$ at a frequency of 999 Hz is applied, and the intensity of the transmitted light oscillating at the same frequency with the applied voltage $\delta I_{\mathrm{RCP,LCP}} = \pm I_0 \mathrm{e}^{-\alpha_0 d}\beta' V_0$ was detected by using a lock-in amplifier. Then, the coefficient β' is calculated as

$$\beta' = \frac{\left(\frac{\delta I_{\mathrm{RCP}}}{I_0 \mathrm{e}^{-\alpha_0 d} V_0} - \frac{\delta I_{\mathrm{LCP}}}{I_0 \mathrm{e}^{-\alpha_0 d} V_0}\right)}{2}. \tag{5.19}$$

To obtain the spectra of the *E*-induced Faraday effect and the *E*-induced MCD, the signals were corrected at 2 nm wavelength intervals from 502 to 786 nm. The sample temperature was controlled by a liquid nitrogen flow cold stage.

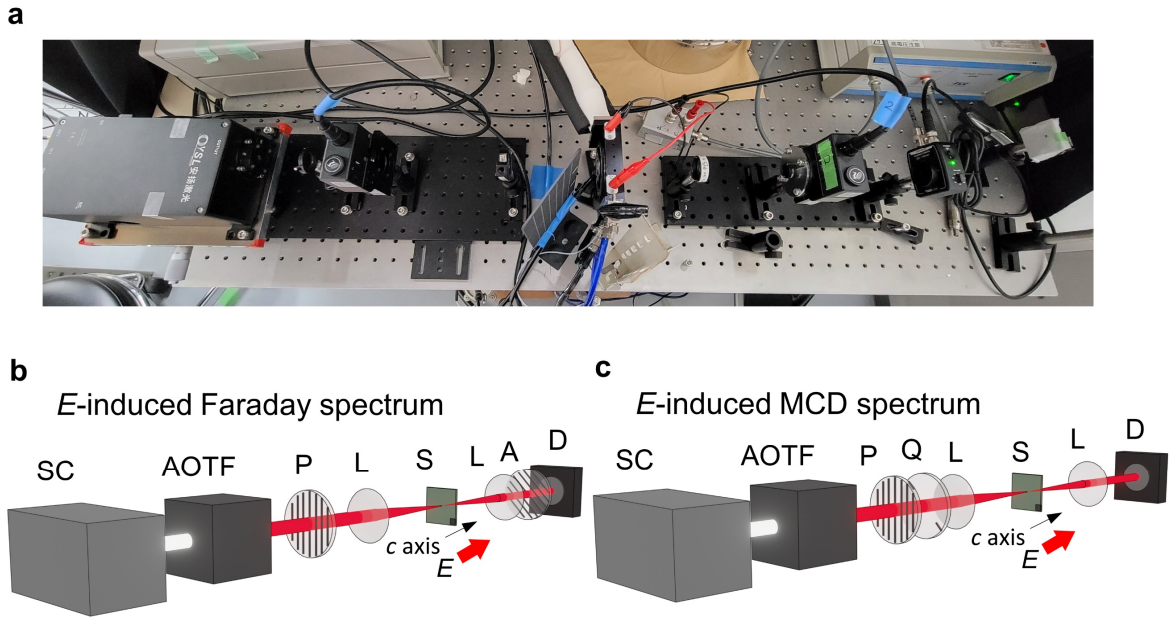

Fig. 5.9 Photograph (**a**) and schematic illustrations (**b**,**c**) of the optical setups for spectral measurements [31]. **b**, *E*-induced Faraday. **c**, *E*-induced MCD. SC: Supercontinuum laser; AOTF: Acousto-optic wavelength tunable filter; P: Polarizer; L: Lens; S: Sample; A: Analyzer; D: Si-detector; Q: Quarter-waveplate.

5.2.4 Spatial distribution measurements of *E*-induced Faraday and *E*-induced MCD

Two-dimensional maps of the *E*-induced Faraday effect and the *E*-induced MCD were obtained by using the field modulation imaging technique [45,46], which was adapted for electrogyration (EG) measurements in ferroaxial materials (see 3.2.2 for details). Figure 5.10 shows schematic illustrations of the optical setups. The measurement system for the *E*-induced Faraday effect is the same with that for EG. In the measurements of *E*-induced MCD, RCP or LCP light is irradiated instead of linearly polarized (LP) light, and the analyzer is removed. Here, the difference in signals under $+V$ and $-V$ is expressed as $\Delta I = I(+V) - I(-V)$ and the average of them is expressed as I. For the *E*-induced Faraday effect, $\Delta I/I$ is approximately proportional to ϕ and expressed as

$$\frac{\Delta I}{I} \cong \frac{4\pi}{180}\beta V. \tag{5.20}$$

Likewise, for the *E*-induced MCD, $\Delta I/I$ is approximately proportional to the magnitude of *E*-induced MCD and expressed as

$$\frac{\Delta I}{I} \cong \pm 2\beta' V, \tag{5.21}$$

where the sign of ± depends on the helicity of incident light. To obtain spatial distributions of small signals of $\Delta I/I$ with suppressing noises, large numbers (15,000) of $\Delta I/I$ maps are captured and averaged. A square-wave bias voltage (up to ±100 V) was applied at a frequency of 20 or 30 Hz, and images were captured at 40 or 60 fps.

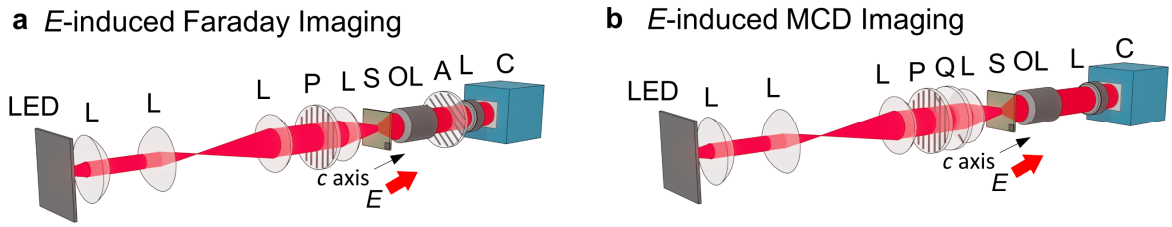

Fig. 5.10 Schematic illustrations of the optical setups for spatial distribution measurements of **a** *E*-induced Faraday and **b** *E*-induced MCD [31]. LED: LED light source; L: Lens; P: Polarizer; S: Sample; OL: Objective lens; A: Analyzer; C: sCMOS camera; Q: Quarter-waveplate.

5.2.5 Spatial distribution measurements of NRR

The spatial distribution measurements of NRR were performed by employing the polarization modulation imaging technique [47]. Figure 5.11 shows a schematical illustration of the optical setup. Here, the transmission axis of the analyzer and the fast axis of the liquid crystal variable retarder is set at 45° against the transmission axis of the polarizer. The polarization of incident light, i.e., LP, RCP, and LCP, can be switched by tuning a voltage applied to the liquid crystal variable retarder (LCC1223T-A, Thorlabs). In this setting, when LP, RCP or LCP light is irradiated onto a material which exhibits NRR, the intensities of reflected light (I_{LP}, I_{RCP}, and I_{LCP}) are described as [47]

$$I_{\mathrm{LP}} = \frac{1}{2}|\sin\theta - i\varepsilon\cos\theta + (\cos\theta + i\varepsilon\sin\theta)|^2 I_0 \tag{5.22}$$

$$I_{\mathrm{RCP}} = \frac{1}{2}|\sin\theta - i\varepsilon\cos\theta + i(\cos\theta + i\varepsilon\sin\theta)|^2 I_0 \tag{5.23}$$

$$I_{\mathrm{LCP}} = \frac{1}{2}|\sin\theta - i\varepsilon\cos\theta - i(\cos\theta + i\varepsilon\sin\theta)|^2 I_0 \tag{5.24}$$

where θ [rad] is a rotation angle and ε [rad] is the ellipticity of reflected light, I_0 is the intensity of incident light. Then θ can be calculated as

$$\theta = \frac{1}{2}\sin^{-1}\frac{2I_{\mathrm{LP}} - (I_{\mathrm{RCP}} + I_{\mathrm{LCP}})}{(1-\varepsilon^2)I_0} \tag{5.25}$$

When θ and ε are small enough and the absorption of the material is neglected, equation (5,25) can be assumed as

$$\theta \approx \frac{2I_{\mathrm{LP}} - (I_{\mathrm{RCP}} + I_{\mathrm{LCP}})}{2(1-\varepsilon^2)(I_{\mathrm{RCP}} + I_{\mathrm{LCP}})} \approx \frac{I_{\mathrm{LP}} - I_{\mathrm{RCP}}}{2I_{\mathrm{RCP}}} = \frac{\Delta\tilde{I}}{\tilde{I}}. \tag{5.26}$$

$\Delta\tilde{I}/\tilde{I}$ is calculated for each pixel of the camera, and large numbers (15,000) of $\Delta\tilde{I}/\tilde{I}$ maps are captured and averaged to detect small signals of θ. The polarization of light was modulated at a frequency of 20 Hz, and images were captured at 40 fps. However, even with this averaging process, finite backgrounds mainly due to sample tilting against the irradiated light remain, which prevent evaluating intrinsic NRR signals. To minimize such backgrounds, a $\Delta\tilde{I}/\tilde{I}$ map obtained at $T > T_{\mathrm{N}}$ was subtracted from that

obtained at $T < T_N$. Also, a 3×3 median filter was applied to the images to suppress noises.

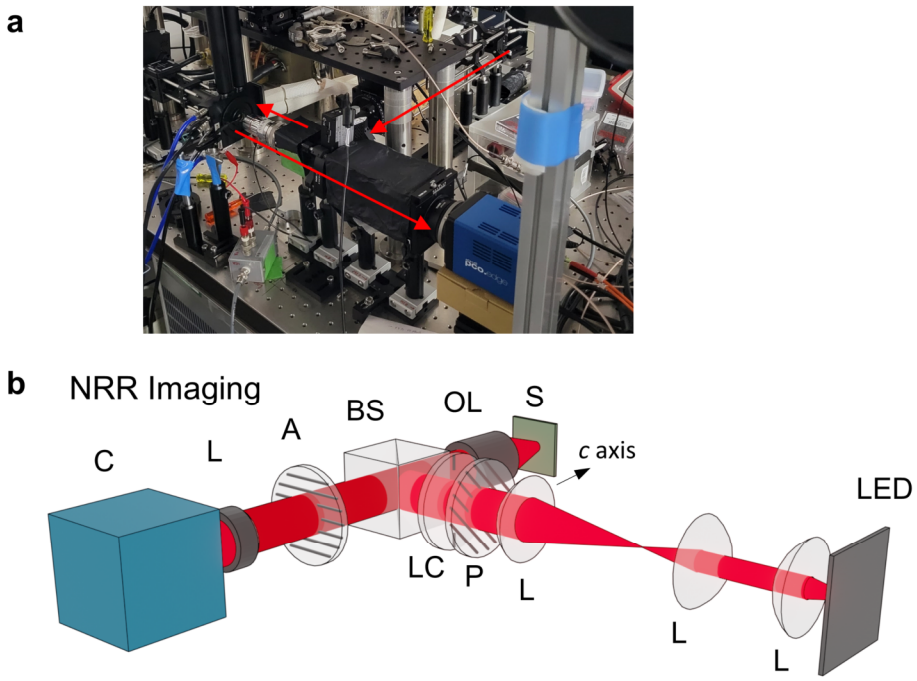

Fig. 5.11 Photograph (**a**) and schematic illustration (**b**) of the optical setups for spatial distribution measurements of NRR [31]. The red arrows in panel (**a**) depict light path. LED: LED light source; L: Lens; P: Polarizer; LC: Liquid crystal variable retarder; BS: Beam splitter S: Sample; OL: Objective lens; A: Analyzer; C: sCMOS camera.

5.3 Results and discussion

5.3.1 Spectra of *E*-induced Faraday and *E*-induced MCD

Prior to the measurements, single domain states of L+ and L- were prepared by cooling the sample from $T > T_N$ while applying magnetic (**H**) and electric (**E**) fields. This ME cooling procedure stabilizes the L+ and L- states when $H_cE_c > 0$ and $H_cE_c < 0$, respectively [48]. Here, H_c (E_c) represents **H** (**E**) along the *c* axis.

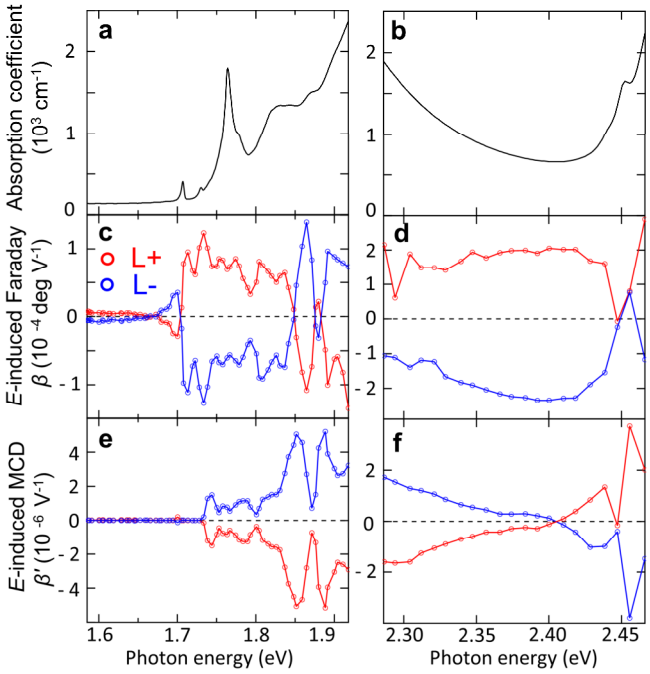

Fig. 5.12 Spectra of *E*-induced Faraday effect and *E*-induced MCD at 83 K [31]. **a,b,** Enlarged absorption spectra in the geometry **k** ∥ *c* at 1.58 eV < E_{ph} < 1.92 eV (**a**) and 2.28 eV < E_{ph}< 2.47 eV (**b**). **c**-**f** Spectra of *E*-induced Faraday effect (**c**,**d**) and those of *E*-induced MCD (**e**,**f**) in the geometry with **k** ∥ **E** ∥ *c* at 1.58 eV < E_{ph} < 1.92 eV (**c**,**e**) and 2.28 eV < E_{ph} < 2.47 eV (**d**,**f**). The red and blue dots correspond to the signals obtained in the single L+ and L- domains, respectively.

Figures 5.12**c**-**f** show the spectra of *E*-induced Faraday effect and *E*-induced MCD obtained at 83 K after ME cooling with $\mu_0 H_c \approx +0.2$ T and E_c of opposite signs [+56 kV cm^{-1} (red) and -56 kV cm^{-1} (blue)]. The cooling magnetic and electric fields were removed before the measurements. The spectra were measured in the photon energy range of 1.58 eV < E_{ph} < 2.47 eV. However, at 1.92 eV < E_{ph} < 2.28 eV, absorption was too strong to obtain meaningful signals. Thus, Fig. 5.12 displays spectra at 1.58 eV < E_{ph}< 1.92 eV (Figs. 5.12**c**,**e**) and 2.28 eV < E_{ph} < 2.47 eV (Figs. 5.12**d**,**f**). The spectra show almost complete sign reversals upon the reversal of the domain states (compare the red and blue dots in Figs. 5.12**c**-**f**), confirming that the spectra exactly reflect the *E*-induced Faraday effect and the *E*-induced MCD.

5.3.2 Frequency dependences of *E*-induced Faraday and *E*-induced MCD

Now let us discuss the structures of the spectra. For the *E*-induced Faraday effect and the *E*-induced MCD in Cr_2O_3, the spin allowed transition to the excited state $^4T_{2g}$ from the ground state $^4A_{2g}$ is expected to give the largest contribution [34,49]. The broad absorption peak centered at 2.1 eV and extended from 1.7 to 2.4 eV corresponds to this transition (see Fig. 5.8) [50]. In the followings, we discuss the frequency dependences of the *E*-induced Faraday effect and the *E*-induced MCD based on the crystal-field theory and pseudo-Stark effect.

Figure 5.13 shows the energy diagram of Cr^{3+} ion in Cr_2O_3 [34]. The contribution to the complex Faraday rotation from the Cr^{3+} ion at site A (see Fig. 5.4), $\Phi_A(\omega)$, is described as [34,49]

$$\Phi_A(\omega) = \frac{2\pi\omega}{n\hbar c} p_\alpha^2 (\omega - i\Gamma_\alpha) \left\{ \frac{1}{\left(\omega_{C(\alpha)g}^2 - \omega^2 + \Gamma_\alpha^2\right) + 2i\omega\Gamma_\alpha} - \sum_{i=1,2,3} \frac{a_{A_i}^2(\alpha)}{\left(\omega_{A_i(\alpha)g}^2 - \omega^2 + \Gamma_\alpha^2\right) + 2i\omega\Gamma_\alpha} \right\} \quad (5.27)$$

where ω is an angular frequency of incident light, $n = (n_+ + n_-)/2$ is the averaged complex refractive index of RCP (n_+) and LCP (n_-) light, p_α^2 is the average dipole moment for the transition from the ground state $^4A_{2g}$ to the excited state $^4T_{2g}$, α represents a spin configuration, Γ is a damping factor, $\hbar\omega_{C,A_i(\alpha)g}$ is the excitation energies to the C and A_i states, which are the split $^4T_{2g}$ state due to the trigonal field, the spin-orbit interaction and the exchange interaction, $a_{A_i}^2(\alpha)$ is the occupation probability of the A_i state. The real and imaginary parts of $\Phi_A(\omega)$ correspond to the Faraday rotation and magnetic circular dichroism, respectively.

When an electric field is not applied, the Cr^{3+} ion at site B exhibits the same magnitude but opposite sign contribution, and thus spontaneous Faraday effect is forbidden as a unit cell. Meanwhile, under an electric field along the c axis (E_c), finite magnetization is induced due to the linear ME effect, i.e., $m_A + m_B \neq 0$ where $m_{A(B)}$ is magnetization at site A(B). In addition, the ground and excited states are shifted (called pseudo Stark shift) [34,51], which makes the excitation energies of $\hbar\omega_{C,A_i(\alpha)g}$ distinct between the site A and B as

$$\omega_{C,A_ig}^{A(B)} = \omega_{C,A_i(\alpha)g} \pm |A_1^0|(\chi_0 + \chi_{C,A_i})E_c \approx \omega_{C,A_i(\alpha)g} \pm \Delta_E \tag{5.28}$$

where A_1^0 is the magnitude of the odd trigonal field, χ_0 and χ_{C,A_i} are coefficients which represent mixing of the wave functions of the states of opposite parity with the wave functions of the ground and excited (C, A_i) states, respectively, by the odd trigonal field (see Fig. 5.13). Here, we assumed that $\chi_C \approx \chi_{A_i}$ and Δ_E represents the effects of an applied electric field. The sign of ± depends on the site A or B. Then, the contributions from the Cr^{3+} ions at site A and B are calculated as

$$\begin{aligned} & m_A\Phi_A(\omega) + m_B\Phi_A(\omega) \\ & = m_A\frac{2\pi\omega}{n\hbar c}p_\alpha^2(\omega - i\Gamma_\alpha)\left\{\frac{1}{\left(\left(\omega_{C(\alpha)g} + \Delta_E\right)^2 \pm \Delta_E\omega^2 + \Gamma_\alpha^2\right) + 2i\omega\Gamma_\alpha}\right. \\ & \left. - \sum_{i=1,2,3}\frac{a_{A_i}^2(\alpha)}{\left(\left(\omega_{A_i(\alpha)g} + \Delta_E\right)^2 - \omega^2 + \Gamma_\alpha^2\right) + 2i\omega\Gamma_\alpha}\right\} \\ & + m_B\frac{2\pi\omega}{n\hbar c}p_\alpha^2(\omega - i\Gamma_\alpha)\left\{\frac{1}{\left(\left(\omega_{C(\alpha)g} - \Delta_E\right)^2 \pm \Delta_E\omega^2 + \Gamma_\alpha^2\right) + 2i\omega\Gamma_\alpha}\right. \\ & \left. - \sum_{i=1,2,3}\frac{a_{A_i}^2(\alpha)}{\left(\left(\omega_{A_i(\alpha)g} - \Delta_E\right)^2 - \omega^2 + \Gamma_\alpha^2\right) + 2i\omega\Gamma_\alpha}\right\} \end{aligned} \tag{5.29}$$

In the following calculation, we assume that the effect of the trigonal field is much greater than the spin-orbit interaction for the splitting of the $^4T_{2g}$ state and $a_{A_2}^2(\alpha) = a_{A_3}^2(\alpha) = 0$ [34]. We also assume that the damping factor Γ_α and the effect of pseudo-Stark shift are small and $\Gamma_\alpha^2, \Delta_E^2 \approx 0$. Under these assumptions, the real part (Re) and imaginary part (Im) of equation 5.29 are given as

$$\mathrm{Re}(5.29) \approx \frac{2\pi\omega^2}{n\hbar c} p_\alpha^2 \left[(m_\mathrm{A} + m_\mathrm{B}) \left(\frac{1}{\omega_{C(\alpha)g}^2 - \omega^2} - \frac{1}{\omega_{A_1(\alpha)g}^2 - \omega^2} \right) \right.$$

$$\left. - (m_\mathrm{A} - m_\mathrm{B}) \left(\frac{2\Delta_E \omega_{C(\alpha)g}}{\left(\omega_{C(\alpha)g}^2 - \omega^2\right)^2} - \frac{2\Delta_E \omega_{A_1(\alpha)g}}{\left(\omega_{A_1(\alpha)g}^2 - \omega^2\right)^2} \right) \right], \quad (5.30)$$

$$\mathrm{Im}(5.29) \approx \frac{2\pi\omega}{n\hbar c} p_\alpha^2 \Gamma_\alpha \left[(m_\mathrm{A} + m_\mathrm{B}) \left(\frac{\omega_{C(\alpha)g}^2 + \omega^2}{\left(\omega_{C(\alpha)g}^2 - \omega^2\right)^2} - \frac{\omega_{A_1(\alpha)g}^2 + \omega^2}{\left(\omega_{A_1(\alpha)g}^2 - \omega^2\right)^2} \right) \right.$$

$$\left. - (m_\mathrm{A} - m_\mathrm{B}) \left(\frac{2\Delta_E \omega_c (\omega_c^2 + 3\omega)^2}{\left(\omega_{C(\alpha)g}^2 - \omega^2\right)^3} - \frac{2\Delta_E \omega_{A_1(\alpha)g} \left(\omega_{A_1(\alpha)g}^2 + 3\omega\right)^2}{\left(\omega_{A_1(\alpha)g}^2 - \omega^2\right)^3} \right) \right]. \quad (5.31)$$

As shown in these equations, at an angular frequency near $\omega_{C,A_i(\alpha)g}$, the effect from the antiferromagnetic order parameter l = m_A - m_B is dominant both for the real and imaginary parts of equation (5.29). The contribution to the Faraday effect from a unit cell is given by $2\left(m_\mathrm{A}\Phi_\mathrm{A}(\omega) + m_\mathrm{B}\Phi_\mathrm{A}(\omega)\right)$, and a general expression can be obtained by summing it over all the spin states and the number of unit cells in a crystal. Thus, the *E*-induced Faraday effect and *E*-induced MCD as a function of frequency around the resonance frequency $\omega_{C,A_i(\alpha)g}$ are obtained as

$$\phi \propto l\omega\Delta_E \left\{ \frac{\omega_C}{(\omega_C^2 - \omega^2)^2} - \frac{\omega_{A_1}}{\left(\omega_{A_1}^2 - \omega^2\right)^2} \right\} \text{ and} \quad (5.32)$$

$$\alpha_\mathrm{MCD} \propto l\Gamma\Delta_E \left\{ \frac{\omega_C(\omega_C^2 + 3\omega^2)}{(\omega_C^2 - \omega^2)^3} - \frac{\omega_{A_1}\left(\omega_{A_1}^2 + 3\omega^2\right)}{\left(\omega_{A_1}^2 - \omega^2\right)^3} \right\}. \quad (5.33)$$

These equations indicate that the spectrum of ϕ around the resonance frequencies is of dispersive type (i.e., exhibits a sign reversal), while that of α_MCD is of absorptive type (i.e., exbibits no sign reversal). As mentioned above, the spectra around the $^4T_{2g}$ peak centered at 2.1 eV were not obtained because of strong absorption. However, it is seen that the sign of the *E*-induced Faraday effect gets reversed between E_ph < 2.1 eV and E_ph > 2.1 eV while that of *E*-induced MCD does not (compare the right end of Figs. 5.12**c**,**e** and the left end of Figs. 5.12**d**,**f**). Thus, the obtained spectra do not contradict the calculations.

The three absorption peaks at 1.706 and 1.729, and 1.763 eV (see Fig. 5.8) correspond to the spin-forbidden transitions to the exited states of ^2E_g and $^2T_{1g}$, respectively [50,52]. They can contribute to the *E*-induced Faraday effect and the *E*-induced MCD by the assistance of the spin-orbit interaction between these states and the $^4T_{2g}$ state [42]. Thus, peak structures observed at around 1.7-1.8 eV in Figs. 5.12**c**,**e** will derive from these spin-forbidden transitions. Relatively large and sharp peaks are also observed at around 1.8-1.9 eV in Figs. 5.12**c**,**e**. In particular, the largest *E*-induced MCD of 5×10^{-6} V^{-1} is observed at 1.852 and 1.889 eV. These peaks will be related to the shoulder structures in the absorption spectrum at around 1.83-1.87 eV. However, the relationships between these shoulder structures and the

electronic transitions are unclear [50].

Located between the two spin allowed transitions of $^4T_{2g}$ and $^4T_{1g}$ [50], the spectra shown in Figs. 5.12**d**,**f** (2.28 eV < E_{ph} < 2.47 eV) are expected to be influenced by these transitions. As seen in Fig. 5.12**f**, the *E*-induced MCD spectrum crosses the zero line at 2.405 eV. This may suggest that the $^4T_{1g}$ and $^4T_{2g}$ transitions have contributions of opposite signs to the *E*-induced MCD spectrum. The dispersive peak structure at around 2.45 eV in the *E*-induced MCD spectrum will correspond to the absorption peak at the same energy, which is assigned to the transition to the $^2T_{2g}$ state [50]. We note that the largest *E*-induced Faraday effect of about 2×10^{-4} deg V^{-1} is observed at 2.35 eV < E_{ph} < 2.42 eV, which is about 15 to 20 times larger than those observed in the near-infrared region at around 100 K [34,35].

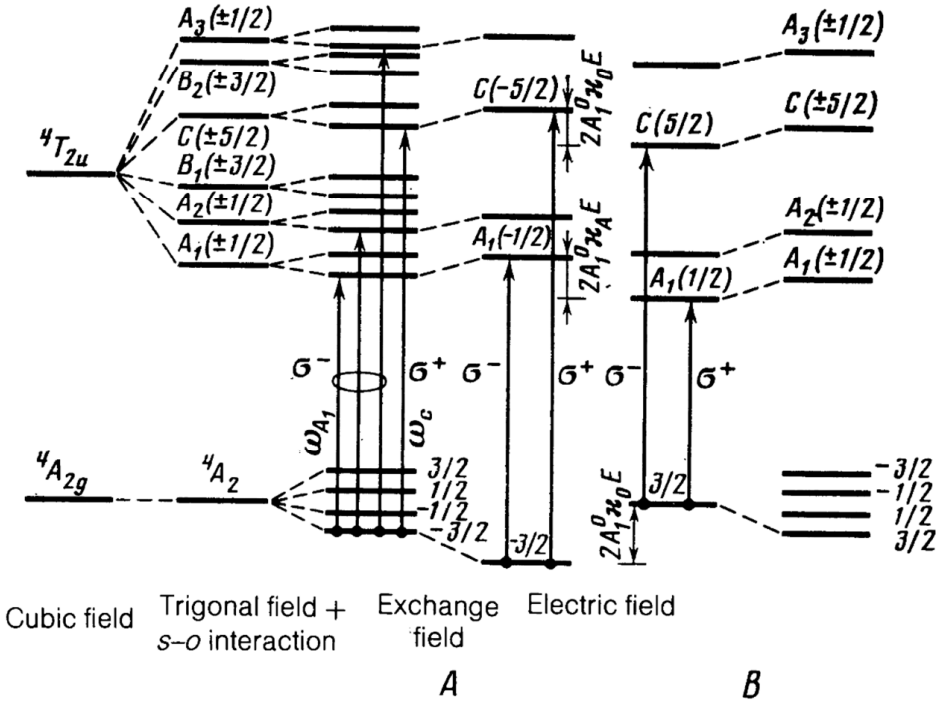

Fig. 5.13 The energy diagram of Cr^{3+} in Cr_2O_3 [34]. It shows splitting of the ground $^4A_{2g}$ and excited $^4T_{2g}$ states (first column) due to the trigonal field and spin-orbit interaction (second column), the exchange field (third column) and the Stark effect due to an applied electric field (fourth column for Site *A* and fifth column for Site *B*). "±5/2", "±3/2" and "±1/2" denote the total spin angular momentum of each state. The arrows with the symbol σ^+ (σ^-) represent optical transitions with right (left) circularly polarized light.

5.3.3 Temperature dependence of *E*-induced Faraday and *E*-induced MCD

The spectra of the *E*-induced Faraday effect were measured at various temperatures. Figure 5.14**a** shows the *T* dependence at selected photon energies of 1.70 and 2.34 eV while Fig. 5.14**b** shows the spectra in the photon energy range of 1.58 eV < E_{ph} < 1.80 eV at 83, 200, 305, and 307 K. These *T* profiles were obtained for the L+ single domain. As shown in Figs. 5.14**a**,**b**, the signals vanish at 307 K (≈ T_N). When

comparing the T profiles at 1.70 and 2.34 eV (compare the red and green dots in Fig. 5.14**a**), one can find that the latter one well obeys the T dependence of the AFM order parameter of Cr_2O_3 while the former one does not. The data at 2.34 eV is well fitted by the function of AFM order parameter [53,54]

$$l(T) = l_0(T_N - T)^{0.35} \ (T < T_N) \tag{5.34}$$

as shown in the green curve in Fig. 5.14**a**. Here, l_0 is a fitting parameter. On the other hand, the E-induced Faraday effect at 1.70 eV does not obey this function, and changes its sign at around 175 K. This is most likely because the photon energy of 1.70 eV corresponds to the energy at which the spin-forbidden transition driven peak develops at low temperatures (see Fig. 5.14**b**). As mentioned in 5.1.3, the T dependence of the E-induced Faraday effect is discussed in the context of competing contributions from the AFM order parameter l and the ME susceptibility α_{33} in ref. [35]. However, such a discussion cannot be directly applied to the current case in which the development of the peak structures with decreasing temperature is clearly observed.

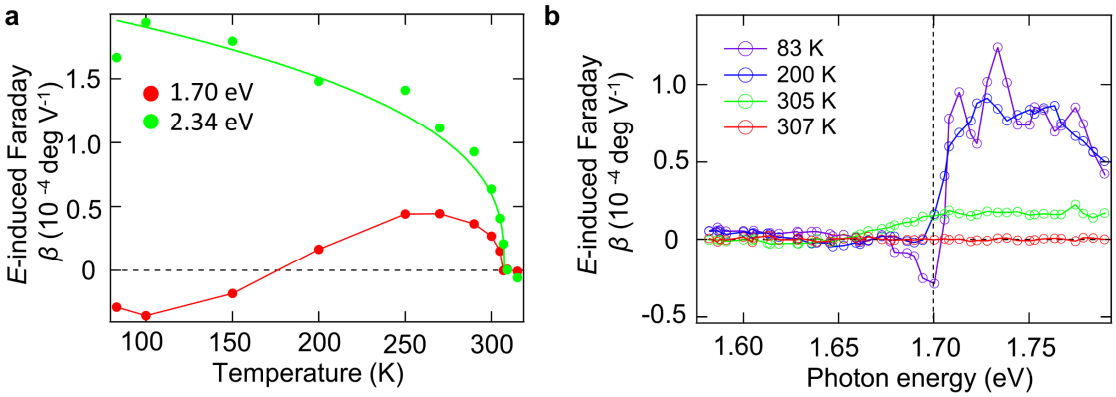

Fig. 5.14 Temperature (T) dependence of the E-induced Faraday effect [31]. **a**, T dependence of the E-induced Faraday effect at E_{ph} = 1.70 eV (red dots) and 2.34 eV (green dots). The green curve is the fitting by the function of the AFM order parameter given in equation (5.34). The red line is a guide to the eye. **b**, The spectra of the E-induced Faraday effect in the photon energy region of 1.58 eV < E_{ph} < 1.80 eV at 83 K (purple), 200 K (blue), 305 K (green) and 307 K (red). The dashed line denotes the photon energy of E_{ph} = 1.70 eV at which the characteristic T dependence was observed in panel (**a**).

5.3.4 AFM domain observation

After characterizing the spectra of the E-induced Faraday effect and the E-induced MCD in Cr_2O_3, we moved on to the domain imaging using these effects. First, we utilized the E-induced Faraday effect. Figures 5.15**a**-**f** show the two-dimensional maps of the E-induced Faraday effect obtained with using monochromatic LED light sources of 1.70 (Figs. 5.15**a**-**c**) and 2.34 eV (Figs. 5.15**d**-**f**). The images obtained at 270 (Figs. 5.15**a**,**d**), 200 (Figs. 5.15**d**,**g**), and 83 K (Figs. 5.15**e**,**h**) are shown. In these images, clear contrasts of red (positive $\Delta I/I$) and blue (negative $\Delta I/I$) are observed. These contrasts correspond to positive and negative signs of the E-induced Faraday effects, and thus reflect the ferromonopolar AFM domain structures. Consequently, we succeeded in the visualization of AFM domains using the E-induced Faraday effect. The typical domain size is several hundred micrometers, which is consistent

with those obtained by other experimental techniques such as second harmonic generation [24,30]. The contrasts obtained with the 2.34 eV LED light source increase with decreasing temperature (Figs. 5.15**d**-**f**). In contrast, those obtained with the 1.70 eV LED light source decrease with decreasing temperature from 270 K and are reversed at 83 K (Figs. 5.15**a**-**c**). The observed T evolution of the domain contrasts is consistent with that obtained by the spectral measurements (see Fig. 5.14**a**). The magnitudes of the E-induced Faraday effect calculated by using the $\Delta I/I$ averaged over single domain areas are $\beta \approx 3\times10^{-5}$ deg V^{-1} for 1.70 eV and $\beta \approx 1.8\times10^{-4}$ deg V^{-1} for 2.34 eV at 83 K, which are well matched with those obtained by the spectral measurements.

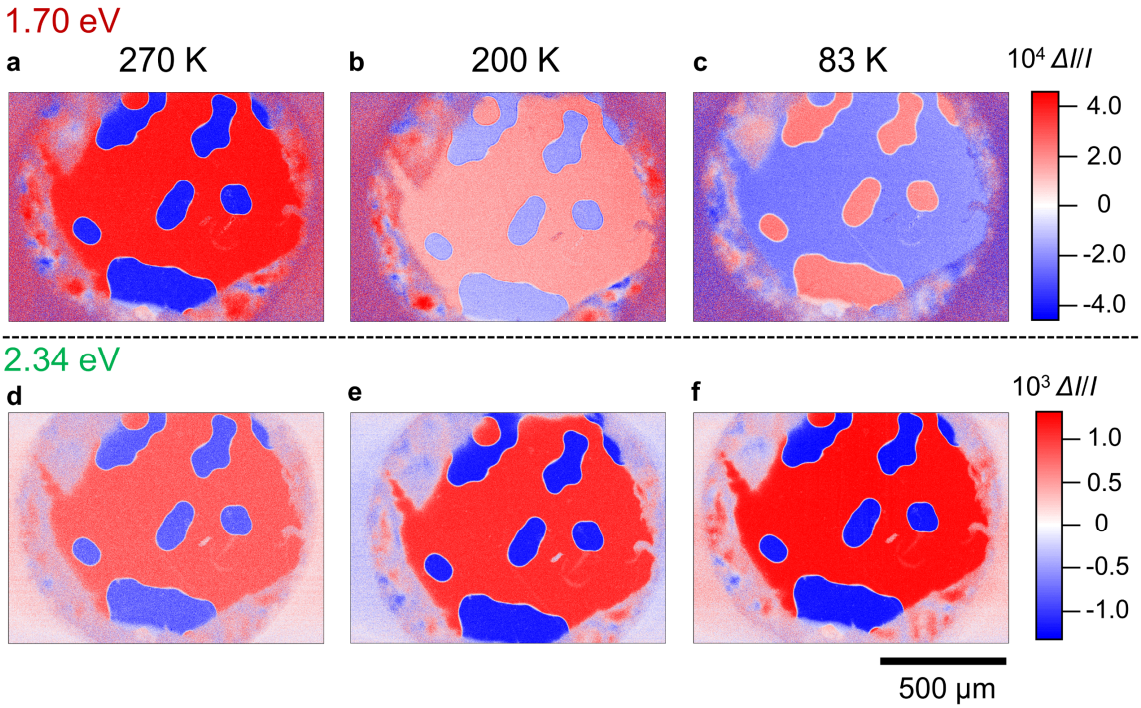

Fig. 5.15 Two-dimensional maps of the E-induced Faraday effect obtained with monochromatic light whose photon energies are E_{ph} = 1.70 eV (**a**-**c**) and E_{ph} = 2.34 eV (**d**-**f**) [31]. The maps were obtained at 270 K (**a**,**c**), 200 K (**b**,**d**), and 83 K (**c**,**e**). In the red and blue regions, the signs of the E-induced Faraday effects are opposite to each other, and thus the contrasts correspond to the AFM domains.

We have also confirmed that the single domain states of L+ or L- are formed by the ME cooling. Figures 5.16**a** and **b** show the domains obtained by cooling the sample across T_N while applying magnetic and electric fields in the setting of $H_cE_c > 0$ and $H_cE_c < 0$, respectively. The magnitudes of the applied fields were $\mu_0H_c \approx +0.2$ T and $E_c = \pm56$ kV cm^{-1}. The domain images were taken at 270 K with the 1.70 eV LED light source. The signals are uniform and the sign of them are opposite between the opposite ME cooling fields.

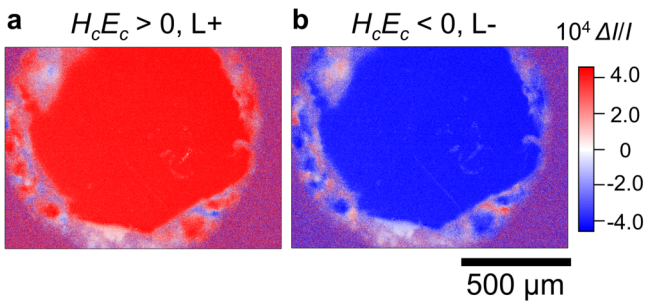

Fig. 5.16 Single domains obtained by the ME cooling [31]. **a**, **b**, Two-dimensional map of the *E*-induced Faraday effect obtained by cooling the sample while applying magnetic and electric fields in the setting of $H_cE_c > 0$ (**a**) and $H_cE_c < 0$ (**b**).

Next, we performed the domain imaging using the *E*-induced MCD effect. Figures 5.17**a** and **b** show the two-dimensional maps of the *E*-induced MCD obtained at 83 K with RCP and LCP incident light, respectively. Here, the 2.34 eV LED was used as a light source. In the images, clear contrasts of positive (red) and negative (blue) signals are observed, which reflect the AFM domain structures. The contrast reversal between the RCP and LCP incident light confirms that the obtained signals come from *E*-induced MCD. The magnitude of *E*-induced MCD obtained in this measurement was $\beta' \approx 9\times10^{-5}$ V^{-1}, which is well matched with that obtained by the spectral measurement.

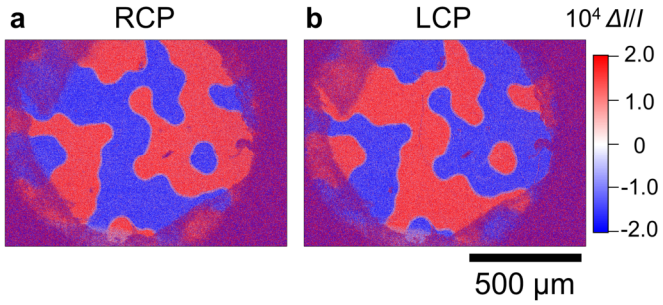

Fig. 5.17 Two-dimensional maps of the *E*-induced MCD effect obtained with right (**a**) and left (**b**) circularly polarized monochromatic light whose photon energy is E_{ph} = 2.34 eV. These images were taken at 83 K [31].

Finally, we performed spatial distribution measurements of NRR. Figures 5.18**a** and **b** show the two-dimensional maps of NRR obtained at 270 K with monochromatic light whose photon energies are 2.10 and 1.91 eV, respectively. Even with the background suppressing process described in 5.2.5, finite backgrounds with some slopes remain. To show the whole domain structures, the color scale is set about 10 times larger than the actual rotation angle. Between the bright and dark regions in these images, the directions of the polarization rotation of the reflected light are opposite. Thus, the contrasts reflect the AFM domain structures. Contrast reversal between the images obtained with 2.10 eV and 1.91 eV light is clearly observed (compare Figs. 5.18**a** and **b**), which is consistent with the previously reported NRR spectrum [41] (see Fig. 5.6). The magnitude of the rotation was calculated by the differences of θ between the adjacent opposite domains. The calculated angles are $|\theta| \approx 3\times10^{-3}$ deg for both energies, which are also consistent with the previous work [41]. Furthermore, a two-dimensional map of the *E*-induced Faraday effect was obtained in the same sample (Fig. 5.18**c**). The domain patterns obtained by using NRR and the *E*-induced Faraday effect are the same. Considering that the penetration depth of light with a photon energy of 2.10 eV is expected to be less than 2 μm from the absorption spectrum,

the NRR maps show the domain structures near the sample surface. Thus, the same domain patterns obtained by NRR and the *E*-induced Faraday effect indicate that the domains are uniform in the thickness direction.

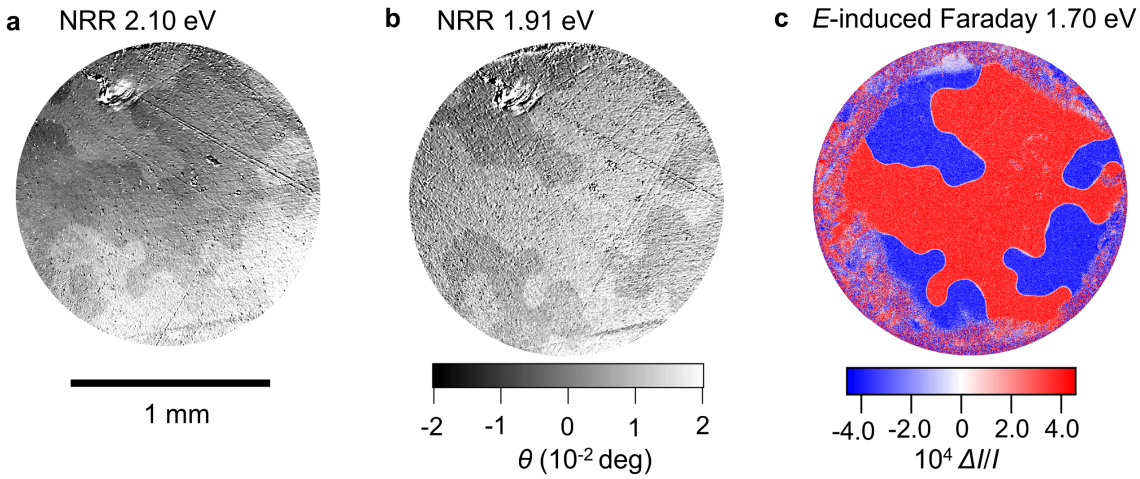

Fig. 5.18 Two-dimensional maps of NRR [31]. **a**,**b**, AFM domain visualized by using NRR with monochromatic light whose photon energies are 2.10 eV (**a**) and 1.91 eV (**b**). The contrasts are reversed between the two. (**c**) Antiferromagnetic domains visualized by using the *E*-induced Faraday effect with monochromatic light whose photon energy is 1.70 eV at the same position with panels (**a**,**b**). The obtained domains were perfectly matched with panels (**a**,**b**). These images were taken at 270 K.

5.4 Conclusion

In summary, we have investigated nonreciprocal optical effects [electric field induced (*E*-induced) Faraday effect, the electric field induced magnetic circular dichroism (*E*-induced MCD), and the spontaneous nonreciprocal rotation of reflected light (NRR)] originating from ferromonopolar order in Cr_2O_3, focusing on their spectra and spatial distributions. The spectral measurements of *E*-induced Faraday effect and *E*-induced MCD show that large enhancements of the effects occurring at frequencies around the transition to the ${}^4T_{2g}$ states. In our bulk samples, the effects at the center energy of the transition could not be obtained due to strong absorption. Since magnitudes of these *E*-induced nonreciprocal optical effects are independent of the sample thickness, it will be an interesting future work to measure the effects at the peak center in thin film samples.

Up until now, the smallness of the nonreciprocal optical effects studied here has hindered antiferromagnetic domain observation through their spatial distribution measurements. In our measurements, however, by employing the field and polarization modulation imaging techniques, antiferromagnetic domains were clearly visualized by utilizing these effects. These results showcase that nonreciprocal optical effects constitute an effective method for visualizing ferromonopolar antiferromagnetic domains. Compared with other techniques for the AFM domain observation such as SHG [24] or x-ray magnetic circular dichroism [26,27], systems using nonreciprocal optical effects offer

the advantage of convenience, as they do not require high-power laser or synchrotron radiation facilities. In particular, NRR measurement can be performed in a reflection setting without applying an electric field, making applicable to wide range of materials.

References

[1] I. E. Dzyaloshinskii, *On the Magneto-Electrical Effect in Antiferromagnetics*, Zh. Exp. Teor. Fiz. **33**, 881 (1959).

[2] D. N. Astrov, *The Magnetoelectric Effect in Antiferromagnetics*, J. Exp. Theor. Phys. **38**, 984 (1960).

[3] N. A. Spaldin, M. Fiebig, and M. Mostovoy, *The Toroidal Moment in Condensed-Matter Physics and Its Relation to the Magnetoelectric Effect*, J. Phys. Condens. Matter **20**, 434203 (2008).

[4] S. Hayami, H. Kusunose, and Y. Motome, *Toroidal Order in Metals without Local Inversion Symmetry*, Phys. Rev. B **90**, 024432 (2014).

[5] S. Hayami, H. Kusunose, and Y. Motome, *Emergent Spin-Valley-Orbital Physics by Spontaneous Parity Breaking*, J. Phys. Condens. Matter **28**, 395601 (2016).

[6] M. T. Suzuki, T. Koretsune, M. Ochi, and R. Arita, *Cluster Multipole Theory for Anomalous Hall Effect in Antiferromagnets*, Phys. Rev. B **95**, 094406 (2017).

[7] H. Watanabe and Y. Yanase, *Group-Theoretical Classification of Multipole Order: Emergent Responses and Candidate Materials*, Phys. Rev. B **98**, 245129 (2018).

[8] S. Hayami, M. Yatsushiro, Y. Yanagi, and H. Kusunose, *Classification of Atomic-Scale Multipoles under Crystallographic Point Groups and Application to Linear Response Tensors*, Phys. Rev. B **98**, 165110 (2018).

[9] M. Yatsushiro, H. Kusunose, and S. Hayami, *Multipole Classification in 122 Magnetic Point Groups for Unified Understanding of Multiferroic Responses and Transport Phenomena*, Phys. Rev. B **104**, 054412 (2021).

[10] H. Kusunose and S. Hayami, *Generalization of Microscopic Multipoles and Cross-Correlated Phenomena by Their Orderings*, J. Phys. Condens. Matter **34**, 464002 (2022).

[11] S. Hayami and H. Kusunose, *Microscopic Description of Electric and Magnetic Toroidal Multipoles in Hybrid Orbitals*, J. Phys. Soc. Jpn. **87**, 033709 (2018).

[12] H. Kusunose, R. Oiwa, and S. Hayami, *Complete Multipole Basis Set for Single-Centered Electron Systems*, J. Phys. Soc. Jpn. **89**, 104704 (2020).

[13] H. Kusunose, *Description of Multipole in f-Electron Systems*, J. Phys. Soc. Jpn. **77**, 064710 (2008).

[14] Y. Kuramoto, H. Kusunose, and A. Kiss, *Multipole Orders and Fluctuations in Strongly Correlated Electron Systems*, J. Phys. Soc. Jpn. **78**, 072001 (2009).

[15] P. Santini, S. Carretta, G. Amoretti, R. Caciuffo, N. Magnani, and G. H. Lander, *Multipolar Interactions in F-Electron Systems: The Paradigm of Actinide Dioxides*, Rev. Mod. Phys. **81**, 807 (2009).

[16] R. Oiwa and H. Kusunose, *Rotation, Electric-Field Responses, and Absolute Enantioselection in Chiral Crystals*, Phys. Rev. Lett. **129**, 116401 (2022).

[17] J.-I. Kishine, H. Kusunose, and H. M. Yamamoto, *On the Definition of Chirality and Enantioselective Fields*, Isr. J. Chem. **62**, e2022000 (2022).

[18] N. A. Spaldin, M. Fechner, E. Bousquet, A. Balatsky, and L. Nordström, *Monopole-Based Formalism for the Diagonal Magnetoelectric Response*, Phys. Rev. B **88**, 094429 (2013).

[19] T. R. McGuire, E. J. Scott, and F. H. Grannis, *Antiferromagnetism in a Cr_2O_3 Crystal*, Phys. Rev. **102**, 1000 (1956).

[20] L. M. Corliss, J. M. Hastings, R. Nathans, and G. Shirane, *Magnetic Structure of Cr_2O_3*, J. Appl. Phys. **36**, 1099 (1965).

[21] V. J. Folen, G. T. Rado, and E. W. Dtalder, *Anisotropy of the Mangetoelectric Effect in Cr_2O_3*, Phys. Rev. Lett. **6**, 607 (1961).

[22] R. R. Birss, *Symmetry & Magnetism* (North-holland publishing company, Amsterdam, 1966).

[23] E. Kita, A. Tasaki, and K. Siratori, *Application of SQUID Magnetometer to the Measurement of Magnetoelectric Effect in Cr_2O_3*, Jpn. J. Appl. Phys. **18**, 1361 (1979).

[24] M. Fiebig, D. Fröhlich, G. Sluyterman v. L., and R. V. Pisarev, *Domain Topography of Antiferromagnetic Cr_2O_3 by Second-Harmonic Generation*, Appl. Phys. Lett. **66**, 2906 (1995).

[25] P. Schoenherr, L. M. Giraldo, M. Lilienblum, M. Trassin, D. Meier, and M. Fiebig, *Magnetoelectric Force Microscopy on Antiferromagnetic 180◦ Domains in Cr_2O_3*, Materials **10**, 1051 (2017).

[26] N. Wu, X. He, A. L. Wysocki, U. Lanke, T. Komesu, K. D. Belashchenko, C. Binek, and P. A. Dowben, *Imaging and Control of Surface Magnetization Domains in a Magnetoelectric Antiferromagnet*, Phys. Rev. Lett. **106**, 087202 (2011).

[27] Y. Shiratsuchi, T. V. A. Nguyen, and R. Nakatani, *Magnetoelectric Control of Antiferromagnetic Domain of Cr_2O_3 Thin Film Toward Spintronic Application*, J.Magn. Soc. Jpn. **42**, 119 (2018).

[28] P. Appel, B. J. Shields, T. Kosub, N. Hedrich, R. Hübner, J. Faßbender, D. Makarov, and P. Maletinsky, *Nanomagnetism of Magnetoelectric Granular Thin-Film Antiferromagnets*, Nano Lett. **19**, 1682 (2019).

[29] N. Hedrich, K. Wagner, O. V. Pylypovskyi, B. J. Shields, T. Kosub, D. D. Sheka, D. Makarov, and P. Maletinsky, *Nanoscale Mechanics of Antiferromagnetic Domain Walls*, Nat. Phys. **17**, 574 (2021).

[30] M. S. Wörnle, P. Welter, M. Giraldo, T. Lottermoser, M. Fiebig, P. Gambardella, and C. L. Degen, *Coexistence of Bloch and Néel Walls in a Collinear Antiferromagnet*, Phys. Rev. B **103**, 094426 (2021).

[31] T. Hayashida, K. Arakawa, T. Oshima, K. Kimura, and T. Kimura, *Observation of Antiferromagnetic Domains in Cr_2O_3 Using Nonreciprocal Optical Effects*, Phys. Rev. Res. **4**, 043063 (2022).

[32] B. Krichevtsov, V. Pavlov, and R. Pisarev, *Nonreciprocal Rotation of the Polarization Plane of Light in the Antiferromagnet Cr_2O_3 Which Is Linear and Quadratic in the Electric Field*, JETP Lett. **44**, 607 (1986).

[33] T. H. O'Dell and E. A. D. White, *Electric Field Induced Faraday Rotation in Chromic Oxide*, The Philosophical Magazine: A Journal of Theoretical Experimental and Applied Physics **22**, 649 (1970).

[34] B. B. Krichevtsov, V. V. Pavlov, and R. V. Pisarev, *Nonreciprocal Optical Effects in Antiferromagnetic Cr_2O_3 Subjected to Electric and Magnetic Fields*, Zh. Eksp. Teor. Fiz **94**, 284 (1988).

[35] J. Wang and C. Binek, *Dispersion of Electric-Field-Induced Faraday Effect in Magnetoelectric Cr_2O_3*, Phys. Rev. Appl. **5**, 031001 (2016).

[36] R. Hikita, H. Taniguchi, T. Shinkai, and T. Kohmoto, *Dynamics of the Electric-Field Induced Magnetization in Antiferromagnetic Chromium Oxide Observed by Faraday Rotation*, J. Phys. Conf. Ser. **1220**, 012017 (2019).

[37] K. Du, X. Xu, C. Won, K. Wang, S. A. Crooker, S. Rangan, R. Bartynski, and S.-W. Cheong, *Topological Surface Magnetism and Néel Vector Control in a Magnetoelectric Antiferromagnet*, npj Quantum Mater. **8**, 17 (2023).

[38] J. H. Jung, M. Matsubara, T. Arima, J. P. He, Y. Kaneko, and Y. Tokura, *Optical Magnetoelectric Effect in the Polar $GaFeO_3$ Ferrimagnet*, Phys. Rev. Lett. **93**, 037403 (2004).

References

[39] Y. Tokura and N. Nagaosa, *Nonreciprocal Responses from Non-Centrosymmetric Quantum Materials*, Nat. Commun. **9**, 3740 (2018).

[40] R. M. Hornreich and S. Shtrikman, *Theory of Gyrotropic Birefringence*, Phys. Rev. **171**, 1065 (1968).

[41] B. B. Krichevtsov, V. V. Pavlov, R. V. Pisarev, and V. N. Gridnev, *Magnetoelectric Spectroscopy of Electronic Transitions in Antiferromagnetic Cr_2O_3*, Phys. Rev. Lett. **76**, 4628 (1996).

[42] M. Muto, Y. Tanabe, T. Iizuka-Sakano, and E. Hanamura, *Magnetoelectric and Second-Harmonic Spectra in Antiferromagnetic*, Phys. Rev. B **57**, 9586 (1998).

[43] P. S. Pershan, *Magneto - Optical Effects*, J. Appl. Phys. **38**, 1482 (1967).

[44] Y. Kaneko and Y. Tokura, *Floating Zone Furnace Equipped with a High Power Laser of 1 KW Composed of Five Smart Beams*, J. Cryst. Growth **533**, 125435 (2020).

[45] Y. Uemura, S. Arai, J. Tsutsumi, S. Matsuoka, H. Yamada, R. Kumai, S. Horiuchi, A. Sawa, and T. Hasegawa, *Field-Modulation Imaging of Ferroelectric Domains in Molecular Single-Crystal Films*, Phys. Rev. Appl. **11**, 014046 (2019).

[46] T. Hayashida, Y. Uemura, K. Kimura, S. Matsuoka, D. Morikawa, S. Hirose, K. Tsuda, T. Hasegawa, and T. Kimura, *Visualization of Ferroaxial Domains in an Order-Disorder Type Ferroaxial Crystal*, Nat. Commun. **11**, 4582 (2020).

[47] T. Ishibashi et al., *Magneto-Optical Imaging Using Polarization Modulation Method*, J. Appl. Phys. **100**, 093903 (2006).

[48] P. J. Brown, J. B. Forsyth, and F. Tasset, *A Study of Magnetoelectric Domain Formation in Cr_2O_3*, J. Phys. Condens. Matter **10**, 663 (1998).

[49] J. F. Dillon, H. Kamimura, and J. P. Remeika, *Magneto-Optical Properties of Ferromagnetic Chromium Trihalides*, J. Phys. Chem. Solids **27**, 1531 (1966).

[50] S. D. McClure, *Comparison of the Crystal Fields and Optical Spectra of Cr_2O_3 and Ruby*, J. Chem. Phys. **38**, 2289 (1963).

[51] W. Kaiser, S. Sugano, and D. L. Wood, *Splitting of the Emission Lines of Ruby by an External Electric Field*, Phys. Rev. Lett. **6**, 605 (1961).

[52] K. A. Wickersheim, *Optically Observed Exchange Splittings in Antiferromagnetic Cr_2O_3*, J. Appl. Phys. **34**, 1224 (1963).

[53] R. V. Pisarev, B. B. Krichevtsov, and V. V. Pavlov, *Optical Study of the Antiferromagnetic-Paramagnetic Phase Transition in Chromium Oxide Cr_2O_3*, Phase Transitions **37**, 63 (1991).

[54] E. Fischer, G. Gorodetsky, and S. Shtrikman, *Critical Behaviour of the Magnetoelectric Effect in Cr_2O_3*, Le Journal de Physique Colloques **32(C1)**, 650 (1971).

Chapter 6
Summary

In this thesis, we have investigated three different ferroic orders: ferrochiral, ferroaxial, and ferromonopolar orders, focusing on optical phenomena inherent in the respective orders. Here, we summarize the results obtained in each chapter and discuss the future prospects of the research.

In Chapter 2, we demonstrated observation and control of ferrochiral domains in $Ba(TiO)Cu_4(PO_4)_4$ (BTCPO) [1,2]. By obtaining two-dimensional maps of optical rotation (OR) over a wide temperature range, we clearly visualized the formation process of ferrochiral domains in BTCPO. We also investigated the temperature dependence of OR across different wavelengths, leading to the discovery of an unusual temperature-induced sign reversal of OR at 880 nm.

Our successful control of ferrochiral domains was enabled by the irradiation of a focused laser beam. We proposed a possible mechanism of this domain switching in terms of local heating that leads to the reconstruction of domain boundaries. Importantly, this method of controlling domains through laser irradiation does not rely on the conjugate field associated with ferroic ordering, making it a potentially effective way for manipulating domains of other ferroic orders, which have no simple conjugate field, such as ferroaxial order.

It should be noted that the control of ferrochiral order using its conjugate field has yet to be accomplished. Considering the symmetry, irradiation with circularly polarized light should be effective. Recently, the possibility of chirality control by circularly polarized light has been reported in 1*T*-$TiSe_2$ [3]. However, the existence of chirality itself in this material is still under debate [4,5]. It is necessary to validate the effects of circularly polarized light on the control of ferrochiral order in BTCPO and other ferrochiral materials.

In Chapters 3 and 4, we investigated ferroaxial order. In the two ferroaxial materials $NiTiO_3$ and $RbFe(MoO_4)_2$, we successfully visualized ferroaxial domains by spatial distribution measurements of the linear electrogyration (EG) effect [6,7]. This constitutes the first instance of visualizing ferroaxial domains, and it will be a milestone for the advancement of research on ferroaxial order. Furthermore, we examined the influence of phase transitions on domain formation in both $NiTiO_3$ and $RbFe(MoO_4)_2$. This was accomplished by varying the sample's annealing conditions and assessing the temperature dependence of the EG effect. Following our pioneering work, recent studies have reported visualizations of ferroaxial domains using other effects, such as second harmonic generation [8,9] and helicity-resolved Raman spectroscopy [10].

For the further advancement of research on ferroaxial order, it is crucial to realize the following

three subjects:

Firstly, we should explore new phenomena and functionalities inherent in the ferroaxial order. One notable example is the electric-field-induced chirality, as demonstrated in Chapter 4. We reported the discovery of electric-field-induced magnetochiral dichroism in $NiTiO_3$ [11]. Chirality is closely related to the emergence of various phenomena, and ferroaxial materials offer promising platforms for the electric-field-control of such phenomena. In addition, it has been proposed that ferroaxial order induces transverse responses, whereby input external fields result in output conjugate quantities along the direction perpendicular to both the ferroaxial moment and the applied field [12–15]. Demonstration of such transverse responses will be interesting future work.

Secondly it is important to expand the range of ferroaxial materials. Recently, we have demonstrated the exploration of ferroaxial materials by using a regular expression search and the symmetry detection algorithm [16]. Moreover, a chemical guideline for exploring ferroaxial materials has been proposed in refs. [17,18], and ferroaxial order induced by magnetic ordering has been discussed in ref. [19]. We will continue to identify new ferroaxial materials by utilizing these exploration guidelines.

Lastly, the switching of ferroaxial order by applying external fields is of utmost importance. Very recently, it has been reported that the ferroaxial domains of 1*T*-TaS_2 were controlled by triggering the motion of the domain boundaries through the application of an electric field [18]. However, control of ferroaxial order by directly accessing the order itself has not yet been achieved. It should be noted that certain species inducing ferroaxial order (e.g., $4/mmm \rightarrow 4/m$) are also classified as ferrobielastic species, which is one of the secondary ferroics [20]. Thus, the simultaneous application of shear and uniaxial stresses could be promising fields for controlling ferroaxial order.

In Chapter 5, we explored nonreciprocal optical effects in the ferromonopolar antiferromagnet Cr_2O_3 [21]. Through spectral measurements of the electric-induced-Faraday (*E*-induced Faraday) effect and *E*-induced magnetic circular dichroism (*E*-induced MCD), we identified the large enhancements of the effects corresponding to the Cr^{3+} *d-d* transition. Furthermore, we visualized antiferromagnetic (AFM) domains of Cr_2O_3 through spatial distribution measurements of *E*-induced Faraday, *E*-induced MCD, and nonreciprocal rotation of reflected light (NRR). These measurements are performed using tabletop systems and do not require a high-power laser source. Thus, these techniques offer one of the most convenient ways for the visualization of AFM domains in ferromonopolar [diagonal magnetoelectric (ME)] materials. In particular, NRR measurements do not require the application of an electric field and can be performed in the reflection setting. This means they can also be applied to metallic systems. AFM metallics, especially those in which space-inversion and time-reversal symmetries are broken, have gained growing interest due to their potential applications to spintronics devices [22,23]. On the other hand, magnetoelectric couplings have been less investigated in metals because electric polarization responding to a static field is ill-defined. Since NRR is induced by the optical ME effect, measurements of NRR in metallic systems will not be only effective for AFM domain

observations but will also uncover ME coupling in metallic systems.

This thesis demonstrates the crucial role of optical phenomena in investigating ferroic orders. We hope that the achievements made in this thesis will further promote research on ferroic orders.

References

[1] T. Hayashida, K. Kimura, D. Urushihara, T. Asaka, and T. Kimura, *Observation of Ferrochiral Transition Induced by an Antiferroaxial Ordering of Antipolar Structural Units in $Ba(TiO)Cu_4(PO_4)_4$*, J. Am. Chem. Soc. **143**, 3638 (2021).

[2] T. Hayashida, K. Kimura, and T. Kimura, *Switching Crystallographic Chirality in $Ba(TiO)Cu_4(PO_4)_4$ by Laser Irradiation*, J. Phys. Chem. Lett. **13**, 3857 (2022).

[3] S.-Y. Xu et al., *Spontaneous Gyrotropic Electronic Order in a Transition-Metal Dichalcogenide*, Nature **578**, 545 (2020).

[4] C. W. Chuang, Y. Tanaka, M. Oura, K. Rossnagel, and A. Chainani, *Attractive Coulomb Interaction, Temperature-Dependent Hybridization, and Natural Circular Dichroism in 1T- $TiSe_2$*, Phys. Rev. B **102**, 195102 (2020).

[5] H. Ueda et al., *Correlation between Electronic and Structural Orders in 1T−$TiSe_2$*, Phys. Rev. Res. **3**, L022003 (2021).

[6] T. Hayashida, Y. Uemura, K. Kimura, S. Matsuoka, D. Morikawa, S. Hirose, K. Tsuda, T. Hasegawa, and T. Kimura, *Visualization of Ferroaxial Domains in an Order-Disorder Type Ferroaxial Crystal*, Nat. Commun. **11**, 4582 (2020).

[7] T. Hayashida, Y. Uemura, K. Kimura, S. Matsuoka, M. Hagihala, S. Hirose, H. Morioka, T. Hasegawa, and T. Kimura, *Phase Transition and Domain Formation in Ferroaxial Crystals*, Phys. Rev. Mater. **5**, 124409 (2021).

[8] H. Yokota, T. Hayashida, D. Kitahara, and T. Kimura, *Three-Dimensional Imaging of Ferroaxial Domains Using Circularly Polarized Second Harmonic Generation Microscopy*, npj Quantum Mater. **7**, (2022).

[9] X. Guo et al., *Ferrorotational Domain Walls Revealed by Electric Quadrupole Second Harmonic Generation Microscopy*, Phys. Rev. B **107**, L180102 (2023).

[10] G. Liu et al., *Electrical Switching of Ferro-Rotational Order in Nanometre-Thick 1T-TaS_2 Crystals*, Nat. Nanotechnol. (2023).

[11] T. Hayashida, K. Kimura, and T. Kimura, *Electric Field-Induced Magnetochiral Dichroism in a Ferroaxial Crystal*, Proc. Natl. Acad. Sci. *in press*.

[12] S.-W. Cheong, S. Lim, K. Du, and F.-T. Huang, *Permutable SOS (Symmetry Operational Similarity)*, npj Quantum Mater. **6**, 58 (2021).

[13] S. Hayami, R. Oiwa, and H. Kusunose, *Electric Ferro-Axial Moment as Nanometric Rotator and Source of Longitudinal Spin Current*, J. Phys. Soc. Jpn. **91**, 113702 (2022).

[14] J. Nasu and S. Hayami, *Antisymmetric Thermopolarization by Electric Toroidicity*, Phys. Rev. B.**105**, 245125 (2022).

[15] A. Inda and S. Hayami, *Nonlinear Transverse Magnetic Susceptibility under Electric Toroidal Dipole Ordering*, J. Phys. Soc. Jpn. **92**, 043701 (2023).

[16] S. Yamagishi, T. Hayashida, R. Misawa, K. Kimura, M. Hagihala, T. Murata, S. Hirose, and T. Kimura, *Ferroaxial Transitions in Glaserite-Type Compounds: Database Screening, Phonon Calculations, and Experimental Verification*, Chem. Mater. **35**, 747 (2023).

[17] T. Nagai, Y. Mochizuki, S. Yoshida, and T. Kimura, *Chemical Aspect of Displacive-Type Ferroaxial Phase Transition from Perspective of Second-Order Jahn-Teller Effect: NASICON Systems as an Example*, J. Am. Chem. Soc. **145**, 8090 (2023).

[18] T. Nagai and T. Kimura, *Chemical Switching of Ferroaxial and Nonferroaxial Structures Based on Second-Order Jahn–Teller Activity in $(Na,K)_2Hf(BO_3)_2$*, Chem. Mater. **35**, 4109 (2023).

[19] S. Hayami, *Ferroaxial Moment Induced by Vortex Spin Texture*, Phys. Rev. B **106**, 144402 (2022).

[20] R. E. Newnham and L. E. Cross, *Symmetry of Secondary Ferroics. II*, Mater. Res. Bull. **9**, 1021 (1974).

[21] T. Hayashida, K. Arakawa, T. Oshima, K. Kimura, and T. Kimura, *Observation of Antiferromagnetic Domains in Cr_2O_3 Using Nonreciprocal Optical Effects*, Phys. Rev. Res. **4**, 043063 (2022).

[22] T. Jungwirth, X. Marti, P. Wadley, and J. Wunderlich, *Antiferromagnetic Spintronics*, Nat. Nanotechnol. **11**, 231 (2016).

[23] P. Wadley et al., *Electrical Switching of an Antiferromagnet*, Science **351**, 587 (2016).

Acknowledgements

I extend my profound gratitude to all those who have contributed their efforts to the successful completion of this doctoral degree.

First and foremost, I am deeply indebted to my supervisor Prof. Tsuyoshi Kimura, whose invaluable advice and steadfast support have been indispensable. His vast knowledge, rich experience, and benevolence have fueled my resolve to overcome many research challenges. Dr. Kenta Kimura (Osaka Metropolitan University) deserves special acknowledgment for imparting a wealth of experimental techniques and providing insightful comments and innovative suggestions.

Numerous collaborators have bolstered my research. I sincerely appreciate Dr. Uemura, Dr. Matsuoka, and Prof. Hasegawa at the University of Tokyo for supporting the measurements using the field-modulation imaging system, which was crucial in visualizing ferroaxial domains. In particular, Prof. Hasegawa, my secondary supervisor in the MERIT-WINGS Course, provided invaluable discussions. Acknowledgements also extend to Dr. Morikawa and Prof. Tsuda at Tohoku University for conducting CBED measurements in $NiTiO_3$, and to Dr. Urushihara and Assoc. Prof. Asaka at NITech for supplying the crystallographic data of $Ba(TiO)Cu_4(PO_4)_4$. I am thankful to Dr. Hirose at Murata Co., Ltd. for sputtering ITO electrodes on the samples and for his enlightening discussions. My gratitude also goes to Dr. Hagihala at the Materials Science Research Center, Japan Atomic Energy Agency, for his assistance with neutron scattering measurements in $RbFe(MoO_4)_2$.

I owe a debt of gratitude to Prof. Fiebig at ETH Zurich for accommodating my stay with his FERROIC group for five months. My thanks also extend to the FERROIC group members, especially to Ms. Jingwen, Mr. Zemp, and Dr. Wang, for their assistance with my experiments on second-harmonic generation, and to Ms. Thissen for her support during my stay in Switzerland and her administrative assistance.

Moreover, I wish to express my gratitude to all the former and current members of Kimura Lab. Special mention goes to our past and present secretaries - Ms. Endo, Ms. Kaneko, Ms. Okajima, and Ms. Hori, who managed administrative matters; Dr. Misawa, for his Python, Labview, and Igor coding support as well as engaging daily discussions; and Mr. Arakawa, for his help with measurements in Cr_2O_3 and for his stimulating discussions.

This thesis has been financially supported by Research Fellowship for Young Scientists DC2, JSPS, and World-leading Innovative Graduate Study Program for Materials Research, Industry, and Technology (MERIT-WINGS) of the University of Tokyo,

Last but certainly not least, my deepest gratitude is directed towards my family and friends, whose unwavering support throughout my studies has been an unending source of strength and inspiration.